12-2012

Azimuthal Seismic First-Arrival Tomography as a Proxy for Hydraulically Conductive Subsurface Fracture Networks

Matthew Brooks Edmunds
medmunds@utk.edu

To the Graduate Council:

I am submitting herewith a thesis written by Matthew Brooks Edmunds entitled "Azimuthal Seismic First-Arrival Tomography as a Proxy for Hydraulically Conductive Subsurface Fracture Networks." I have examined the final electronic copy of this thesis for form and content and recommend that it be accepted in partial fulfillment of the requirements for the degree of Master of Science, with a major in Geology.

Gregory S. Baker, Major Professor

We have read this thesis and recommend its acceptance:

Ed Perfect, Glenn Tootle

Accepted for the Council:
Carolyn R. Hodges

Vice Provost and Dean of the Graduate School

(Original signatures are on file with official student records.)

Azimuthal Seismic First-Arrival Tomography as a Proxy for Hydraulically Conductive Subsurface Fracture Networks

A Thesis Presented for the
Master of Science
Degree
The University of Tennessee, Knoxville

Matthew Brooks Edmunds
December 2012

DEDICATION

This thesis is dedicated to my father, Phillip H. Edmunds, who taught me the value of a questioning, scientific mind and encouraged me to use this outlook as a tool to explore, understand, and appreciate the wonder of the natural world.

ACKNOWLEDGEMENTS

First, I would like to thank my thesis committee; Dr. Gregory S. Baker, Dr. Ed Perfect, and Dr. Glenn Tootle, for all of the help and ideas along the way in creating this body of work. I would also like to extend a heartfelt thanks to my primary advisor, Dr. Greg Baker, as well as the Department of Earth and Planetary Sciences for pulling for me through this process, and helping out with the appropriation of GTA appointments on a semester by semester basis, such that I could continue this work and complete my thesis.

I would also like to thank all of the people who have helped me collect my data in the field, Christian Hunkus, Rachel Storniolo, Bart Weitering, Cliff Mauroner, and Kaleb Flem. There were many hot and miserable days in the sun with little respite but the good humor of those involved, and the great attitudes and companionship made the task much more bearable.

Finally, I would like to thank the folks at the Oak Ridge National Lab. Dave Watson, Tonia Mehlhorn, Kenneth Lowe, and Scott Brooks were all invaluable in their help with site locations, research direction, and safety training, which are all essential aspects of working successfully in the area.

ABSTRACT

The Oak Ridge Field Research Center (ORFRC) was established by the Environmental Sciences Division (ESD) at the Oak Ridge National Laboratory (ORNL) in Oak Ridge, TN, in order to study the various biogeochemical processes involved in the remediation as well as natural attenuation of a large contaminant plume that is extant in the vicinity of the ORIFRC. A part of this work has been to characterize the movement of this groundwater/contaminant plume with the use of azimuthal seismic first-arrival tomography (ASFT).

Within the general area of the ORIFRC, a 0-2 m layer of generally isotropic anthropogenic fill and unconsolidated soil overlies the deeper structural elements caused by the folding that formed the Valley and Ridge region of East Tennessee. Beneath this layer of fill, a fractured shale transition zone from saprolite to competent bedrock exists. It is suspected that this fracture network forms anisotropic flow conditions where contaminants exist beneath the surface layers.

In an effort detect fracture-driven hydrologic anisotropy, we have collected surface SFT profiles at 10° intervals around a central point at the NT-2 site at ORNL. Each seismic survey consisted of a 96-channel survey with a 0.5 m offset, and shot points located at every fourth receiver along the line. The resultant tomograms were converted from XZ plane cross-sections to XY plane cross-sections. The resultant map-view velocity profiles showed a dramatic decrease in seismic isotropy with depth, as well as delineating the

saprolite/bedrock transition zone at the NT-2 site. Two additional datasets have been collected approximately one half kilometer (Km-1 site) and one kilometer (Km-2 site) down valley from NT-2. Both of these datasets agree with the direction and degree of anisotropy present at the NT-2 site, and both were able delineate the transition between saprolite and competent bedrock, underscoring the efficacy and replicability of this experimental method. All of these datasets were compared to measured fracture set orientations in trenched saprolitic shale as well as measured hydrologic anisotropy with positive results in order to establish the accuracy of ASFT relative to conventional methods of hydrologic testing.

TABLE OF CONTENTS

LIST OF TABLES

LIST OF FIGURES

CHAPTER 1: INTRODUCTION

1.1 Introduction

Seismic first-arrival tomography (SFT) has become a powerful tool in the non-destructive investigation of subsurface geological, geothermal, and hydrological characteristics at numerous sites around the world (e.g., Bregman, et. al, 1989; Heincke et. al, 2006; Lanz et. al, 1998; Morey and Schuster, 1999; Watson et. al, 2005; Zelt et. al, 2006; and Zollo, et. al, 1998). The versatility of SFT can provide new insight into subsurface features since spatial imaging resolution has increased with new processing techniques and raypath modeling algorithms. Much work has been done in locating subsurface voids, karst features and water bodies (eg. Gaines, 2011; Watson, et al., 2005; Chen et al., 2010); however, few if any investigations have been conducted in the use of SFT for the detection of smaller-scale shallow subsurface anisotropic features such as fracture and lineation networks.

The S-3 Pond site in the Bear Creek Valley of the Oak Ridge National Laboratory (ORNL) in Oak Ridge, TN, was built in 1951 as a repository for waste associated with the activities of ORNL at the time. Disposal of waste materials such as uranium, technetium, nitrates, and other heavy metals continued from the ponds' inception in 1951 until 1983. At this point, the ponds were denitrified, drained, and capped, but the fact that the ponds were not lined led to the formation of a large secondary pollution plume that extends well east of the pond location roughly parallel to geologic strike into the Bear Creek Valley.

The Oak Ridge Integrated Field Research Challenge (ORIFRC) program was established in 2007 by the United States Department of Energy in order to investigate contaminant flow pathways caused by the anthropogenic activities in and near the S-3 pond site. It is believed that the contamination plume emanating from beneath the S-3 site flows along a preferred subsurface hydraulic conduit directly through an area known as the NT-2 site. The nature of contaminant flow in and around the NT-2 site, however, is not fully understood.

The purpose of this investigation is to use azimuthal seismic first arrival tomography (ASFT) in an effort to characterize subsurface fracture networks down gradient from the S-3 ponds at the NT-2 site and beyond (e.g., two additional sites, Km-1 and Km-2). The fracture networks are suspected to be hydrologic drivers that divert subsurface flow away from the expected down-gradient flow direction and add a component of horizontal transmissivity to the flow regime. With ASFT, we confirm the presence of this hydrologic anisotropy as well as determine its direction and, to some extent, its relative directional influence.

1.2 Motivation

During initial site characterization for remediation (as well as other) efforts at any site, initial models are created in order to understand the shallow subsurface hydrologic flow regime. This understanding of the subsurface hydraulic flow can have an effect on future decision making with respect to the

future direction of any project in question. The problem with this procedure is that, often, erroneous values are incorporated into these initial hydrologic models that lead to inaccuracy in the model. With an inaccurate subsurface hydrologic model, any suppositions made are no more than conjecture on the part of the scientists working on the site. As a specific example, sites are often considered to be hydrologically isotropic for the sake of simplicity in the creation of initial models, which leads to inaccurate prediction and limits the functionality of the model.

Isotropy is generally assumed because it is very expensive and time consuming to determine whether anisotropy exists at the site, given the current methodology of drilling boreholes and conducting pump tests. This type of testing is invasive to the *in-situ* environment, and can affect the measurements being taken, as well as being very time consuming, expensive (particularly as multiple wells are necessary for the detection of hydrologic anisotropy) and counterproductive to remediation efforts. With this new seismic methodology for determining subsurface hydrologic anisotropy, a non-invasive “quick and dirty” characterization of any given site can be conducted at a fraction of the expense, temporally and fiscally, of the established methods. A survey of this type could be conducted, processed and interpreted within one or two weeks at an approximate investment of $100,000 for equipment costs. However, this fiscal investment is a singular commitment, and any number of subsequent surveys could be collected with minimal equipment maintenance cost. As another alternative, this type of

work could be subcontracted to an organization specializing in geophysical data collection and interpretation. This alternative would be more expensive as a long term solution, but would not require in-house knowledge, experience, or equipment in the contracting organization.

1.3 Objectives

The primary objective of this study is to determine whether azimuthal seismic first arrival tomography (ASFT) is a viable method for the detection and characterization of fracture-driven anisotropy at the NT-2 site at the Oak Ridge National Laboratory. The work represented in this study has two primary components: 1) conducting a feasibility and proof of concept investigation in an area with fairly well known geological and hydrological parameters, 2) to apply the aforementioned methodology to areas down gradient within the same stratigraphic rock in an effort to determine the “real-world” value of this method and whether it is feasible to use in sites with unknown hydrology and geology.

The use of SFT as a method by which to investigate hydrogeological parameters *in situ* is a relatively new concept, but has been demonstrated in the detection of perched water bodies as well as injected water plumes (e.g., Gaines 2011). Efforts have been made by some to use azimuthal electrical resistivity in order to study subsurface fracture networks and/or hydrogeological anisotropy (e.g., Carlson 2010, Boadu 2005) with good success. The electrical resistivity method does have some drawbacks, however. Dry joint sets or very low salinity

fluid could reduce the influence of the fracture sets in the data, for example. The objective of this study is to determine whether ASFT is an effective method to measure these subsurface fracture networks that could (and often do) influence subsurface hydrology. We will accomplish this by comparing collected ASFT datasets to measured fracture orientations as well as measured directions of hydrologic anisotropy within the Bear Creek Valley at ORNL.

1.4 Hypotheses

This research will include two related hypotheses: (1) ASFT will provide a methodology for the delineation of anisotropic zones based on seismic velocity variations governed by interconnected fracture networks, and that this seismic information can be used as a proxy for preferred fracture driven hydrogeological flow direction, and (2), the ASFT methodology will prove accurate (relative to conventional methods) for characterizing vertical zones of anisotropic flow of the NT-2 site and two other sites at the ORIFRC within the Oak Ridge Reservation.

The premise of these hypotheses is that seismic energy travels faster in a direction parallel with fracture sets and slower in a direction perpendicular to them. This is the case because as a seismic wave encounters a fracture in parallel, some amount of the energy is transmitted through the matrix media, while some of the energy is transmitted through the fracture (which could be air filled or filled with some type of material, i.e., water, clay, etc.). The energy that travels through the lithified media between the fractures will retain media dependent velocity (which is faster than velocity through a fracture) and will not

be affected (insofar as first arrival time) by the low velocity zones that the fractures represent. When propagating seismic energy encounters a fracture set perpendicular to its travel direction, it is inevitably forced to cross the low velocity zone caused by the fracture, and will therefore have a slower first arrival time, as there are no seismic “fast lanes” in this scenario (Fig 1). This phenomena takes place both above and below the water table. Air filled fractures (above water table) would represent a seismic low velocity zone relative to the matrix media. Below the water table, the fractures and matrix media would be water filled, and so the same principal would apply. The only case where a fracture may be water filled while the surrounding matrix material would not be saturated would be during the early stages of a stormflow event, and regional drainage through the vadose zone or oversaturation of the vadose zone due to increased infiltration would quickly create a homogeneous environment with respect to matrix/fracture saturation, and thus not critically affect seismic velocity.

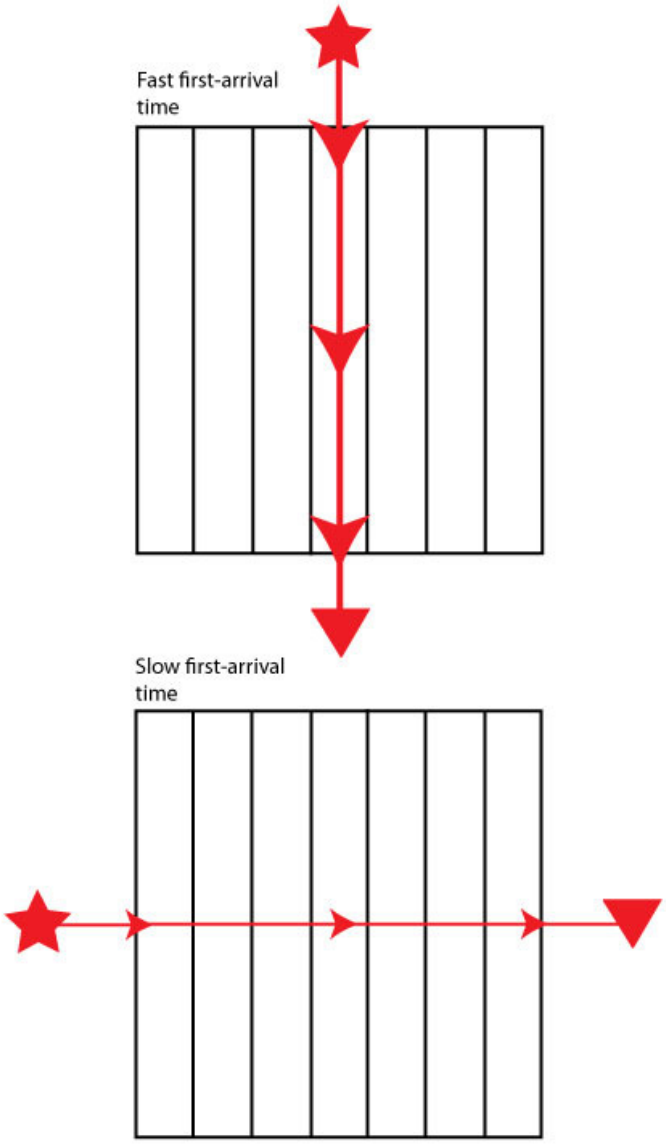

Figure 1: A map view schematic of the behavior of seismic energy as it encounters a fracture set. The source is represented by the star and the receiver is represented by the triangle.

CHAPTER 2
GEOPHYSICAL TECHNIQUES AND METHODS

2.1 Seismic first-arrival tomography

Seismic first-arrival tomography is a geophysical method that utilizes measured travel times from a seismic source to a series of receivers (geophones) to construct a 2D cross-sectional velocity model of the subsurface. Travel times (i.e., a function of seismic velocity) are affected primarily by the mechanical properties of subsurface media, most notably bulk modulus, shear modulus, and density (*see* Gaines, 2011). The fundamental physics that dictate wave propagation in the subsurface are fairly simple, and follow Snell's law of refraction at rheological boundaries. At some critical incident angle, the refracted wave travels along a layer boundary in the subsurface at the velocity of the deeper (faster) layer, and sends a wave front (head waves) back to the surface be picked up by the receivers (Fig. 2). This process depends on the fact that deeper layers in the subsurface typically have higher seismic velocities than shallower layers.

The geophones are used to measure the amplitude response of incoming energy from the subsurface, and capture the time that energy takes to arrive from the shot. These data yield a waveform for each geophone that yields the elastic wave amplitude fluctuations through time for each position on the surface. The first-arrival time of energy from the shot at each geophone is manually picked, and this information is used to create an inverted velocity model of the subsurface.

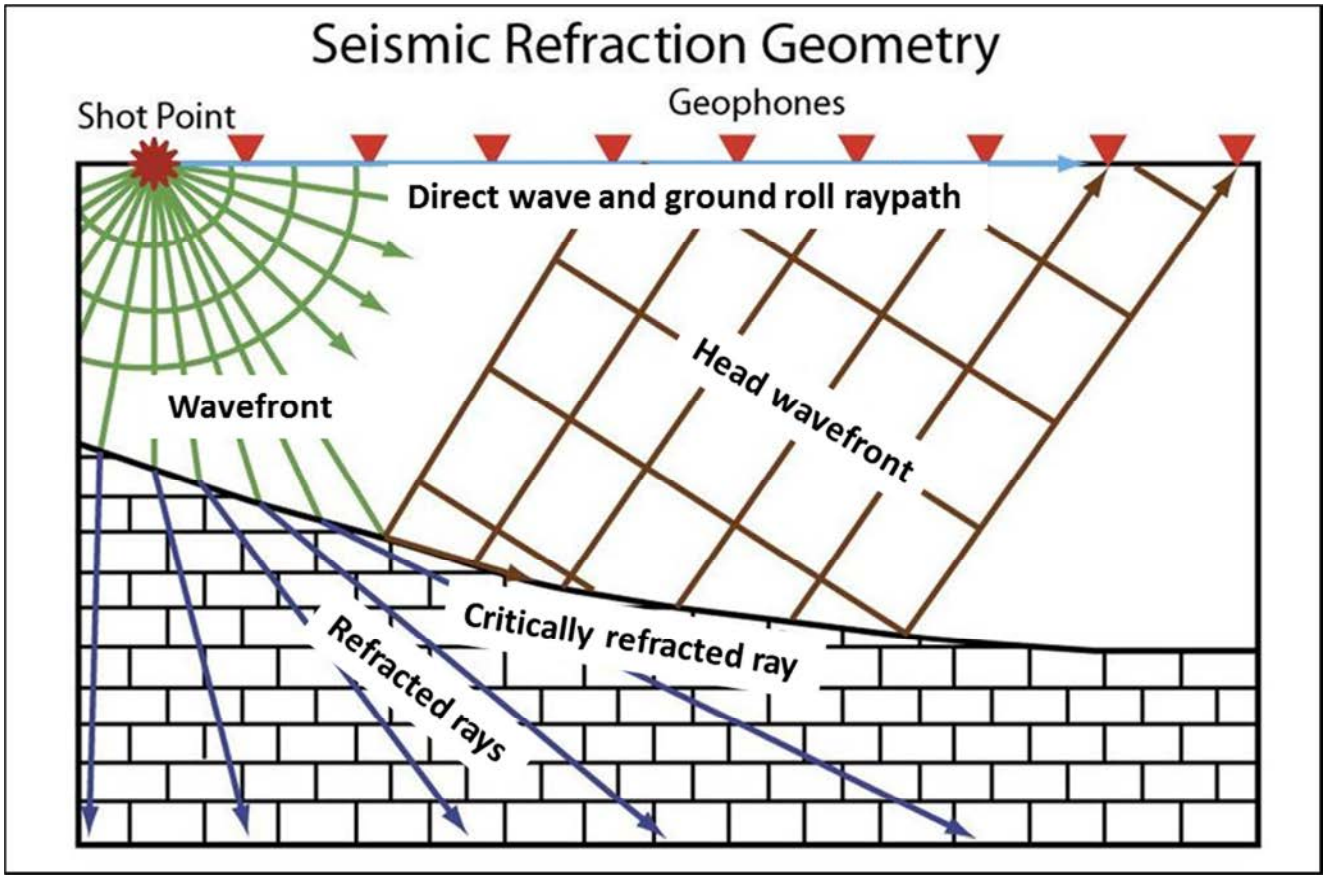

Figure 2: A visual representation of the geometry of seismic refraction. From the shot point, the ground roll raypath moves along the surface while the direct waves propogate into the subsurface. As the direct wavefront encounters a velocity boundary, its energy is refracted deeper into the subsurface, until the incident angle of the incoming energy causes it to refract along the velocity boundary. This ray causes the head wavefront to propagate back towards the surface at a higher velocity than that of the direct wavefront.

There are several methods of creating these inversion models, including but not limited to least squares approaches (Aki et. al, 1977), back projection methods (Humphreys, 1988), as well as variations and combinations of these basic techniques. For this study, we use the WET (Waveform Eikonal Traveltime) inversion technique (Schuster, 1993). The WET method is numerically more suited to creating an accurate velocity gradient (horizontally as well as vertically) rather than to, delineate discrete horizontal velocity boundaries.

2.1.1 Acquisition methods and Parameters

The purpose of this study is to ascertain whether seismic first-arrival tomography is a suitable method to detect hydrologic anisotropy. To this end, it was decided to conduct a series of seismic transects that rotated around their center points at 10° intervals in order to get full 360° coverage in the resultant velocity models (Fig. 3). Each individual seismic line varied from 36 m to 48 m, depending on the physical constraints of the particular site where the surveys were conducted. In each case, the longest line possible was used, as the limiting factor for depth penetration is maximum line offset. Every line had a geophone spacing of 0.5 meters, and shot points were taken every 2 m (every fourth geophone) with a hammer-strike energy source for all seismic lines. While 0.5 m geophone spacing is not commonly used for this type of work, it was decided upon because this is a new methodology, and higher spatial resolution than necessary was preferable to lower resolutions given the time each radial survey takes to collect.

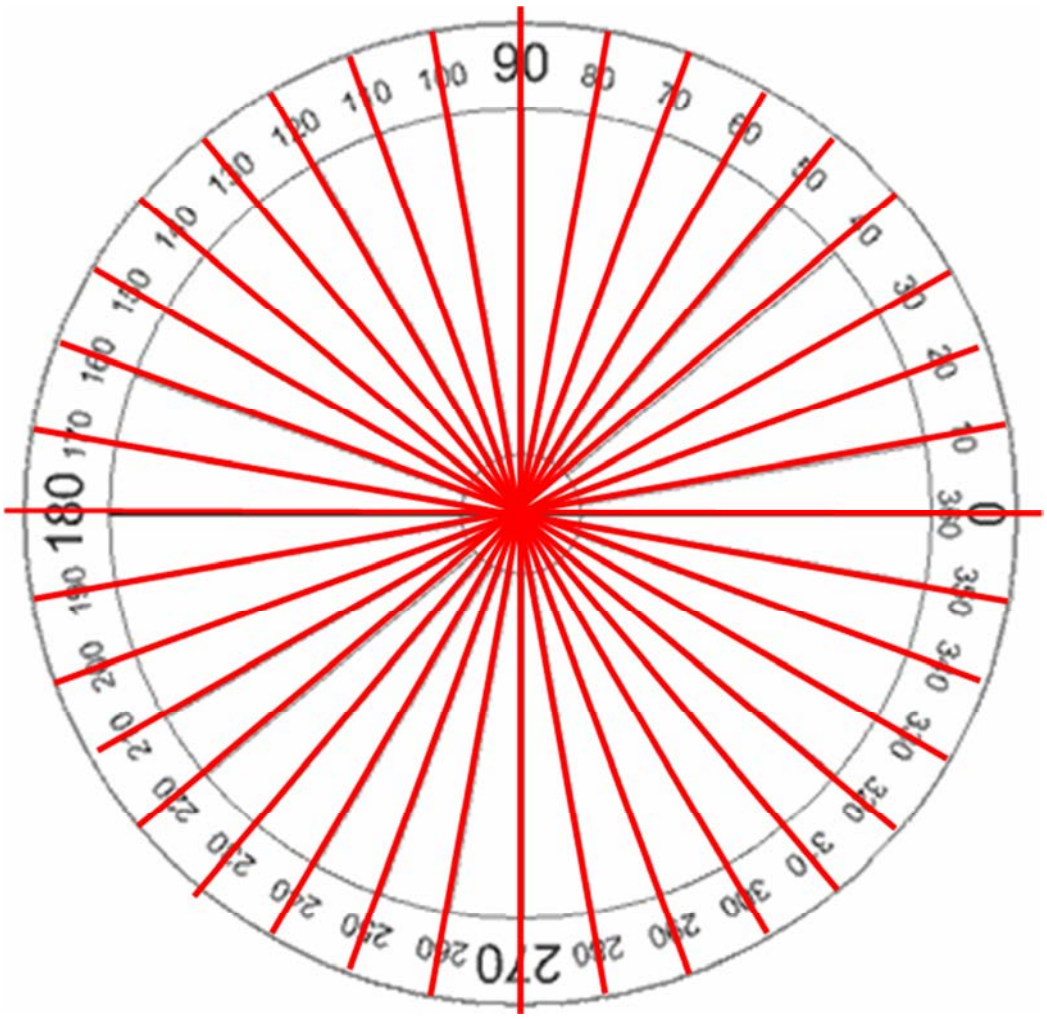

Figure 3: A conceptual model of an azimuthal seismic survey in map view. Each red line represents an individual seismic profile, and these profiles rotate around their centerpoints at ten degree intervals.

The equipment used to collect these data in the field is standard, and consists of up to four Geodes™ (manufactured by Geometrics, Inc.), which are portable seismographs that each allow for a maximum of 24 input channels, giving this system a maximum of 96 input channels. These Geodes are attached to take-out cables that are then attached to the individual 40-Hz Mark Products geophones. The Geodes are connected to each other in series, with three "slave" units all connected linearly to a "master" unit by data cables. Also attached to the master Geode is a hammer cable that ends in a trigger device such that the recording begins within fractions of a millisecond of the impact of the hammer. A laptop computer is connected to the master Geode, and allows for real time observation and manipulation of the waveform data as well as acquisition parameters. All of the aforementioned equipment is powered in the field by 12V deep cycle marine batteries.

While collecting data in the field for this research, the record length for each shot was 0.25 s, and the sampling interval for each record was set at 0.125 ms. The data at each shot point was stacked to improve signal to noise ratio on the final waveform, and the number of stacks varied from 2 to 5, depending on ambient noise levels in the external environment. As a general rule, the lowest number of stacks possible was used that produced a waveform from which the first breaks could easily be identified. The critical measurement in SFT data is the arrival time; thus, fluctuations in the amplitude of that arrival are not critical

and variability from stacking or by changing the individual who is using the hammer is relatively unimportant. The key issue is simply generating sufficient energy that a first arrival is clearly detected above the background noise.

2.2 Tomographic processing

In order to generate an accurate tomogram of the subsurface, a variety of processing steps must be undertaken. The raw waveform data must be manually observed and first arrival times must be picked for each geophone waveform (i.e., seismic trace). This process must be repeated for each shot point along a survey. The picked first-arrival data (representing the fastest travel time for every shot-geophone pair in the entire experiment) must then be imported into some inversion software suite, and the arrival times are used to generate a velocity model of the subsurface. After the velocity models for each line have been generated (which is standard for any SFT survey), they must be further manipulated for ASFT analysis to generate “map view” velocity distributions at discrete depth intervals in the subsurface.

2.2.1 Picking first arrival times

The first step in the processing workflow is to manually pick the first arrival times of the energy that is propagated outward from the shot point. Each trace on the dataset corresponds to the geophone that samples the arriving energy, and forms the horizontal axis of the dataset as source-to-receiver distance in meters. The vertical axis of the dataset is time in milliseconds, and so the

distance travelled away from the shot point and the time taken for that travel can easily be seen for each geophone placement. The amplitudes of the wavelets are generally increased, normalized, and clipped for ease of interpretation-as previously noted, the time of the arrival is the critical parameter, not the amplitude of the arrival. The arrival time is chosen for each trace along the waveform. This is repeated for each shot point in the survey to generate a pick file encompassing every source/receiver pair that is then used to generate a velocity tomogram. For one ASFT survey described in this research, eighteen pick files must be generated, one corresponding to each seismic transect in the survey. An example of a picked waveform can be seen in Figure 4.

2.2.2 Importing data into Rayfract™

Once the first arrivals have all been determined, they must be imported into some type of inversion software. In this case, we have used the Rayfract™ software package. This package was selected over other available tomographic inversion packages because it utilized the WET algorithm that is ideally suited to sensitivity in both the vertical and horizontal directions.

The first step in importing the data is to create a header file for the tomogram that is to be generated. This header includes survey geometry, equipment used to collect the data, dates and times of data collection, and the name of the group or individual that conducted the survey. Once the header file has been created, the pick file from each shot point along the survey line is individually imported through the software's GUI.

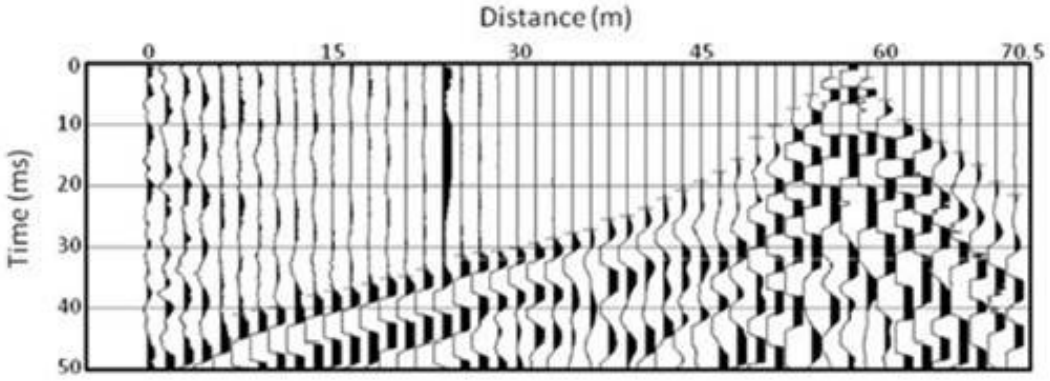

Figure 4: An example of seismic waveform data moving outward from the shot point in time. The x-axis is distance in meters and the y-axis is time in ms. The horizontal lines at the top of each wavelet are the manually picked first arrival times.

2.2.3 Generating the velocity tomogram

Once the data have been imported, an initial velocity gradient model must be determined. This model is generated using the XTV inversion technique (Gawlas, 2001), where three separate methods are utilized for the velocity calculations: Modified Dix inversion, Intercept Time inversion, or Delta-t-V inversion. The inversion method used depends on the circumstances present in the data. The previously inputted pick files are sorted by common midpoint (CMP) and then by unsigned offset (described in detail in Diebold and Stoffa, 1981), and then input into the XTV algorithm, and the appropriate inversion method is applied.

The Modified Dix inversion is used in the instance of a reflected wave, and as such, is not often appropriate to near surface geophysics (e.g., Sheriff and Geldart, 1982). For this technique, the layer thickness, h, and average layer velocity, v, are calculated using equations (1) and (2) respectively:

$$h = \frac{\Delta}{2}\sqrt{\frac{Vt}{\Delta} - 1} \qquad (1)$$

$$v = \sqrt{\frac{V\Delta}{t}} \qquad (2)$$

Where: Δ = unsigned offset between shot point and receiver
t = traveltime between shotpoint and receiver, separated by offset Δ.
V = measured apparent velocity at the bottom of the layer

The Intercept time inversion assumes that there is the critical refraction and that both the overburden and basement layers have a constant velocity. For these reasons, this method is commonly used in near surface geophysics when layer boundaries are the target of investigation (Sheriff and Geldart, 1982). This method calculates layer thickness (h) using equations (3) and (4):

$$\tau = t - \frac{\Delta}{\mathrm{V}} \tag{3}$$

$$\mathrm{h} = \frac{\tau}{2\sqrt{\left(1/v_1\right)^2 - \left(1/V\right)^2}} \tag{4}$$

Where: Δ = unsigned offset between shot point and receiver
t = traveltime between shotpoint and receiver, separated by offset Δ
τ = intercept time
v_1 = velocity of the overlying (previously determined) layer
V = measured velocity at the bottom of the layer

The Delta-t-V (Gradient layer inversion method) assumes a diving wave ray as well as a constant velocity gradient, creating a raypath that dives in a gradient velocity field and then returns to the surface (Lay and Wallace, 1995). This method can also (in some cases) account for velocity inversions in the subsurface. In this model, the velocity is a function of depth, z, and adheres to the following equation (5):

$$\mathrm{v(z)} = \alpha \cdot z + v_0$$

Where: α = rate of change in velocity
v_0 = velocity at the top of the modeled layer
Z = depth in meters

Given that the velocity gradient is assumed constant, the circular arc followed between the shot point and the receiver is described with equations (6) and (7):

$$\Delta(v) = \frac{2}{\alpha}\sqrt{V^2 - v_0^2} \quad (6)$$

$$t(v) = \frac{2}{\alpha} arc\left(\frac{V}{v_0}\right) \quad (7)$$

and the layer thickness (h) is calculated by equation (8):

$$h = \frac{\Delta}{2}\sqrt{\frac{V - v_0}{V + v_0}} \quad (8)$$

Where: α = rate of change in velocity
z = depth
v_0 = the velocity of the overlying (previously determined) layer
V = the measured velocity at the bottom of the layer

The inversion method used for the creation of the initial velocity model varies based on conditional factors in the data. All three equations are used to calculate the velocity, and then the most appropriate solution is selected based

on the strengths of each method. Namely, the Modified Dix method is used if there are reflections in the data, the Intercept Time method is used if there are dramatic increases in velocity (indicative of a layer boundary and critically refracted waves), and the Delta-t-V method is used in the event that there are velocity inversions. Any of these methods will produce a gradient velocity model (Fig. 5) that is then compared to the measured travel times in order to begin optimizing the tomographic model.

After generating the initial model, the eikonal equation (Schuster and Quintus-Bosz, 1993) is solved iteratively using the least squares method over a series of adjacent nodes (representing the subsurface over the area of the survey) in order to determine the minimum travel time possible between any given source-receiver pair. This process is repeated for all source-receiver pairs for which real data was collected.

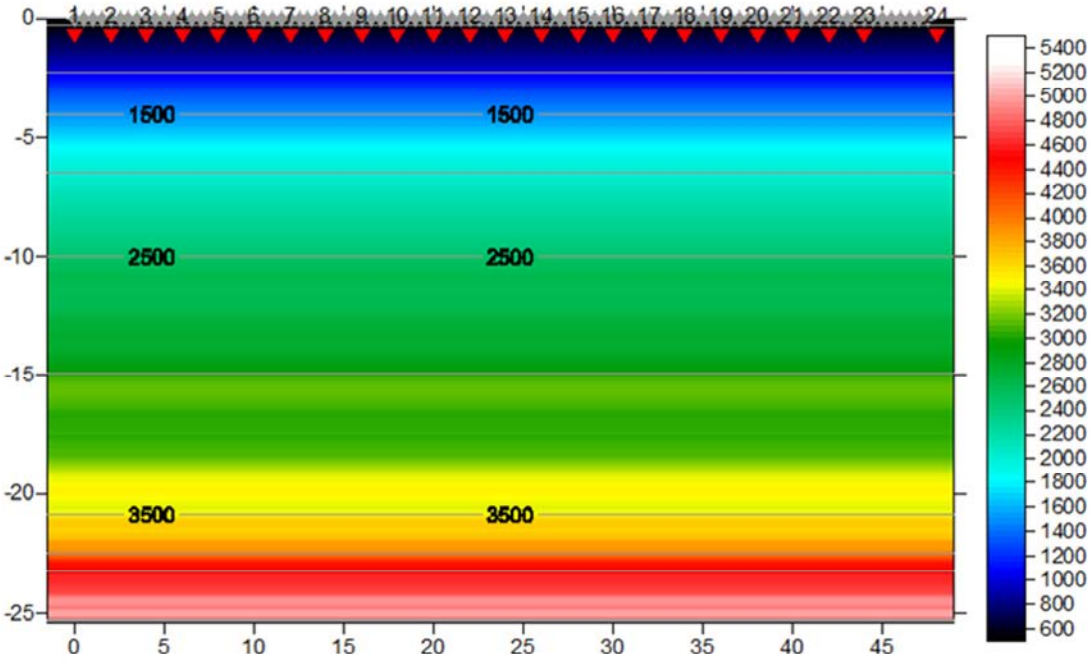

Figure 5: An example of an initial gradient model produced using the XTV inversion scheme.

These travel times, once calculated from a given source point and receiver point, are recalculated with the source and receiver switched. The two calculated travel times are then subtracted, and then added to the observed travel time of the original source-receiver pair, yielding a minimum travel time and pathway from the source to the receiver (raypath). This process is repeated for all source-receiver pairs, and the end result is a raypath coverage diagram (Fig. 6) that shows the raypaths going from all shot points to all receivers in the survey. This raypath coverage diagram, along with the initial velocity model, is used for the creation of the final inversion (Fig. 7).

The WET inversion scheme differs from other ray-tracing methods, in that it uses “fat rays” that are modeled after finite frequency effects such as diffraction and scattering using the Fresnel volume approach (Watanabe, 1999). This method models the propagation of first-break energy in a more physically realistic way than “thin-ray” methods (Rohdewald, 2010). The WET algorithm forward models synthetic travel times to all grid nodes using an Eikonal solver (Lecomte, 2000), and the travel time residuals are then back-projected along calculated raypaths. This process is repeated for all source-receiver pairs and the raypaths are updated with this information, completing the first iteration of the inversion process (Gaines, 2010). These steps are repeated iteratively until the model reaches convergence (which is a manually set threshold value of RMS error in the tomographic inversion) or the set number of iterations dictated by the user. Often, model convergence is reached with relatively few iterations (10 or so), but

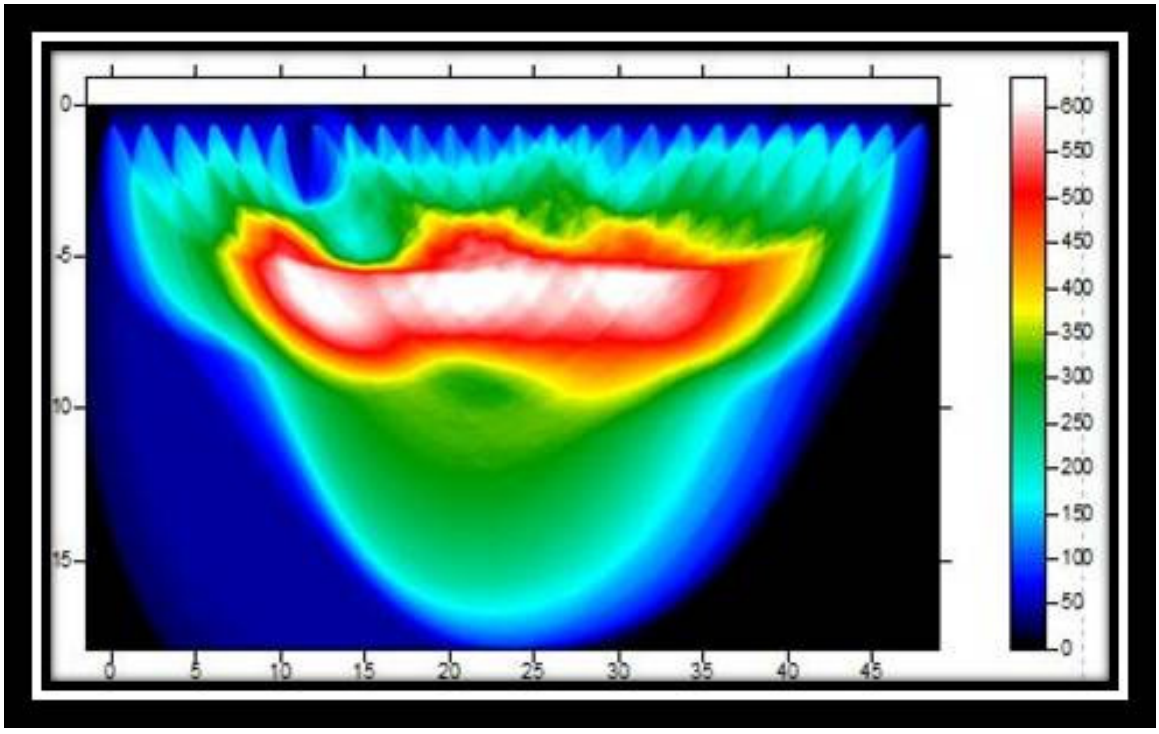

Figure 6: An example of a raypath coverage model produced with the XVT inversion method. Raypaths from all shot points to all recievers are shown along with intersection density.

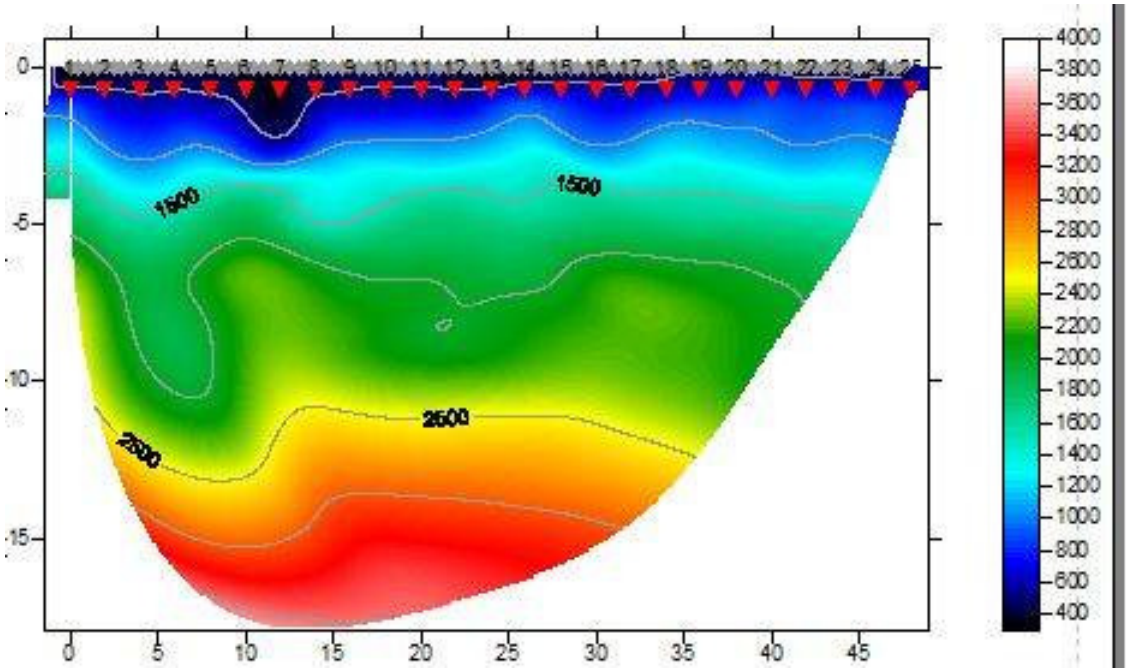

Figure 7: An example of a final velocity model produced by WET inversion.

for this study, 75 iterations were set so that the velocity gradients would smooth out and produce a more highly resolved set of horizontal velocity maps. For this experiment, a large number of iterations were preferable, but often using too many iterations can smooth out velocity features in the subsurface.

2.3 Post processing to generate radial plots

In order to gain an idea of the degree of anisotropy detected by this methodology, and the critical innovative step in the ASFT method in addition to the survey design, the data have to be converted from XZ plane cross sections to XY plane velocity "maps" at discrete depths. To do this, horizontal "slices" of all eighteen seismic surveys are taken with the intersecting center point as the common tie point between all of the lines. These slices are taken at discrete depth intervals, and in this fashion, the nature of isotropy/anisotropy can be studied azimuthally as a function of depth, or the conditions can be observed at any particular depth of interest.

2.3.1 Re-gridding tomographic data

In order to create radial plots of the data, the data have to be changed to a format that is more easily manipulated. The first step in transforming this data to a useable format is to convert all of the velocity grids into XYZ files. This is accomplished by simply saving the velocity grid as an XYZ data file in Golden Software's Surfer™ package. All of the velocity grids could then be opened in a spreadsheet format. The XYZ files list X as the horizontal position along the

seismic line, Y as depth, and the Z coordinate is the seismic velocity for that particular XY coordinate location. A single tomographic dataset will produce an XYZ file with 250,000 to 300,000 entries with irregular depth intervals based on the total number of nodes generated in the tomographic inversion process. The data, then, must be re-gridded within Surfer. For this work, the data were re-gridded into depth intervals of 0.5 m, cutting out a large portion of unneeded data and making the size much more manageable. The new grid still left all X coordinates in the data, and the only X coordinate of interest for this study is that where all of the lines intersect at the center point of each line. While the value of this X location changed based on survey length, the target coordinate was always the center point of the survey in question. To restrict the data to only those points at the center of the survey lines, the re-gridded data were imported into Microsoft Excel™ and filtered such that only the sought after X coordinate remained. This process was repeated for each line in the survey and transformed into a usable spreadsheet (Table 1). Depth formed rows, and azimuth the columns, while velocity at a given depth and azimuth filled in the sheet. This format allows for simple transformation and manipulation of the data, as well as ease in running validation statistics.

2.3.2 Generating compass diagrams in Matlab™

After the data have been re-gridded and organized, some form of visual presentation is necessary to easily observe any anisotropic condition that may

	0 deg	10 deg	20 deg	30 deg	40 deg	50 deg
0	367.7815	376.0783	401.058	475.1351	386.1914	367.19
-0.5	353.5864	377.6278	359.3279	320.7229	282.7269	272.5261
-1	367.495	385.0235	336.9215	258.4604	278.3167	283.0149
-1.5	426.6717	450.3713	394.1753	301.116	388.4817	417.0759
-2	513.4367	534.7734	495.8978	399.5523	436.9227	555.1789
-2.5	600.8987	628.9207	635.16	604.9723	449.8707	650.43
-3	697.6045	732.0157	797.0992	952.2737	544.5504	726.0111
-3.5	805.8148	853.99	962.3544	1364.92	829.8376	802.7599
-4	936.7751	1014.006	1103.732	1287.293	1153.277	902.3145
-4.5	1098.803	1210.385	1208.949	938.3366	1333.738	1034.989
-5	1267.686	1416.765	1296.209	916.6005	1428.893	1231.491
-5.5	1473.507	1598.728	1387.314	1411.658	1460.183	1454.127
-6	1758.504	1813.997	1497.562	2025.127	1552.89	1663.416
-6.5	1966.316	2112.06	1656.649	2301.369	1697.302	1827.408
-7	2067.335	2315.838	1888.094	2466.383	1851.811	1937.61
-7.5	2167.596	2384.256	2213.209	2583.39	1974.853	2021.658
-8	2300.148	2420.124	2526.166	2629.761	2045.532	2105.492
-8.5	2453.924	2480.085	2766.607	2681.767	2077.057	2201.25
-9	2601.237	2569.107	2929.224	2728.684	2092.518	2303.659
-9.5	2702.234	2648.494	3073.586	2642.414	2101.339	2414.537
-10			3242.896	2561.885	2135.223	2549.508
-10.5			3401.638	2558.105	2217.34	2680.44

-11			**3532.077**	**2616.235**	**2266.265**	**2793.825**
-11.5			**3613.781**	**2721.938**	**2336.673**	**2916.644**
-12				**2861.775**	**2528.964**	**3049.953**
-12.5				**3022.11**	**2760.126**	**3180.158**
-13				**3187.457**	**2967.18**	**3314.853**
-13.5				**3345.959**	**3136.651**	**3452.861**
-14				**3489.936**	**3275.197**	**3576.715**
-14.5				**3615.855**	**3407.007**	**3660.334**
-15				**3725.812**	**3515.203**	
-15.5				**3827.837**		
-16				**3933.89**		
-16.5				**4051.758**		
-17				**4178.99**		
-17.5				**4315.095**		
-18				**4455.554**		
-18.5				**4588.385**		
-19				**4705.952**		
-19.5				**4809.887**		
-20				**4909.896**		
-20.5				**5013.06**		**……**

Table 1: An example of the Excel spreadsheet used to manipulate the data. Columns are azimuth and rows are depth.

emerge from the dataset. In order to graphically depict the velocities at the central intersection point of all seismic lines, a compass diagram was decided upon as the ideal form. This is a relatively straightforward graphic, similar to a polar plot, but the seismic velocities at each azimuth are depicted as a vector magnitude, with direction indicating azimuth and length describing the magnitude of the seismic velocity (Fig. 8). These images are relatively simple to create in Matlab™ (see Appendix 4 for code), although the resolution of the output image is rather poor. In order to combat this problem, the images were imported into Adobe Illustrator™, and a sharper image was overlaid. The Adobe images took a slightly different form than the Matlab images, having red dots at the endpoint of each vector arrow, but should be read the same way and yield a much cleaner and sharper final image (Fig. 9).

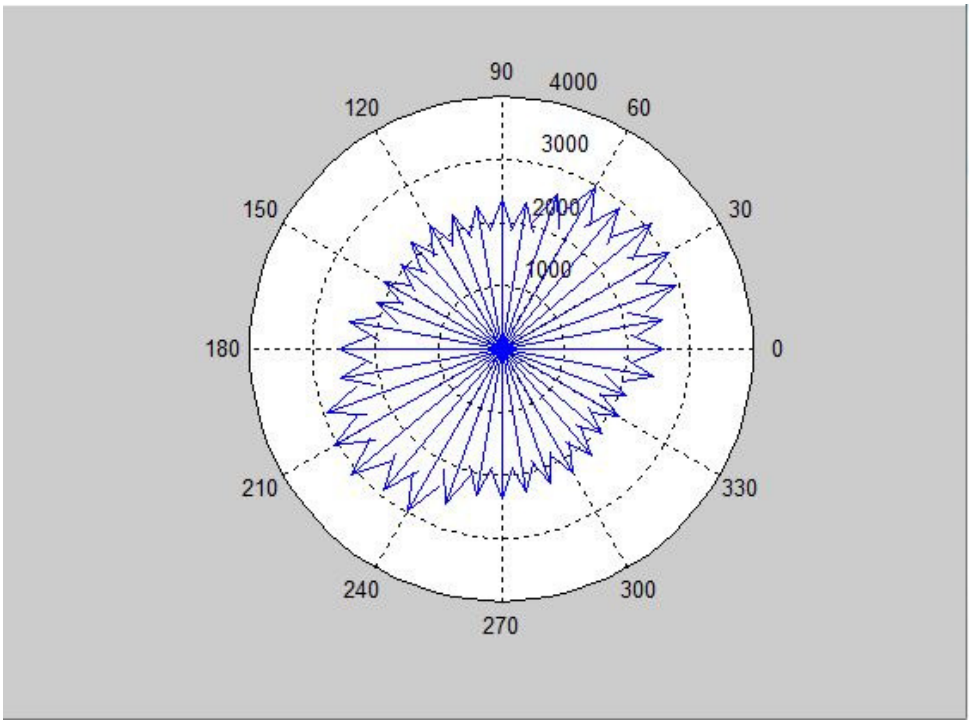

Figure 8: An example of an output compass diagram from Matlab. This particular image represents the horizontal anisotropy at the NT-2 site at a depth of 10.5 m. Fractures in the long direction would increase the seismic velocity.

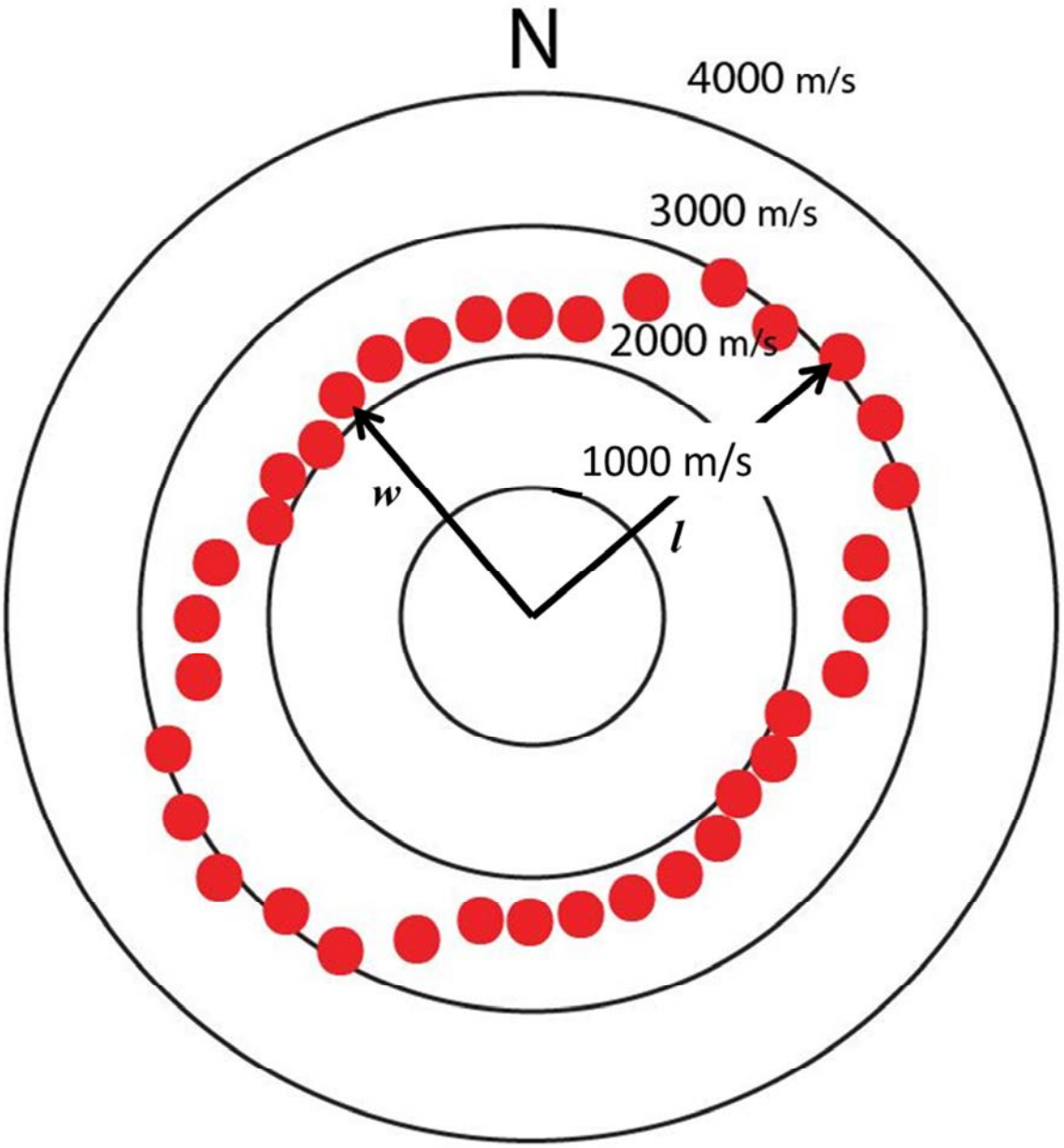

Figure 9: An example of the reworked image. This represents the same data seen in Fig. 8. The seismically fast direction (*l*) and the seismically slow direction (*w*) that are later used in statistical analysis are also shown.

2.3.3 Validation Statistics

Once the data had been converted to a visually presentable form, it could be seen whether anisotropy was or was not present at any given depth, however some statistical tests were needed to give the “eyeball” evaluation mathematical weight. The first thing to evaluate was the changing nature of the axial ratios (isotropy vs. anisotropy) of the dataset as a function of depth. For this, each depth slice was evaluated for anisotropy using an equation that creates an anisotropy ratio by dividing the square of the long velocity axis with the square of the axis perpendicular to that long axis, which results in a seismic equivalent permeability anisotropy ratio (SEPAR) (equation 9) and the results were graphed against depth for some idea of how anisotropy is related to depth at the particular site in question.

$$\text{SEPAR} = {}^{l^2}\!/_{w^2} \qquad (9)$$

Where: $l =$ magnitude of maximum seismic velocity
w = magnitude of seismic velocity perpendicular to maximum

This equation was developed in order to establish some equivalency between the current industry standard permeability anisotropy ratio (PAR) and these seismically derived anisotropy ratios. The industry standard PAR is equal to the maximum hydraulic conductivity ($Kmax$) divided by the minimum hydraulic conductivity ($Kmin$):

$$\text{PAR} = {Kmax}/{Kmin} \tag{10}$$

This relationship is generated using the well-recognized permeability ellipse concept (Fetter, 2001) in which the long axis (direction of maximum hydrologic anisotropy) is defined as:

$$l = {1}/{\sqrt{Kmin}} \tag{11}$$

while the short axis (direction of minimum hydrologic anisotropy, perpendicular to the long axis) is defined as:

$$w = {1}/{\sqrt{Kmax}} \tag{12}$$

For the seismic anisotropy ellipses, the magnitude of the fastest seismic velocity represents the long axis of the ellipse, while the velocity orthogonal to this fast direction represents the short axis of the ellipse, so a relationship between seismic velocity magnitude and maximum and minimum hydraulic conductivities is formed thus:

$$\left.{l}\middle/{w = \frac{{1}/{\sqrt{Kmin}}}{{1}/{\sqrt{Kmax}}} = \frac{\sqrt{Kmax}}{\sqrt{Kmin}}}\right. \tag{13}$$

Therefore,

$$l^2/w^2 = Kmax/Kmin \quad (14)$$

And so

SEPAR ~ PAR

A more detailed treatment of this analysis is discussed further in Chapters 3 and 4 of this manuscript.

The second step in is to validate any conclusions reached about the relative isotropy/anisotropy observed in all depth intervals in all surveys. This is accomplished by performing a runs test of the observed velocity data at a 95% significance level. The purpose of the runs test is to determine the randomness or non-randomness of the seismic data at each depth interval. This test of randomness accomplishes two things: Firstly, it helps to establish some significance to degrees of anisotropy encountered in the data. By definition, any distribution of data that is not perfectly uniform is anisotropic, but if the qualitatively observed anisotropy can be said to come from a non-random dataset, the dataset in question can be considered significantly anisotropic. Secondly, running this test at each depth interval in a dataset can help demarcate the point in the subsurface at which some significant driver (in this

case fracture sets) begin controlling the data (by removing noise) rather than random causes. This information, then, could be used to make inferences about the presence of hydrostratigraphic boundaries and their locations in the subsurface. The results of these analyses will also be discussed further in Chapters 3 and 4 of this manuscript.

CHAPTER 3: USING NON-LINEAR REGRESSION METHODS FOR CHARACTERIZING FIRST-ARRIVAL SEISMIC TOMOGRAMS IN THE DETECTION OF ANISOTROPY IN SUBSURFACE FRACTURE NETWORKS

[This chapter is to be submitted as a manuscript to the journal GEOPHYSICS. Therefore, it includes its own abstract, etc., and has some text and figures overlap with other chapters]

3.1 Abstract

The Oak Ridge Integrated Field Research Challenge (ORIFRC) project is funded by the U.S. Department of Energy's (DOE's) Subsurface Biogeochemical Research (SBR) Program in order to study the various biogeochemical processes involved in the remediation as well as natural attenuation of a large contaminant plume that is extant in the vicinity of the former ORIFRC in Oak Ridge, TN. A part of this work has been to characterize the movement of this groundwater/contaminant plume with the use of seismic first-arrival tomography (SFT).

Underlying the soils in this area, a fractured shale transition zone (from saprolite to competent bedrock) exists at variable depth and thickness. The fracture network in the bedrock- and to a lesser degree in the saprolite-are suspected to form an anisotropic hydraulic flow network at this site with groundwater and contaminants being transported preferentially parallel to the strike of bedding planes.

In an effort to detect this fracture-driven hydrologic anisotropy, we have conducted azimuthal SFT (ASFT) profiles at 10° intervals rotated around a central point. Each seismic profile consists of a 96-channel line with a 0.5 m receiver offset, and sledgehammer shot points located at every fourth receiver (2 m) along the line. The resultant tomograms are converted from XZ plane cross-sections to XY plane polar plots. Initial azimuthal velocity maps are tested statistically in order to verify qualitative assessments of anisotropy. Runs tests at

each depth interval show that the resultant velocity distributions are either random distributions of data or non-random distributions of data at a 95% level of confidence. The non-randomness of data distributions can be attributed to fractures that control the seismic velocity, and the demarcation between random and non-random data over the entire dataset can be used to infer the depth of the saprolite/bedrock transition zone.

3.2 Introduction

The Oak Ridge Field Research Center (ORFRC) was established by the Environmental Sciences Division (ESD) at the Oak Ridge National Laboratory in order to study the various biogeochemical processes involved in the remediation as well as natural attenuation of a large contaminant plume that is extant in the vicinity of the S-3 Pond area within the ORFRC (U.S. DOE, 1997). A part of this work has been to characterize the behavior of this groundwater/contaminant plume with the use of SFT.

Strong efforts have been made to temporally characterize the plume directly adjacent to the S-3 site (e.g. Gaines 2011), but geophysical investigations relating to the larger scale hydrological modeling efforts at the ORFRC have been sporadic. The ability to characterize anisotropic flow conditions in the subsurface without the cumbersome use of multiple boreholes/well tests would save significant amounts of time and money, while simultaneously increasing the accuracy of any hydraulic models created in order

to characterize the area in and around the ORFRC. It has been proposed that the use of SFT could be applied azimuthally around a central point of interest to create intersecting velocity profiles around this central point. These velocity profiles (existing in the XZ plane) could then be manipulated into XY plane map-view profiles at some assigned depth interval(s). These map-view velocity profiles could then be used to determine seismic anisotropy in the subsurface at any given depth.

The S-3 Pond Site overlies a layer of anthropogenic fill (mostly gravel) that was used to cap the ponds at the cessation of their use as a dumping area in 1988 (Gaines, 2011; U.S. DOE, 1997). Beneath this layer of fill, a transition zone of saprolitic Nolichucky Shale exists, gaining competency as one moves deeper into the subsurface. This transition zone is highly fractured and variable in its lithologic consistency, and in some instances, acts as an impermeable cap layer, while in other cases allows infiltration into the deeper fracture zones in the unit. This rock unit strikes an N55°E, and has as dip of approximately 45° to the southeast (Hatcher et. al, 1992).

Subsurface flow networks at the Oak Ridge National Laboratory Field Research Center are one of the dominant controls of subsurface contamination distribution (Gaines, 2011; Watson. 2005). While one would expect the contaminant plume (and the driving subsurface hydrology) to ascribe to the general rule of flowing in the down-dip direction, the extent and geometry of the

subsurface fracture networks in the shale beds could be a secondary controlling mechanism to the flow of subsurface water and contaminants.

This contaminant plume flows from the S-3 ponds towards the NT-2 area, which is situated almost due west of the S-3 site, and does not contain the volume of anthropogenic fill present at the S-3 site, but shares the same subsurface geology. For this reason, the NT-2 site has been chosen to determine a methodology for the use of ASFT in determining possible anisotropic fracture patterns in the transition zone between the saprolitic shale and the competent bedrock, as well as to characterize the nature of the overall pattern of regional fractures as a function of depth.

3.2.1 Geographic setting

The Oak Ridge National Lab is situated in East Tennessee, within the western portion of the Valley and Ridge province of the Appalachian Region. The lab is approximately twenty five miles west of the city of Knoxville and approximately 6.5 miles east of the eastern Cumberland Escarpment. The S-3 and NT-2 sites are located in what is known as Area 3, at the western edge of the Y-12 facility (Fig. 10). The NT-2 site is situated in Bear Creek Valley between Pine Ridge to the Northeast, and Chestnut Ridge to the Southwest, and lies within the Y-12 facility near the intersection of Bear Creek Road and Haul Road. The NT-2 site itself is a rectangular plot that is approximately 120m by 55m, and has very little topographic relief, although there is a slight decrease in elevation from the southern end of the site to the northern end. The eastern boundary of

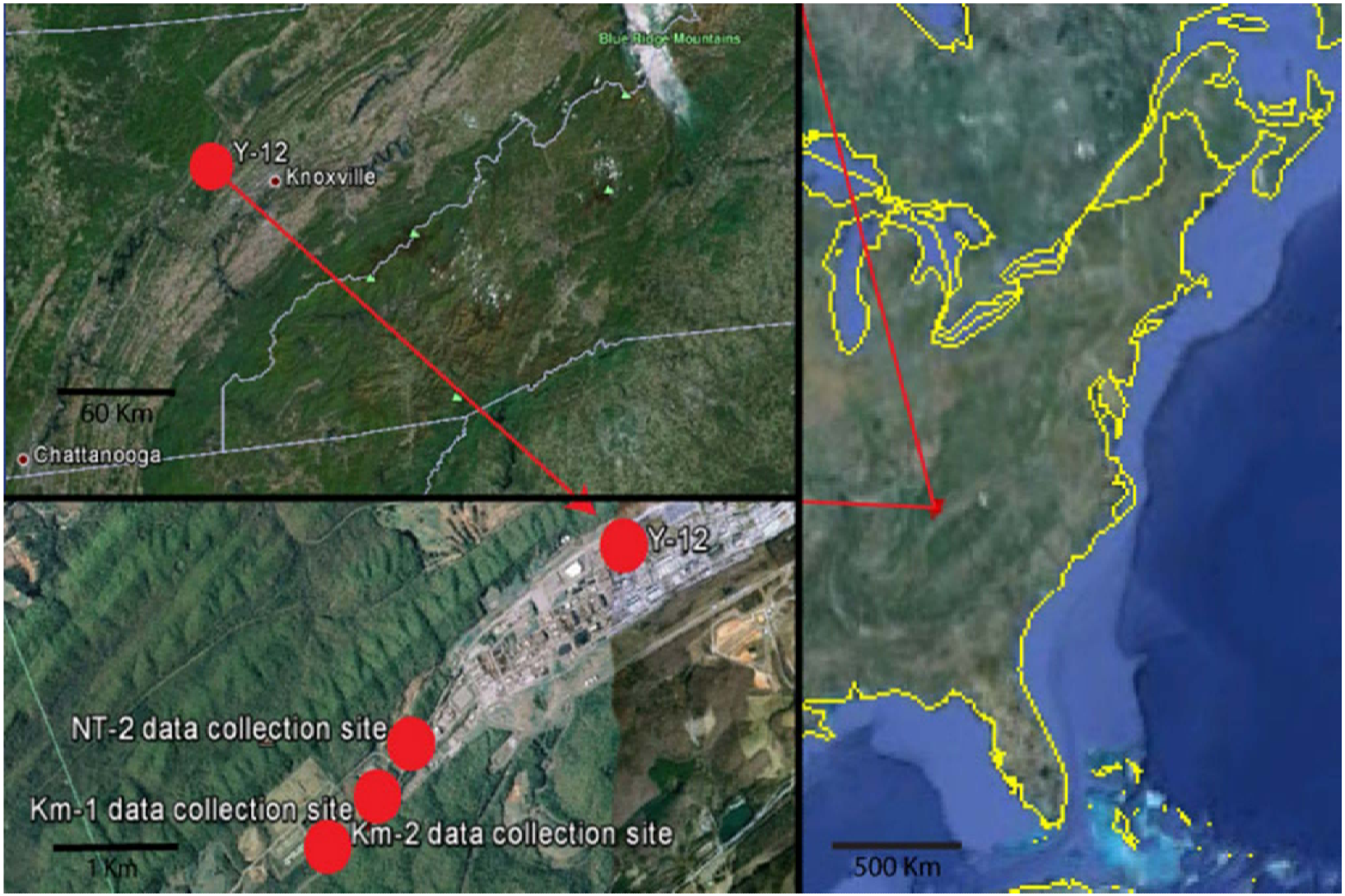

Figure 10: A map showing the location of Y-12 as well as the NT-2 data collection site. Images courtesy of Google Earth™. In all cases, north is toward the top of the figure.

the site is an area of light tree cover, while the western end of the site terminates along Haul RoadE. The primary groundcover is grass, although there is a gravel access road that enters the site from the western side halfway down Haul Road and continues on to the rough midpoint of the site.

3.2.2 Geologic Setting

The Oak Ridge National Laboratory is situated within the western Valley and Ridge Province of the Appalachian region. This region is characterized by a series of approximately ten northeast striking thin-skinned thrust faults, two of which bound the Oak Ridge Reservation: the Copper Creek thrust fault and the Whiteoak Mountain thrust fault. Bear Creek Valley lies southeast of the Whiteoak Mountain fault, which forms the crest of Pine Ridge (directly adjacent to Bear Creek Valley) (Hatcher, et al. 1992). Figures 11 and 12 display a regional geologic map and cross section of the area. At the NT-2 site, borehole data exists from wells GW-828 and GW-829, which lie directly adjacent to the specific area of examination within the NT-2 area. Core samples from these boreholes confirm a relatively uniform stratigraphic column throughout the area of investigation. Both boreholes were drilled into the Nolichucky Shale unit, which is middle to upper Cambrian, and contained within the Conasauga Group. It is approximately 152 m thick. Well GW-828 encountered weathered bedrock (locally considered saprolite) at a depth of 2.3 m that continues to a depth of 11.8 meters. This saprolite consists primarily of thinly laminated shale with some

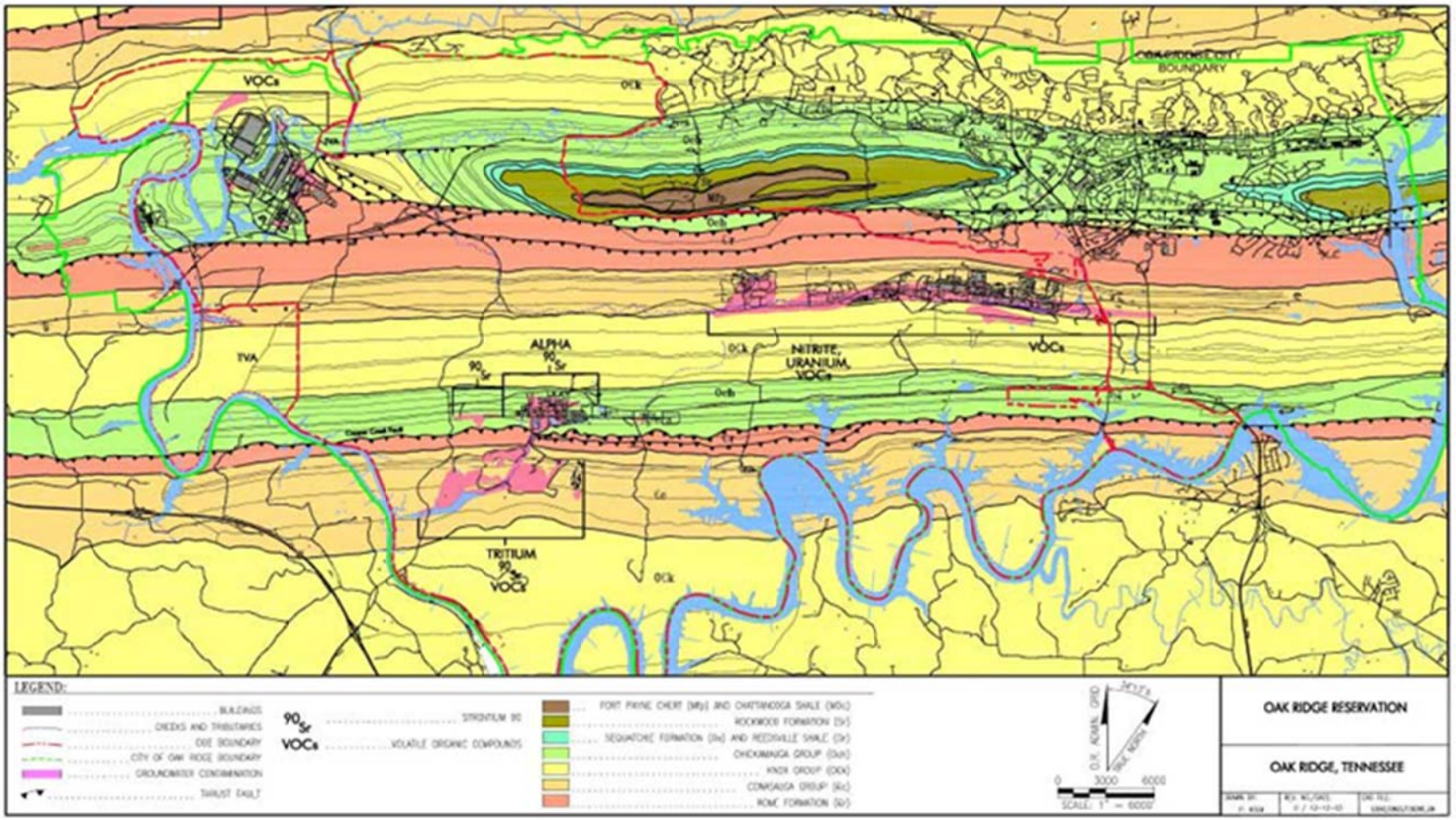

Figure 11: A geologic map of the Bear Creek Valley and the surrounding area. Modified from Hatcher et al., 1992.

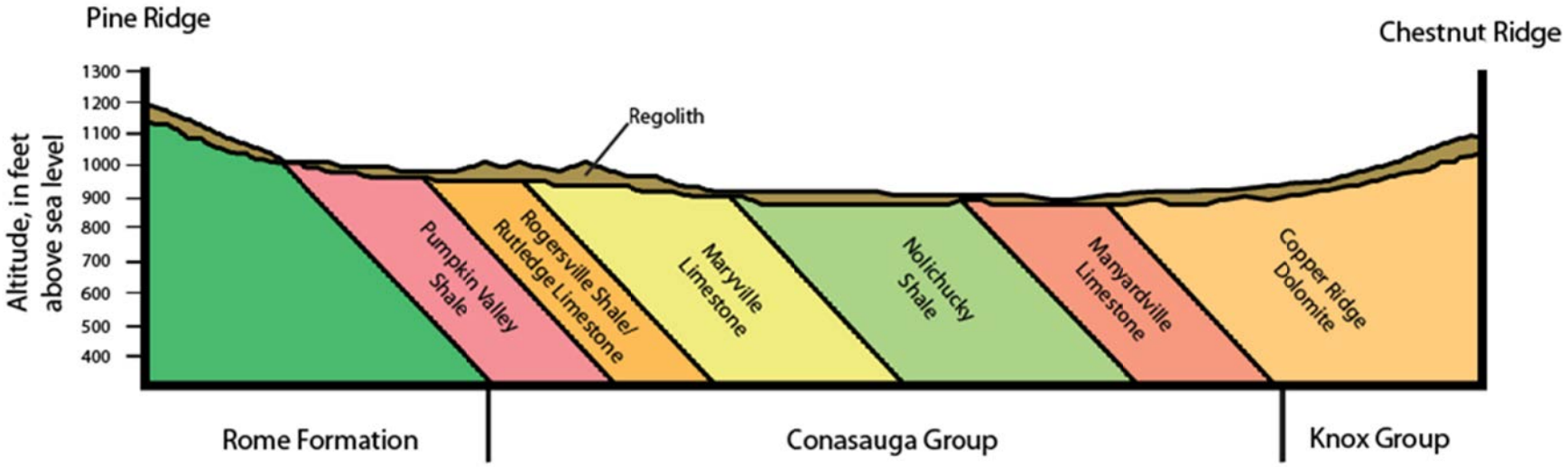

Figure 12: A basic geologic cross-section of the Bear Creek Valley. It begins with Pine Ridge to the north of the map in Fig. 10, and ends at Chestnut Ridge in the south. Modified from Dreier, et al., 1988.

micritic inclusions. Competent bedrock is encountered at 11.8 meters, and consists of thinly layered shale beds with inclusions of massive oolitic or pelitic micrite beds. The shale increases in lithological consistency with depth. Core samples from well GW-829, located approximately 25 meters to the south of GW-828, show roughly the same lithologies and thicknesses as well GW-828, but the saprolitic shale zone begins at 0.4 m depth and continues to a depth of 9.1 meters, where competent bedrock is encountered (Science Applications International, 1995).

3.3 METHODOLOGY

3.3.1 Seismic equipment

The equipment used to collect these data in the field is industry standard, and consists of up to four Geodes™ (manufactured by Geometrics, Inc.), which are portable seismographs that each allow for a maximum of 24 input channels, giving this system a maximum capacity of 96 input channels. These Geodes are attached to take-out cables that are then attached to the individual 40-Hz Mark Products geophones. The geophones used were traditional "passive" magnet and coil units. The Geodes are connected to each other in series, with three "slave" units all connected linearly to a "master" unit by data cables. Also attached to the master Geode is a hammer cable that ends in a trigger device such that the recording begins within fractions of a millisecond of the impact of the sledge. A laptop computer is connected to the master Geode,

and allows for real time observation and manipulation of the waveform data as well as acquisition parameters. All of the aforementioned equipment is powered in the field by 12V deep cycle marine batteries.

3.3.2 Acquisition parameters

While collecting data in the field, the record length for each shot is 0.25 s, and the sampling interval for each record is set at 0.125 ms. The data at each shot point is stacked to improve signal to noise ratio on the final amplitude data, and the number of stacks varies from 2 to 5 (depending on ambient noise levels in the external environment). As a general rule, the lowest number of stacks possible is used that produces a waveform from which the first breaks can easily be identified.

3.3.3 Site preparation and data acquisition

The data for this investigation were collected April 4 and April 6, 2011. The first step in the process was laying out a circle with markers at 10° intervals around a central point and a 24 m radius (**see Fig. 2**). The surveying was done by establishing a center point, and then calculating the short side of the isosceles triangle with two 24 m (radii) long sides when this circle is divided into 36 equal triangles. The length of this short triangle side was 2.11 m, which was marked off on a piece of 1.25” diameter PVC pipe as a distance measuring device. Next, flags were placed 24 m away from the center oriented perfectly north-south with the aid of a Brunton compass. Using these as starting points, flags were placed

every 2.11 meters from the previous flags with a 24 m string to act as a radius, creating a circle divided into 10° segments with a 48 m diameter. Each 10° increment now has a 48m distance between itself and its compliment (0,180; 10,190; 20,200; etc.). A 48 m seismic line was then set up and a SFT survey was run on each of these lines from 0° to 170°, resulting in full 360° coverage at 10° increments.

After the site had been prepared, geophones were placed in the ground at 0.5 m intervals from one end (0°) to the other (180°) of the circle. All cables and seismographs were set up and connected appropriately, and sledgehammer shots were taken along the line at 2 m intervals and recorded. After the terminus of the survey, all equipment was moved 10° around the circle to the next survey point, and the process was repeated until all 18 seismic surveys were complete.

3.3.4 Data processing

After all of the raw data were acquired, the first arrival times of the seismic wavefront for each shot point along each linear transect was manually picked (see Fig. 3), and these pick files were imported into Rayfract™, a software suite that creates a velocity model of the subsurface based on the picked first arrival data. After creating an initial gradient model, the software is used to iterate the model to improve fit to the actual collected seismic traveltimes until a convergent velocity model of the subsurface is constructed. For further discussion pertaining to this process, see chapter 2, section 2.3. This process was repeated for each of the 18 seismic transects, creating 18 seismic velocity

tomograms that intersect at their X-coordinate center points (24 m) and cover a full 360° radially in 10° increments. All 18 of these velocity tomograms can be seen in Appendix 1, section 2: Velocity tomograms.

The next step in the processing workflow was to export these XZ velocity profiles as XYZ files into a spreadsheet, in this case Microsoft Excel™. Each XYZ file contains an X coordinate along the seismic line, a Y coordinate denoting depth, and a Z coordinate denoting seismic velocity. These files were all manually transformed into a table that set depth versus directional azimuth, and was filled in with the seismic velocities of each particular point. Once this table was constructed, the data from each depth interval were input into MATLAB, and a compass diagram was produced that shows the magnitude of each seismic velocity at each azimuthal direction (see Fig. 7). These compass diagrams are analogous to polar plots that show the magnitude of the velocity as well as the azimuthal direction as an arrow. These figures were then re-drawn with Adobe Illustrator™ for ease of interpretation. These original and re-drawn compass diagrams can all be seen in Appendix 1 section 3: Compass diagrams. In order to analyze the data for anisotropy, one must first determine some criterion for assessing anisotropy. The equation chosen for this analysis is equation (9), giving the SEPAR for each depth interval in the data:

$$\text{SEPAR} = {}^{l^2}\!/_{w^2}$$

Where: l = magnitude of maximum seismic velocity

w = magnitude of seismic velocity perpendicular to maximum

The value resultant from this equation for anisotropy is expressed as a number greater than one in the case of anisotropic data, and unity in the case of perfectly isotropic data. The larger the resultant value of the calculation, the greater the amount of anisotropy expressed in the radial dataset in question. This calculation was performed on each radial dataset going from 0 m in depth to -11.5 m in depth (the depth limit of consistent data coverage), and the results were graphed in order to identify any trends in the data (Fig. 13). The second step in assessing the data is to determine which data points represent significant anisotropy. This is accomplished using a runs test with a 95% level of confidence. The test is conducted on each radial velocity distribution, and the results posit that a data point is either random or non-random. Randomness is assessed by the amount of noise in the dataset, and so a non-random dataset would have little noise, establishing its' anisotropic significance.

3.4 RESULTS AND DISCUSSION:

In the case of the NT-2 data, the data are random down to a depth of 3 m, and all data at and below 3.5 m is significantly anisotropic by way of being non-random. The inference is that at a depth of 3.5 m, some factor emerges to control noise in the data, in this case, fracture sets. At a depth of 5.5 m, an inflection point in the data is evident, and beyond this point, the character of the

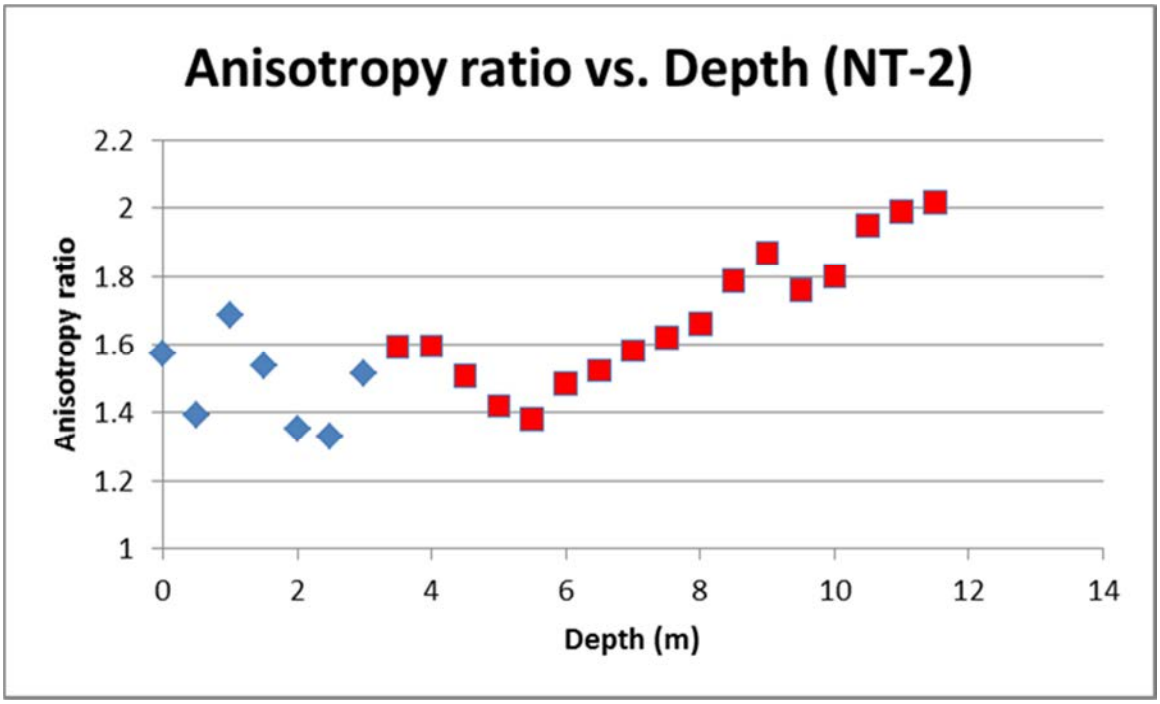

Figure 13: A chart showing the anisotropy ratio of each horizontal velocity profile versus its depth in meters. The square red data points indicate non-random data distributions as determined by runs tests. The diamond blue data points represent random datasets as determined by the runs tests. All runs tests were conducted at the 95% confidence level ($p \leq 0.05$). The region between the beginning of non-random data (3.5m depth) and the inflection point in the behavior of the anisotropy ratios (5.5 m) may represent the transition zone between saprolite and bedrock being expressed in the data at the NT-2 site.

data changes, namely to a strong positive correlation between degree of anisotropy and depth. This inflection in the behavior in the data could be the delineation between saprolite and bedrock. If this is true, the emergence of fracture control is seen at at 3.5 m depth, and a change in the nature of this control at a depth of 5.5 m. This 2 m zone in the subsurface, then could be the expression of the transition zone between saprolite and bedrock in the data.

3.5 CONCLUSIONS

The purpose of this investigation was to assess the efficacy of the newly developed ASFT method in the field, as well as to test the theoretical methodology developed for this analysis technique for functionality. The field scale experiment performed at the NT-2 site at ORNL allowed a demonstration of ASFT methodology. The experimental design was showed to be valid, and the results of this new methodology were robust, while the mechanics of the survey method proved functional. The data gathered at NT-2 demonstrate the presence of seismic anisotropy in the subsurface at the site at a variety of depth intervals. The significance of the anisotropy is assumed if the visually assessed anisotropy resulted from some controlling (non-random) factor. This was tested using a statistical runs test for detecting non-randomness. All of the depth intervals from the surface to a depth of 3 m proved random, and so any anisotropy detected at these depth intervals can be considered insignificant in attempting to detect fracture networks in the subsurface. Anisotropy at depth intervals from 3.5 m to

11.5 m all proved statistically non-random, and can be said to result from some controlling factor, in this case, fracture networks in the subsurface. Further, a region from the beginning depth of significant data (3.5 m) to an inflection point in the behavior of the anisotropy at a depth of 5.5 m may delineate the extent of the transition zone from saprolite to bedrock. These depth values demarcating the transition zone correlate well with borehole data from the NT-2 site, although these boreholes do not directly measure the depth to transition at the exact point within the site where this study was conducted.

CHAPTER 4: THE USE OF ASFT TO ASSESS THREE SITES IN THE ORIFRC FOR HYDROLOGIC ANISOTROPY

[This chapter is to be submitted as a manuscript to the journal Groundwater. Therefore, it includes its own abstract, etc., and has some text and figure overlap with other chapters]

4.1 Abstract

The Oak Ridge Integrated Field Research Challenge (ORIFRC) project is funded by the U.S. Department of Energy's (DOE) Subsurface Biogeochemical Research (SBR) program in order to study the various biogeochemical processes involved in the remediation as well as natural attenuation of a large contaminant plume that is extant in the vicinity of the ORIFRC in the Bear Creek Valley of Oak Ridge, TN. A part of this work has been to characterize the movement of this groundwater/contaminant plume with the use of seismic first-arrival tomography (SFT).

Underlying the soils in and around this site, there exist three primary hydrostratigraphic units: (1) a clayey weathered rock unit that retains original bedding planes and fracture structure (regionally termed saprolite), (2) a transition zone between this saprolitic shale and bedrock, and (3) compentent Nolichucky Shale bedrock. The saprolitic zone is, as a general rule, low in permeability and between 3 and 10 m thick in the Bear Creek Valley. The transition zone tends toward irregularity in its transmissivity due to high fracture content and a lower density of clay minerals, thus it tends toward higher permeability. Primary fracture sets in this zone yield a strong horizontal hydrologic anisotropy (8:1) parallel to regional strike of bedding planes. The underlying bedrock unit has a high frequency of fracture sets causing a high degree of horizontal anisotropy, but is less permeable than the transition zone due to smaller fracture apertures and higher competency in the matrix media.

In an effort to characterize this fracture-driven horizontal hydrologic anisotropy, we have conducted azimuthal SFT (ASFT) profiles at 10° intervals intersecting at a central point. Each seismic profile consists of a variable number of receiver channels (between 72 and 96, depending on spatial constraints of each particular acquisition site) with a 0.5 m receiver offset, and sledgehammer shot points located at every fourth receiver (2 m) along the line. The resultant velocity tomograms are converted from XZ plane cross-sections to XY plane polar plots that show an azimuthal velocity distribution at discrete depth intervals. Three azimuthal datasets were collected: (1) at the NT-2 site, southwest of the S-3 disposal ponds, (2) approximately one half kilometer down valley (to the southwest) of the NT-2 collection site (Km-1), and (3) approximately one kilometer down valley (to the southwest) of the NT-2 collection site (Km-2). Each of these sites remains situated in the Nolichucky shale unit, and each are expected to share similar structural characteristics. All three surveys show a significant increase in the degree of northeast-southwest trending seismic anisotropy as a function of depth. Two of the three datasets delineate the three primary hydrostratigraphic units of the area. The seismic anisotropy demonstrated by these datasets correlates well with observed hydrologic anisotropy in the region, and an intermediary relationship between the two types of data is established.

4.2 Introduction

The Oak Ridge Integrated Field Research Challenge (ORIFRC) was established in 2007 by the United States Department of Energy (DOE). The purpose of the program was to investigate the various processes that result in natural attenuation of a (mostly) immobile contaminant plume in the vicinity of the S-3 waste disposal ponds, located in the Y-12 complex of the Oak Ridge National Lab (ORNL). Also under investigation were various anthropogenic remediation techniques, and part of this enquiry was the use of near-surface geophysics to characterize the physical parameters and dimensions of this plume over time using seismic first-arrival tomography (SFT; e.g., Gaines, 2011). In order to fully understand the contaminant transport pathways at the S-3 site and its surrounding area, a more in-depth investigation into the larger scale hydrology at ORNL is appropriate.

Geophysical efforts to improve hydrologic models throughout the ORIFRC complex have been sporadic, and as a general rule, hydrologic isotropy is assumed in current subsurface flow models of the site. The ability to characterize the (potentially) anisotropic flow conditions in the areas around the ORIFRC without resorting to cumbersome methodology that is currently in place would increase the accuracy of any subsurface models subsequently created in a temporally efficient manner as well as increase the conceptual understanding of secondary contaminant transport pathways that may exist. It is proposed that the use of SFT could be applied in an azimuthal fashion, with several linear surveys

intersecting at a central point, as a methodology by which hydrologic anisotropy could be detected and parameterized. The vertical plane velocity tomograms could be transformed into horizontal plane velocity distributions at specific target depths, or a continuum of depth slices could be created to characterize anisotropy at a certain point as a function of depth.

The S-3 pond site was created in 1951 as an area where the waste associated with the enrichment of weapons-grade uranium could be disposed of. The four ponds are approximately 5 m deep, and have a total capacity of 10 million gallons. A large variety of contaminated material had been deposited in the ponds, including uranium, technetium, nitrates, etc., until they were drained, filled, and capped in 1988 (US DOE, 1997; Watson, et al., 2005). Given the fact that the ponds were unlined, a large groundwater contaminant plume has formed in the subsurface below and adjacent to the ponds' location, and this contaminant plume is acting as a secondary contamination source for the surrounding area (Watson, et al., 2005). While it is generally expected that the groundwater flow creating this secondary contamination would travel an a geologically down-dip direction, several studies of the hydrology in the area confirm that there exists a large degree of horizontal anisotropy in the subsurface flow regime, and that groundwater/contaminant pathways may not travel in the expected methods by the expected pathways (Moline et al., 1998; Schreiber et al., 1999). Investigations into the fracture distributions and orientations in the shallow subsurface suggest that this hydrologic anisotropy could be driven by

intersecting sets of fractures as a secondary flow pathway to bedding plane interfaces (Dreier et al., 1987; Bailey, 1988).

The use of azimuthal seismic first-arrival tomography (ASFT) is applied to three sites within the ORIFRC in an effort to detect and characterize this fracture driven hydrologic anisotropy. The first data acquisition site is the NT-2 site (NT-2 dataset), situated in the Bear Creek Valley where North Tributary 2 intersects with Bear Creek. Two additional data collection sites were situated approximately one kilometer (Km-1 dataset) and two kilometers (Km-2 dataset) down valley from NT-2. These sites were chosen because they are all situated in the Nolichucky Shale rock unit, and share similar geologic characteristics to the S-3 pond area. At each of these sites, an azimuthal dataset was collected that consisted of eighteen linear seismic surveys taken at 10° radial intervals that all intersect at a central point. These surveys produce a series of XZ plane velocity tomograms that are converted into XY plane velocity distributions at discrete depth intervals. The results of these horizontal plane velocity distributions visually describe the extent and orientation of seismic anisotropy as a function of subsurface depth. These seismic datasets are compared to hydrologic datasets in order to establish the efficacy of using seismic methods to describe hydrologic characteristics in the subsurface in the area in and around the ORIFRC.

4.3 Background

The sites chosen to conduct this investigation are the NT-2 site at the ORIFRC (Fig. 14), as well as two other sites in the Bear Creek Valley that lie

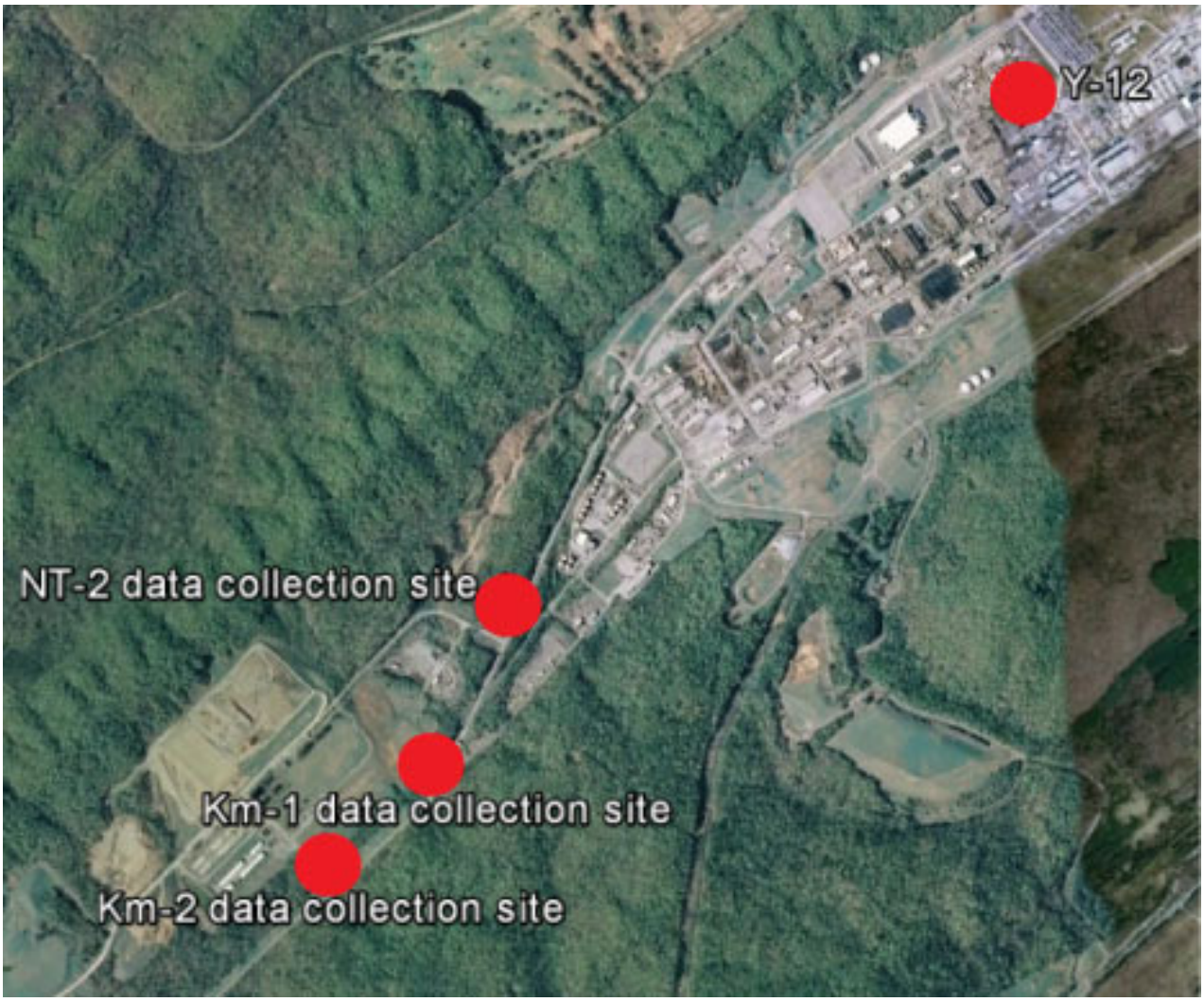

Figure 14: A local map of the locations of the NT-2 site, the Km-1 site, and the Km-2 site. The location of the Y-12 plant is shown for reference. Image Courtesy of Google Earth™.

approximately one half kilometer (Km-1) and one kilometer (Km-2) down valley from the NT-2 site. All of the chosen data acquisition locations share a similar hydrogeologic setting. The region around the ORIFRC is characterized by a series of parallel northeast striking thrust faults, two of which form boundaries to the ORIFRC. To the northwest, the Whiteoak Mountain fault forms pine ridge, which bounds upper portion of the study area. The Valley's southeast terminus is the Copper Creek fault (Hatcher et al., 1992). The Bear Creek Valley is underlain by Cambrian rocks that strike approximately north 55° east, and dip between 30° and 70° to the southeast, with an average dip angle of 45° (see Figs. 10 and 11). These Cambrian rocks are composed of alternating layers of calcareous shales and limestones that form the Conasauga group (Bailey, 1988). Specifically, the survey areas overlie the Nolichucky Shale, which is a middle to upper Cambrian unit and is approximately 152 m thick. Core samples taken from the NT-2 site show a relatively uniform stratigraphic column. Well GW-828 encountered weathered bedrock (locally considered saprolite) at 2.3 m that continues to a depth of 11.8 meters. This saprolite consists primarily of thinly laminated shale with some micritic inclusions. Competent bedrock is encountered at 11.8 meters, and consists of thinly layered shale beds with inclusions of massive oolitic or pelitic micrite beds. The shale increases in lithological consistency with depth. Core samples from well GW-829, located approximately 25 meters to the south of GW-828, show roughly the same lithologies and thicknesses as well GW-828, but the saprolitic shale zone begins at 0.4 m depth

and continues to a depth of 9.1 meters, where competent bedrock is encountered (Science Applications International, 1995). The differences in competency and fracture density in these stratigraphic units have a significant effect on the horizontal hydraulic conductivity of groundwater flow that coincides with the alterations in lithology, thus they will be termed hydrostratigraphic units. A conceptual model of the depths and orientation of these hydrostratigraphic units can be seen in Figure 15.

Several parties have undertaken hydrological characterization of the Nolichucky shale unit in an effort to improve sampling procedures for contaminant observation and remediation in the area. Geirke, et al. (1988) conducted a pumping test that showed an anisotropic drawdown cone that was elongated in the direction of geologic strike. A similar drawdown cone was observed in shallow and deep wells and led to an inferred hydraulic connection between shallow updip wells, deep downdip wells, and the pumping well. On the basis of these results, an 8:1 horizontal strike to dip anisotropy ratio was calculated (Geirke et al., 1988). In a period of time between 1994 and 1998, Moline, et al. (1998) performed several tests, including a noble gas tracer test, continuous coring, a variety of borehole tests, and water chemistry analysis, in an effort to evaluate the flow and transport characteristics of the Nolichucky Shale unit. They concluded that hydraulic transport is predominantly perpendicular to the local hydraulic gradient (Fig. 16), and that although Gierke. et al. (1988) suggested a bedding-parallel connectivity, this connectivity only occurred during

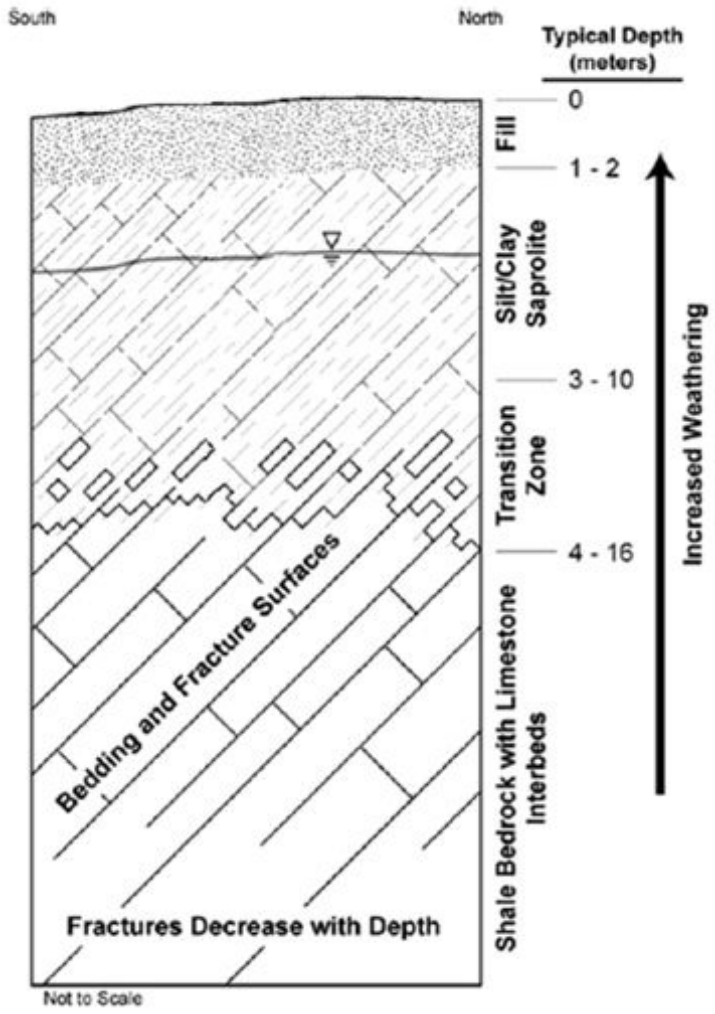

Figure 15: A conceptual model of the locations and orientations of the three primary hydrostratigraphic units in the vicinity of the S-3 disposal ponds. The Nt-2, Km-1, and Km-2 sites would share similar geology.

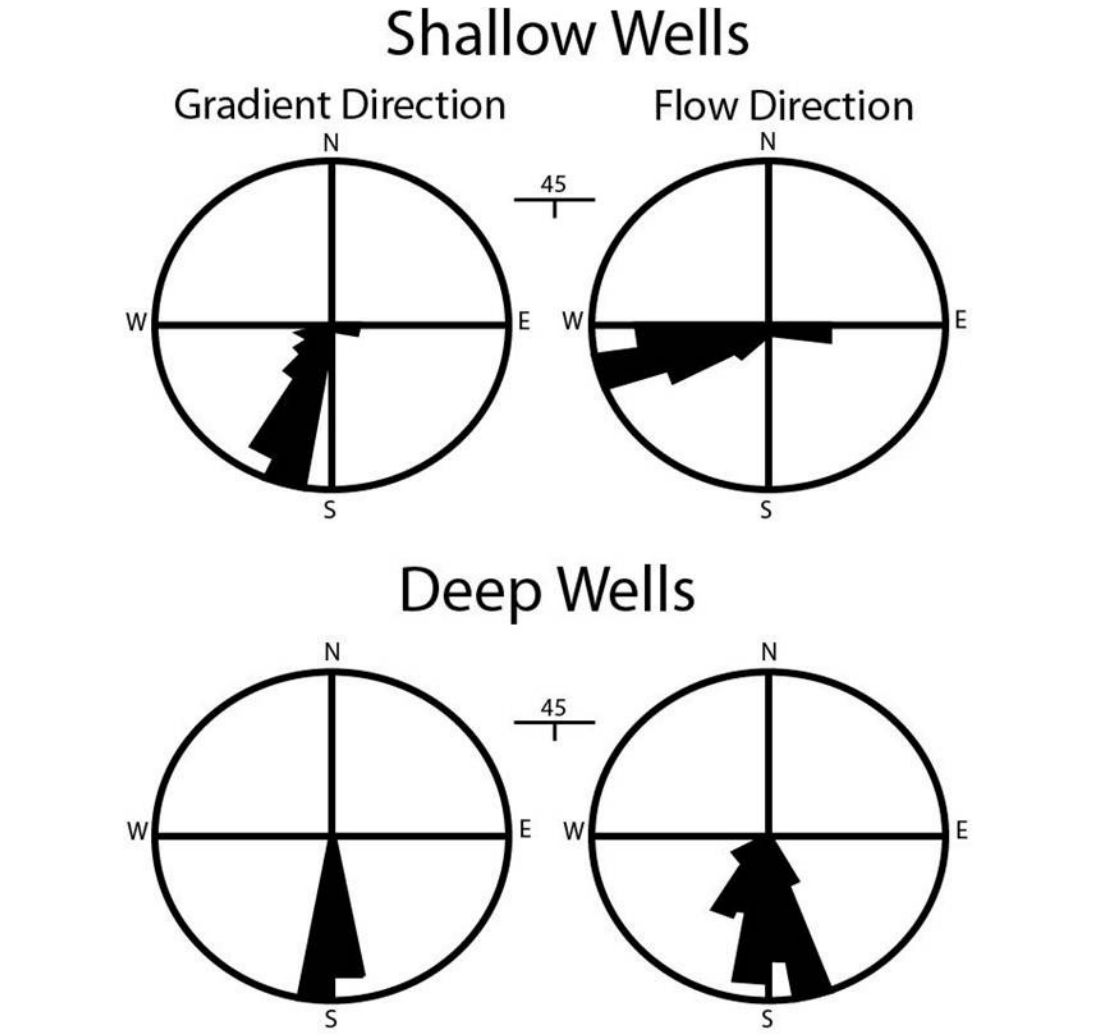

Figure 16: Diagrams depicting the hydraulic gradient as well as predominant flow direction for both deep and shallow wells within the Nolichucky Shale unit. Note that these diagrams were made using ORNL's coordinate system, and these are apparent directions based on that coordinate system. ORNL's coordinate grid is situated approximately 20° counterclockwise of true north. Modified from Moline, et al., 1998.

transient storm events (Moline, et al., 1998). In the same time period, Schrieber et al. (1999) conducted a series of tests using hydrogoechemical facies changes to delineate different flowpaths in the subsurface in the Nolichucky Shale unit. They determined that the flowpaths in this rock unit are controlled by gradients as well as dominant fracture sets (Fig. 17), and that horizontal groundwater flow is close to geologic strike in the area around the saprolite/bedrock interface. This horizontal flow direction could not be explained by gradient analysis (as flowpaths deeper in the subsurface could be), but could be explained by the presence and orientation of fracture sets present at that depth (Schieiber, et al. 1999).

Hydrologic testing appears to indicate that flow in the shallow subsurface is controlled by fracture sets around the saprolite/bedrock boundary. These interconnected fracture sets were first characterized by Dreier and others (1988). This study consisted of the construction of observational trenches constructed in both the Nolichucky Shale and Maryville Limestone units, and recording fracture orientation and density. A constant head tracer test was also conducted to show the effects of these fracture sets on flow in the unsaturated zone at ORNL. Three primary fold related fracture sets were determined: (1) a set of bedding plane parallel fractures, (2) a set of extensional fractures parallel to geologic strike, and (3) a set of extensional fractures perpendicular to geologic strike (Fig. 18). The extensional fractures are perpendicular to each other as well as the bedding plane fractures, forming an orthogonal fracture network. Tracer tests

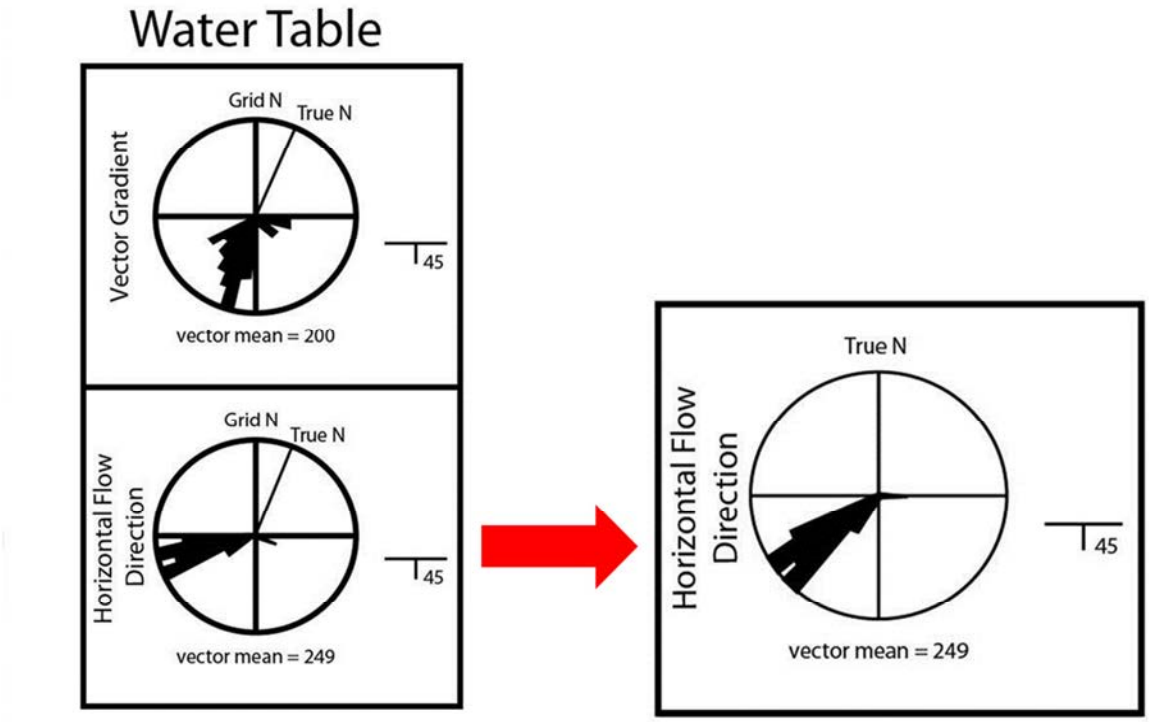

Figure 17: An image showing some of the results of the hydrogeochemical facies change experiments conducted by Schrieber et al. in 1999. The primary horizontal flow direction is shown relative to the ORNL coordinate grid in the lower left, and has been corrected for true north in the lower right of the figure. Modified from Schrieber et al., 1999.

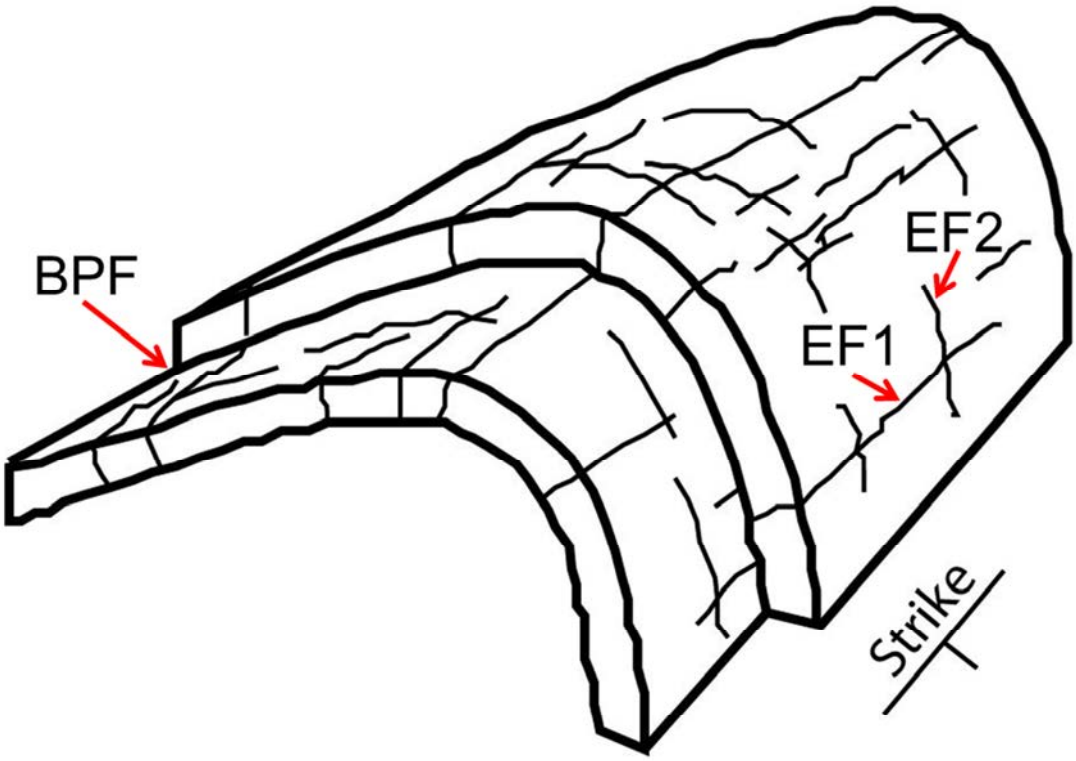

Figure 18: A figure showing the dominant fracture sets in the Nolichucky Shale unit in Bear Creek Valley. BPF are bedding plane fractures parallel with bedding planes, EF1 are extensional fractures parallel with geologic strike, and EF2 are extensional fractures perpendicular to geologic strike. All three fracture sets are arranged such that they form an orthogonal network. Modified from Dreier, et al., 1988.

showed that the preferred flow direction is the vector sum of the intersection of the two extensional fracture sets as well as the strike parallel fracture set with the bedding plane fractures. This vector sum is north 60° east (Fig. 19). From this, it was concluded that the intersection of bedding strike parallel extensional fracture set and any other fracture set exerts a strong influence in flow direction (Dreier, et al., 1988).

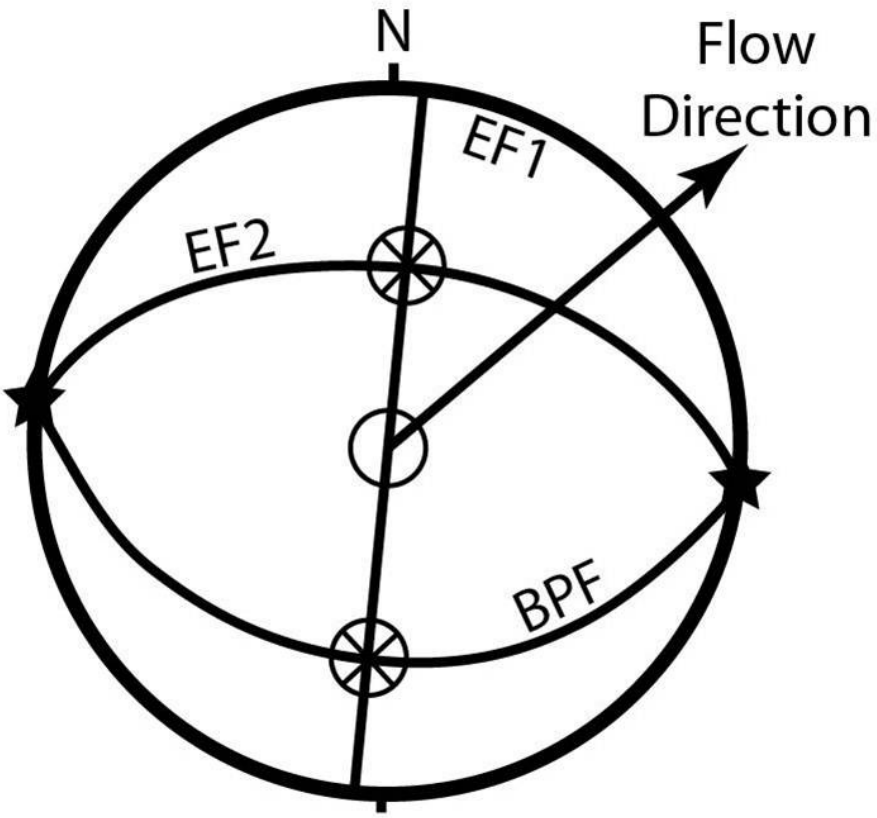

Figure 19: A stereographic image of the primary sets of orthogonal intersecting fractures. Extensional fracture set intersections are marked with an X and a star marks where extensional fracture sets intersect with bedding plane fractures. The vector sum of the EF1-EF2 intersection and the east trending EF2-BPF intersection is approx.. N60E, while the observed preferred flow direction is N50E. Modified from Dreier, et al., 1988.

4.4 Methods

The NT-2 dataset was collected in April, 2010, and the Km-1 and Km-2 datasets were collected in May of 2012. All methodology for the collection and interpretation of these datasets were constant, with the exception of differing survey lengths between the sites due to different spatial constraints at each site. At NT-2, all surveys were 48 m long. At Km-1, survey length varied from 36 m to 48 m, and at Km-2, all surveys were 40 m in length.

The first step in collecting an azimuthal dataset is the layout of the site. At the NT-2 site, a circle with a 48 m radius and markers at 5° intervals along the circumference had to be created around a central point. This was done by first establishing a center point (at the center of the open area available) and then calculating the short side of an isosceles triangle with two 24 m (radii) long sides. For this size triangle, the straight line arc length of a 5° portion of the circumference was 2.09 m. This distance was marked off on a piece of 1.25" diameter PVC pipe to be used as a measuring device. The next step was to place flags due north and south of the center point at a 24 m distance. A piece string with a length of 24 m was tied to the center flag an, using the north and south starting points, flags were places 2.09 m away from the previously placed flags, using the 24 m radius to keep the arc length travelling in a circular fashion. This created a marked circle divided into 5° increments with a 48 m radius. At the Km-1 site, the process was repeated, but using a circle with a straight line arc length of 1.57 m to create a circle with a diameter of 36 m, and at Km-2, an arc

length of 1.75 m was used to create a circle with a diameter of 40 m. At each site, a seismic first arrival survey was run on each 10° increment from 0° to 170°, resulting in full 360° coverage (see Fig. 2). For equipment specifications and collection parameters used, see chapter 3, sections 3.1 and 3.2.

After data collection, the waveform amplitude data was manually picked for first arrival times (see Fig. 3), and these first arrival picks were imported into the Rayfract™ software suite. This software uses the picked first arrival times to create a 2D velocity model of the subsurface. For further discussion into the workings of the program, see chapter 2, section 2.3.

The velocity models are output as cross-sections in the XZ plane, and for the purposes of this study, had to be converted into XY planes around the central point at which all of the seismic surveys intersected. This was accomplished by re-gridding the data in Golden Software Surfer™ into 0.5m depth intervals and saving it as an XYZ file. In this format, the X column denotes X position along the seismic line, the Y column denotes depth, and the Z column displays seismic velocity. These data were filtered such that the only x coordinate used was at 23.5 meters (the center point of all intersecting surveys) and all depth data were in 0.5 m intervals. The filtered data were then transposed into a table in Microsoft Excel™ that displayed velocity as a function of azimuthal direction and depth. MATLAB™ was then used to generate compass diagrams that depict the magnitude of the seismic velocity and its azimuthal direction at the central intersection point in the form of a polar plot for each 0.5 m depth interval (see

Fig. 8). The compass diagrams generated in MATLAB™ are graphically poor and difficult to interpret, and so the figures were reworked in Adobe Illustrator in order to create sharper and easier to interpret visual images (see Fig. 9).

These data (for all three sites) were all subjected to statistical and graphical analysis in order to verify the presence of seismic anisotropy. First, the SEPAR for each depth interval was determined for each site using equation (9), and the results for each experiment were plotted as a function of depth. Statistics were then run to determine the validity of qualitatively observed anisotropy. For each azimuthal survey, the observed velocity distribution at each depth interval was tested for non-randomness using a runs test for the detection of non-randomness at a 95% significance level.. Randomness would imply that the data are insignificant with respect to the control of subsurface fracture sets on seismic anisotropy. The results of the runs tests were incorporated into the anisotropy ratio charts such that the behavior of anisotropy as well as its significance can be seen as a function of depth.

4.5 Results

The anisotropy ratio of each depth interval for all azimuthal surveys was determined using equation (9). The results of this anisotropy analysis for all three datasets can be seen in Figs. 20, 21, and 22. The NT-2 dataset shows a relatively random distribution of anisotropy ratios that range from 1.33 to 1.69 until approximately 5 m in depth, at which point the anisotropy ratio begins to

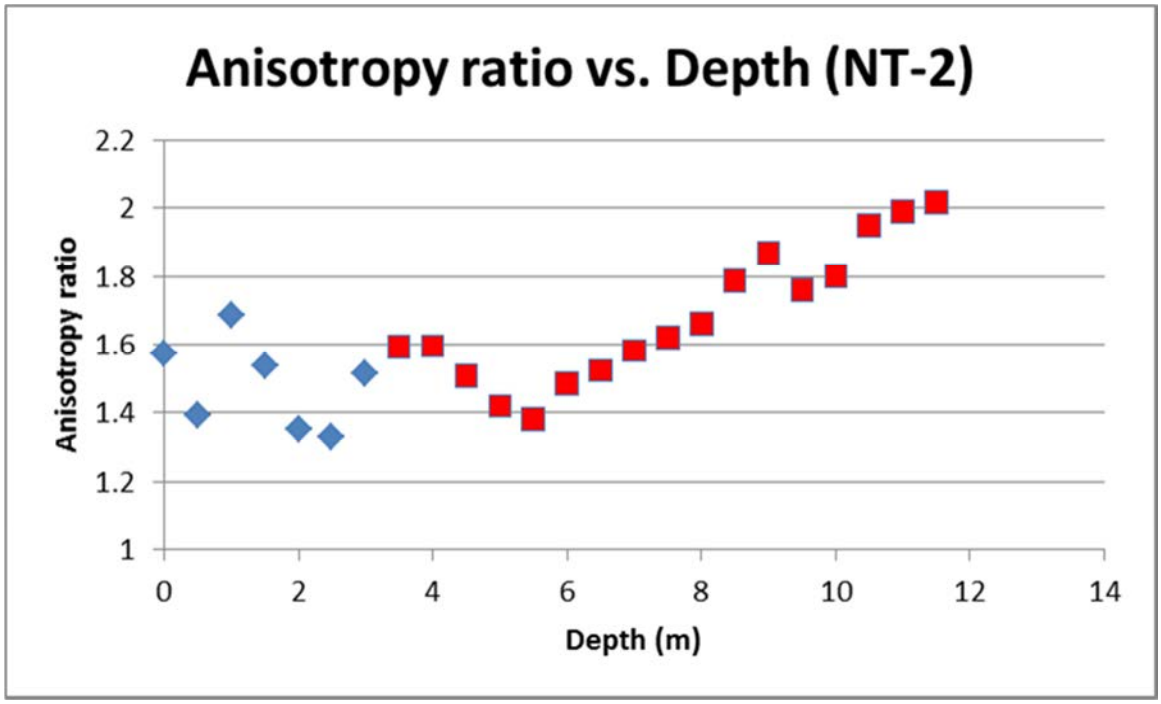

Figure 20: A chart showing the anisotropy ratio of each horizontal velocity profile versus its depth in meters at the NT-2 site. The square red data points indicate non-random data distributions as determined by runs tests. The diamond blue data points represent random datasets as determined by the runs tests. All runs tests were conducted at the 95% confidence level (p≤0.05).

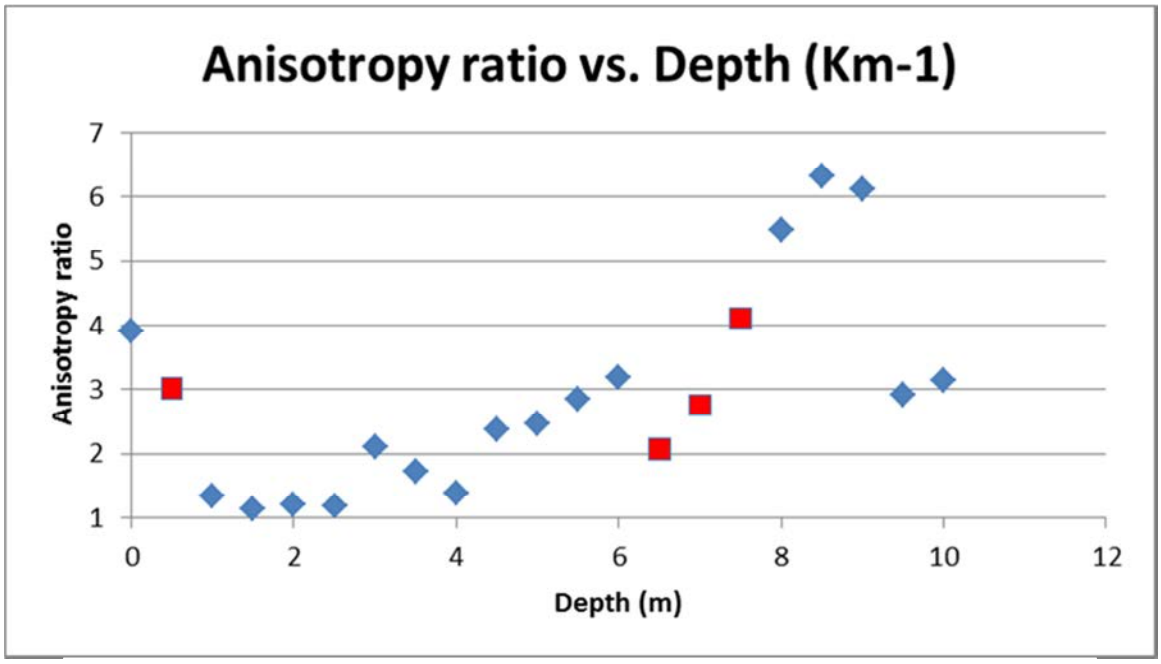

Figure 21: A chart showing the anisotropy ratio of each horizontal velocity profile versus its depth in meters at the Km-1 site. The square red data points indicate non-random data distributions as determined by runs tests. The diamond blue data points represent random datasets as determined by the runs tests. All runs tests were conducted at the 95% confidence level (p≤0.05).

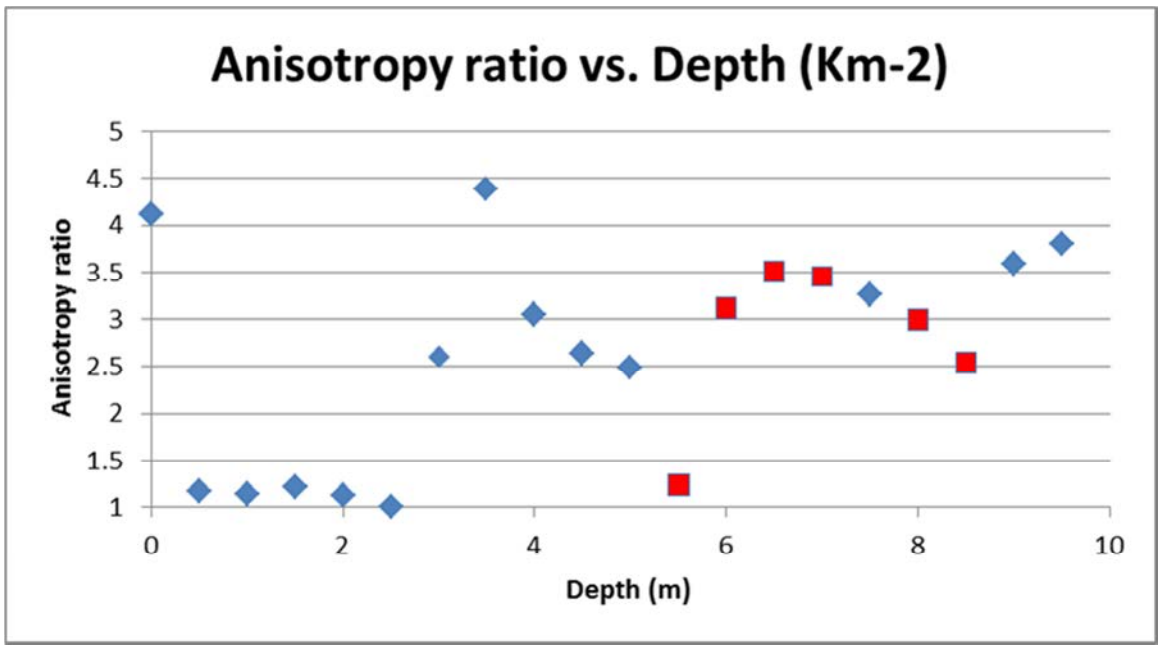

Figure 22: A chart showing the anisotropy ratio of each horizontal velocity profile versus its depth in meters at the Km-2 site. The square red data points indicate non-random data distributions as determined by runs tests. The diamond blue data points represent random datasets as determined by the runs tests. All runs tests were conducted at the 95% confidence level ($p \leq 0.05$).

increase in a positively linear fashion to a high value of 2.02. This dataset has an overall range in anisotropy ratios from 1.33 to 2.02. The Km-1 site does not produce as well behaved a dataset as NT-2, with a larger range and noisier data. The first two data points have relatively high anisotropy ratios (3.91 and 3.02) and then the anisotropy ratios decrease to a value close to unity. From this low value, the anisotropy increases to a high value of 6.32. The final two data points in the series have anomalously low values (relative to the range and pattern of the dataset) of 2.92 and 3.16. The Km-2 dataset behaves more similarly to the NT-2 dataset, in that there is a discrete break in the data, although there is more noise in the data at Km-2. The first point appears to have a relatively high anisotropy ratio (4.12), and then all other values hover near unity until a depth of 2.5 m is reached. At that point, the anisotropy values increase to 4.39 and then fluctuate from very low values (1.23) to a local high value of 3.8.

In looking at all of the radial velocity distributions for each dataset, a qualitative assessment can be reached that states that the anisotropy increases with depth, and that the distributions strongly favor the northeast-southwest direction. Samples of depths 1 m. 3 m, 6 m, and 9 m for each azimuthal dataset can be seen in figures 23, 24, and 25. Sample depths were used rather than the entire series of depths due to space and resolution constraints for the figures. To see all depth intervals for each dataset, refer to Appendices 1, 2, and 3, section 3: Compass diagrams. All three sets of data show a strong northeast-

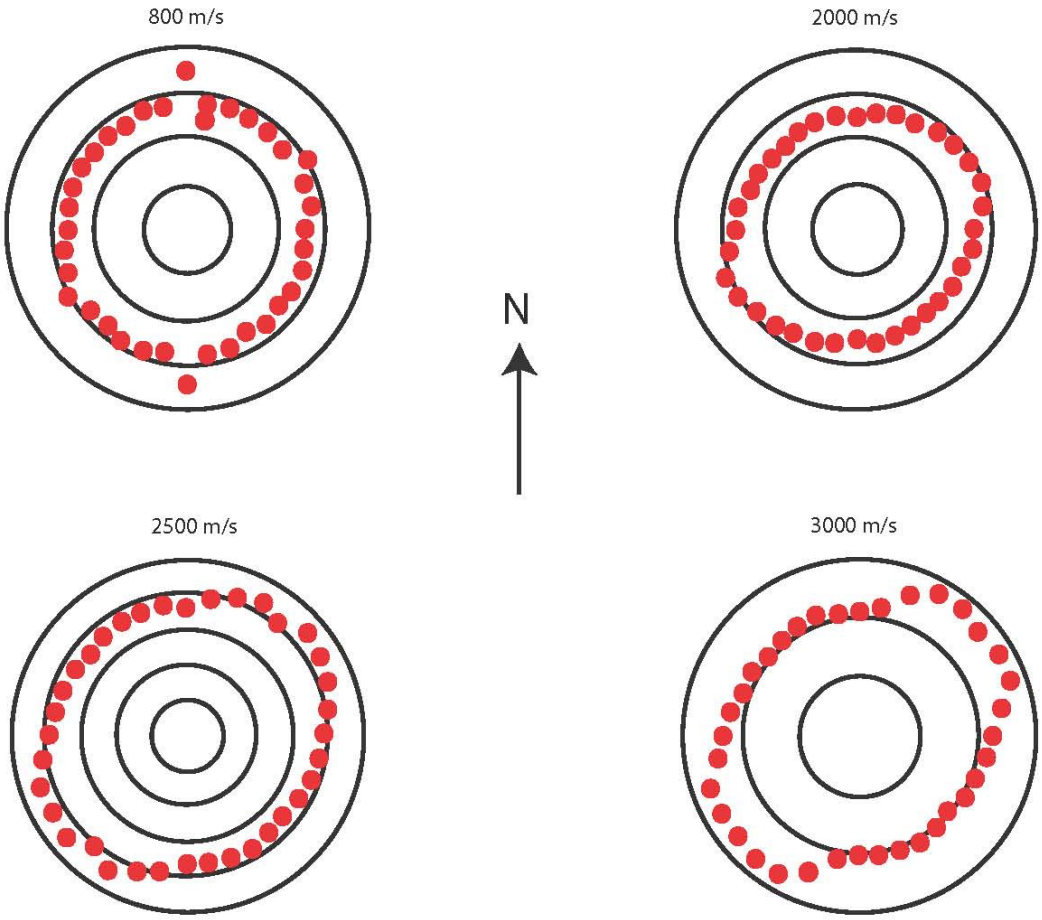

Figure 23: A series of depth slices indicating the magnitude and direction of seismic anisotropy for the NT-2 site. The depths are: 1 m in the top left, 3 m in the top right, 6 m in the bottom left, and 9 m in the bottom right.

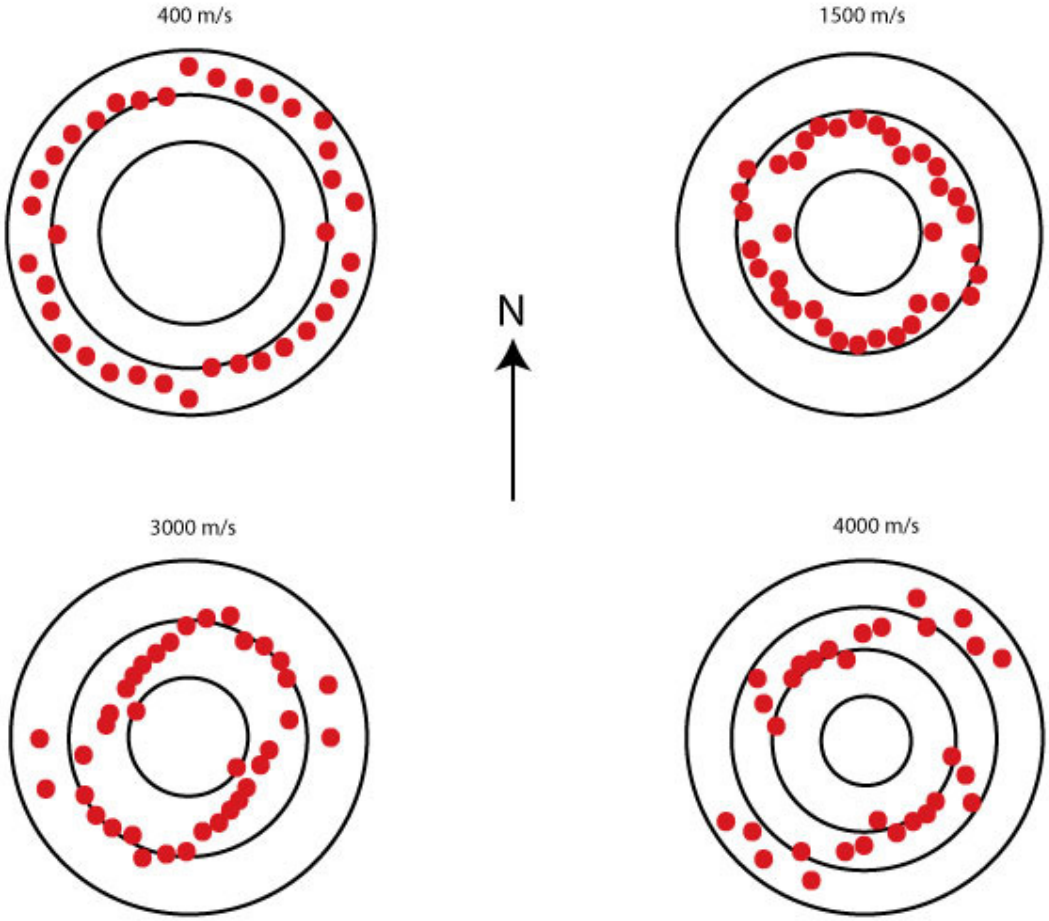

Figure 24: A series of depth slices indicating the magnitude and direction of seismic anisotropy for the Km-1 site. The depths are: 1 m in the top left, 3 m in the top right, 6 m in the bottom left, and 9 m in the bottom right.

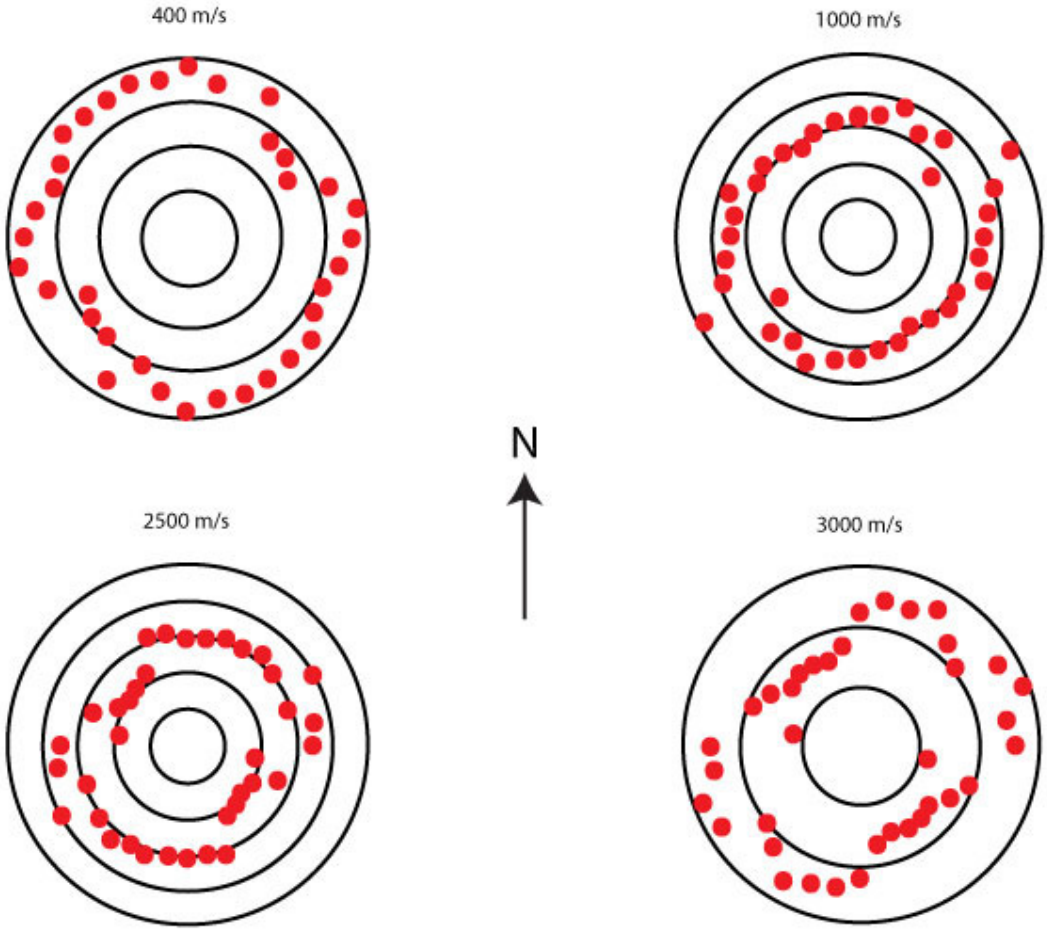

Figure 25: A series of depth slices indicating the magnitude and direction of seismic anisotropy for the NT-2 site. The depths are: 1 m in the top left, 3 m in the top right, 6 m in the bottom left, and 9 m in the bottom right.

southwest verging, seismically fast, direction which corresponds well with the hydrologic anisotropy shown in studies from other authors. Moline (1998) and Schrieber (1999) both demonstrate a preferred anisotropic flow direction to the southwest and Dreier (1988) shows a preferred anisotropic flow direction to the northeast, while Gierke (1988) demonstrates the presence of the near surface hydrologic anisotropy in question.

The general trend of the anisotropy data is to decrease with depth (aside from a few anomalous data points). It remains to be determined, however, whether this increase in SEPAR indicates a significant degree of anisotropy. In order to assign some statistical significance to qualitatively observed anisotropy at depth in the radial velocity distributions, a runs test for non-randomness was performed for each depth interval for each dataset at a 95% significance level. The purpose of the runs test is to determine whether a dataset is random or non-random. In this case, a random dataset is considered insignificant, as it has no controlling factor, while a non-random dataset is considered significant because there is an implied controlling factor in producing non-random data, in this case, fracture sets in the subsurface. For all of these tests, the null hypothesis (μ_0) is that the observed anisotropy ratio is generated by random processes, while the alternative hypothesis (μ_1) is that the observed anisotropy is generated by non-random processes. These tests were run for all three datasets (NT-2, Km-1, and Km-2) at a 95% significance level, and the results for each azimuthal survey can be seen in Figures 21, 22, and 23. The first, and incidentally, most well behaved

dataset from the NT-2 site shows random velocity distributions to a depth of 3 m. At 3.5 m depth, the data become significant and remain so to the terminus of the depth profile at 11.5 m depth. The area in the data distribution between the beginning of significant data and the inflection point in the behavior of the SEPAR may be the extent of the saprolitic transition zone expressing itself in the data. The Km-1 site has far fewer significant velocity distributions, and they are not as well behaved, which may be attributed to higher amounts of noise in the data. There is an anomalous significant data point at 0.5 m depth, beyond which the data remain insignificant to a depth of 6 m. At 6.5 m depth, significant results emerge, and continue to 7.5 m depth. At Km-2, the results fall somewhere between the extremely well behaved nature of the NT-2 dataset and the excessively noisy data from the Km-1 site. The velocity distributions from this dataset remain insignificant to a depth of 5 m, and at 5.5 m begin to demonstrate significance. This trend continues to a depth of 8.5 m (with the exception of a single data point), and the last two data points in the series are insignificant. Some idea of the location of the location of the saprolite/bedrock interface at Km-1 and Km-2 is given at the beginning of significantly anisotropic data, but more information about the subsurface at these sites would be useful to confirm or repudiate this idea.

4.6 Conclusions

Interpretation of the data collected in this study can say several things about the groundwater flow paths in the vicinity of the ORNL, specifically within

the Nolichucky Shale unit in the Bear Creek Valley. Horizontal near-surface hydrologic anisotropy has been confirmed in this area by several studies. It appears that in the shallow subsurface (10's of meters) that groundwater flow does not follow the expected pathway in the down gradient direction, but rather flows horizontally in a direction perpendicular to hydraulic gradient. This horizontal flow has been shown to either move in a northeasterly or southwesterly direction, and is generally attributed to the presence of interconnected fracture networks in the saprolitic soils above solid bedrock. This anisotropic flow moves at its' highest rate near the interface between the saprolitic clays and competent bedrock. These fracture networks are all consistent with a stress field that would cause the folding observed in the region that took place during the compressional episode that formed East Tennessee's Valley and Ridge province. There are three main series of fracture sets that form an orthogonal network: bedding plane parallel fractures, strike parallel elongation fractures, and strike perpendicular elongation fractures. Control on anisotropic flow in the subsurface appears to result from the interaction of the strike parallel elongation fractures, as geologic strike in the region verges to the northeast/southwest, as does the preferential flow in the shallow subsurface.

The purpose of this study was to determine the efficacy of using azimuthal seismic first-arrival tomography (ASFT) as an additional technique for detecting this fracture driven hydrologic anisotropy. Upon examination of the data and statistical analysis of the resultant velocity distributions, several conclusions can

be drawn. Primarily, it is apparent that the seismic high velocity directions coincide with the preferred flow networks in the shallow subsurface (Table 2).

Location	Anisotropy ratio	Orientation	Reference
Bear Creek Valley	N/A	along strike (≈N55E)	Solomon, et al. 1992
Bear Creek Valley	5:1	along strike (≈N55E)	Bailey, 1988
Bear Creek Valley	8:1	along strike (≈N55E)	Gierke, et al. 1988
Bear Creek Valley	10:1	along strike (≈N55E)	Schrieber, et al. 1999
S-3 Ponds	N/A	NE/SW	Shevenell, et al. 1994
SWSA6	N/A	N50E	Dreier, et al. 1988
NT-2 Site	2:1 (Seismic)	N50E	This study
Km-1 Site	6:1 (Seismic	N50E	This study
Km-2 Site	4:1 (Seismic)	N20E	This study

Table 2: A table showing the location, anisotropy ratio, anisotropy orientation, and investigative team for hydrologic and seismic anisotropy in and around Bear Creek Valley. The seismic velocities used to calculate anisotropy ratios and their directions shown for the NT-2, Km-1, and Km-2 sites are the maximum velocity values (and their associated perpendicular minimums) and their azimuths.

This makes sense, as the fractures that control hydrologic anisotropy should form a preferentially fast seismic direction, given that the compressional waves that result from the seismic source would travel more quickly along the linear fracture sets than across them. The fact that hydrologic flow is preferential to *either* the northeast or the southwest while the seismic energy is detected in both directions probably has to do with the dip and plunge of the fracture sets, or where the data was collected relative to groundwater divides in the area. It stands to reason that groundwater flow would travel in the down dip/down plunge direction of the fracture network as groundwater is controlled largely by downward gravitational force, while seismic energy is not sensitive to this condition, and as a result, would travel quickly both up dip/plunge as well as down dip/plunge.

A second type of information that can be drawn from seismic data prepared in this manner is the character of the anisotropy as a function of depth. The extent and character of anisotropy as it descends into the subsurface can provide information about the location of hydrostratigraphic boundaries in the subsurface. Surveys NT-2 and Km-2 show dramatic shifts in the character and significance of seismic anisotropy at discrete depth intervals (at 3.5 m and 5 m depth at NT-2, at 6.5 m depth at Km-1, and at 2.5 m and 5.5 m depth at Km-2). It is possible that this dramatic change in character delineates the interface between saprolitic clays and competent bedrock, although ground truthing at the central intersection point of these two surveys would be necessary to verify this conclusion.

The ASFT methodology was developed as a method to quickly and efficiently ascertain some general idea about the condition of hydrologic anisotropy at any given field site, and in the Bear Creek Valley, has proven to have merit. The fact that the anisotropy in this area is controlled by a distinct fracture network doubtlessly added to the efficacy of this methodology for reasons mentioned above. In an area without predominant fracture networks where hydrologic anisotropy may be controlled by other factors this method may not be as effective as it is at ORNL, or the results may not be as conclusive. It appears that this methodology works well for its intended purpose at this area of exploration, but further experimentation is recommended before its universality in application can be assessed. Also, some data concerning the aperture and

spacing of the controlling fractures as they descend into the subsurface would be useful. If some quantitative relationship between seismic velocity and aperture size could be determined, then more information about the nature of these fracture networks could be input to hydrologic models, dramatically increasing their accuracy and predictive power.

CHAPTER 5: CONCLUSIONS

In order to assess the effectiveness of using seismic first-arrival tomography in an azimuthal manner as a methodology to detect subsurface hydrologic anisotropy, the two components of the original hypothesis will be addressed individually. The first component of the hypothesis:

(1) ASFT will provide a methodology for the delineation of anisotropic zones based on seismic velocity variations governed by interconnected fracture networks, and that this seismic information can be used as a proxy for preferred fracture driven hydrogeological flow direction.

can be considered validated. Initial data collection and analysis indicate that azimuthal seismic surveys can indeed detect anisotropy in the subsurface. This detected anisotropy is seismic in nature, but the results of this study confirm that the causal factors for seismic anisotropy also control hydrologic anisotropy. The hydrology of the area around the ORIFRC is well understood, and the fact that the hydrology is driven by interconnected networks of fracture sets allows it to be detected with seismic methods via seismic velocity as a proxy.

The second component of the hypothesis:

(2) The ASFT methodology prove accurate (relative to conventional methods) for characterizing zones of anisotropic flow of the NT-2 site and two other sites at the ORIFRC within the Oak Ridge Reservation.

may also be considered validated. The seismic data collected in the course of this study visually appears to correlate well with previously collected hydrologic

data at the ORIFRC from several other authors. This seismic methodology is faster and more cost effective than traditional methods at a virgin site where boreholes would have to be drilled and wells installed as a means to characterize subsurface anisotropic flow. Conventional borehole hydrology methods do however, at this point, more accurately assess the extent and nature of any anisotropic flow. To this date, no accurate means of quantifying the extent of horizontal anisotropy with azimuthal seismic first-arrival tomography has been developed. For this reason, it is recommended that ASFT surveys be conducted precluding other, more extensive, means of characterizing a given site in order to form an initial idea of the subsurface flow conditions such that conventional methods can be emplaced more strategically and with more efficiency.

LIST OF REFERENCES

Aki, K., Christoffersson, A., and Husebye, E. S., 1977, Determination of 3-Dimensional Seismic Structure of Lithosphere: Journal of Geophysical Research, v. 82, p. 277-296.

Bailey, Zelda Chapman, 1988, Preliminary evaluation of the ground-water flow in Bear Creek Valley, the Oak Ridge Reservation, Tennessee; USGS Water-Resources investigations report 88-4010, p. 1-12.

Boadu, Fred Kofi, Gyamfi, Joseph, and Owusu, Emmanuel, 2005, Case History: Determining subsurface fracture characteristics from azimuthal resistivity surveys: A case study at Nsawam, Ghana: Geophysics, v. 70, p. B35-B42.

Bregman, N. D., Hurley, P. A., and West, D., F., 1989, Seismic Tomography at a fire-flood site: Geophysics, v. 54.

Carlson, Douglas, 2010, Application of the surface azimuthal electrical resistivity survey method to determine patterns of regional joint orientation in glacial tills: Environmental Geosciences, v. 17, p. 175-192.

Carlson, Douglas, 2010, Use of the azimuthal resistivity technique for determination of regional azimuth of transmissivity: Environmental Geosciences, v. 17, p. 163-174.

Chen, Jinsong, Hubbard, Susan S., Gaines, David, Korneev, Valeri, Baker, Gregory S., Watson, David, 2010, Stochastic estimation of aquifer geometry using seismic refraction data with borehole depth constraints: Water Resources Research, v. 46.

Diebold, J. B., and Stoffa, P. L., 1981, The traveltime equation, tau-p mapping, and inversion of common midpoint data: Geophysics, v. 46, p. 238-254.

Dreier, R., B., Solomon, D., K., and Beaudoin, C., M., 1988, Fracture Characterization in the unsaturated zone of a shallow land burial facility: Environmental Sciences Division report, ORNL, p. 51-59.

Fetter, C. W., 2001, Applied Hydrogelology: New Jersey, Prentice Hall, iv, 598 p.

Gaines, David P., 2011, Advances in Seismic first-arrival tomography [Dissertation], Knoxville, The University of Tennessee

Gawlas, Peter Florian 2001 Ph. D. Thesis. Möglichkeiten eines DMO-Prozesses in der CMPRefraktionsseismik.
LMU Munich: Faculty of Geosciences. See http://edoc.ub.unimuenchen. de/archive/00000222/01/Gawlas_Peter.pdf .

Gierke, W. G., Lozier, W. B., and Pearson, R., 1988, Task 2, Well logging and geohydraulic testing, site characterization, and ground water flow computer model application, vol. 1: Golder Associates Inc, ORNL/Sub/30X-SA706C, ORNL.

Hatcher, R. D. Jr., Lemiszki, P. J., Dreier, R. B., Ketelle, R. H., Lee, R. R., Leitzke, D. A., McMaster, W. M., Foreman, J. L., and Lee, S. Y., 1992, Status report on the geology of the Oak Ridge Reservation, ORNL.

Heincke, Bjorn, Maurer, Hansruedi, Green, Alan G., Willenberg, Heike, Spillman, Tom, and Burlini, Luigi, 2006, Characterizing an unstable mountain slope using shallow 2D and 3D seismic tomography: Geophysics, vol. 71.

Humphreys, E., and Clayton, R. W., 1988, Adaptations of back projection tomography to seismic travel time problems: Journal of Geophysical Research-Solid Earth and Planets, v. 93, p. 1073-1085.

Lanz, Eva, Maurer, Hansruedi, Green, Alan G., 1998, Refraction tomography over a buried waste disposal site: Geophysics, vol. 63.

Lay, T., and Wallace, T. C., 1995, Modern global seismology: San Diego, Academic Press, xii, 521 p.

Lecomte, I. H., Gjoystdal, A. Dahle, and Pederson, O. C., 2000, Improving modeling and inversion in refraction seismics with a first-order Eikonal solver: Geophysical Prospecting, v. 48, p. 437-454.

Moline, Gerilyn R., Schreiber, Madeline E., and Bahr, Jean M., 1998, Representative ground water monitoring in fractured porous systems: Journal of Environmental Engineering, June, p. 530-538.

Schuster, G. T., and Quintus-Bosz, A., 1993, Wavepath Eikonal traveltime inversion: Theory: Geophysics, v. 58, p. 1314-1323.

Science Applications International Corporation, 1995, Fiscal year 1995 well installation program summary Y-12 plant, Oak Ridge, Tennessee: ORNL.

Sheriff, R. E., and Geldart, L. P., 1995, Exploration seismology: Cambidge; New York, Cambridge University Press, xv, 592 p.

Shevenell, L. A., Moore, G.K., and Dreier, R. B., 1994, Contaminant spread and flushing in fractured rocks near Oak Ridge, Tennessee: Groundwater Monitoring and Remediation, v. 14(2), p. 120-129.

Solomon, D. K., Moore, G. K., Toran, L. E., Dreier, R. B., McMaster, W. M., 1992, Status Report: A Hydrologic Framework for the Oak Ridge Reservation, ORNL.

U.S. Department of Energy (US DOE), 1997, Report on the remedial investigation of Bear Creek Valley at the Oak Ridge Y-12 Plant, Oak Ridge, Tennessee: DOE/OR/01-1455/V1&D2.

Watanabe, T., Matsuoka T., and Ashida, Y., 1999, Seismic traveltime tomography using Fresnel volume approach, SEG Houston 1999 Meeting, Expanded Abstracts.

Watson, D. B., Doll, W. E., Gamey, T. J., Sheehan, J. R., and Jardine, P. M., 2005, Plume and lithologic profiling with surface resistivity and seismic tomography: Ground Water, v. 43, p. 169-177.

Zelt, Colin A., Azaria, Aron, and Levander, Alan, 2006, 3D seismic refraction traveltime tomography at a groundwater contamination site: Geophysics, v. 71.

Zollo, A., Gasparini, P., Virieux, J., Biella, G., Boschi, E., Capuano, P., de Franco, R., Dell'Aversana, P., de Matteis, R., de Natale, G., Iannaccone, G., Guerra, I., Le Muer, H., and Mirabile, L., 1998, An image of Mt. Vesuvius obtained by 2D seismic tomography: Journal of Volcanology and Geothermal Research, v. 82.

APPENDICES

Appendix 1: NT-2 Raypath coverage diagrams, Tomograms, and Compass Diagrams

This appendix will show all raypath coverage diagrams, velocity tomograms, and velocity compass diagrams in that order. The raypath coverage diagrams and velocity tomograms will begin with those imaged from the north-south line (azimuth of 0°) and continue to the azimuth of 170°. The compass diagrams will begin at a depth of 0 m, and continue in one half meter increments to the depth of resolution limit (for the NT-2 dataset, this depth is 11.5 m)

Raypath Coverage Diagrams:

0°

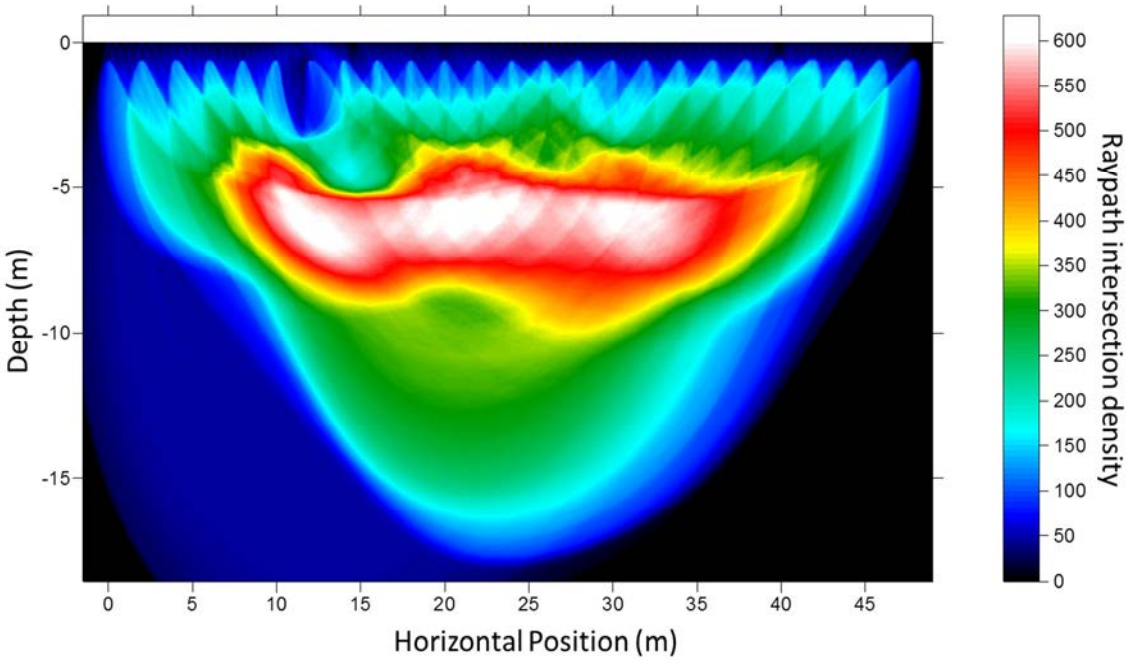

10°

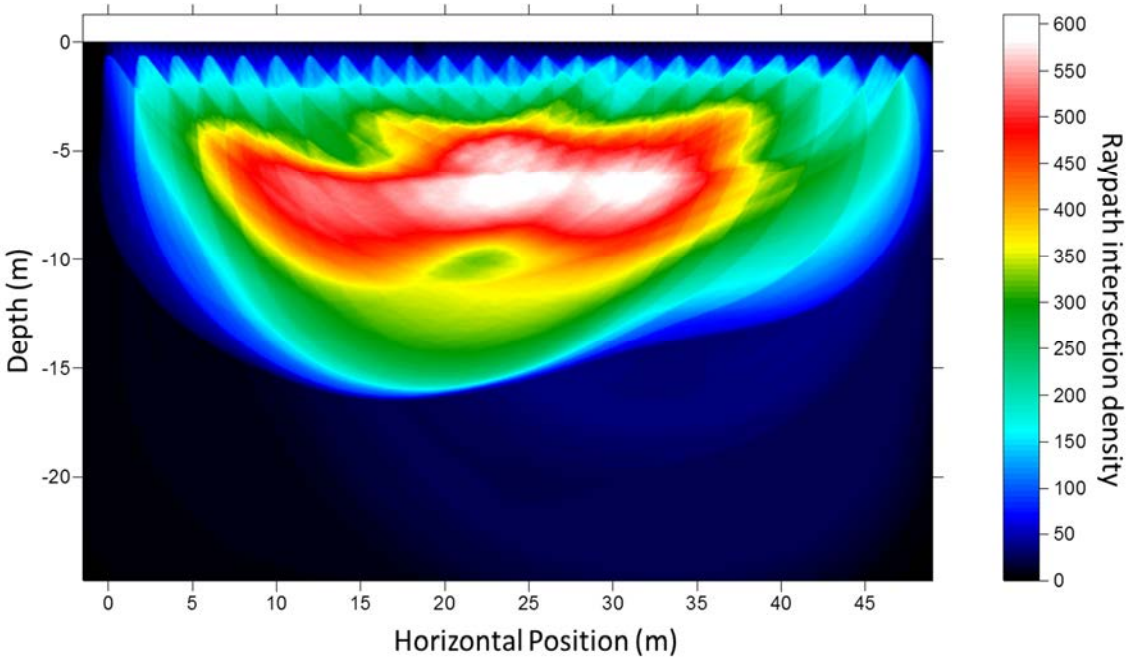
Depth (m)
0
-5
-10
-15
-20
0
5
10
15
20
25
30
35
40
45
Horizontal Position (m)
600
550
500
450
400
350
300
250
200
150
100
50
0
Raypath intersection density

20°

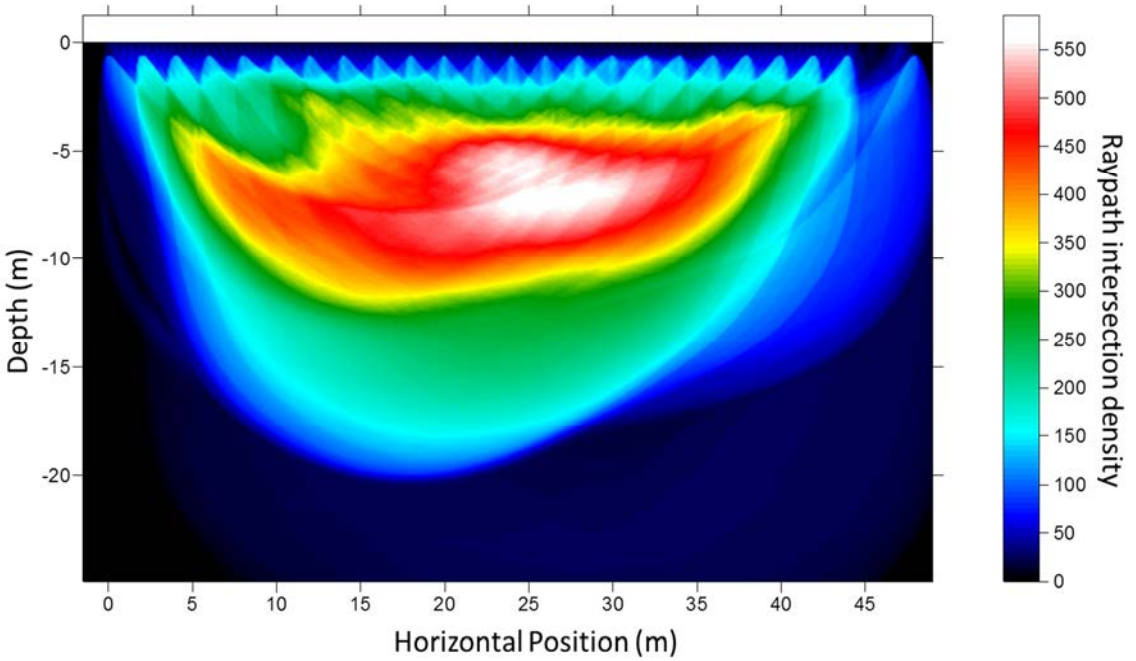
Depth (m)
0
-5
-10
-15
-20
0
5
10
15
20
25
30
35
40
45
Horizontal Position (m)
550
500
450
400
350
300
250
200
150
100
50
0
Raypath intersection density

30°

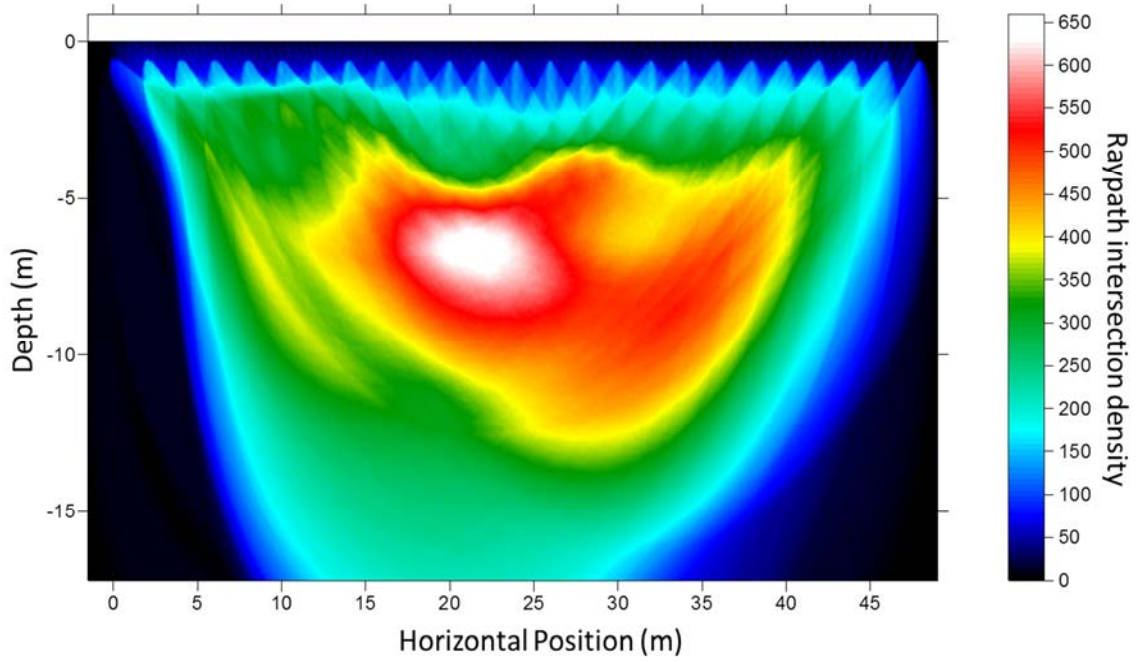
Depth (m)
0
-5
-10
-15
0
5
10
15
20
25
30
35
40
45
Horizontal Position (m)
650
600
550
500
450
400
350
300
250
200
150
100
50
0
Raypath intersection density

40°

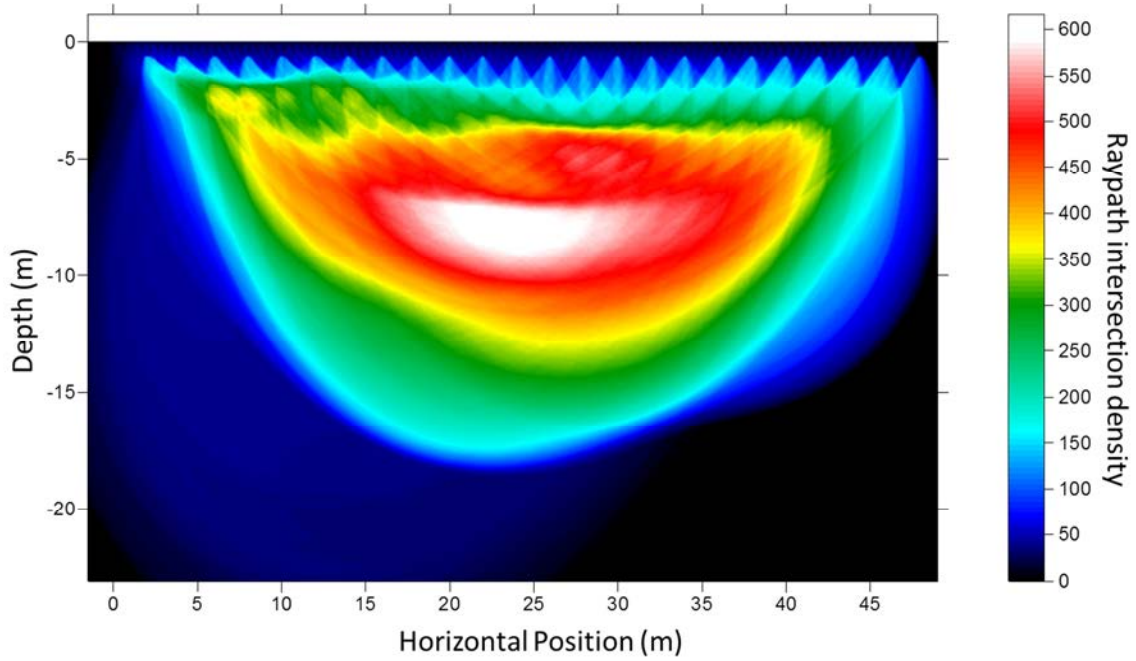
Depth (m)
0
-5
-10
-15
-20
0
5
10
15
20
25
30
35
40
45
Horizontal Position (m)
600
550
500
450
400
350
300
250
200
150
100
50
0
Raypath intersection density

50°

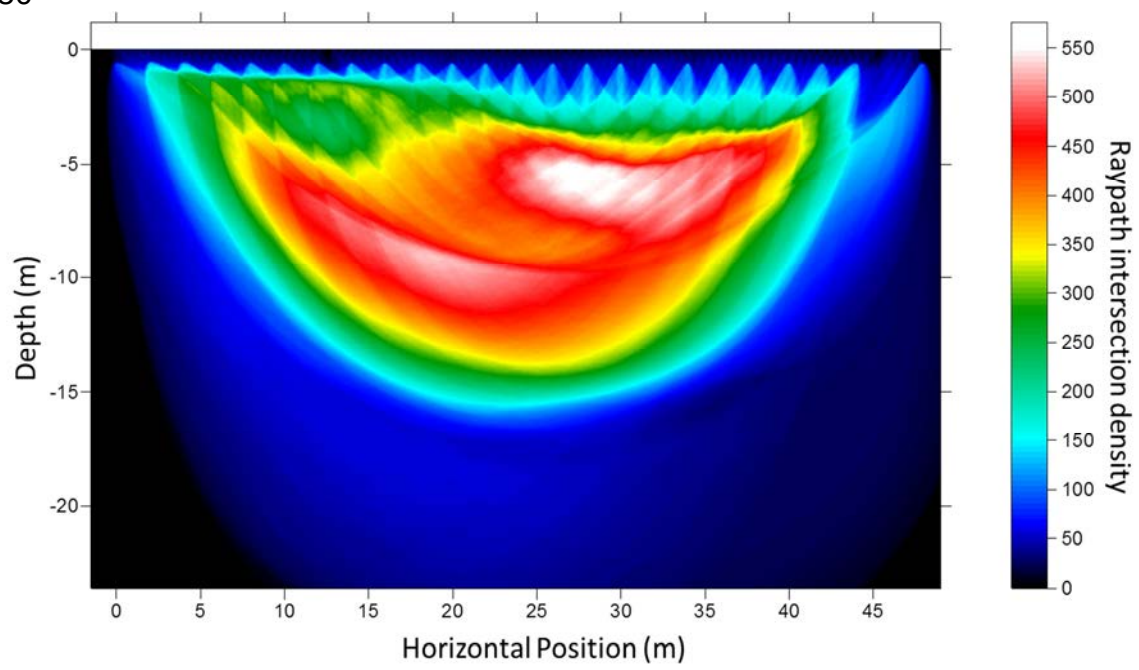
Depth (m)
0
-5
-10
-15
-20
0
5
10
15
20
25
30
35
40
45
Horizontal Position (m)
Raypath intersection density
550
500
450
400
350
300
250
200
150
100
50
0

60°

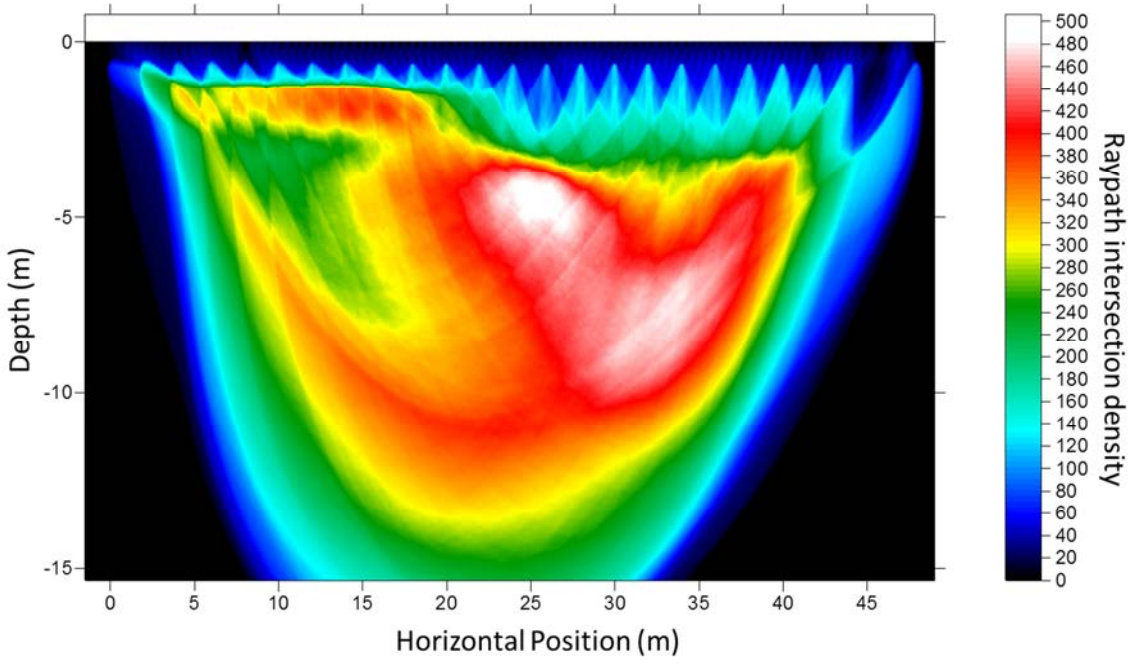
Depth (m)
0
-5
-10
-15
0
5
10
15
20
25
30
35
40
45
Horizontal Position (m)
Raypath intersection density
500
480
460
440
420
400
380
360
340
320
300
280
260
240
220
200
180
160
140
120
100
80
60
40
20
0

70°

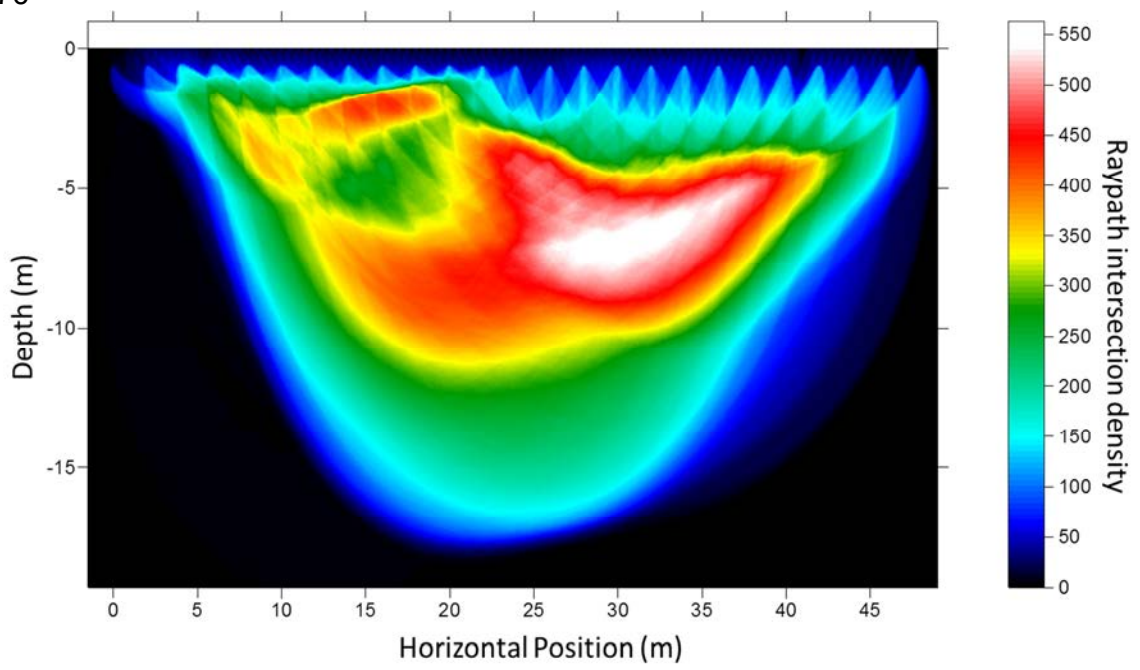
Depth (m)
0
-5
-10
-15
0
5
10
15
20
25
30
35
40
45
Horizontal Position (m)
550
500
450
400
350
300
250
200
150
100
50
0
Raypath intersection density

80°

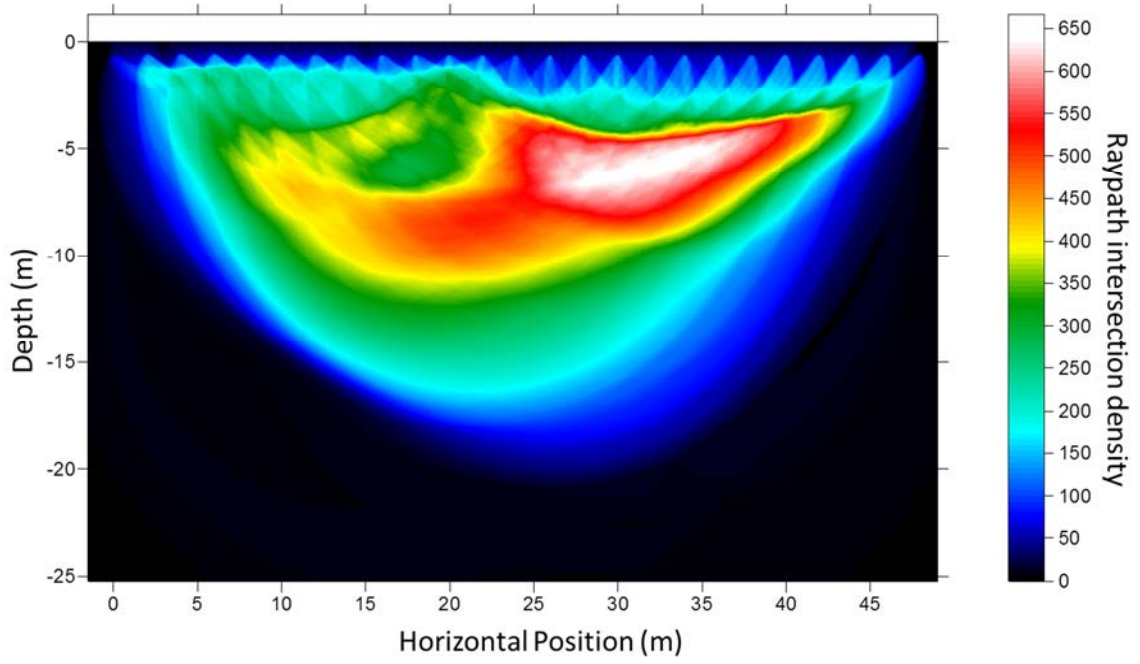
Depth (m)
0
-5
-10
-15
-20
-25
0
5
10
15
20
25
30
35
40
45
Horizontal Position (m)
650
600
550
500
450
400
350
300
250
200
150
100
50
0
Raypath intersection density

90°

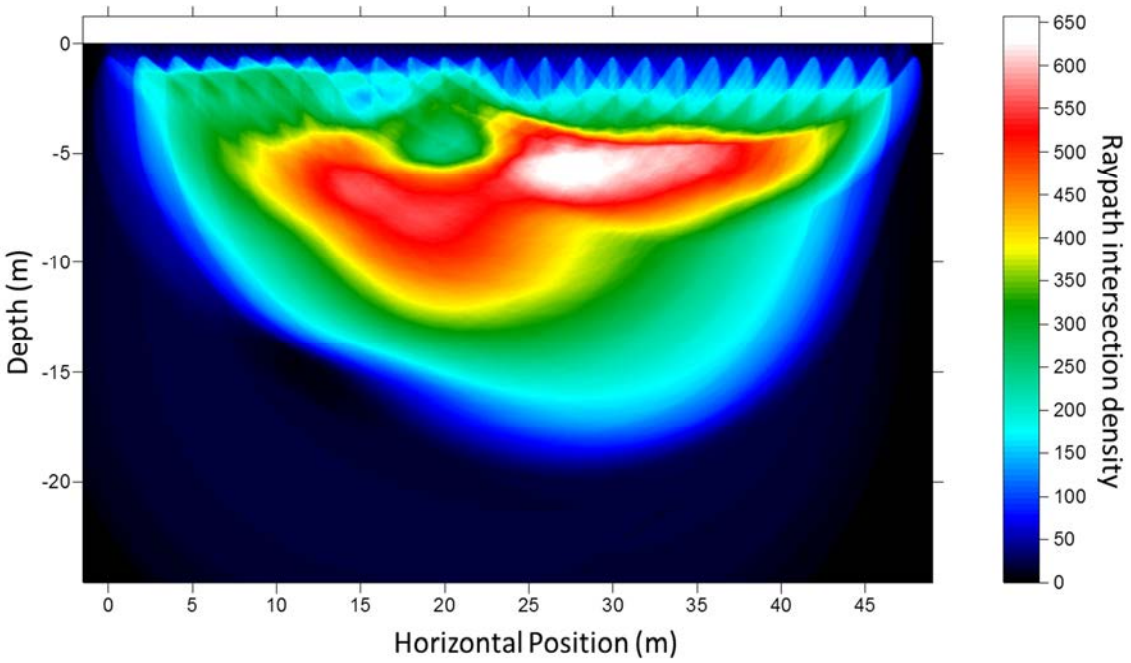
Depth (m)
0
-5
-10
-15
-20
0
5
10
15
20
25
30
35
40
45
Horizontal Position (m)
650
600
550
500
450
400
350
300
250
200
150
100
50
0
Raypath intersection density

100°

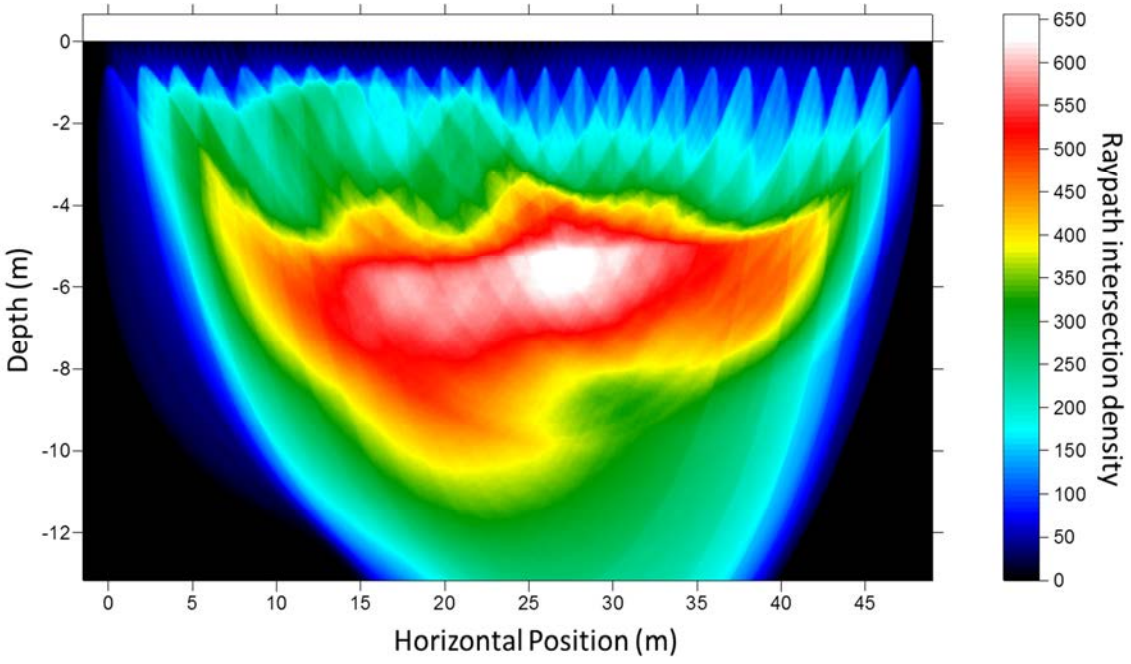
Depth (m)
0
-2
-4
-6
-8
-10
-12
0
5
10
15
20
25
30
35
40
45
Horizontal Position (m)
650
600
550
500
450
400
350
300
250
200
150
100
50
0
Raypath intersection density

110°

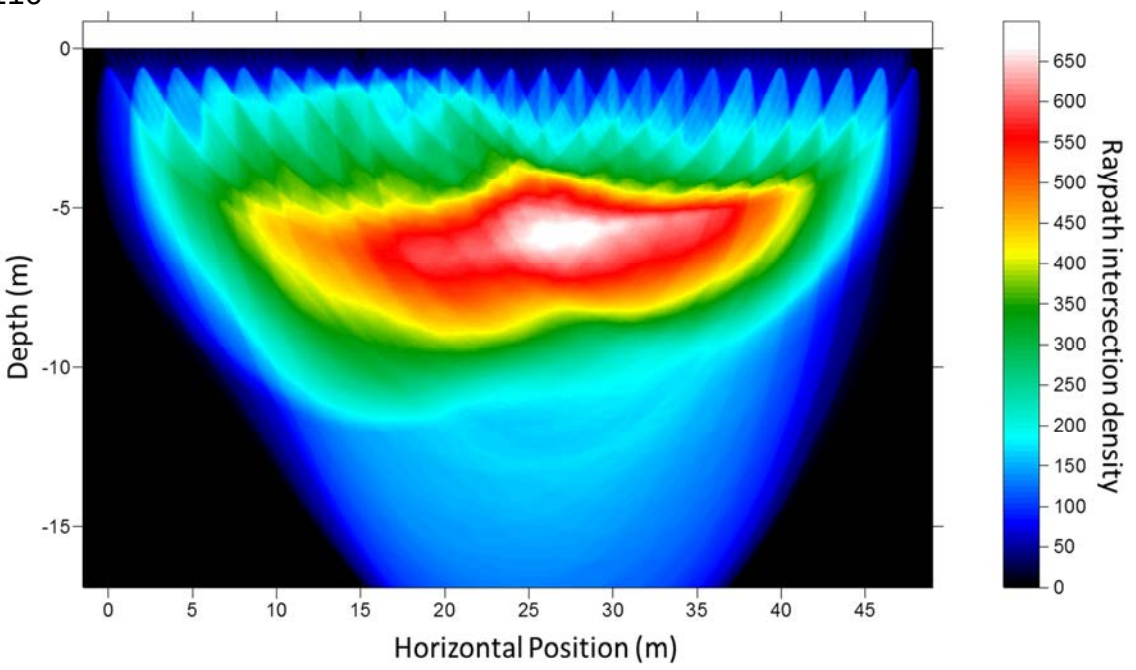
Depth (m)
0
-5
-10
-15
0
5
10
15
20
25
30
35
40
45
Horizontal Position (m)
650
600
550
500
450
400
350
300
250
200
150
100
50
0
Raypath intersection density

120°

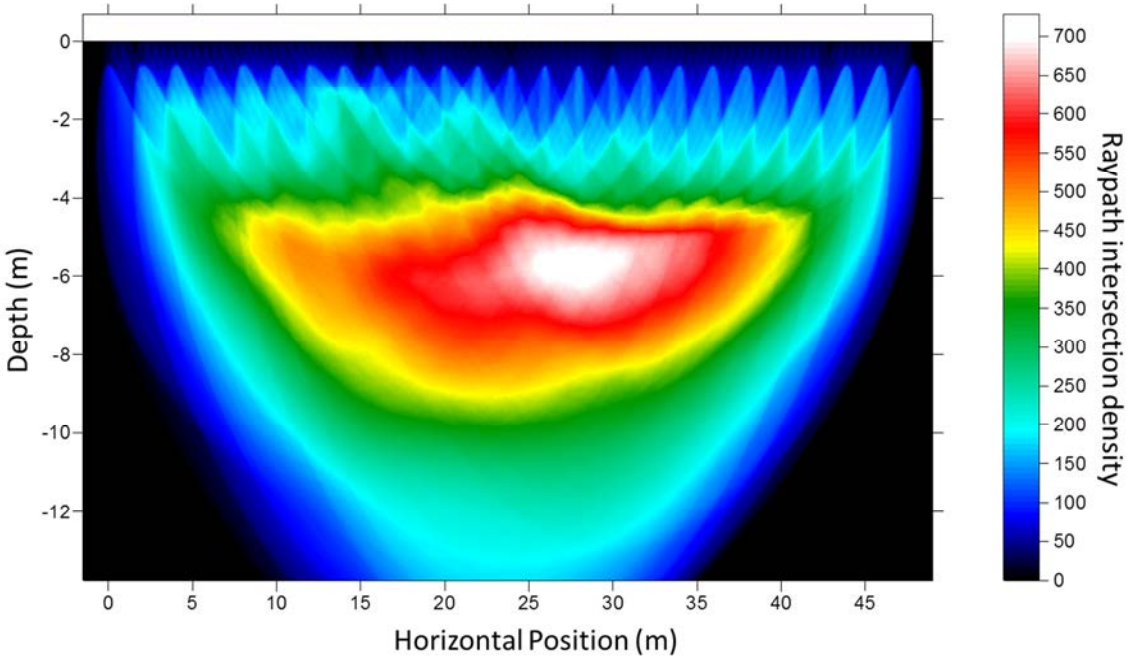
Depth (m)
0
-2
-4
-6
-8
-10
-12
0
5
10
15
20
25
30
35
40
45
Horizontal Position (m)
700
650
600
550
500
450
400
350
300
250
200
150
100
50
0
Raypath intersection density

130°

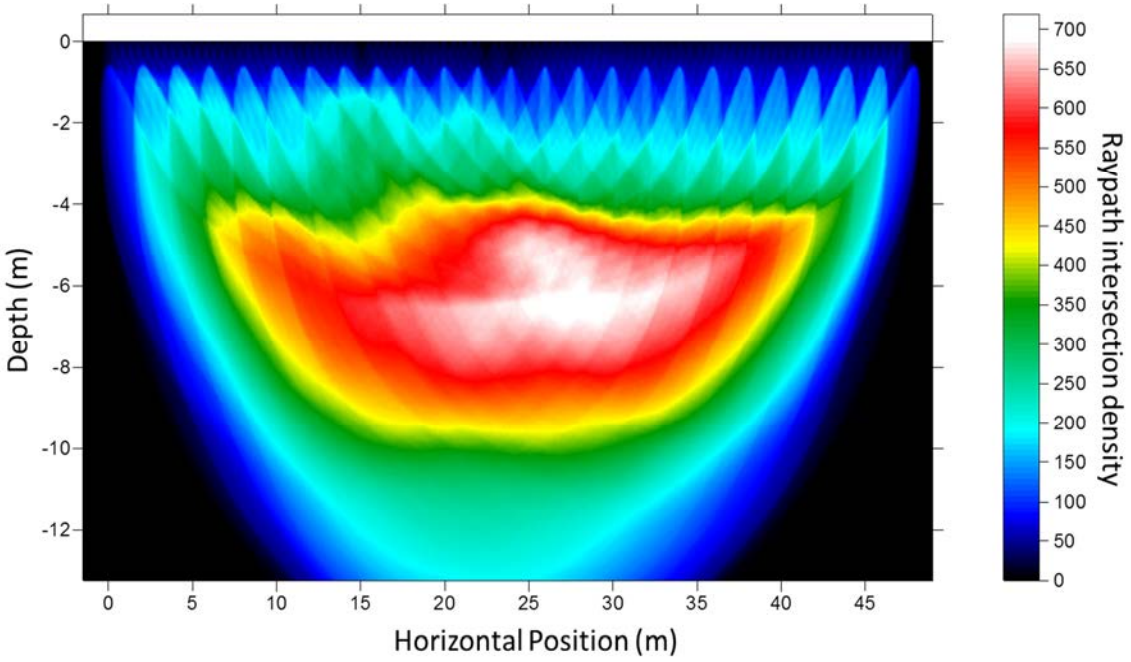
Depth (m)
0
-2
-4
-6
-8
-10
-12
0
5
10
15
20
25
30
35
40
45
Horizontal Position (m)
Raypath intersection density
700
650
600
550
500
450
400
350
300
250
200
150
100
50
0

140°

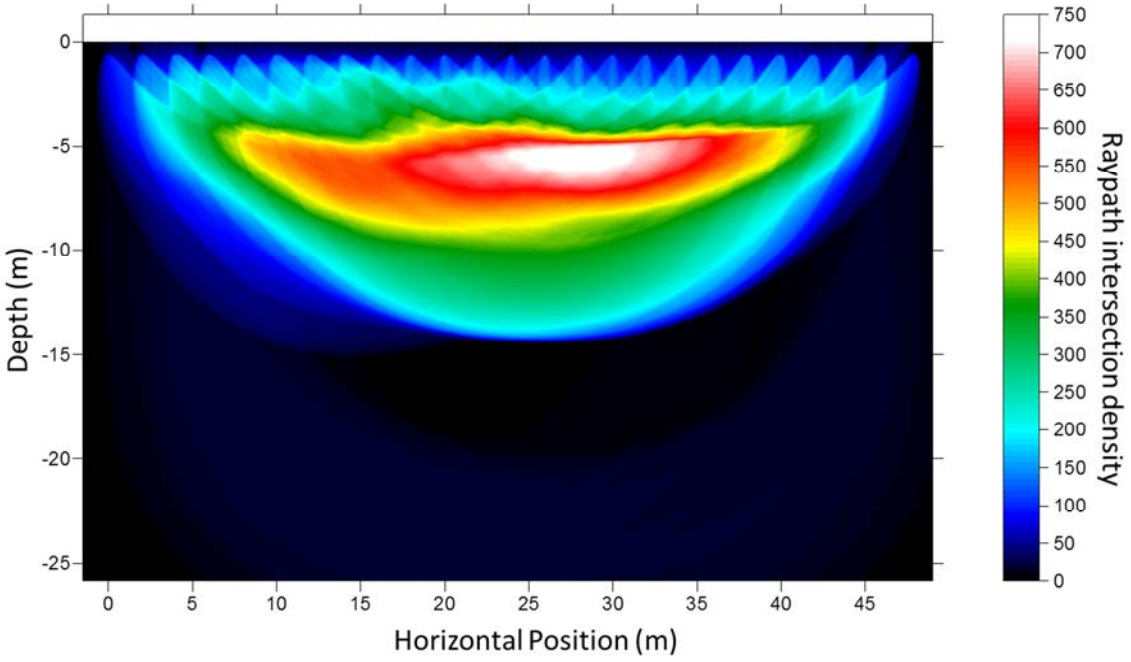
Depth (m)
0
-5
-10
-15
-20
-25
0
5
10
15
20
25
30
35
40
45
Horizontal Position (m)
Raypath intersection density
750
700
650
600
550
500
450
400
350
300
250
200
150
100
50
0

150°

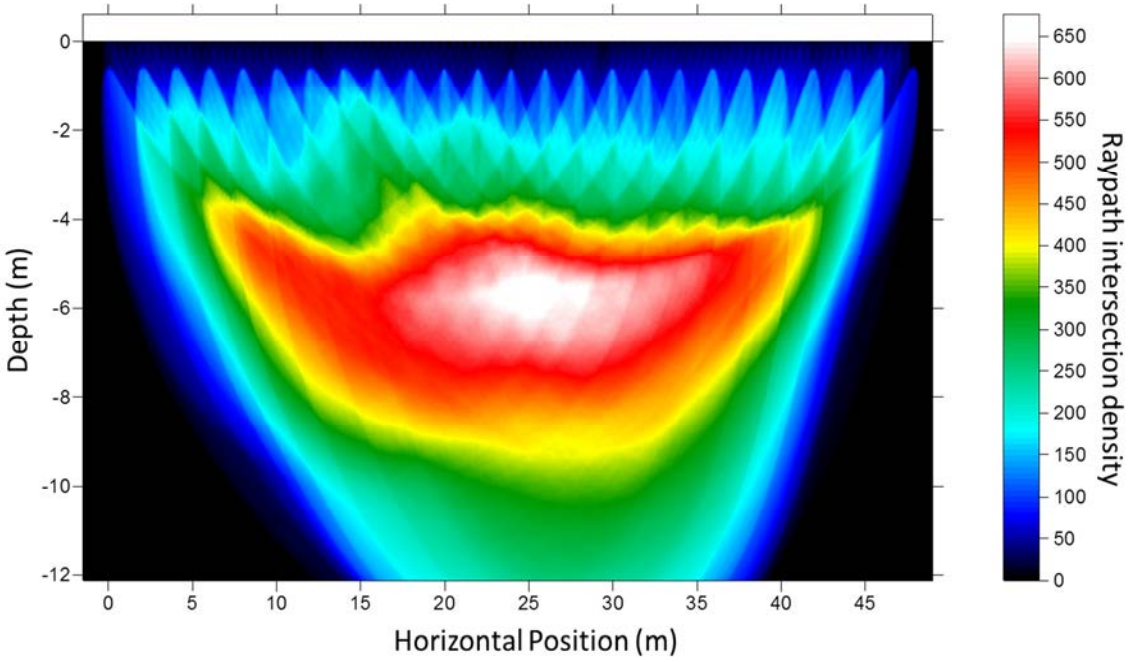
Depth (m)
0
-2
-4
-6
-8
-10
-12
0
5
10
15
20
25
30
35
40
45
Horizontal Position (m)
650
600
550
500
450
400
350
300
250
200
150
100
50
0
Raypath intersection density

160°

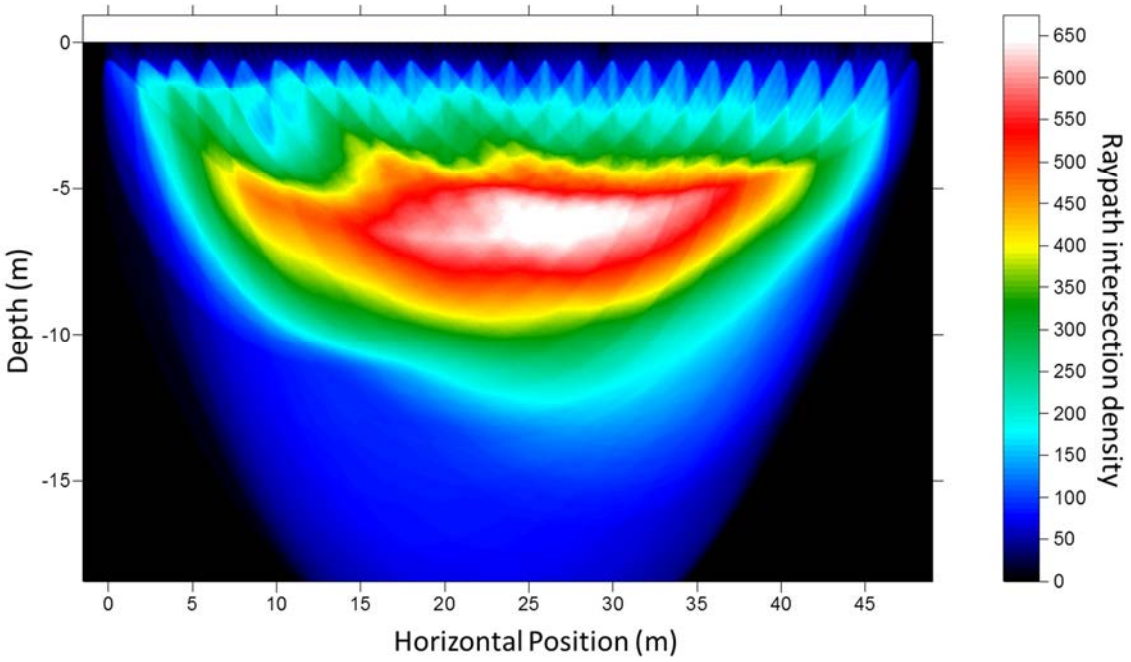
Depth (m)
0
-5
-10
-15
0
5
10
15
20
25
30
35
40
45
Horizontal Position (m)
650
600
550
500
450
400
350
300
250
200
150
100
50
0
Raypath intersection density

170°

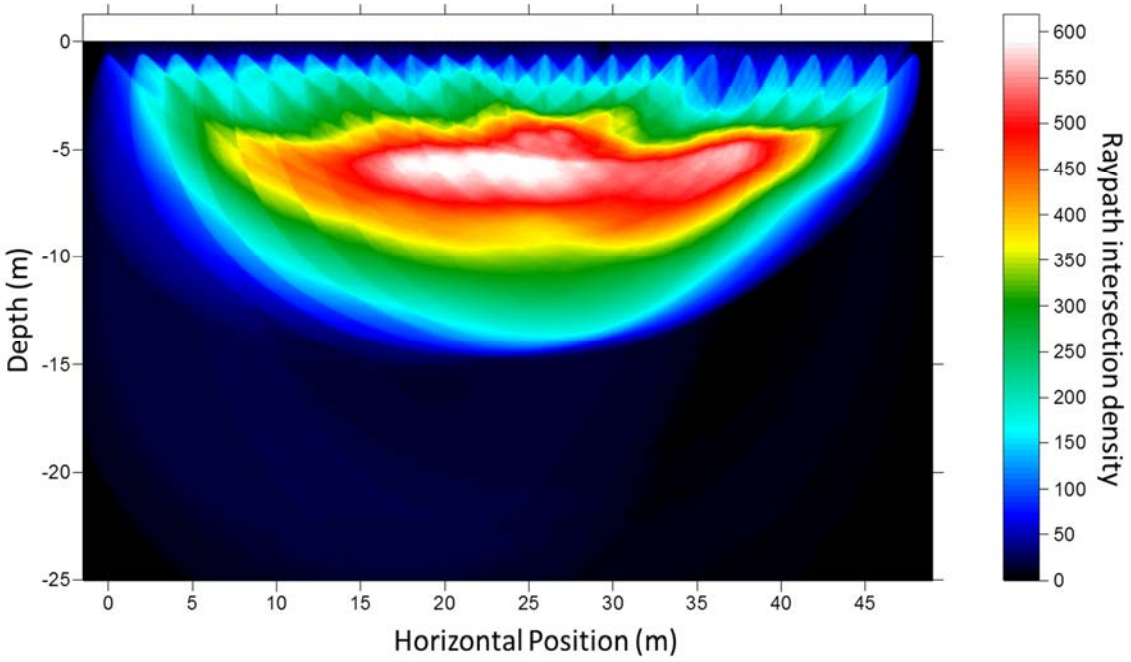

Velocity Tomograms:

0°

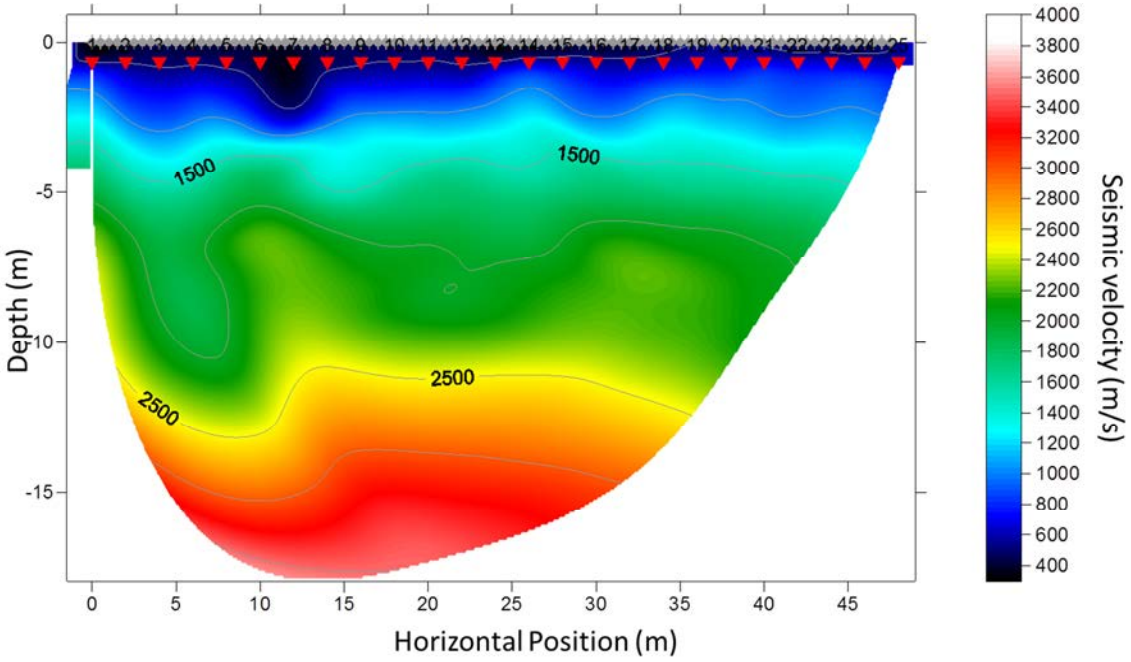

10°

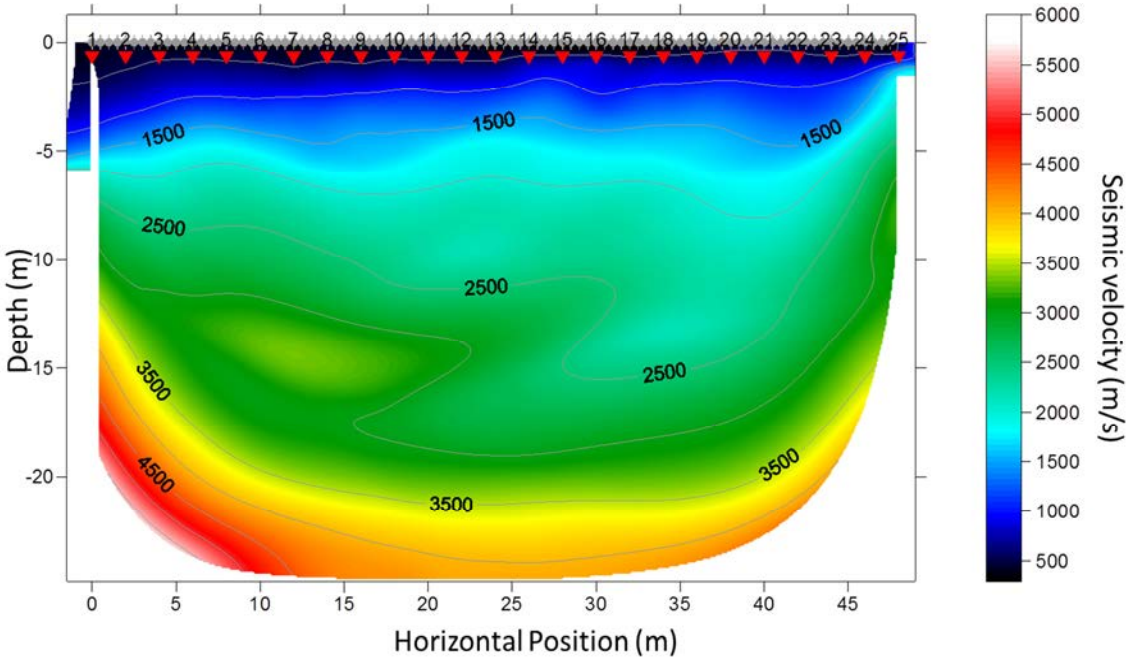
Depth (m)
Horizontal Position (m)
Seismic velocity (m/s)
1500
2500
3500
4500

20°

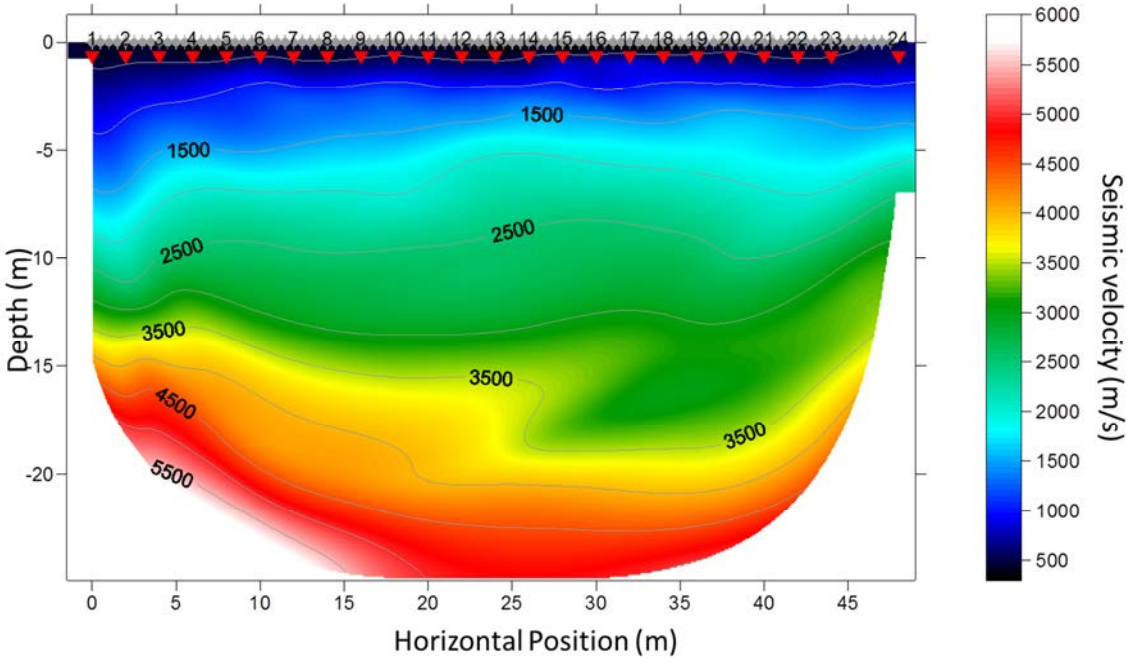
Depth (m)
Horizontal Position (m)
Seismic velocity (m/s)
1500
2500
3500
4500
5500

30°

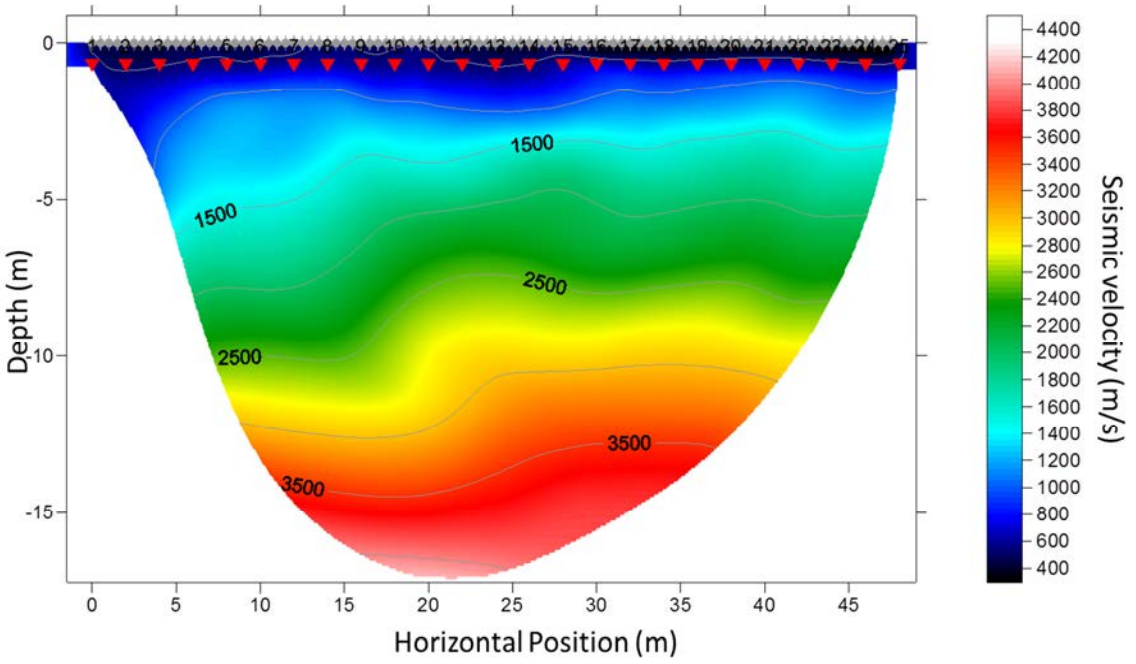
Depth (m)
Horizontal Position (m)
Seismic velocity (m/s)
1500
2500
3500

40°

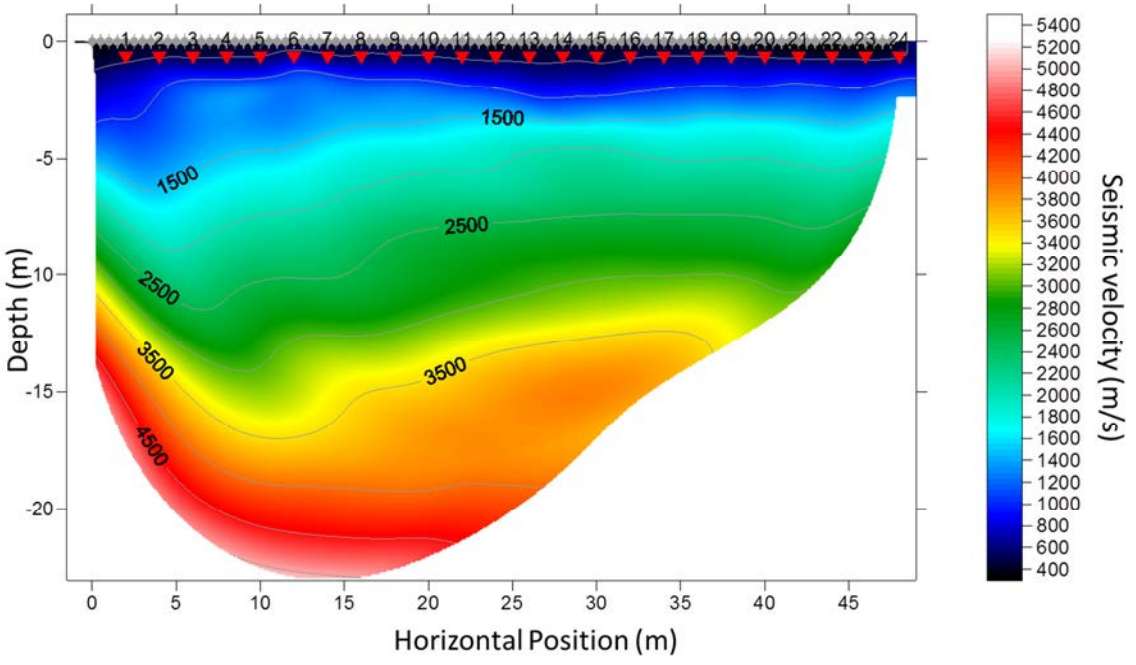
Depth (m)
Horizontal Position (m)
Seismic velocity (m/s)
1500
2500
3500
4500

50°

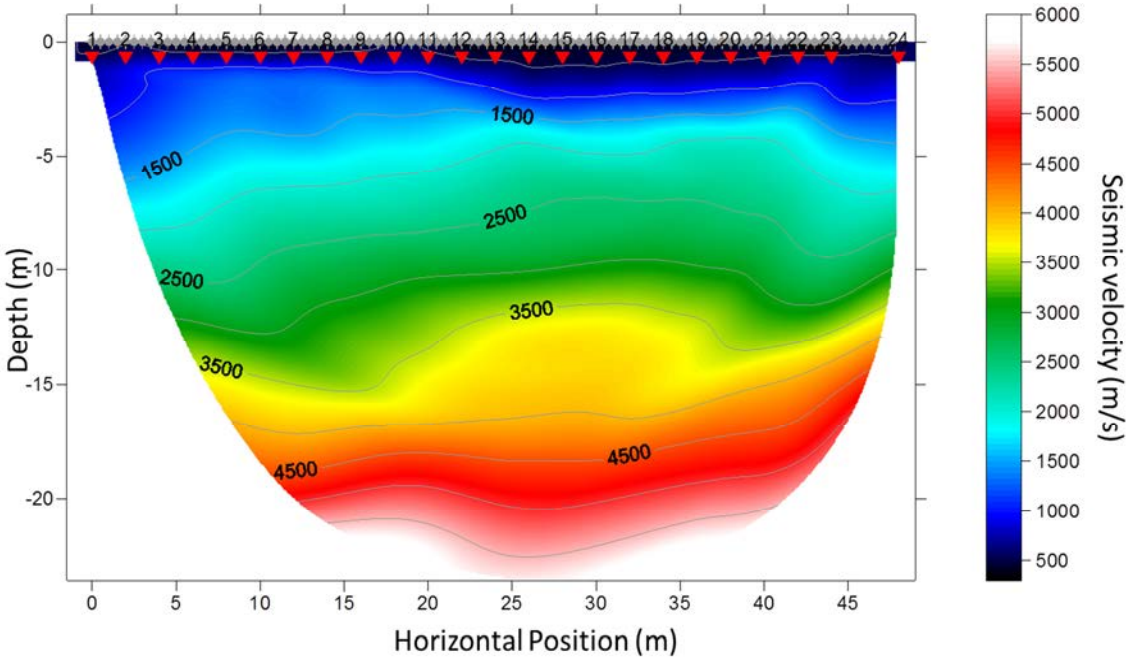
1 2 3 4 5 6 7 8 9 10 11 12 13 14 15 16 17 18 19 20 21 22 23 24
0
-5
-10
-15
-20
Depth (m)
1500
1500
2500
2500
3500
3500
4500
4500
0 5 10 15 20 25 30 35 40 45
Horizontal Position (m)
6000
5500
5000
4500
4000
3500
3000
2500
2000
1500
1000
500
Seismic velocity (m/s)

60°

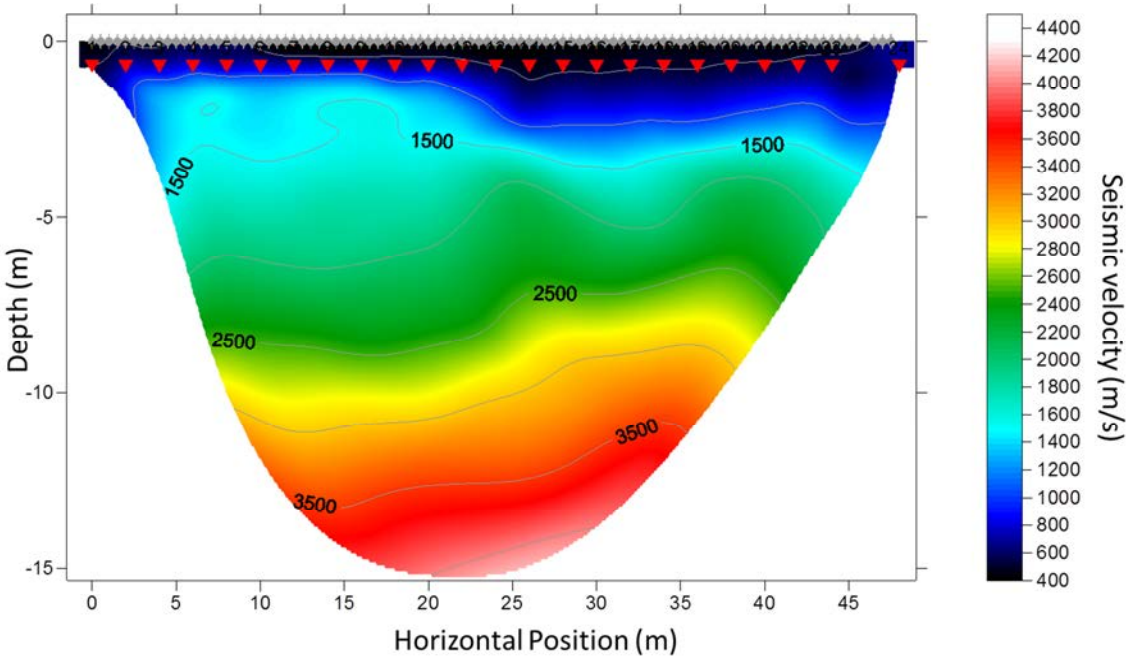
0
-5
-10
-15
Depth (m)
1500
1500
1500
2500
2500
3500
3500
0 5 10 15 20 25 30 35 40 45
Horizontal Position (m)
4400
4200
4000
3800
3600
3400
3200
3000
2800
2600
2400
2200
2000
1800
1600
1400
1200
1000
800
600
400
Seismic velocity (m/s)

70°

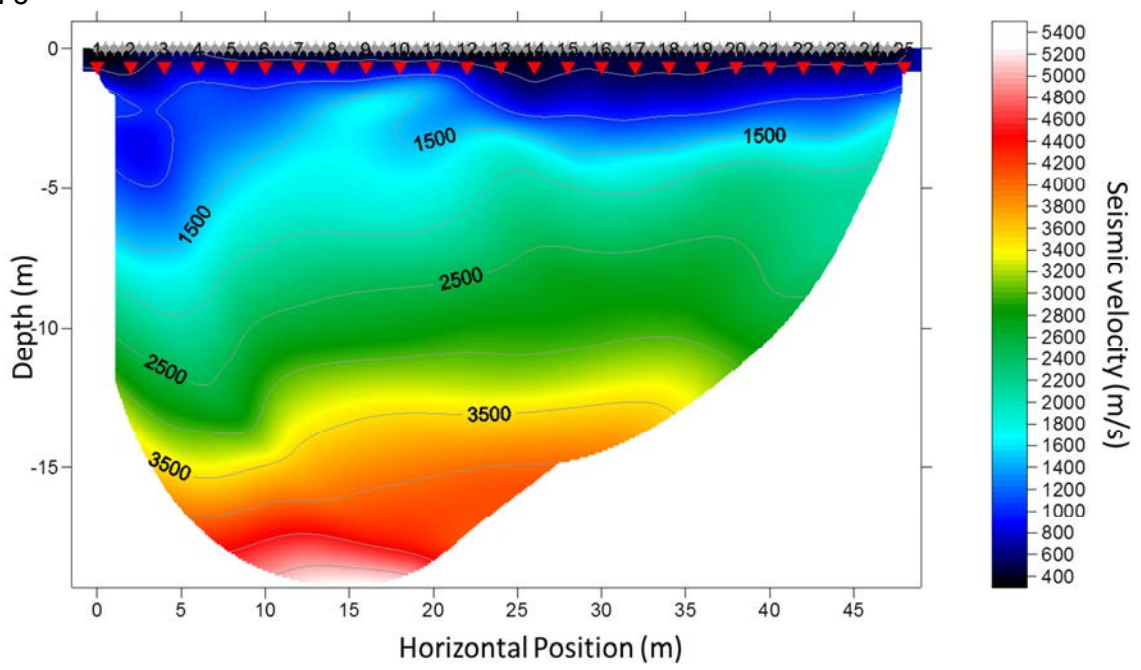
1 2 3 4 5 6 7 8 9 10 11 12 13 14 15 16 17 18 19 20 21 22 23 24 25
0
-5
-10
-15
Depth (m)
1500
1500
1500
2500
2500
3500
3500
0 5 10 15 20 25 30 35 40 45
Horizontal Position (m)
5400
5200
5000
4800
4600
4400
4200
4000
3800
3600
3400
3200
3000
2800
2600
2400
2200
2000
1800
1600
1400
1200
1000
800
600
400
Seismic velocity (m/s)

80°

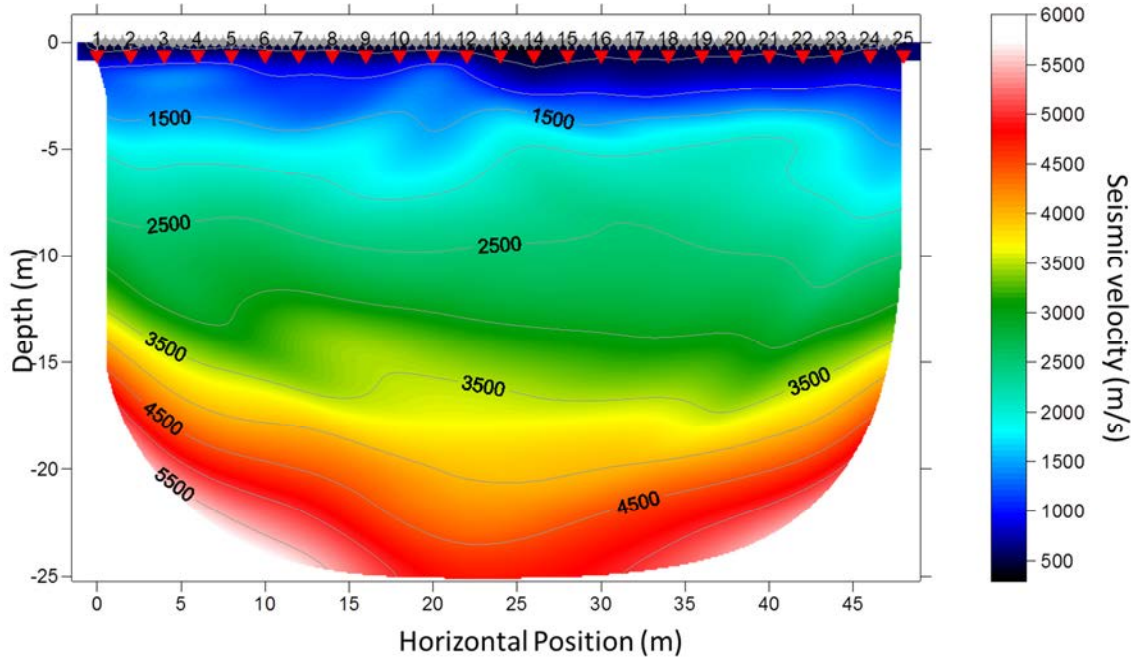
1 2 3 4 5 6 7 8 9 10 11 12 13 14 15 16 17 18 19 20 21 22 23 24 25
0
-5
-10
-15
-20
-25
Depth (m)
1500
1500
2500
2500
3500
3500
3500
4500
4500
5500
0 5 10 15 20 25 30 35 40 45
Horizontal Position (m)
6000
5500
5000
4500
4000
3500
3000
2500
2000
1500
1000
500
Seismic velocity (m/s)

90°

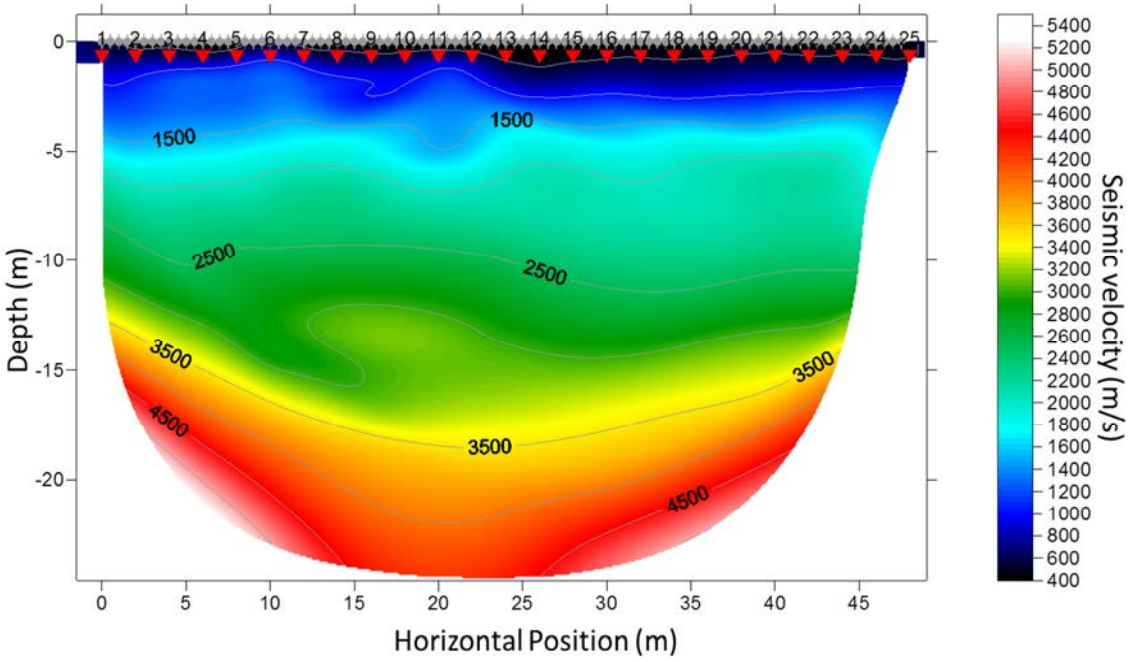
1 2 3 4 5 6 7 8 9 10 11 12 13 14 15 16 17 18 19 20 21 22 23 24 25
0
-5
-10
-15
-20
Depth (m)
1500
1500
2500
2500
3500
3500
3500
4500
4500
0 5 10 15 20 25 30 35 40 45
Horizontal Position (m)
5400 5200 5000 4800 4600 4400 4200 4000 3800 3600 3400 3200 3000 2800 2600 2400 2200 2000 1800 1600 1400 1200 1000 800 600 400
Seismic velocity (m/s)

100°

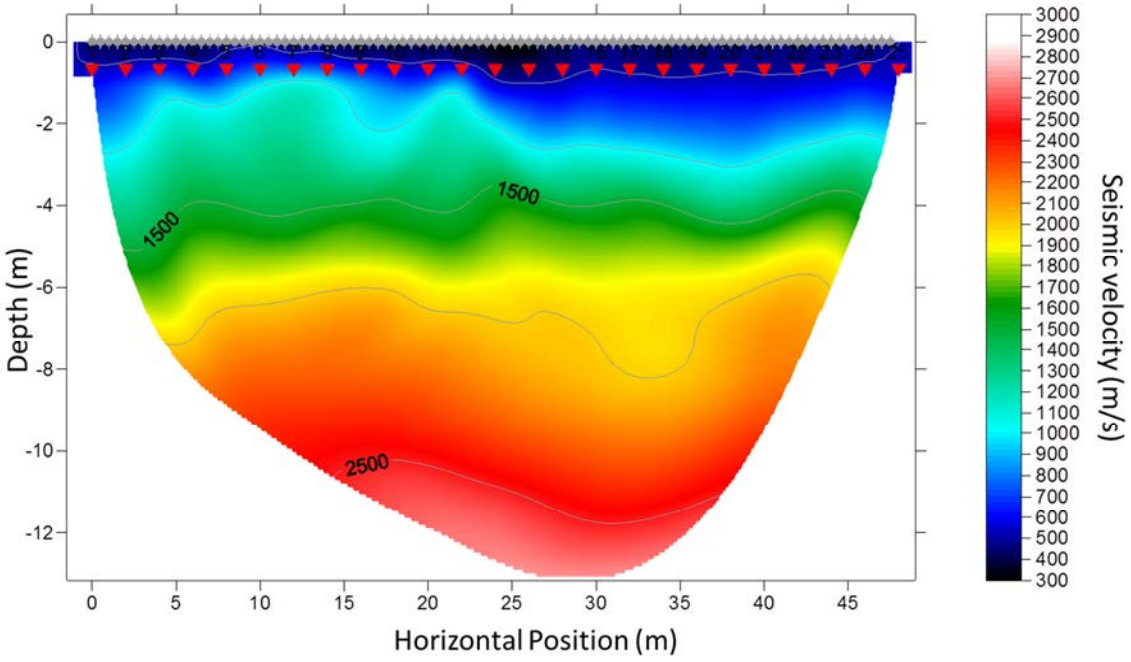
0
-2
-4
-6
-8
-10
-12
Depth (m)
1500
1500
2500
0 5 10 15 20 25 30 35 40 45
Horizontal Position (m)
3000 2900 2800 2700 2600 2500 2400 2300 2200 2100 2000 1900 1800 1700 1600 1500 1400 1300 1200 1100 1000 900 800 700 600 500 400 300
Seismic velocity (m/s)

110°

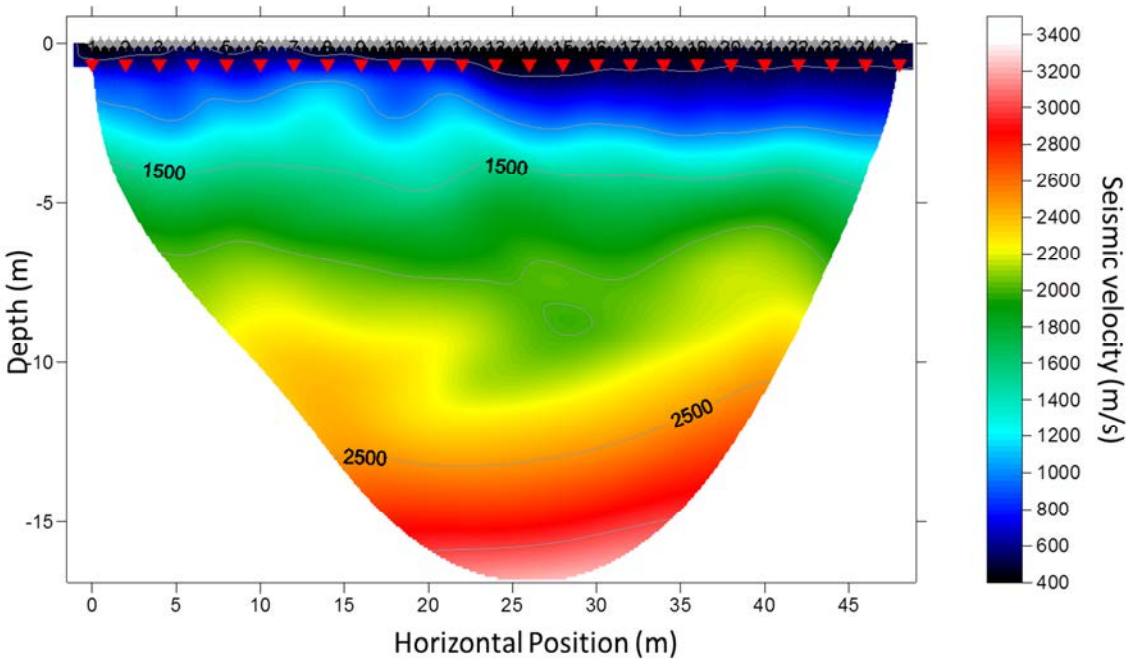
Depth (m)
0
-5
-10
-15
1500
1500
2500
2500
0
5
10
15
20
25
30
35
40
45
Horizontal Position (m)
Seismic velocity (m/s)
3400
3200
3000
2800
2600
2400
2200
2000
1800
1600
1400
1200
1000
800
600
400

120°

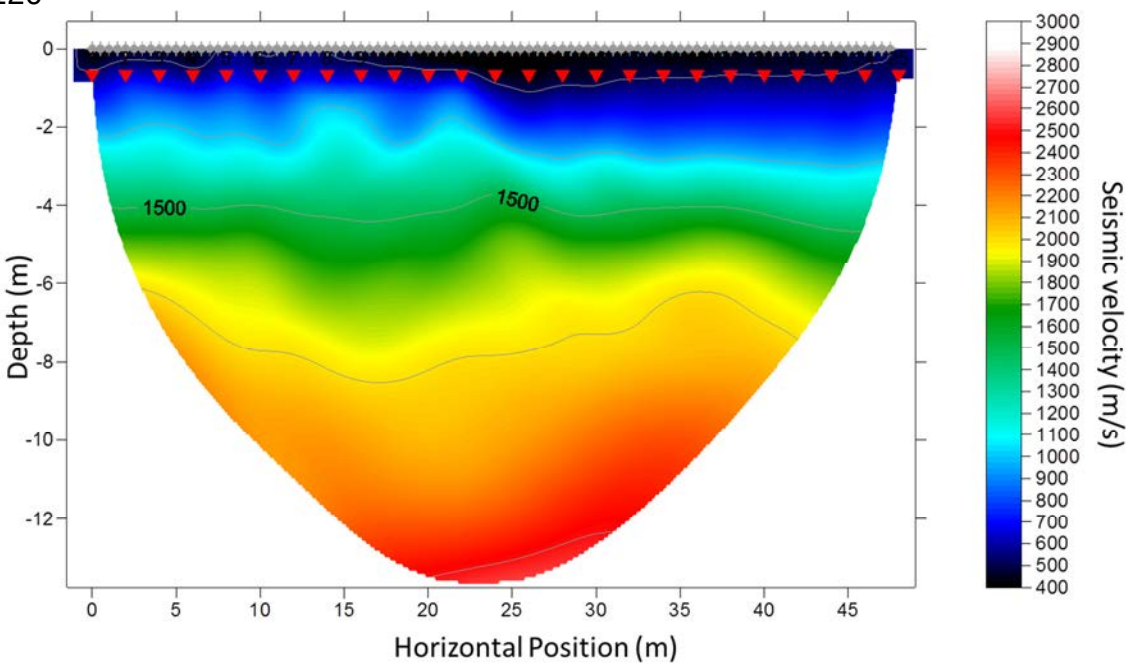
Depth (m)
0
-2
-4
-6
-8
-10
-12
1500
1500
0
5
10
15
20
25
30
35
40
45
Horizontal Position (m)
Seismic velocity (m/s)
3000
2900
2800
2700
2600
2500
2400
2300
2200
2100
2000
1900
1800
1700
1600
1500
1400
1300
1200
1100
1000
900
800
700
600
500
400

130°

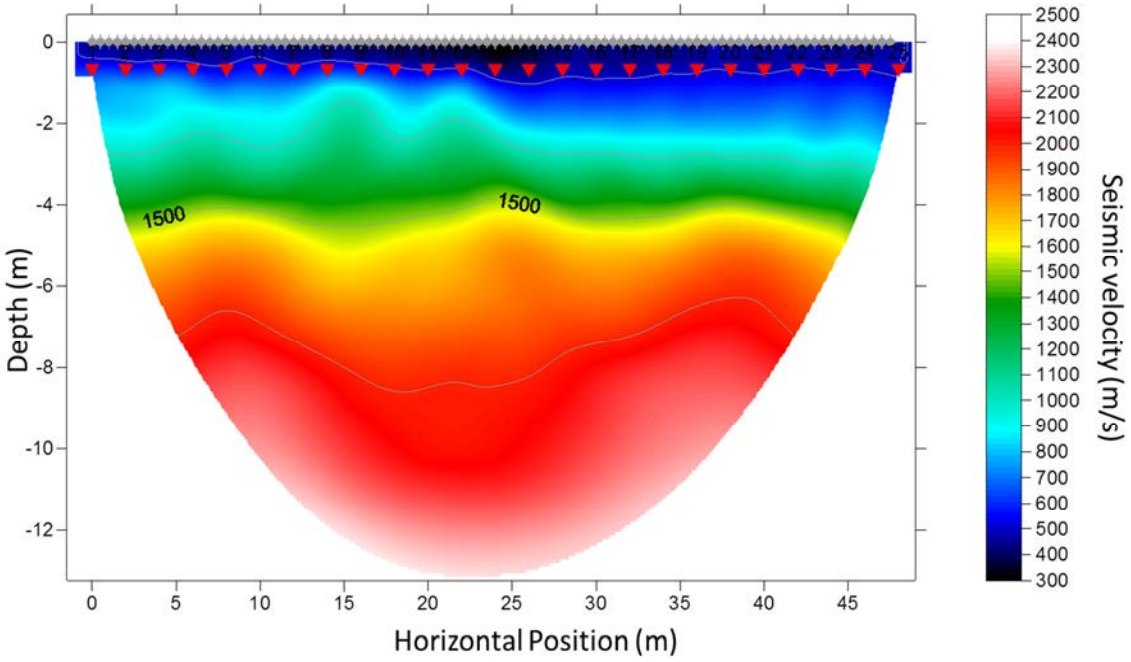
Depth (m)
Horizontal Position (m)
Seismic velocity (m/s)
1500
1500

140°

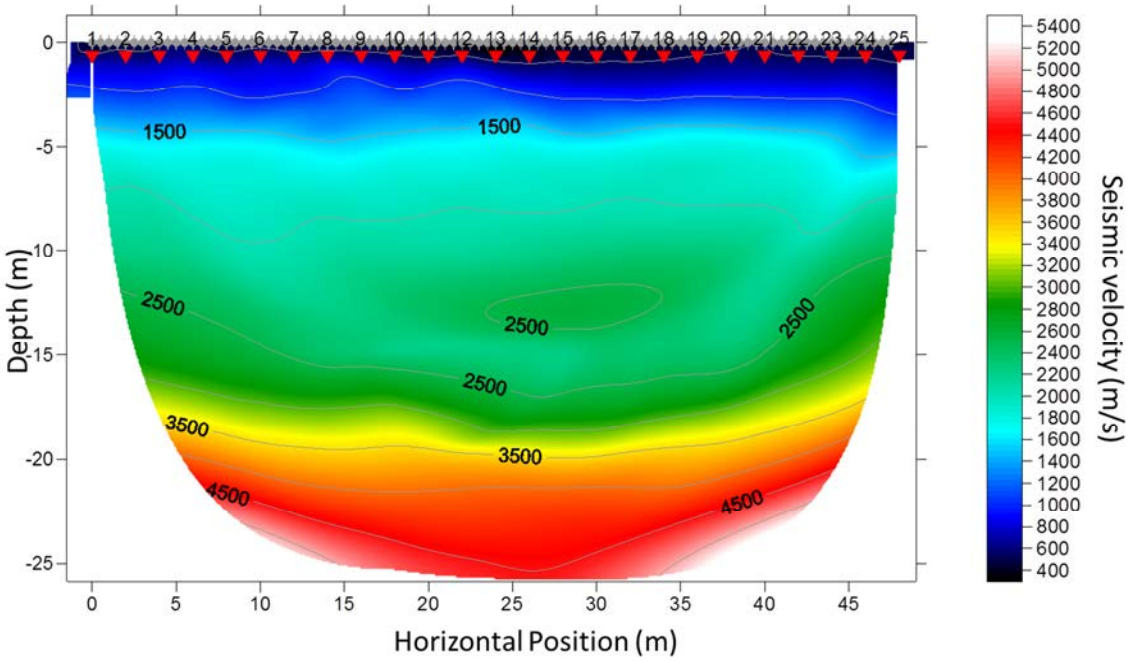
Depth (m)
Horizontal Position (m)
Seismic velocity (m/s)
1500
1500
2500
2500
2500
2500
3500
3500
4500
4500

150°

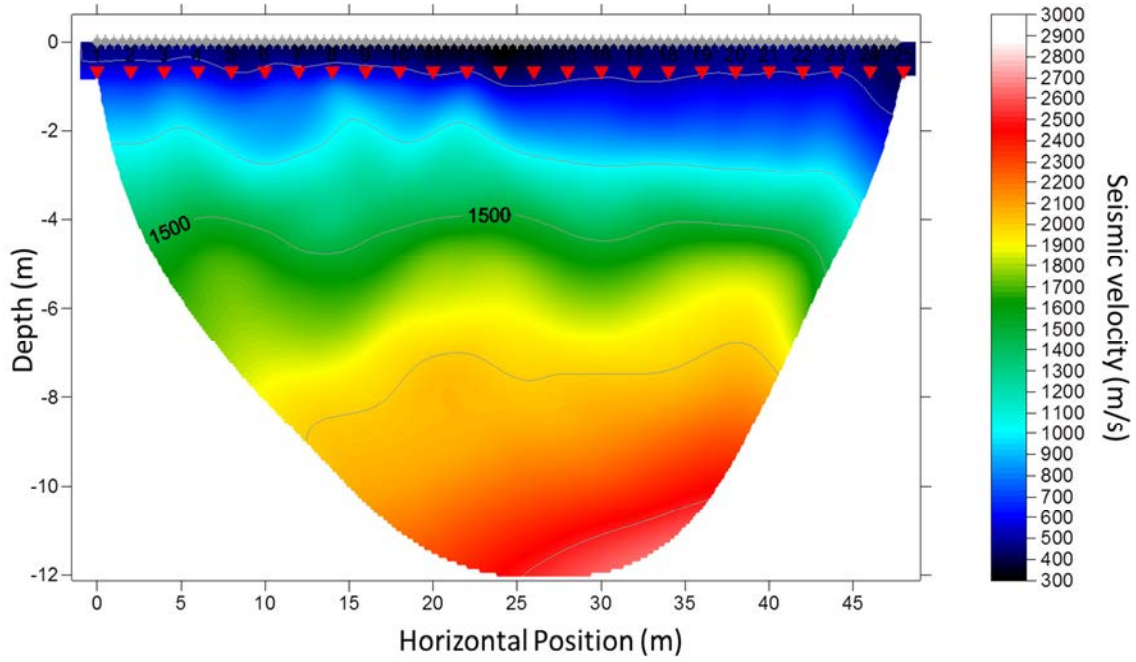
Depth (m)
Horizontal Position (m)
Seismic velocity (m/s)
1500
1500

160°

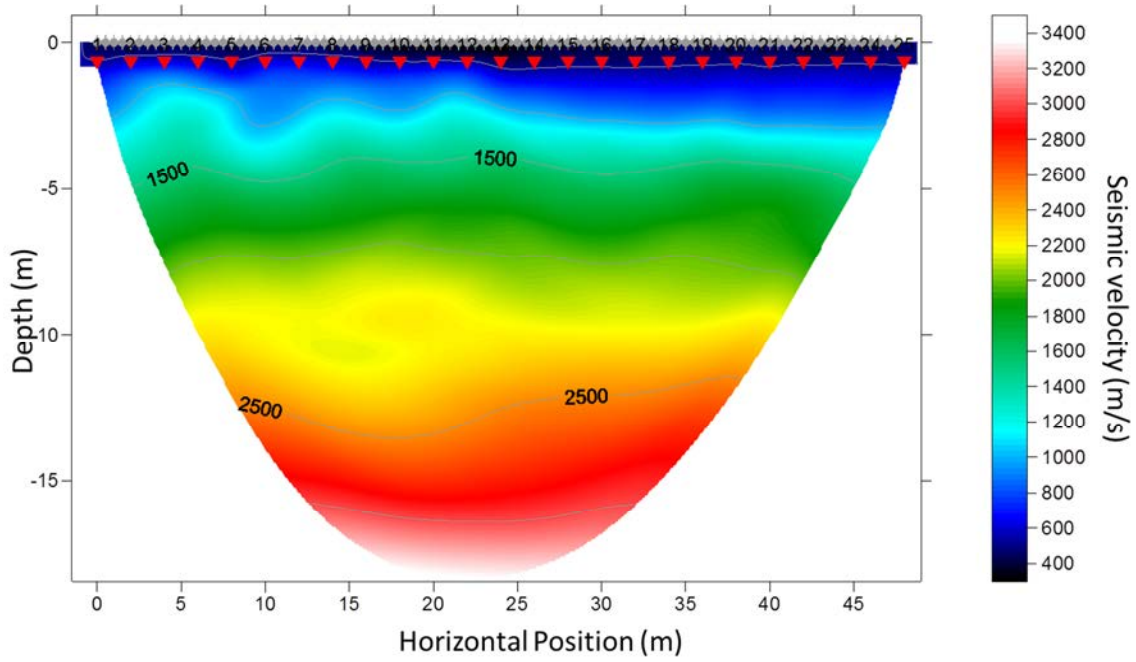
Depth (m)
Horizontal Position (m)
Seismic velocity (m/s)
1500
1500
2500
2500

170°

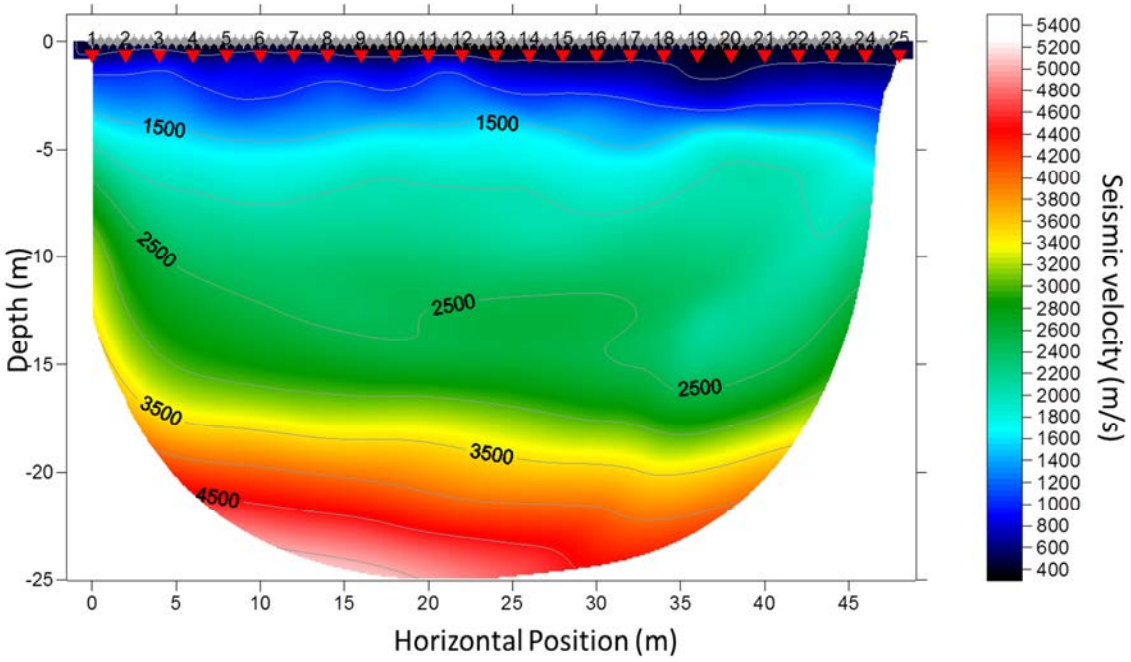

Compass Diagrams:

0 m

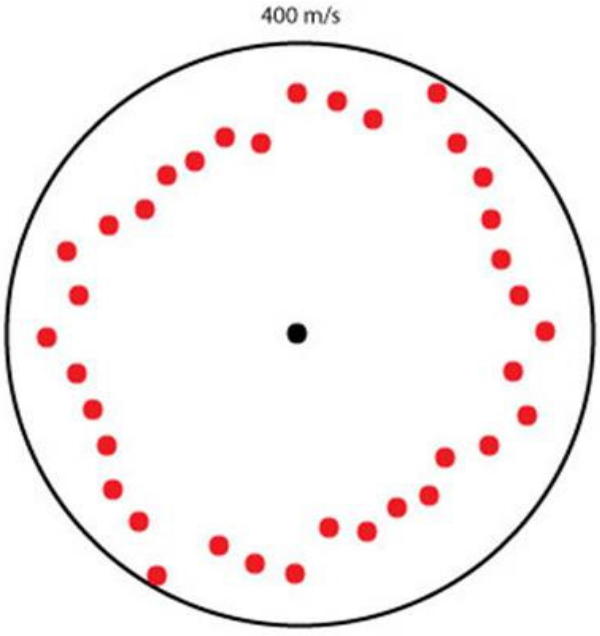

0.5 m

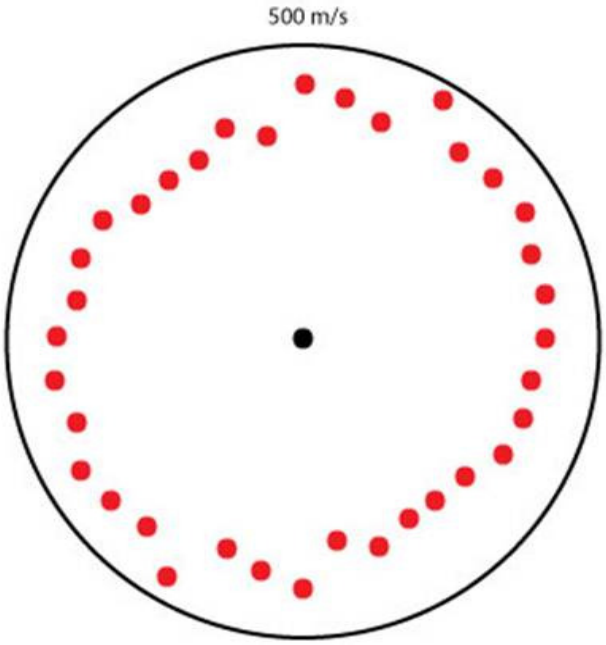

1 m

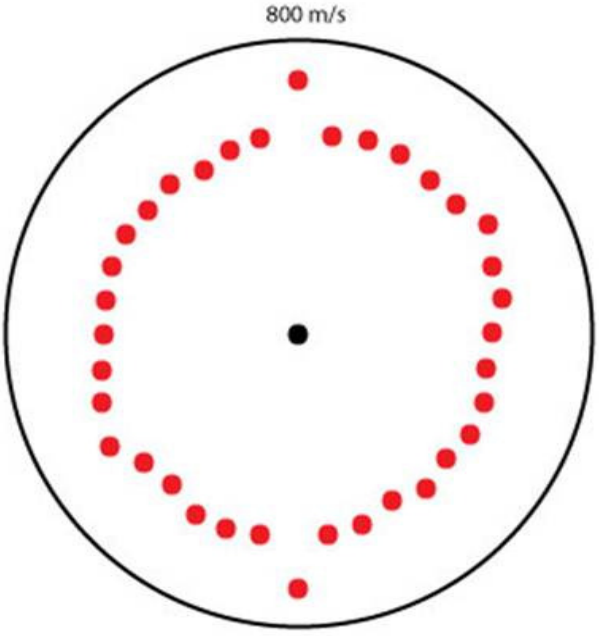

1.5 m

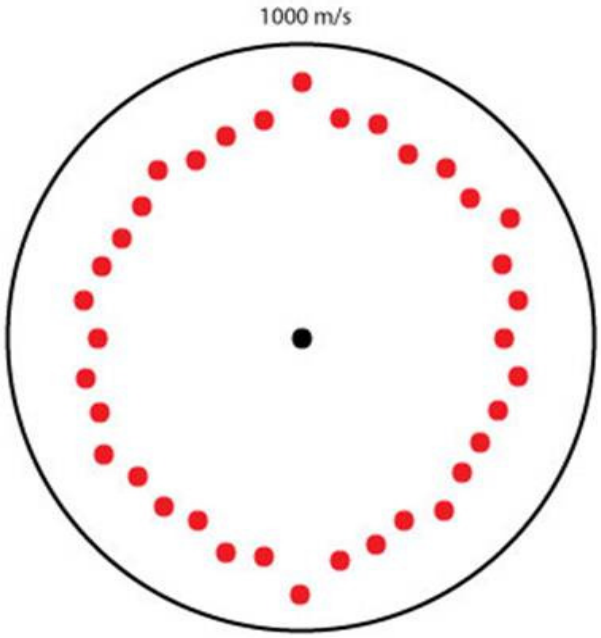

2 m

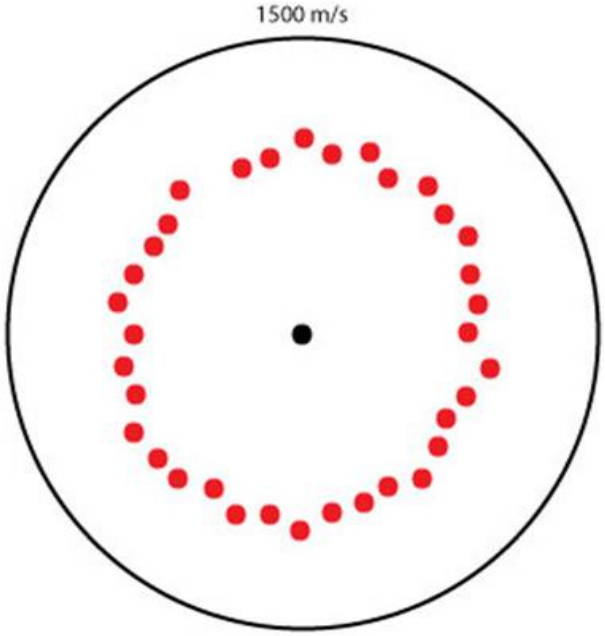

2.5 m

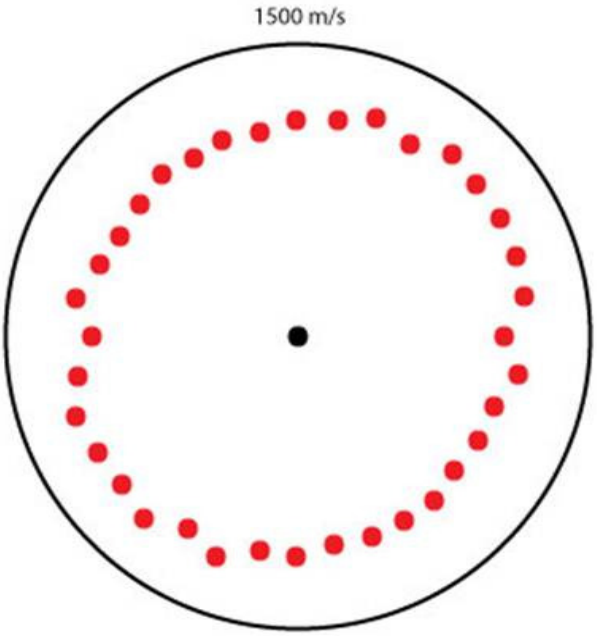

3 m

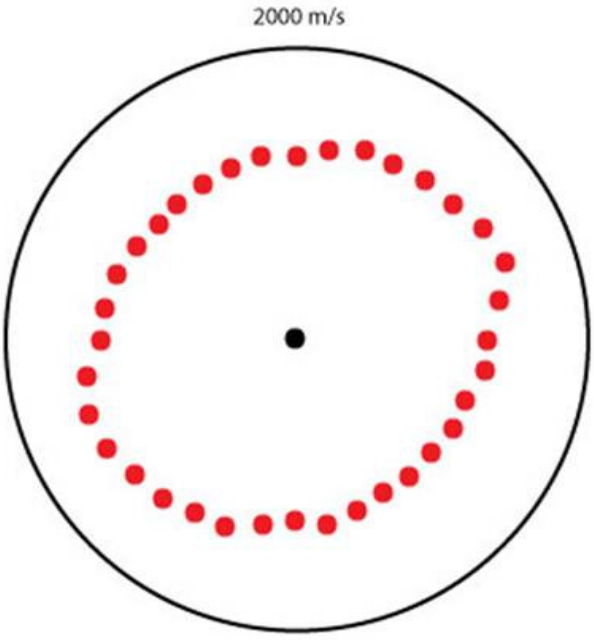

3.5 m

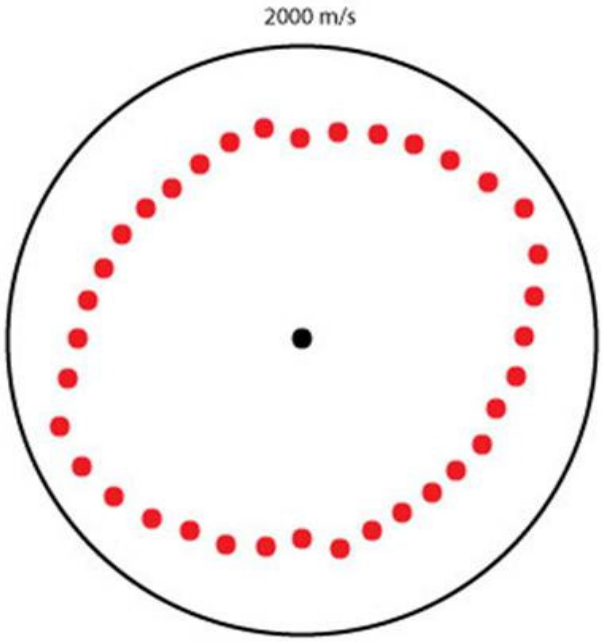

4 m

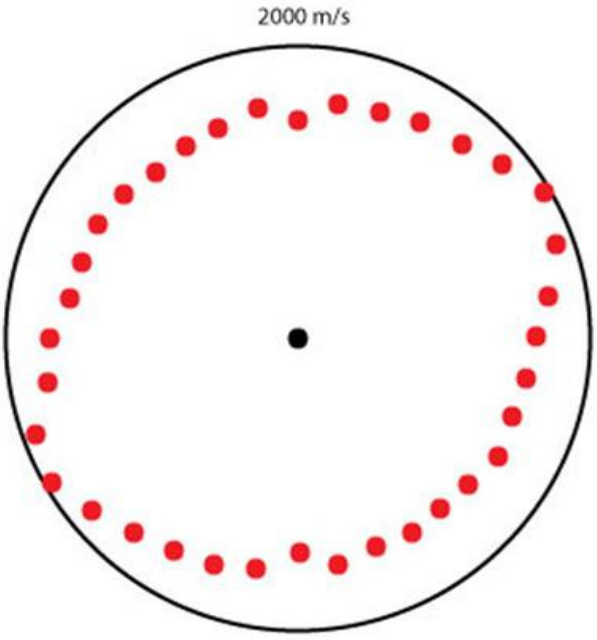

4.5 m

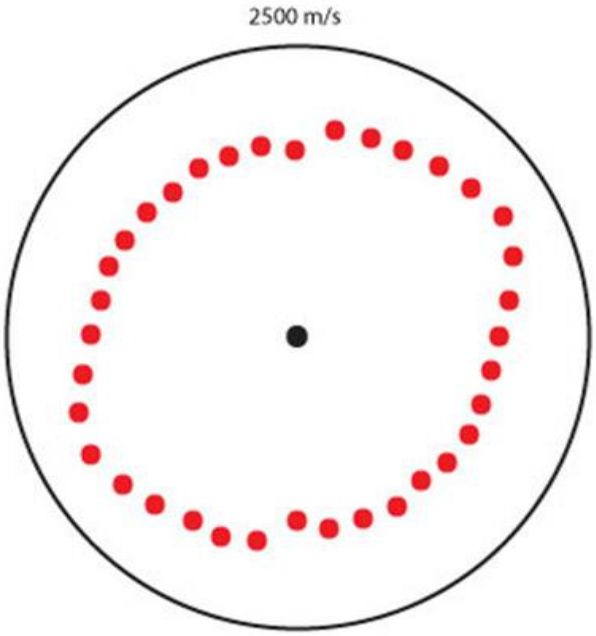

5 m

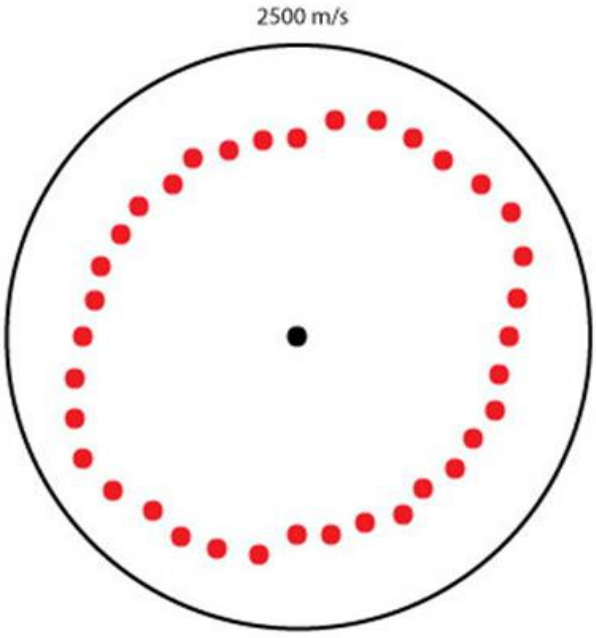

5.5 m

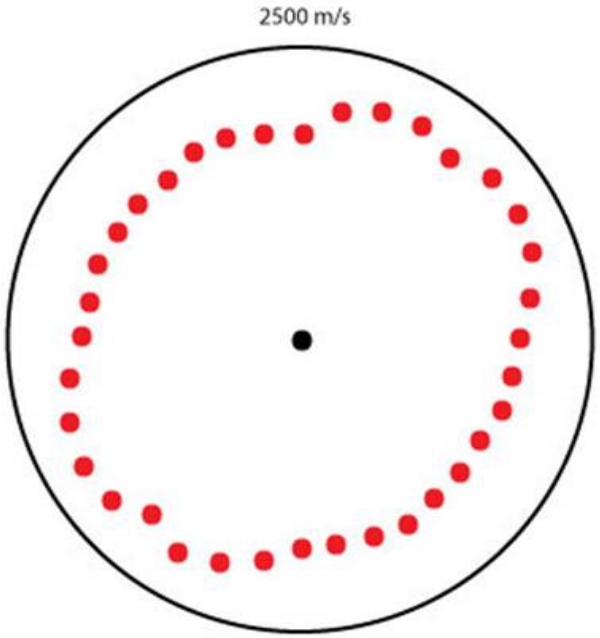

6 m

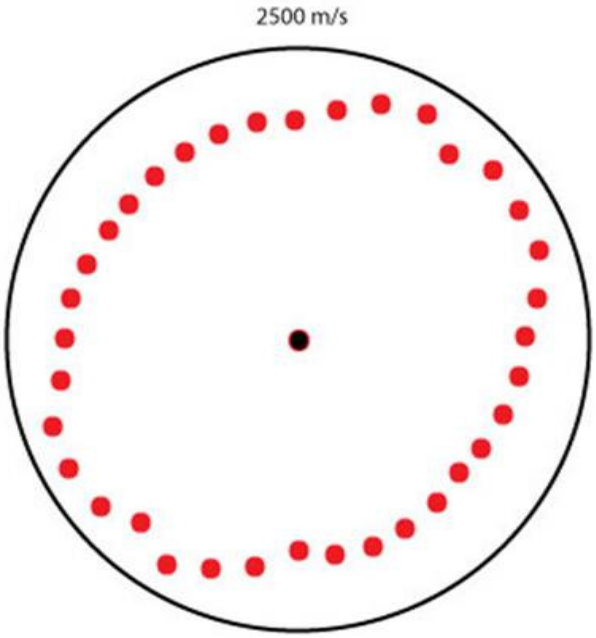

6.5 m

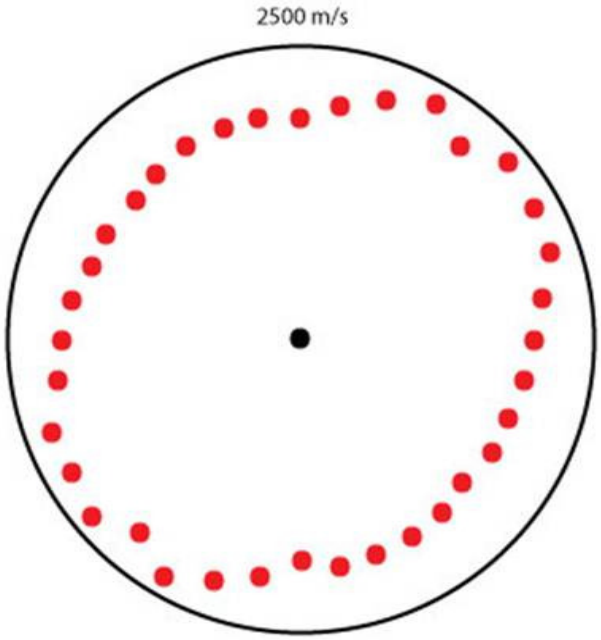

7 m

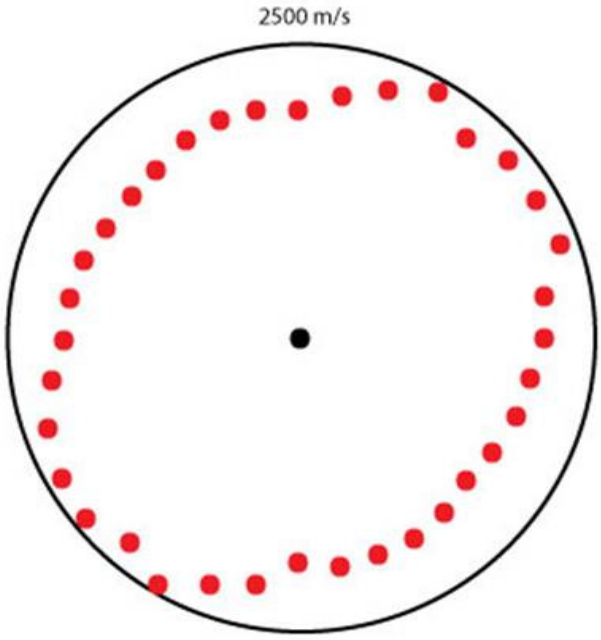

7.5 m

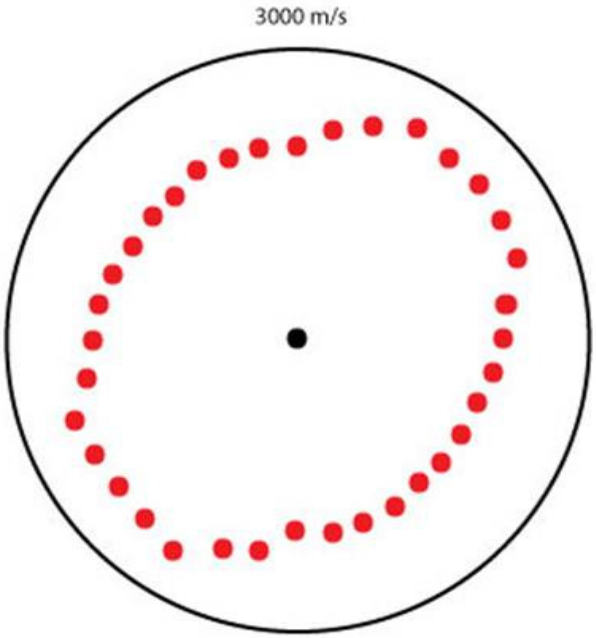

8 m

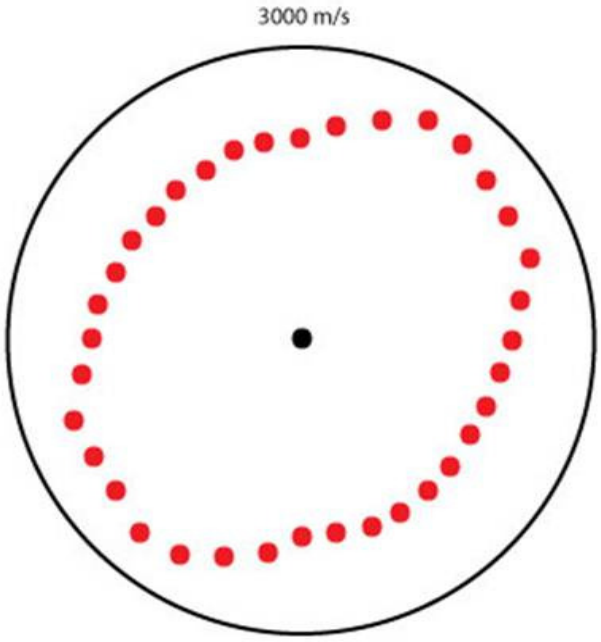

8.5 m

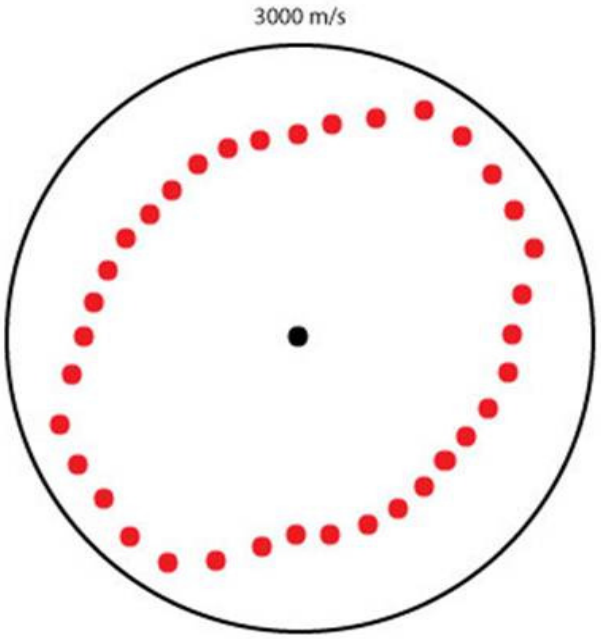

9 m

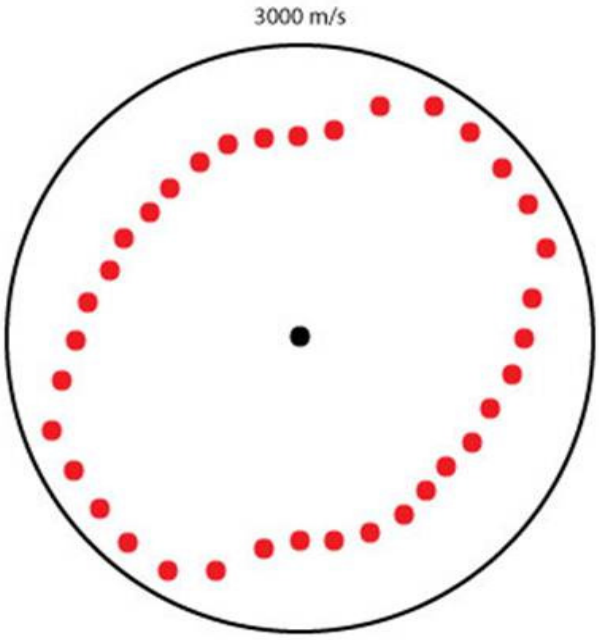

9.5 m

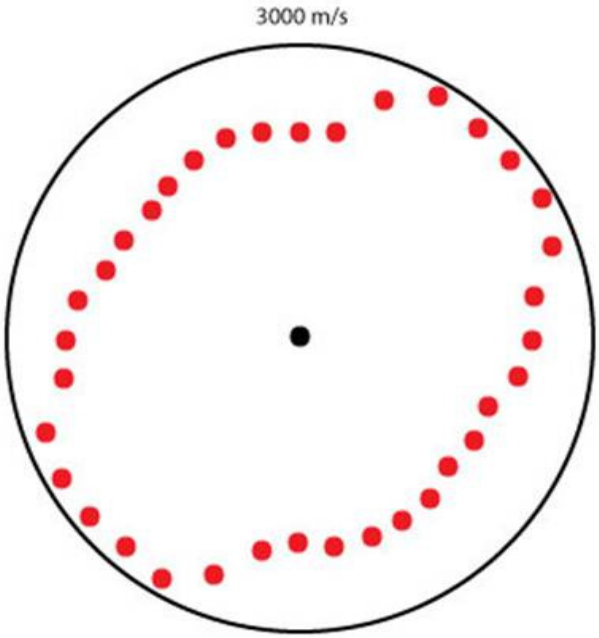

10 m

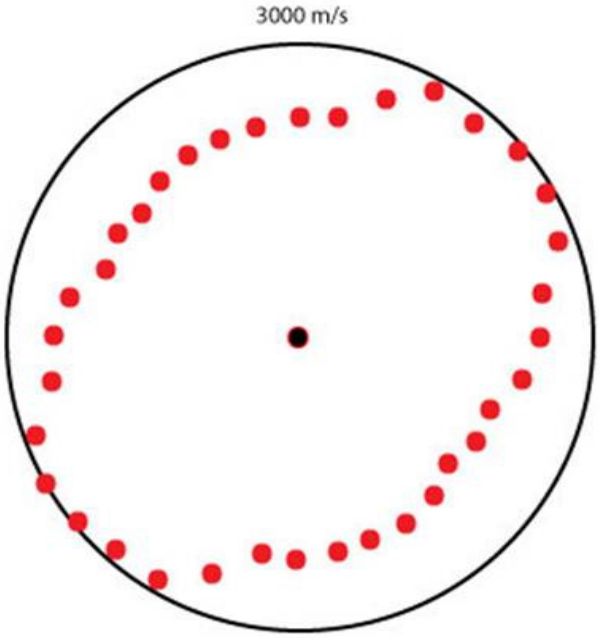

10.5 m

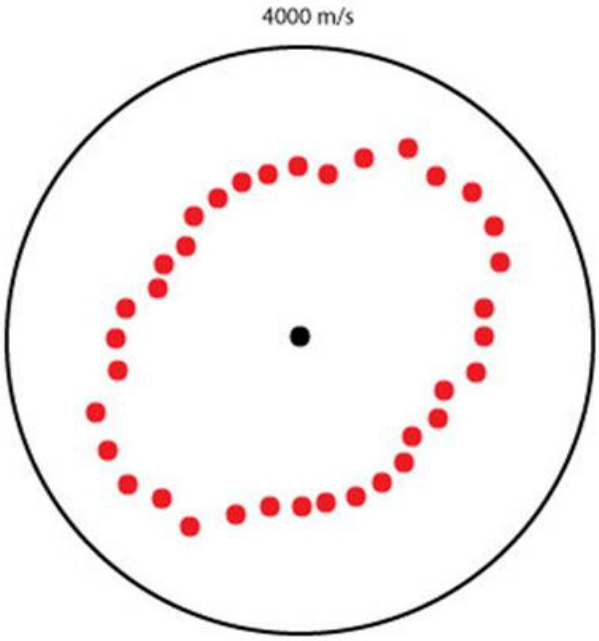

11 m

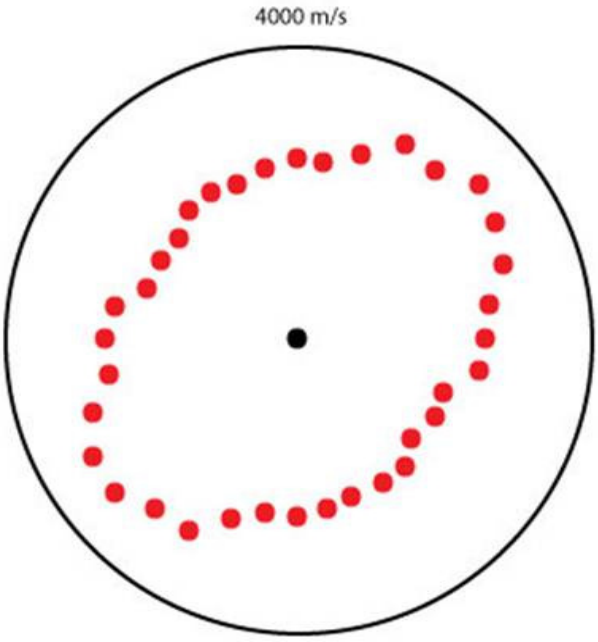

11.5 m

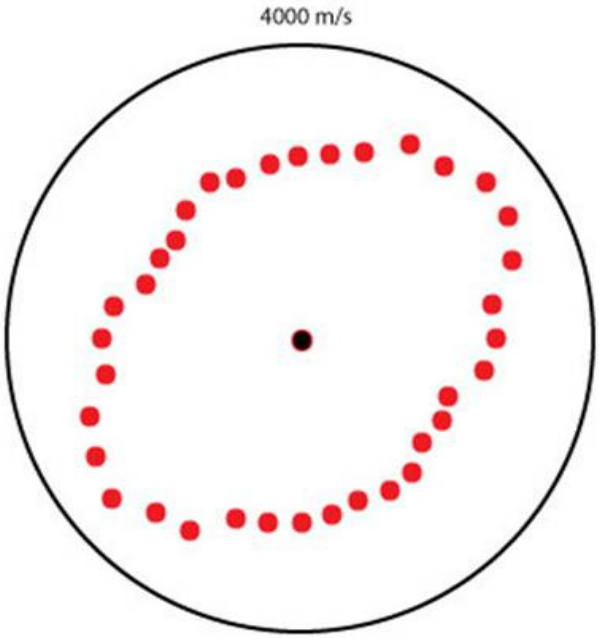

Appendix 2: Km-1 Raypath coverage diagrams, Tomograms, and Compass Diagrams

This appendix will show all raypath coverage diagrams, velocity tomograms, and velocity compass diagrams in that order. The raypath coverage diagrams and velocity tomograms will begin with those imaged from the north-south line (azimuth of 0°) and continue to the azimuth of 170°. The compass diagrams will begin at a depth of 0 m, and continue in one half meter increments to the depth of resolution limit (for the Km-1 dataset, this depth is 10 m)

Raypath Coverage Diagrams:

0°

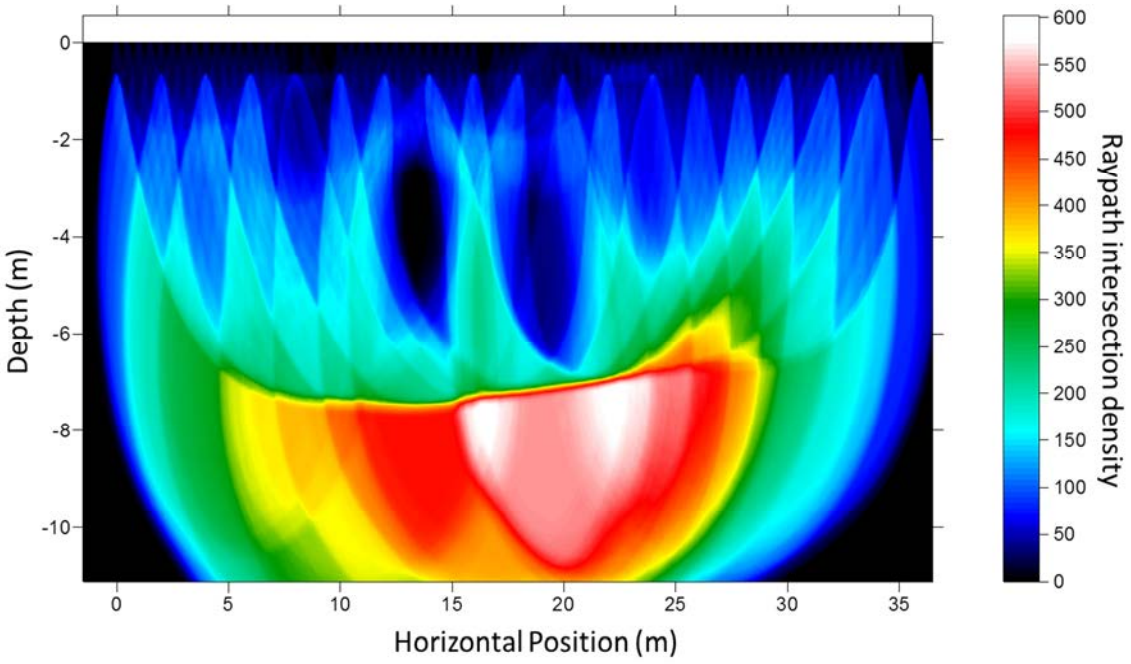

10°

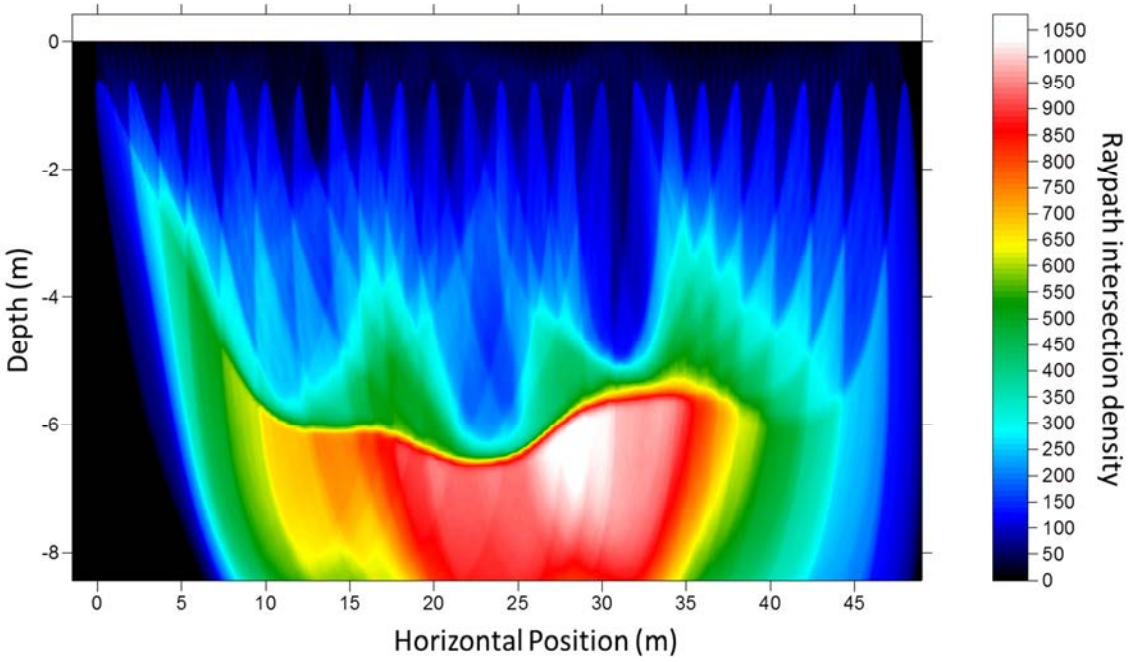
Depth (m)
0
-2
-4
-6
-8
0
5
10
15
20
25
30
35
40
45
Horizontal Position (m)
1050
1000
950
900
850
800
750
700
650
600
550
500
450
400
350
300
250
200
150
100
50
0
Raypath intersection density

20°

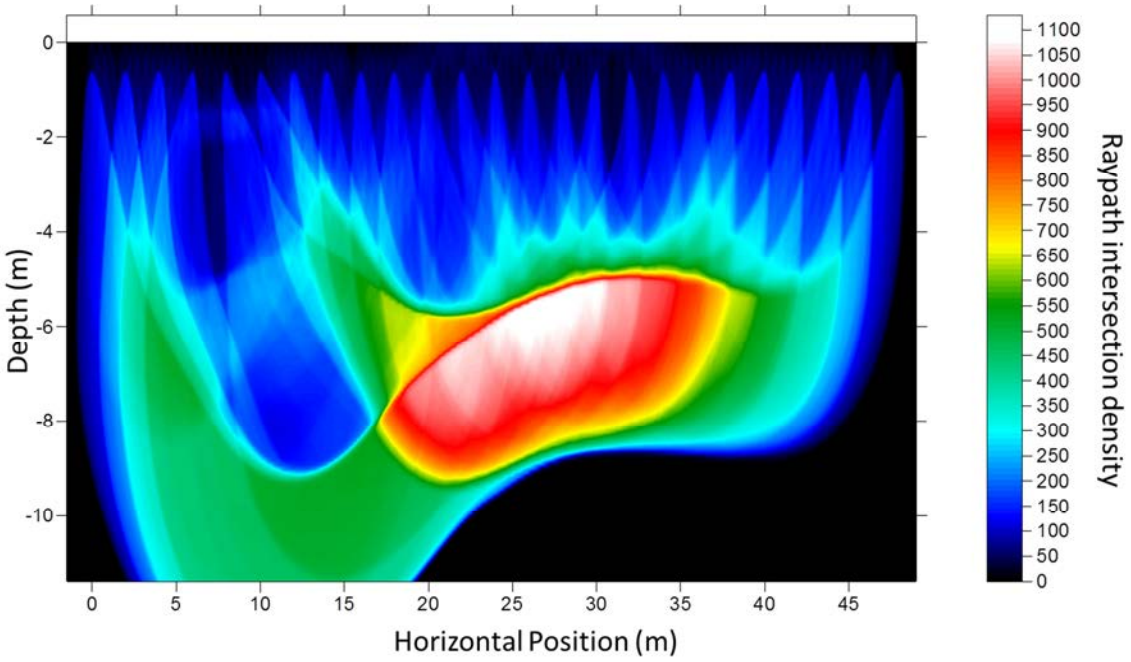
Depth (m)
0
-2
-4
-6
-8
-10
0
5
10
15
20
25
30
35
40
45
Horizontal Position (m)
1100
1050
1000
950
900
850
800
750
700
650
600
550
500
450
400
350
300
250
200
150
100
50
0
Raypath intersection density

30°

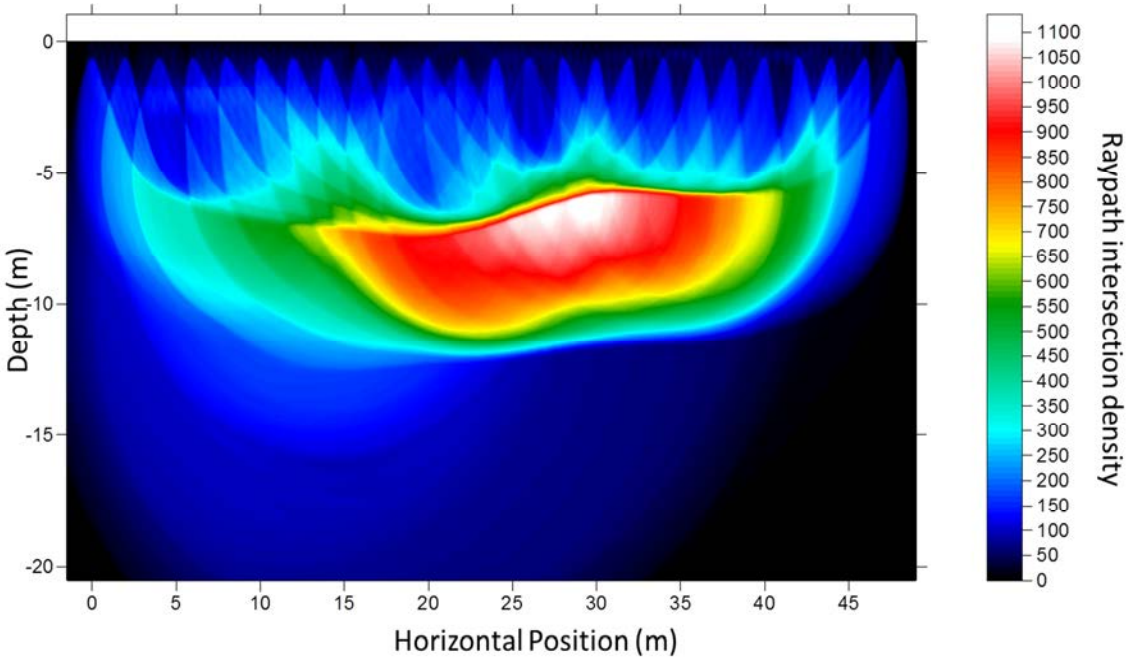
Depth (m)
0
-5
-10
-15
-20
0
5
10
15
20
25
30
35
40
45
Horizontal Position (m)
1100
1050
1000
950
900
850
800
750
700
650
600
550
500
450
400
350
300
250
200
150
100
50
0
Raypath intersection density

40°

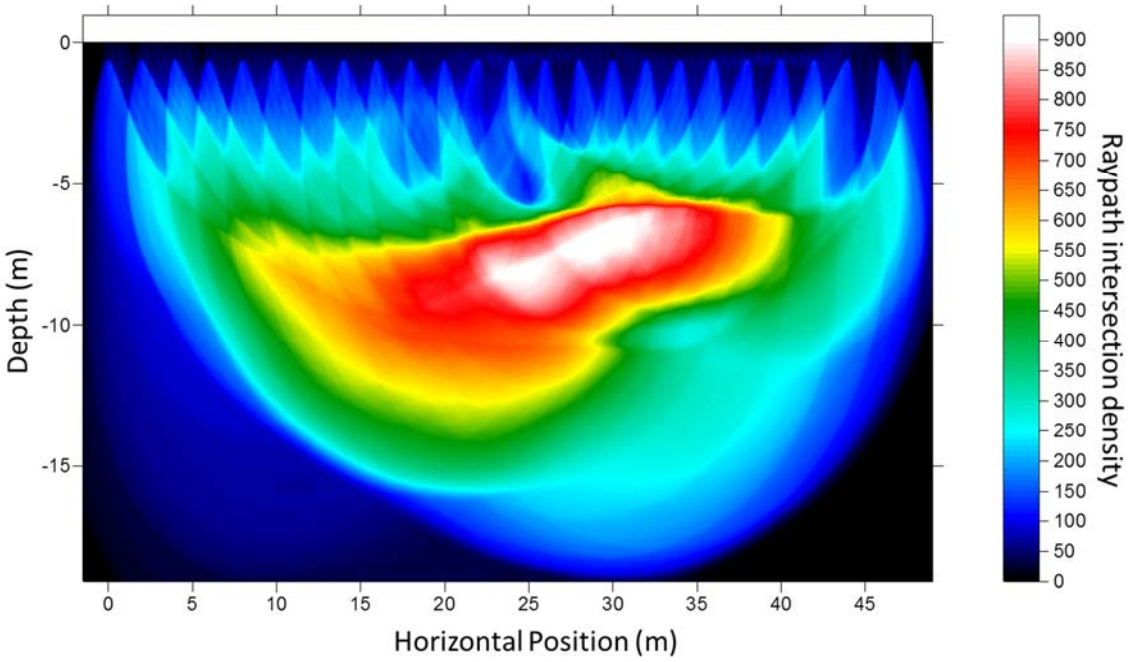
Depth (m)
0
-5
-10
-15
0
5
10
15
20
25
30
35
40
45
Horizontal Position (m)
900
850
800
750
700
650
600
550
500
450
400
350
300
250
200
150
100
50
0
Raypath intersection density

50°

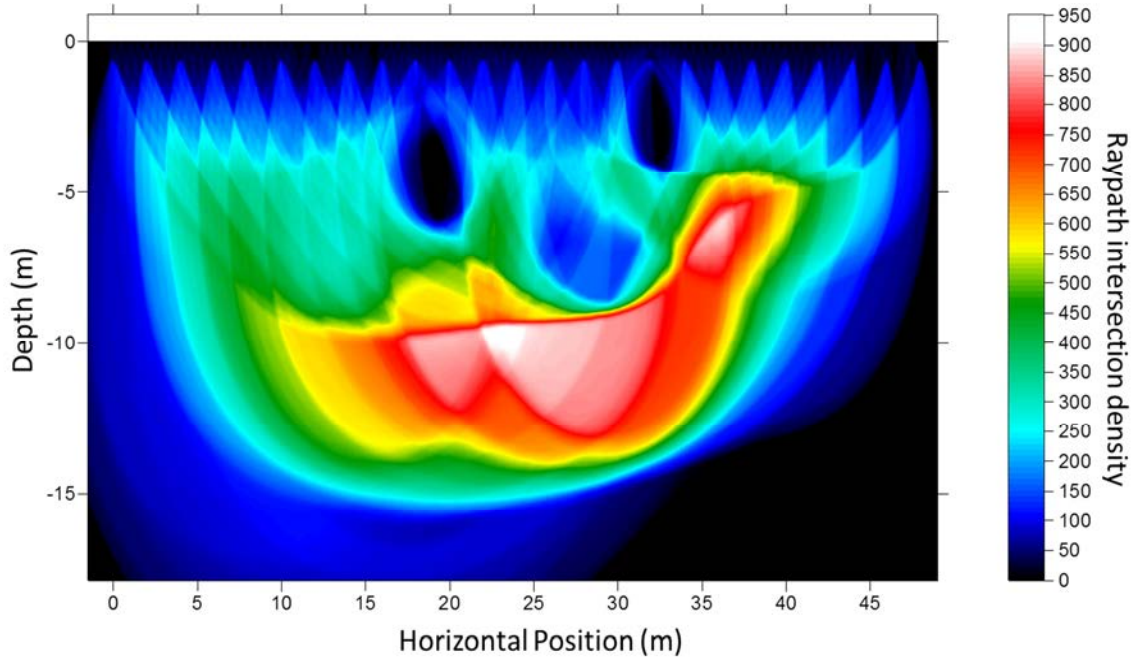
Depth (m)
0
-5
-10
-15
0 5 10 15 20 25 30 35 40 45
Horizontal Position (m)
950 900 850 800 750 700 650 600 550 500 450 400 350 300 250 200 150 100 50 0
Raypath intersection density

60°

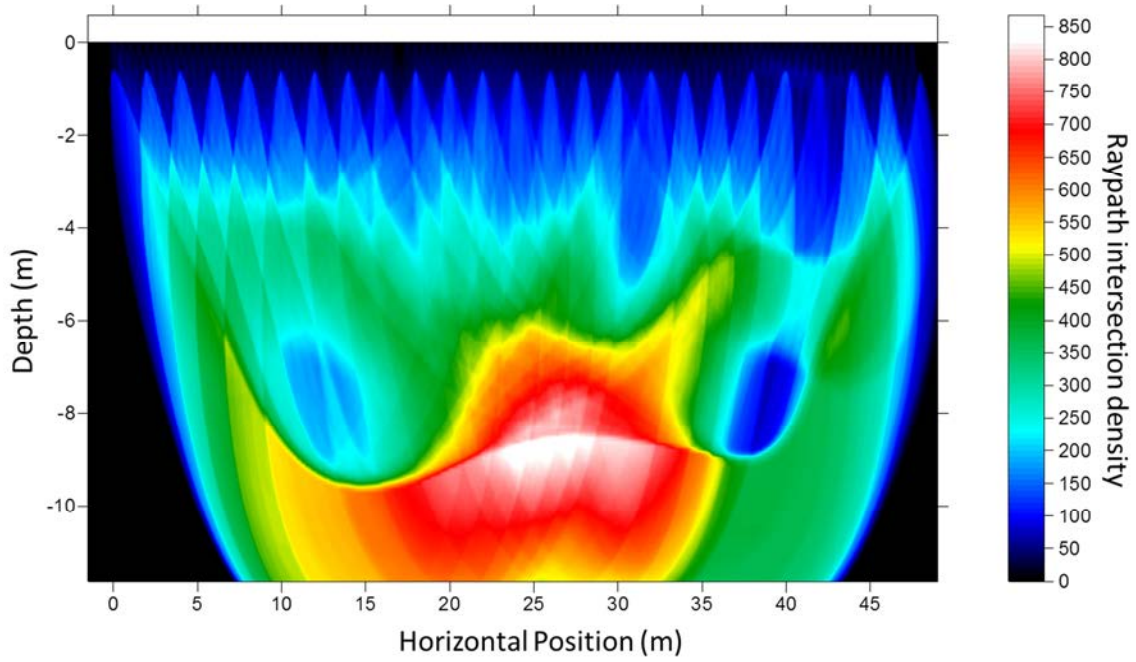
Depth (m)
0
-2
-4
-6
-8
-10
0 5 10 15 20 25 30 35 40 45
Horizontal Position (m)
850 800 750 700 650 600 550 500 450 400 350 300 250 200 150 100 50 0
Raypath intersection density

70°

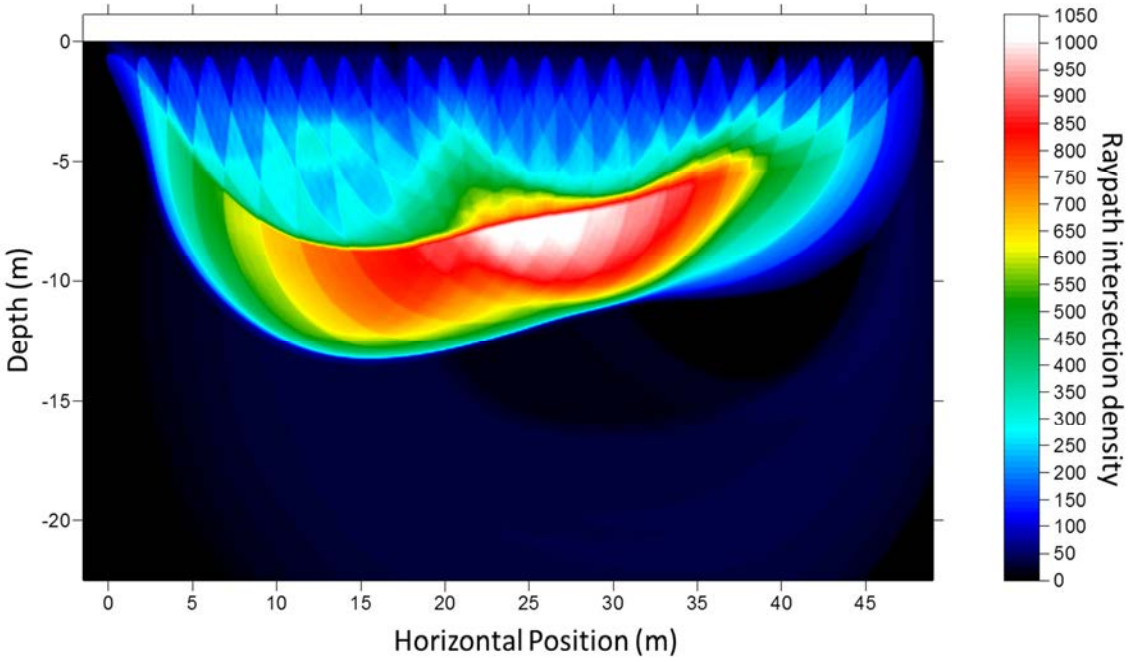
Depth (m)
0
-5
-10
-15
-20
0 5 10 15 20 25 30 35 40 45
Horizontal Position (m)
Raypath intersection density
1050 1000 950 900 850 800 750 700 650 600 550 500 450 400 350 300 250 200 150 100 50 0

80°

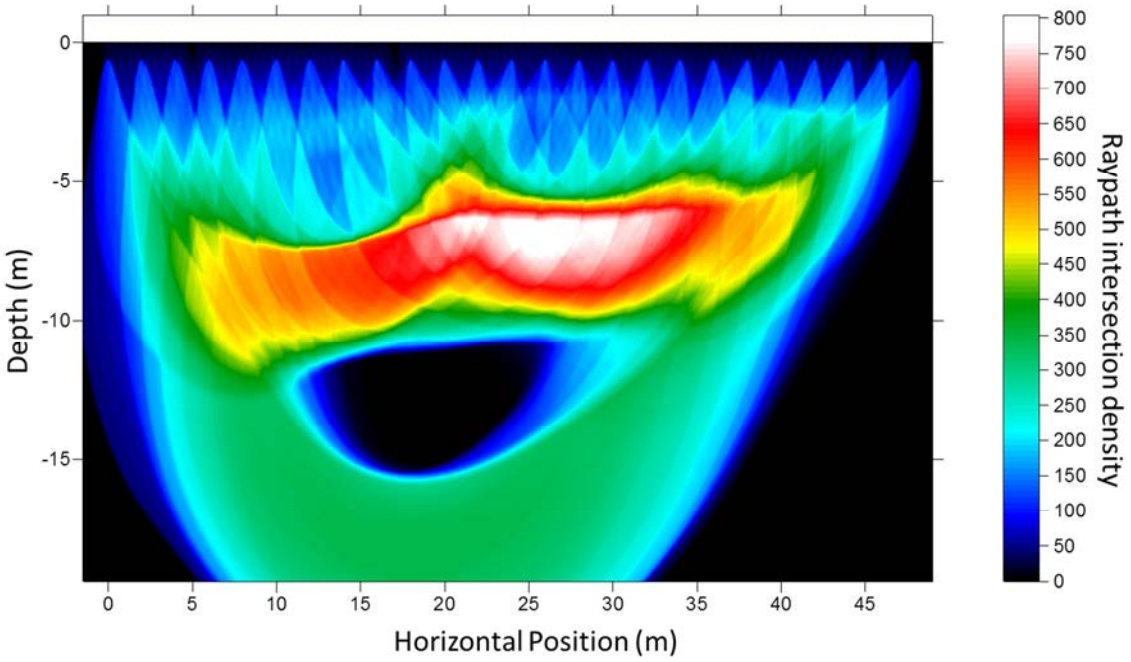
Depth (m)
0
-5
-10
-15
0 5 10 15 20 25 30 35 40 45
Horizontal Position (m)
Raypath intersection density
800 750 700 650 600 550 500 450 400 350 300 250 200 150 100 50 0

90°

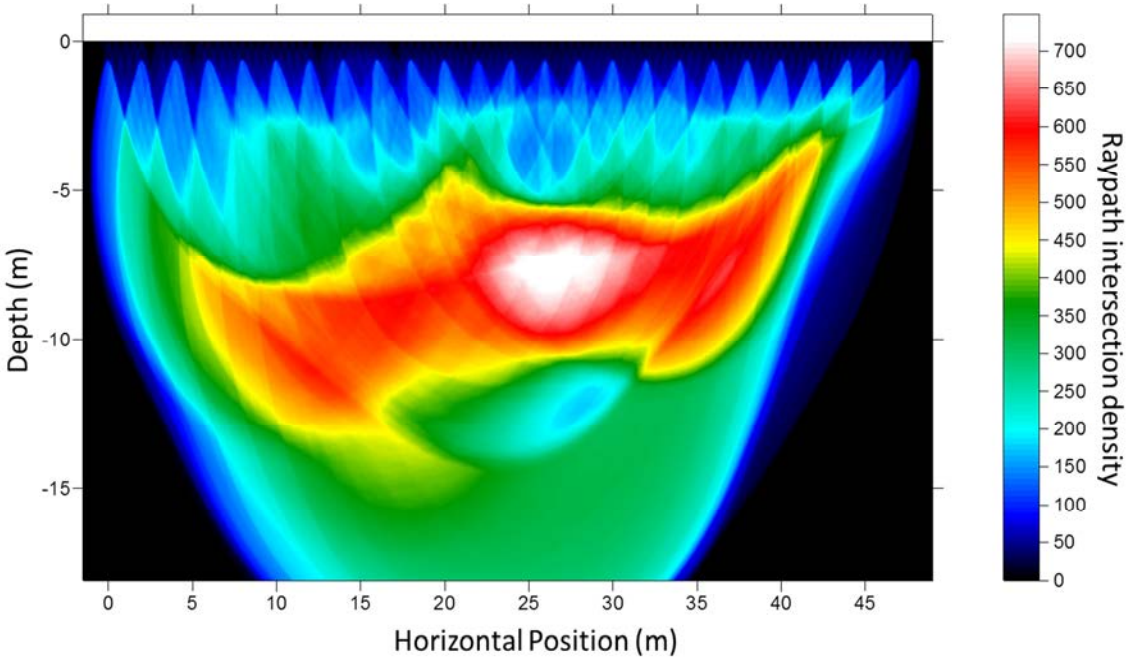
Depth (m)
0
-5
-10
-15
0
5
10
15
20
25
30
35
40
45
Horizontal Position (m)
Raypath intersection density
700
650
600
550
500
450
400
350
300
250
200
150
100
50
0

100°

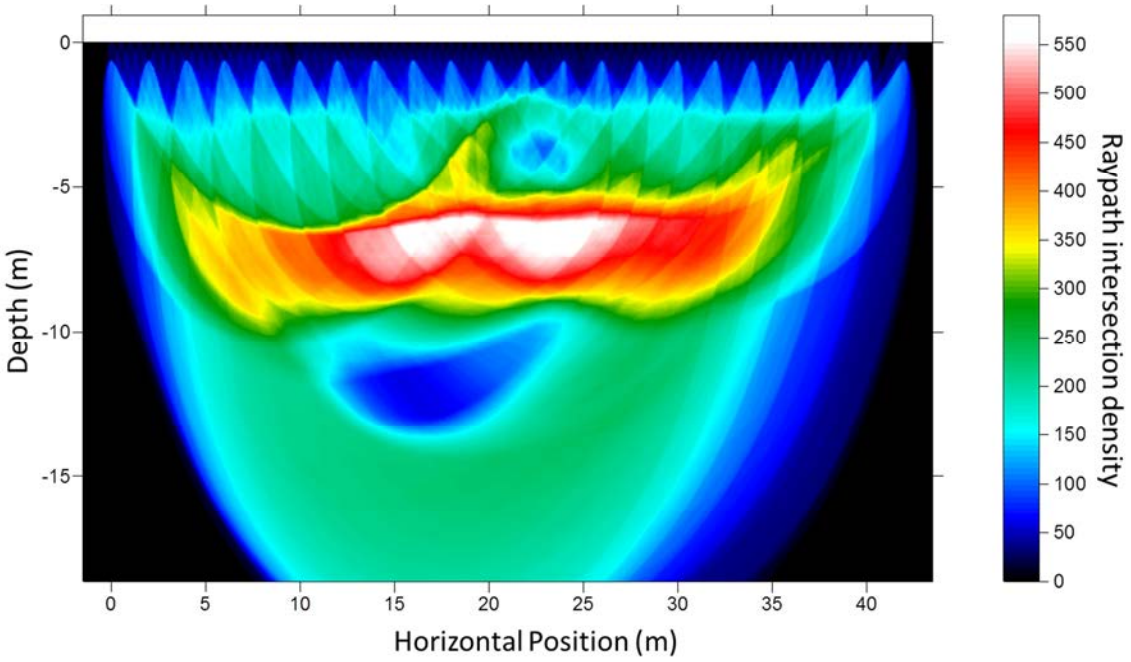
Depth (m)
0
-5
-10
-15
0
5
10
15
20
25
30
35
40
Horizontal Position (m)
Raypath intersection density
550
500
450
400
350
300
250
200
150
100
50
0

110°

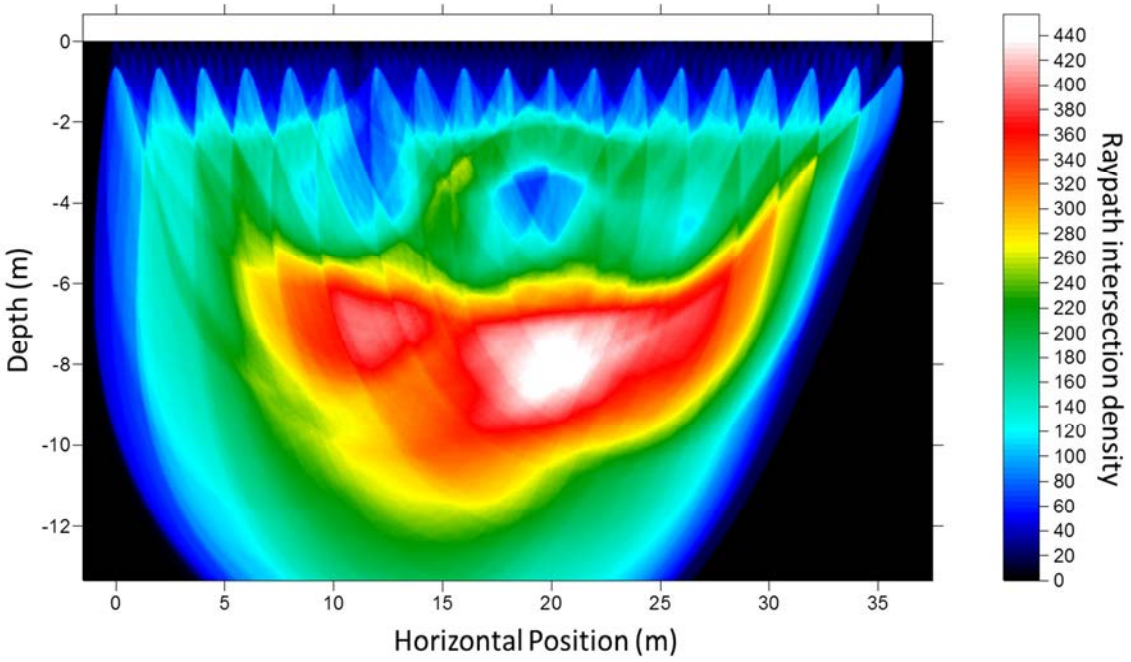
Depth (m)
0
-2
-4
-6
-8
-10
-12
0
5
10
15
20
25
30
35
Horizontal Position (m)
Raypath intersection density
440
420
400
380
360
340
320
300
280
260
240
220
200
180
160
140
120
100
80
60
40
20
0

120°

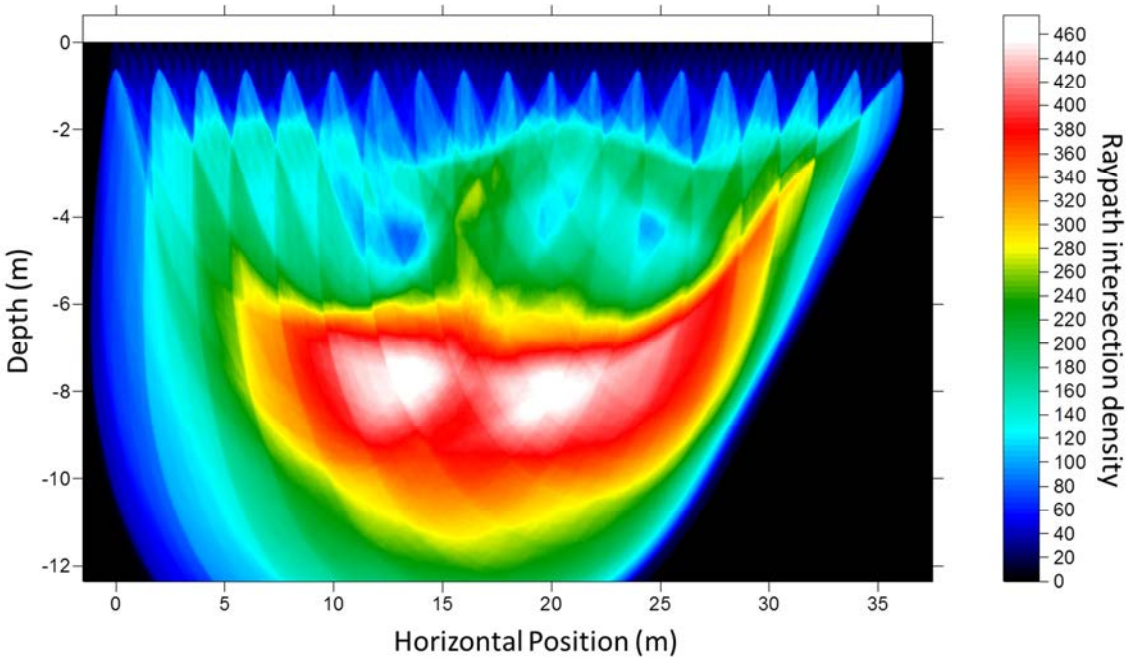
Depth (m)
0
-2
-4
-6
-8
-10
-12
0
5
10
15
20
25
30
35
Horizontal Position (m)
Raypath intersection density
460
440
420
400
380
360
340
320
300
280
260
240
220
200
180
160
140
120
100
80
60
40
20
0

130°

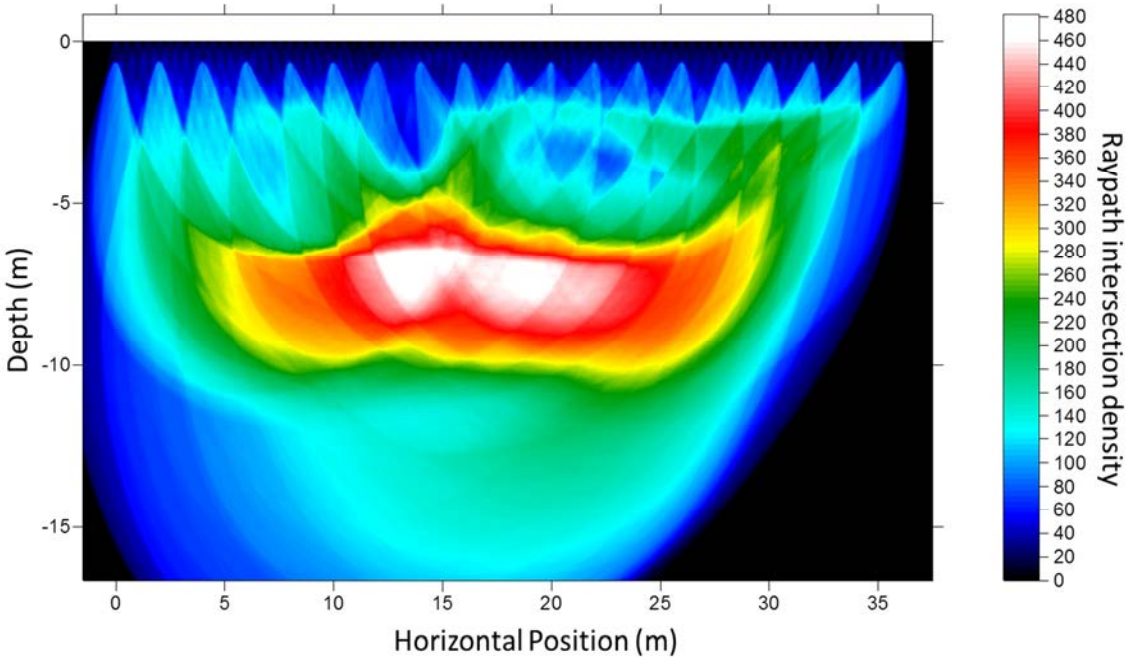
Depth (m)
0
-5
-10
-15
0
5
10
15
20
25
30
35
Horizontal Position (m)
480
460
440
420
400
380
360
340
320
300
280
260
240
220
200
180
160
140
120
100
80
60
40
20
0
Raypath intersection density

140°

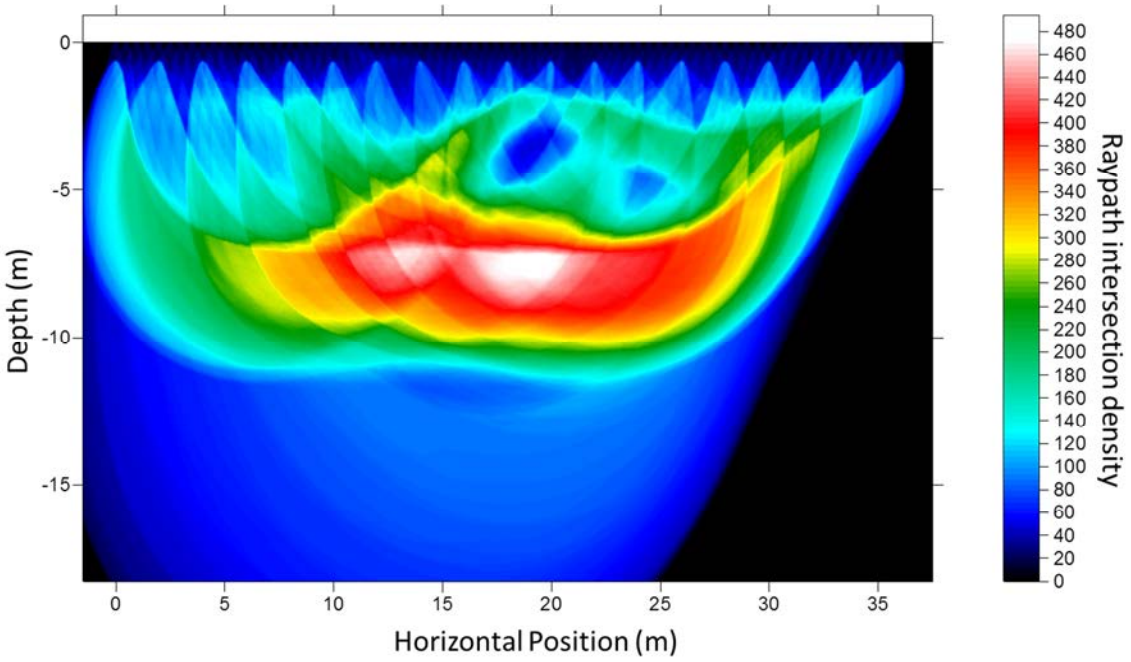
Depth (m)
0
-5
-10
-15
0
5
10
15
20
25
30
35
Horizontal Position (m)
480
460
440
420
400
380
360
340
320
300
280
260
240
220
200
180
160
140
120
100
80
60
40
20
0
Raypath intersection density

150°

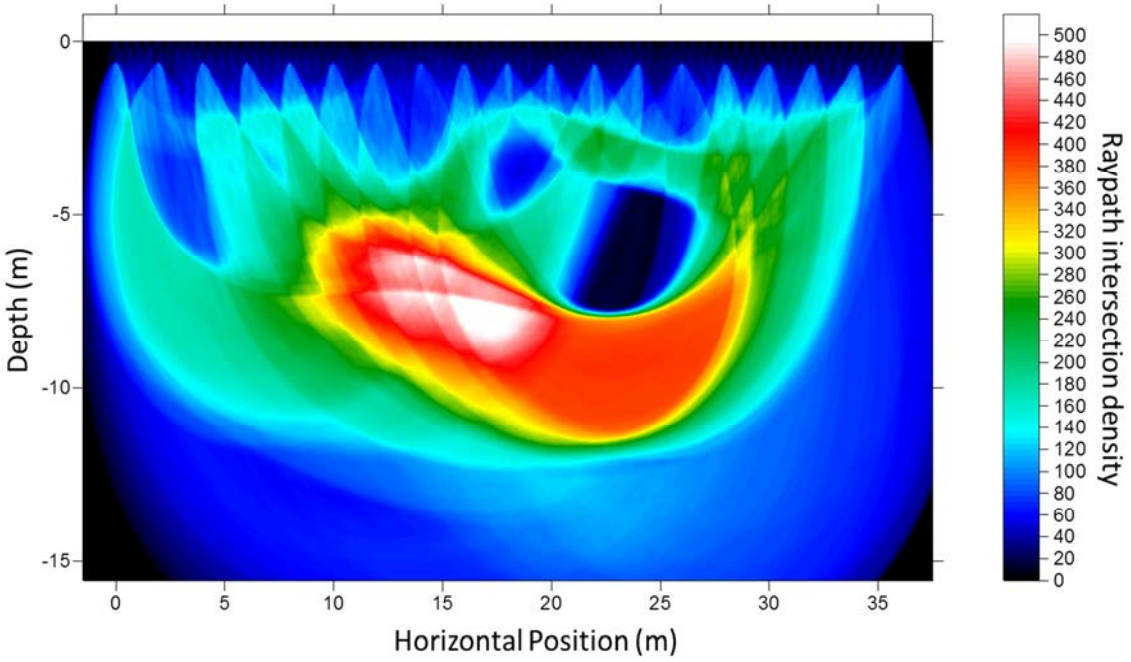
Depth (m)
0
-5
-10
-15
0
5
10
15
20
25
30
35
Horizontal Position (m)
Raypath intersection density
500
480
460
440
420
400
380
360
340
320
300
280
260
240
220
200
180
160
140
120
100
80
60
40
20
0

160°

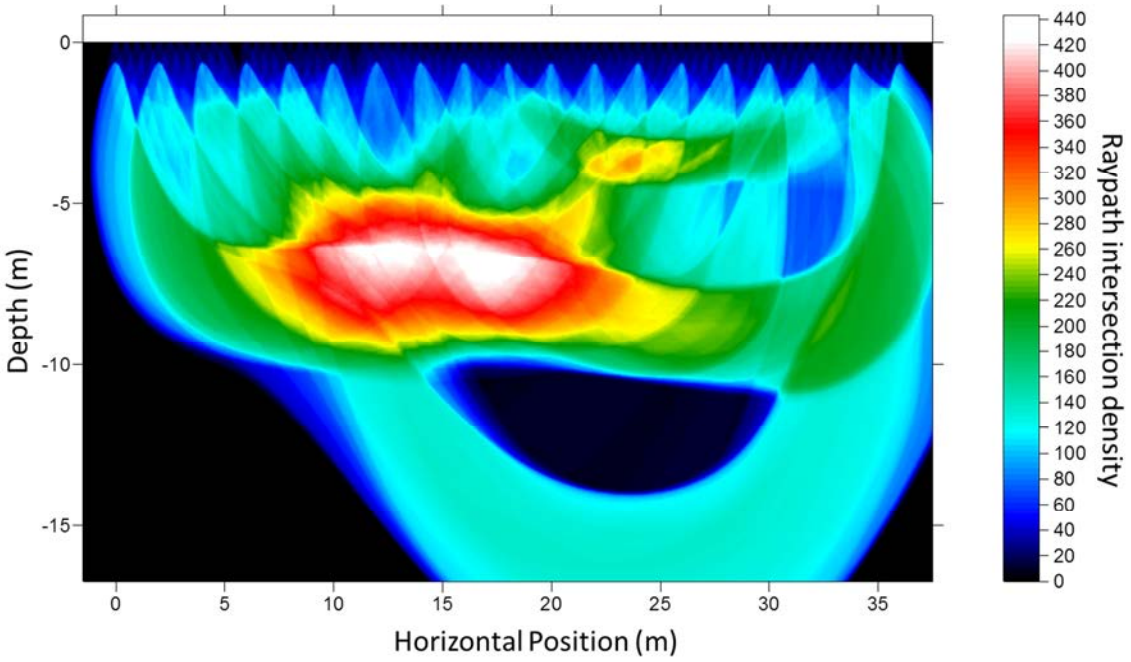
Depth (m)
0
-5
-10
-15
0
5
10
15
20
25
30
35
Horizontal Position (m)
Raypath intersection density
440
420
400
380
360
340
320
300
280
260
240
220
200
180
160
140
120
100
80
60
40
20
0

170°

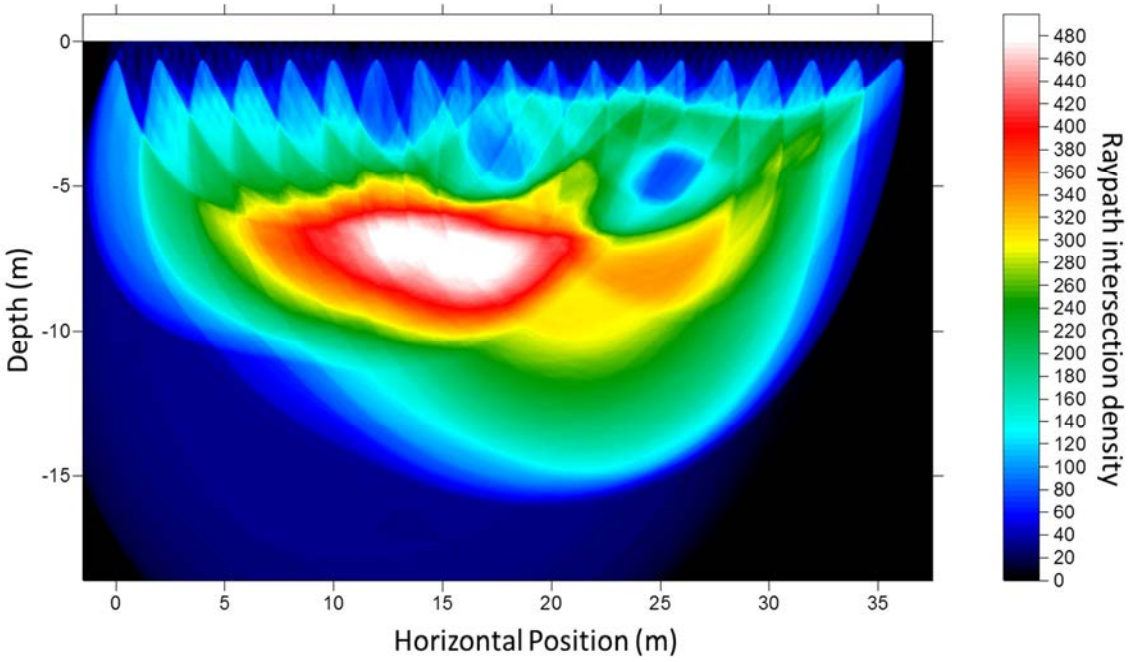

Velocity Tomograms:

0°

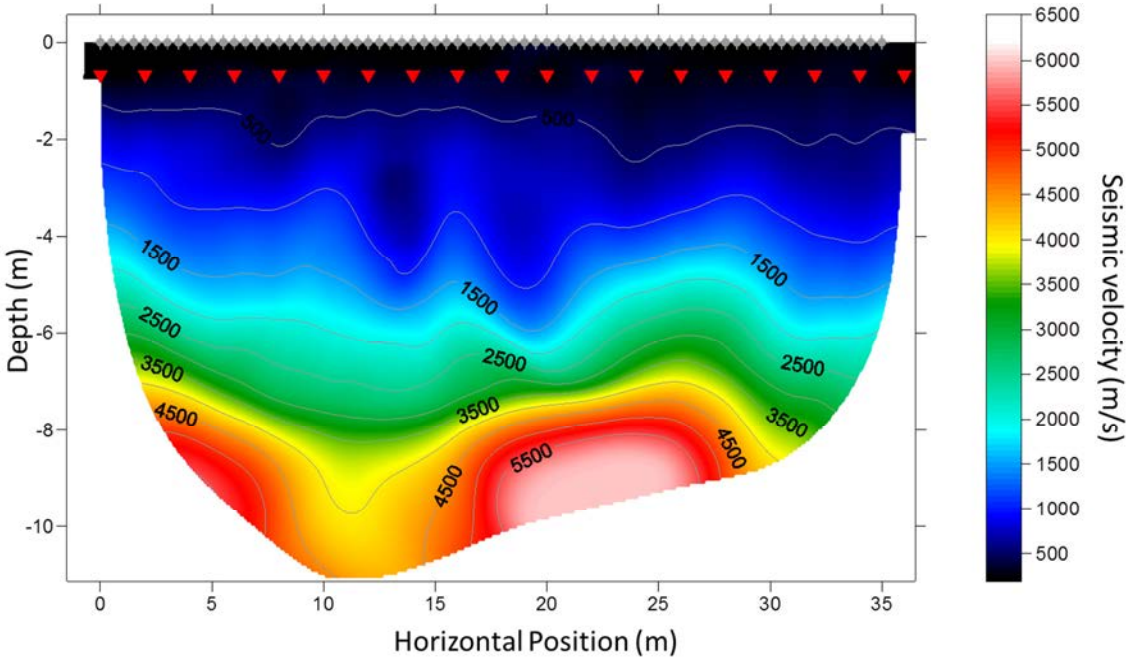

10°

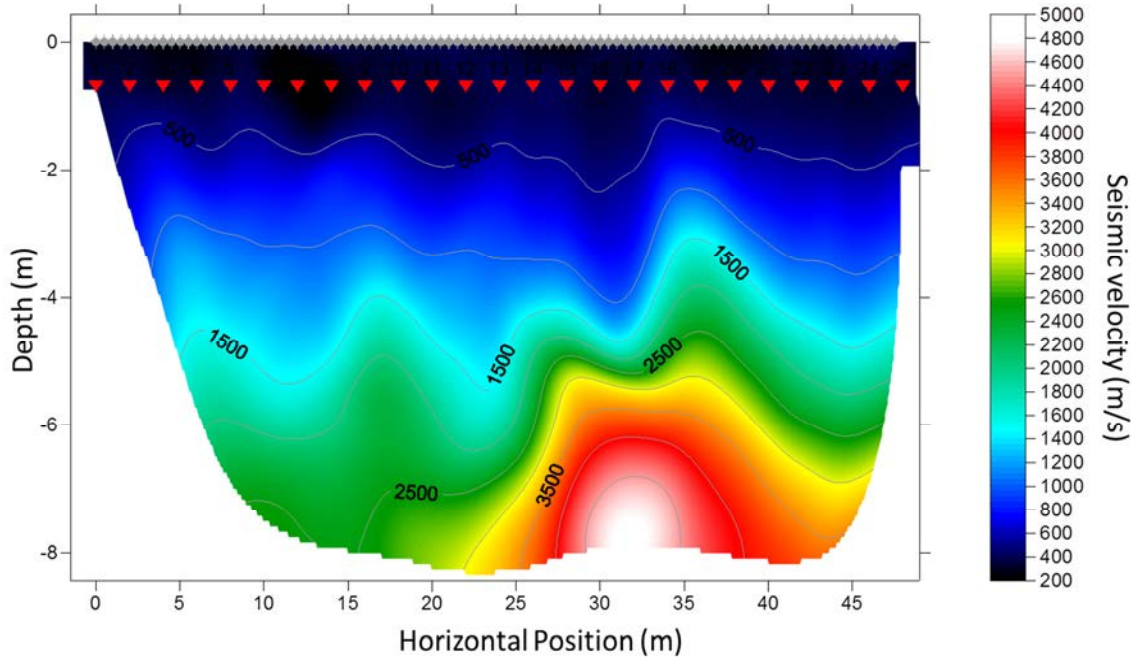
Depth (m)
Horizontal Position (m)
Seismic velocity (m/s)
500
1500
2500
3500

20°

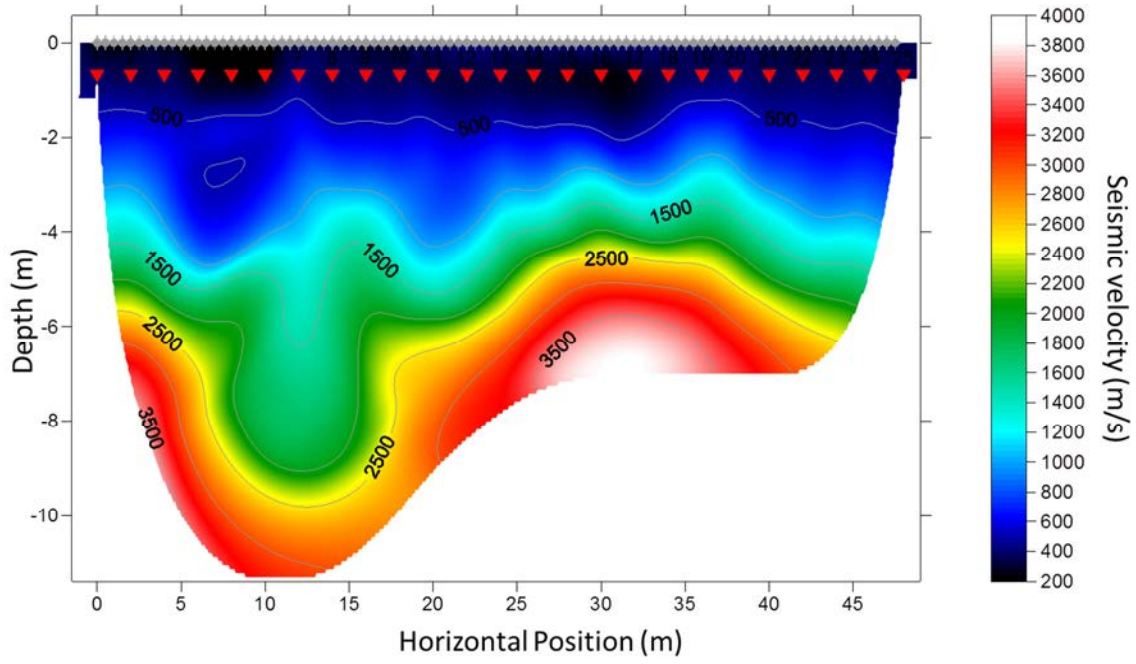
Depth (m)
Horizontal Position (m)
Seismic velocity (m/s)
500
1500
2500
3500

30°

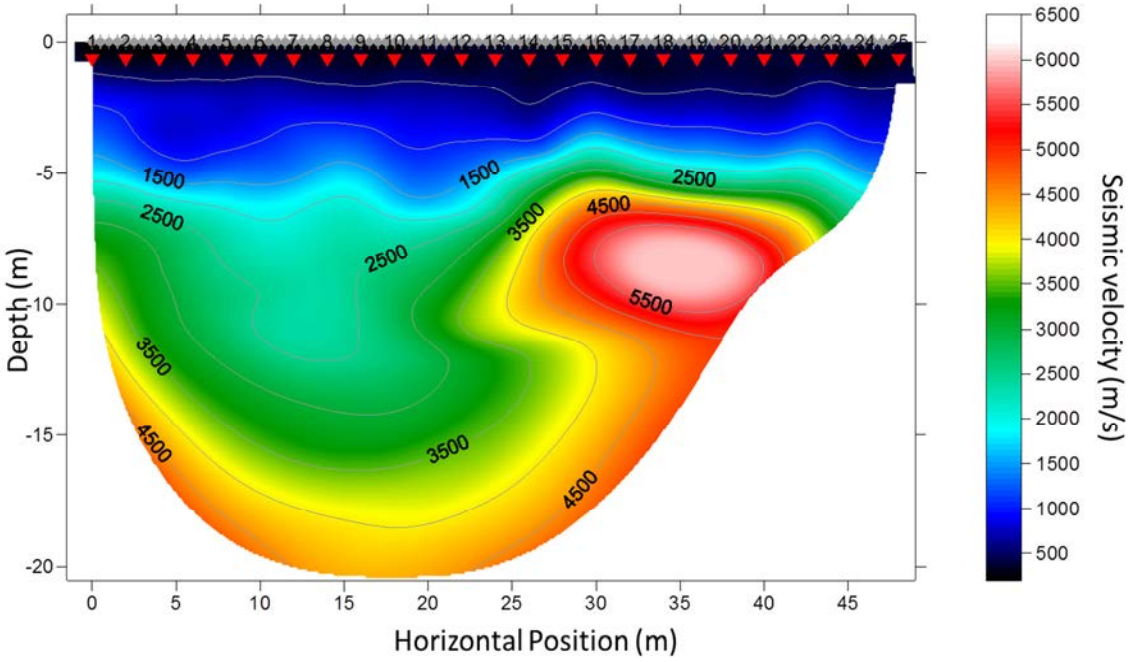
Depth (m)
Horizontal Position (m)
Seismic velocity (m/s)
1500
2500
3500
4500
5500

40°

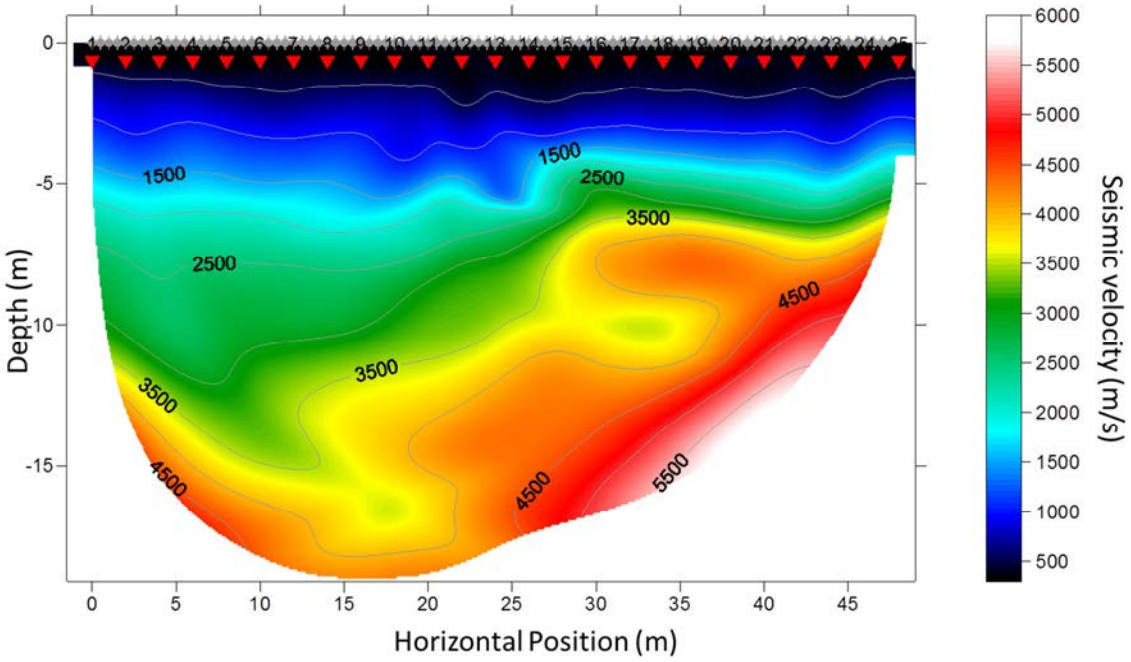
Depth (m)
Horizontal Position (m)
Seismic velocity (m/s)
1500
2500
3500
4500
5500

50°

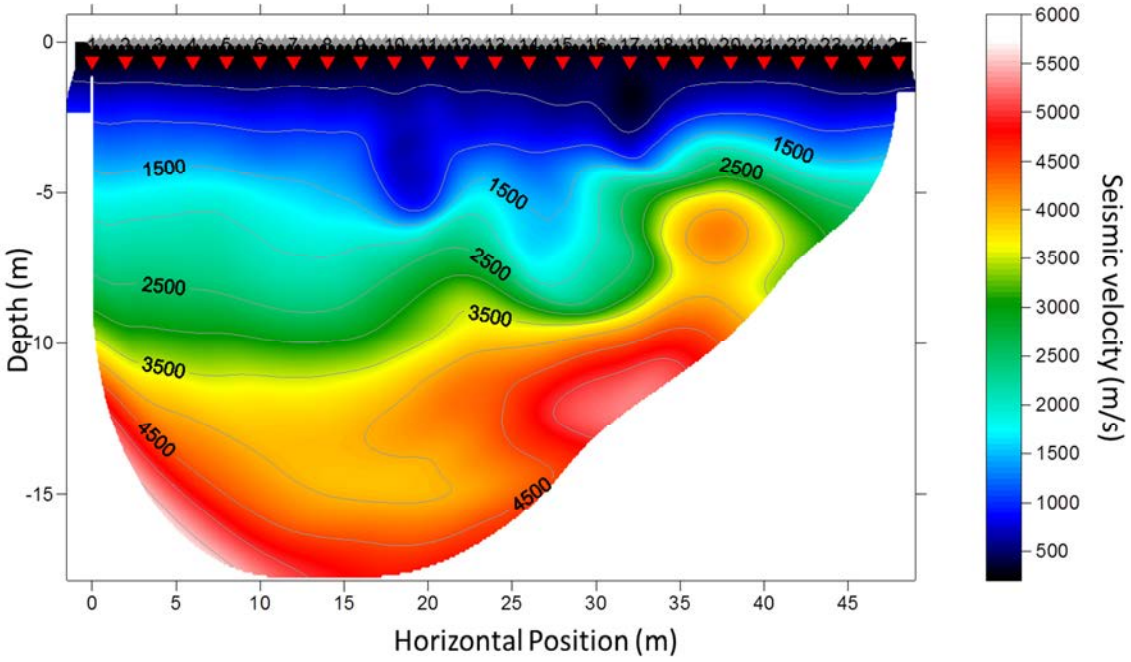
Depth (m)
Horizontal Position (m)
Seismic velocity (m/s)
1500
2500
3500
4500

60°

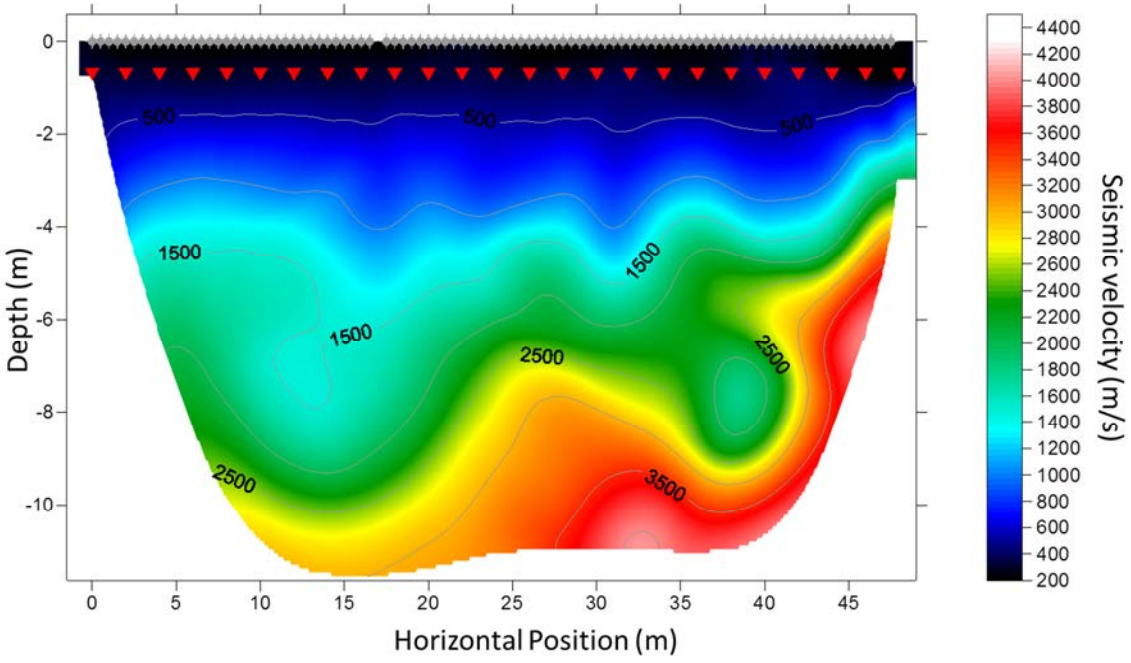
Depth (m)
Horizontal Position (m)
Seismic velocity (m/s)
500
1500
2500
3500

70°

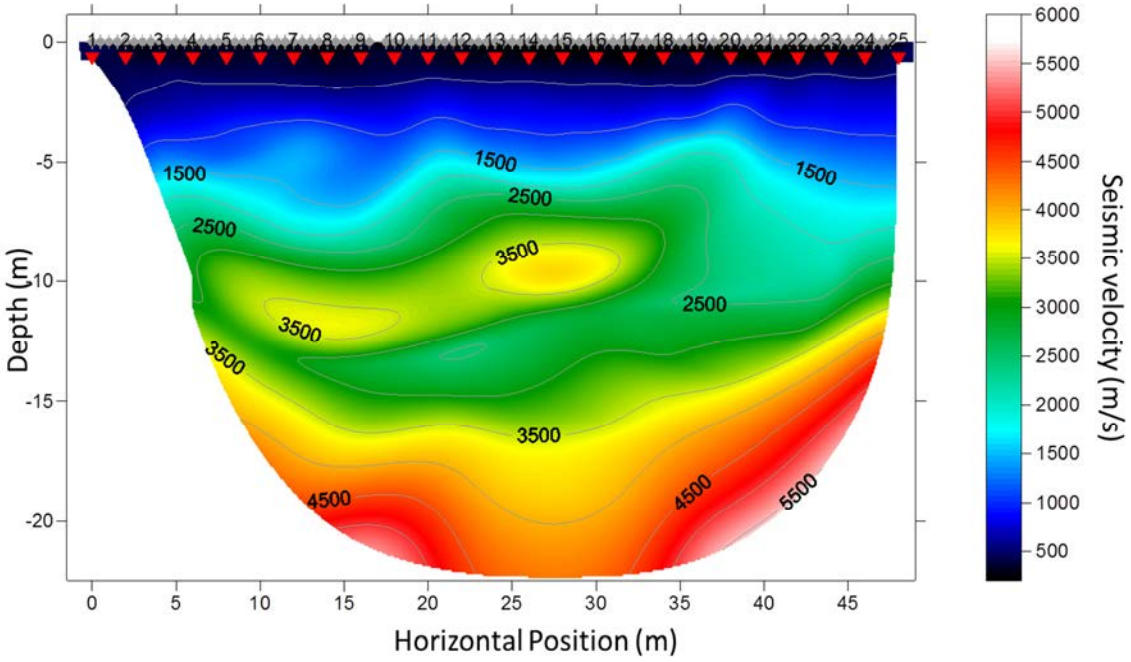
Depth (m)
Horizontal Position (m)
Seismic velocity (m/s)
1500
2500
3500
4500
5500

80°

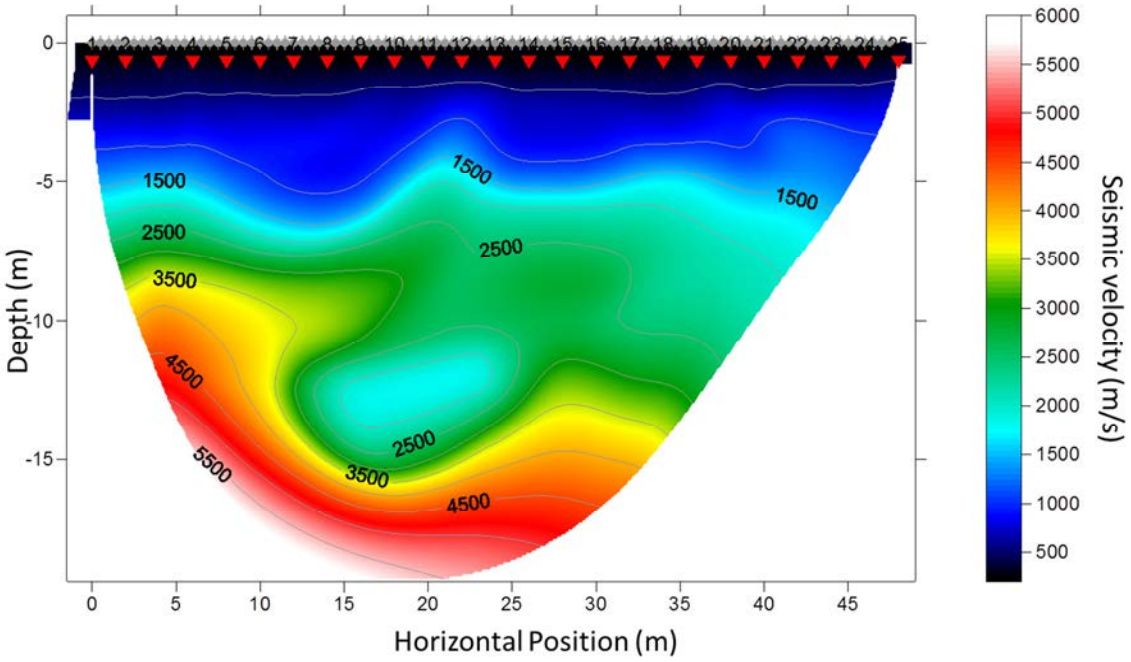
Depth (m)
Horizontal Position (m)
Seismic velocity (m/s)
1500
2500
3500
4500
5500

90°

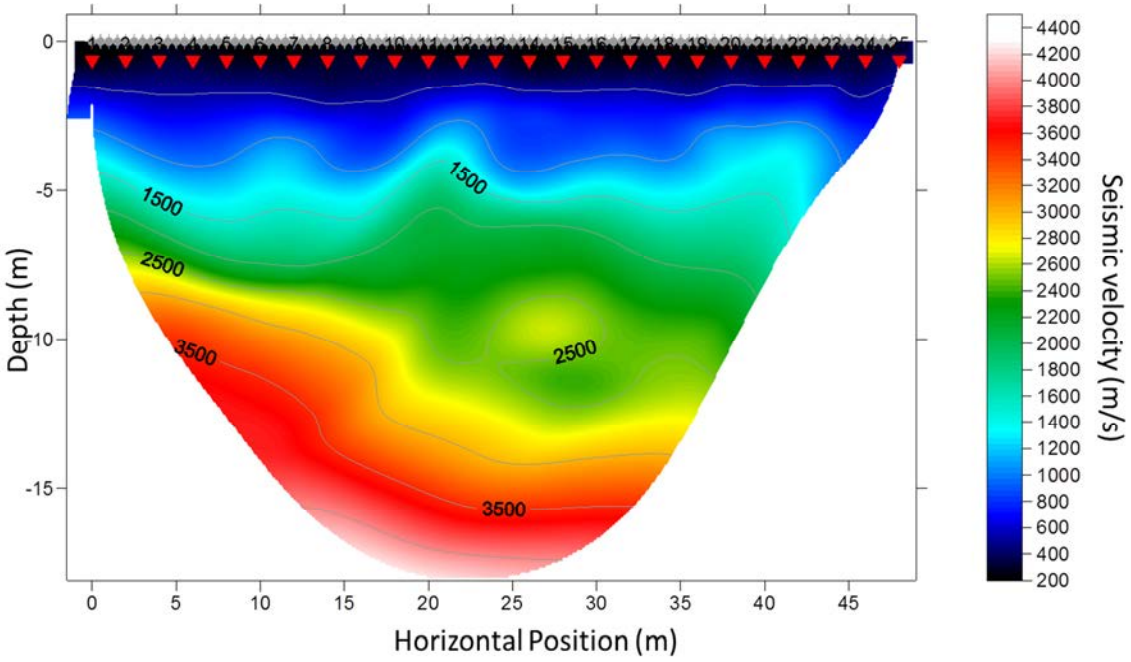
Depth (m)
Horizontal Position (m)
Seismic velocity (m/s)
1500
2500
3500

100°

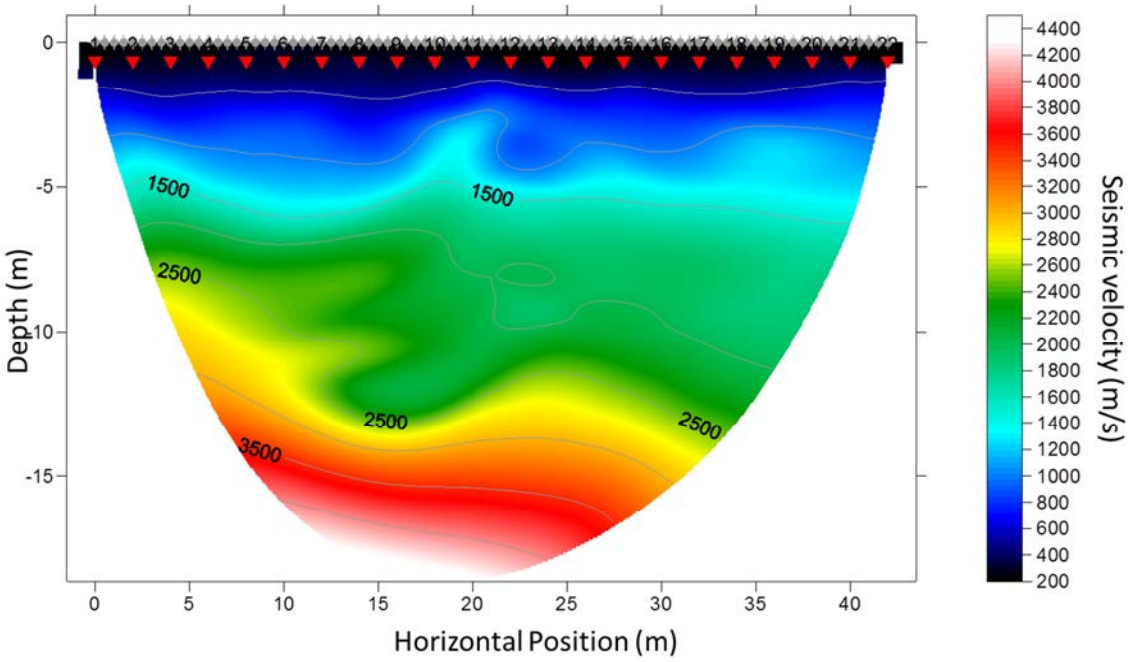
Depth (m)
Horizontal Position (m)
Seismic velocity (m/s)
1500
2500
3500

110°

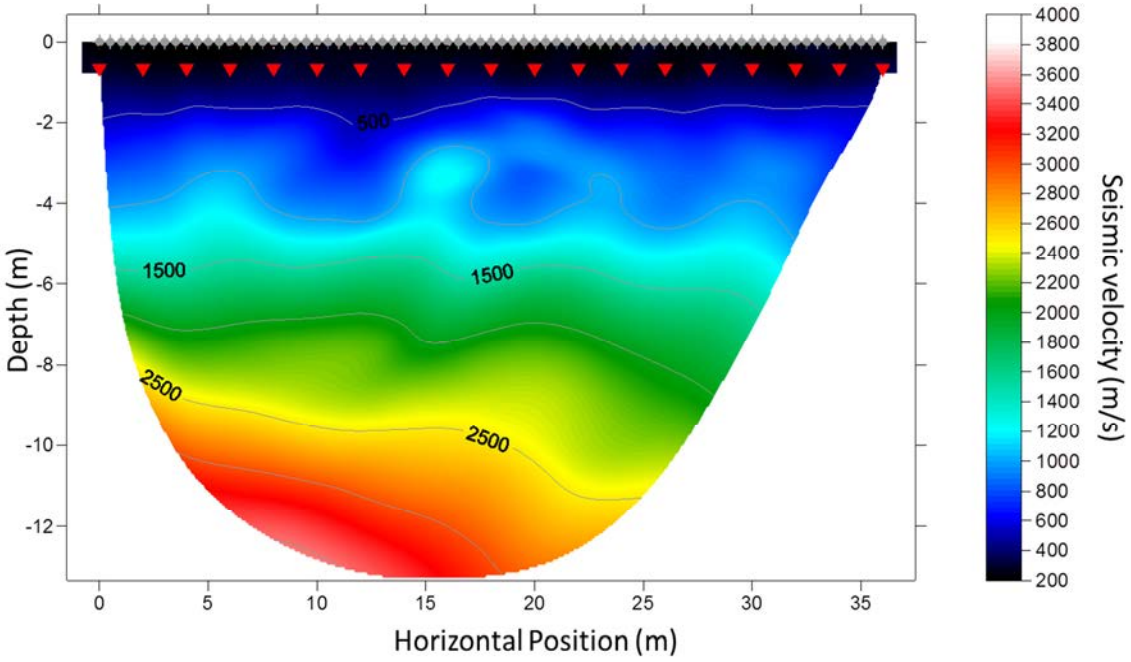
Depth (m)
0
-2
-4
-6
-8
-10
-12
500
1500
1500
2500
2500
0
5
10
15
20
25
30
35
Horizontal Position (m)
4000
3800
3600
3400
3200
3000
2800
2600
2400
2200
2000
1800
1600
1400
1200
1000
800
600
400
200
Seismic velocity (m/s)

120°

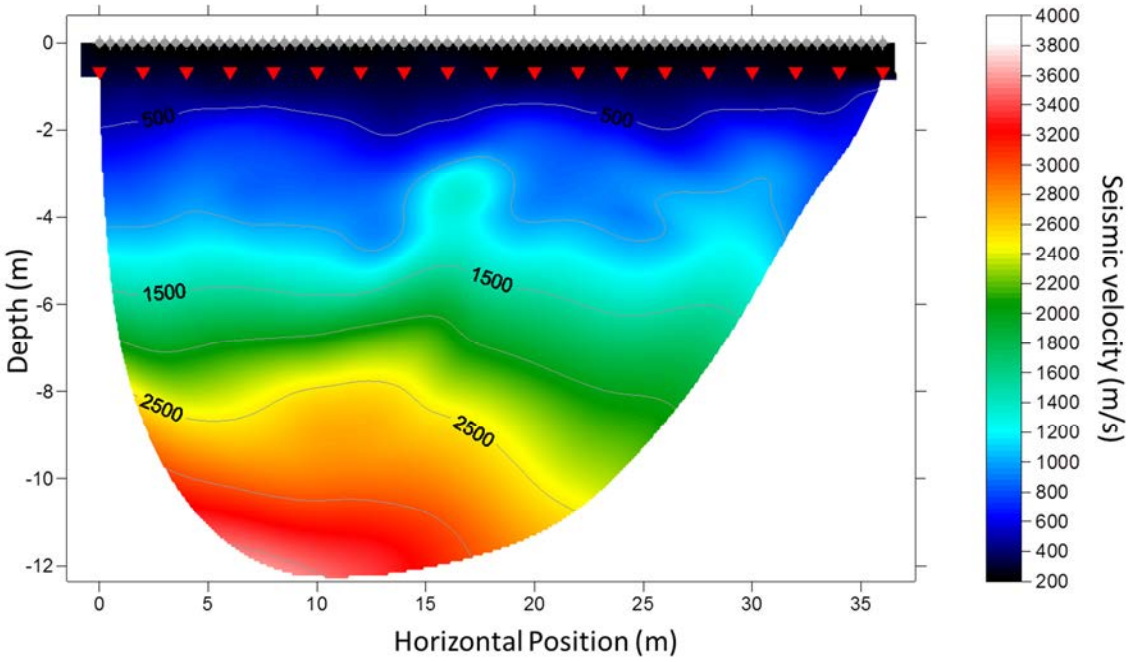
Depth (m)
0
-2
-4
-6
-8
-10
-12
500
500
1500
1500
2500
2500
0
5
10
15
20
25
30
35
Horizontal Position (m)
4000
3800
3600
3400
3200
3000
2800
2600
2400
2200
2000
1800
1600
1400
1200
1000
800
600
400
200
Seismic velocity (m/s)

130°

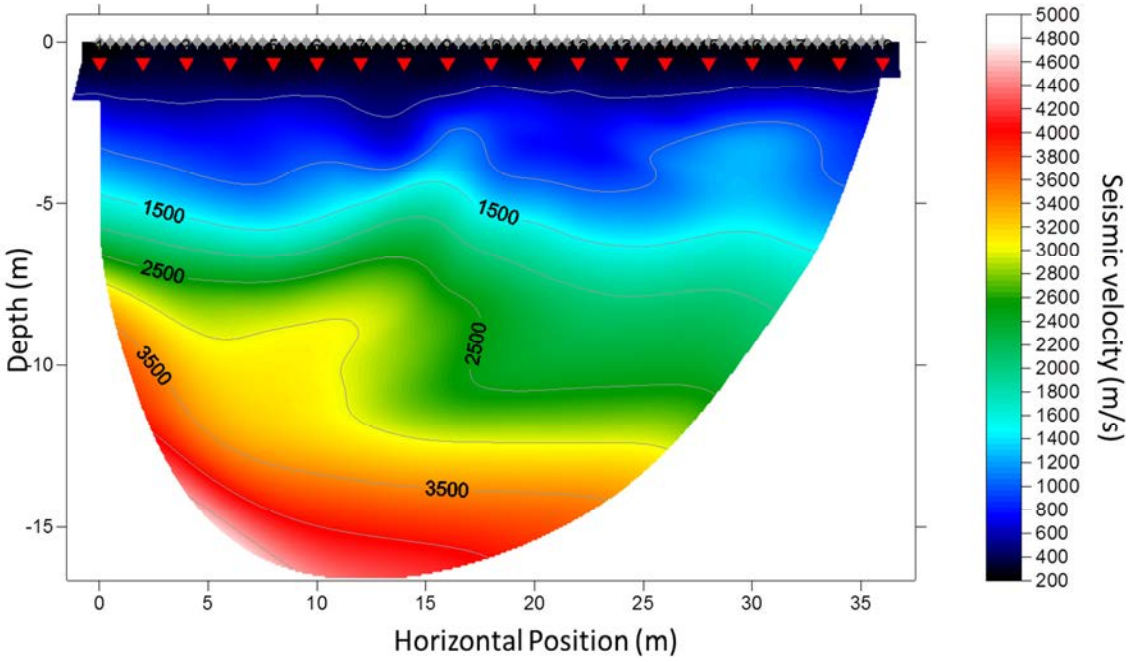
Depth (m)
0
-5
-10
-15
1500
1500
2500
2500
3500
3500
0
5
10
15
20
25
30
35
Horizontal Position (m)
Seismic velocity (m/s)
5000
4800
4600
4400
4200
4000
3800
3600
3400
3200
3000
2800
2600
2400
2200
2000
1800
1600
1400
1200
1000
800
600
400
200

140°

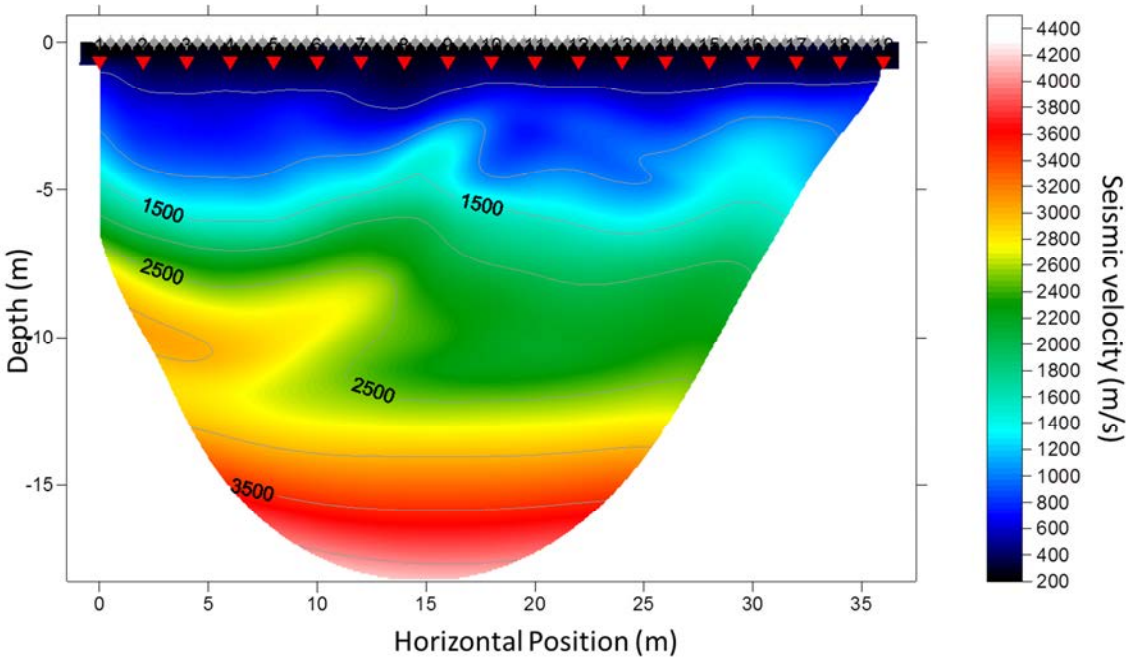
Depth (m)
0
-5
-10
-15
1500
1500
2500
2500
3500
0
5
10
15
20
25
30
35
Horizontal Position (m)
Seismic velocity (m/s)
4400
4200
4000
3800
3600
3400
3200
3000
2800
2600
2400
2200
2000
1800
1600
1400
1200
1000
800
600
400
200

150°

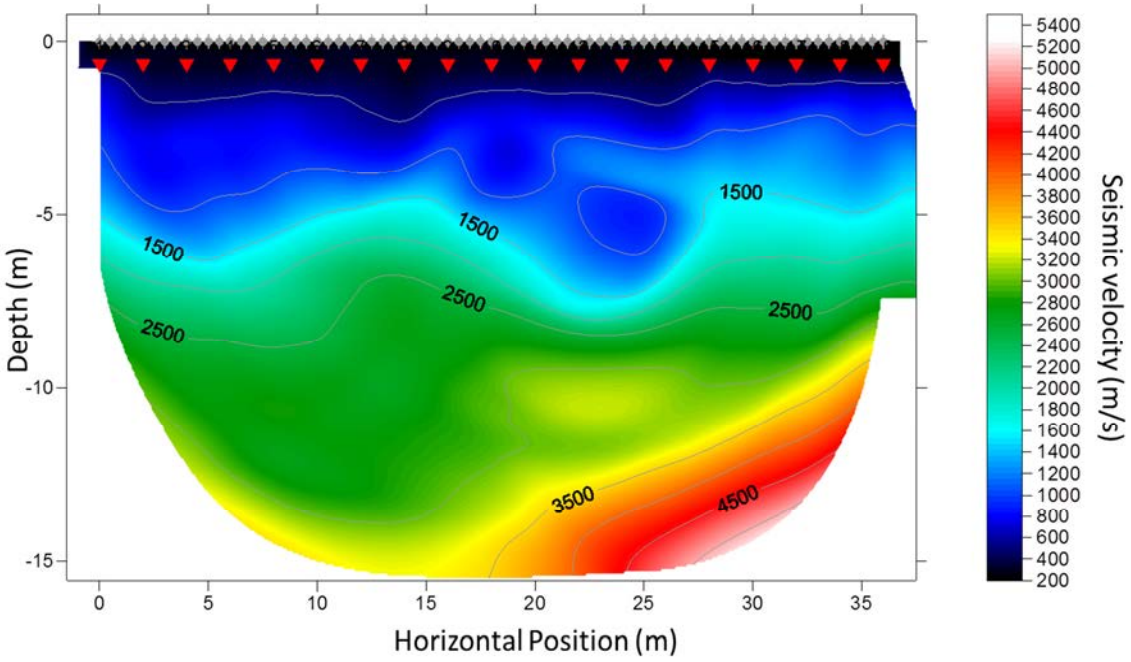
Depth (m)
0
-5
-10
-15
0
5
10
15
20
25
30
35
Horizontal Position (m)
1500
1500
1500
2500
2500
2500
3500
4500
Seismic velocity (m/s)
5400
5200
5000
4800
4600
4400
4200
4000
3800
3600
3400
3200
3000
2800
2600
2400
2200
2000
1800
1600
1400
1200
1000
800
600
400
200

160°

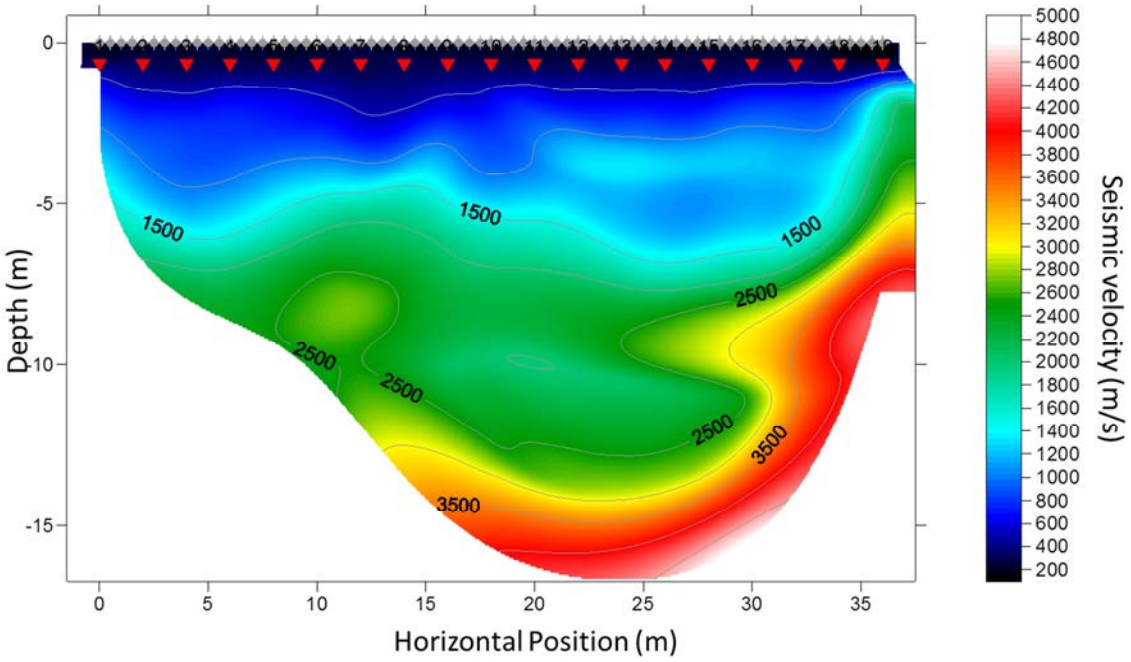
Depth (m)
0
-5
-10
-15
0
5
10
15
20
25
30
35
Horizontal Position (m)
1500
1500
1500
2500
2500
2500
2500
3500
3500
Seismic velocity (m/s)
5000
4800
4600
4400
4200
4000
3800
3600
3400
3200
3000
2800
2600
2400
2200
2000
1800
1600
1400
1200
1000
800
600
400
200

170°

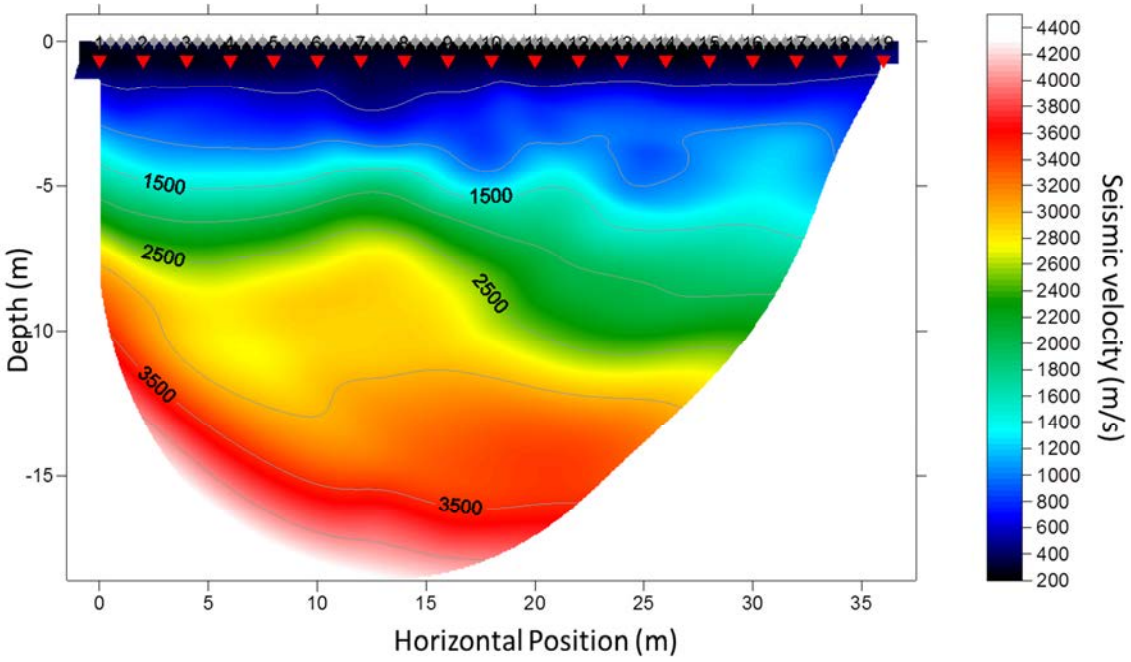

Compass Diagrams:

0 m

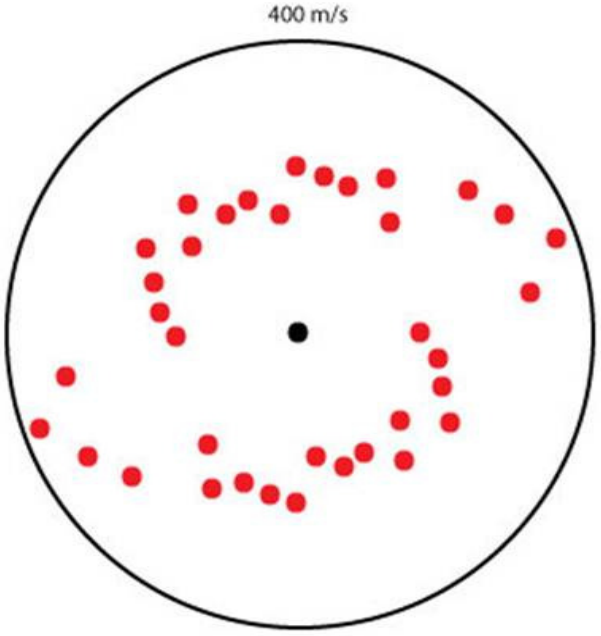

0.5 m

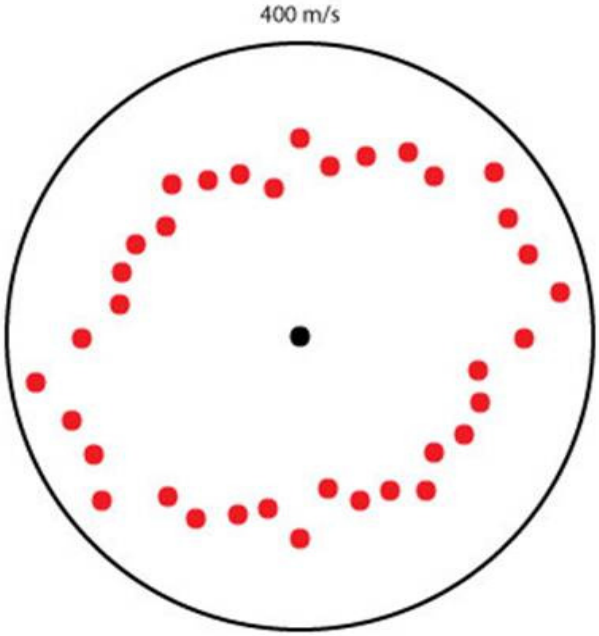

1 m

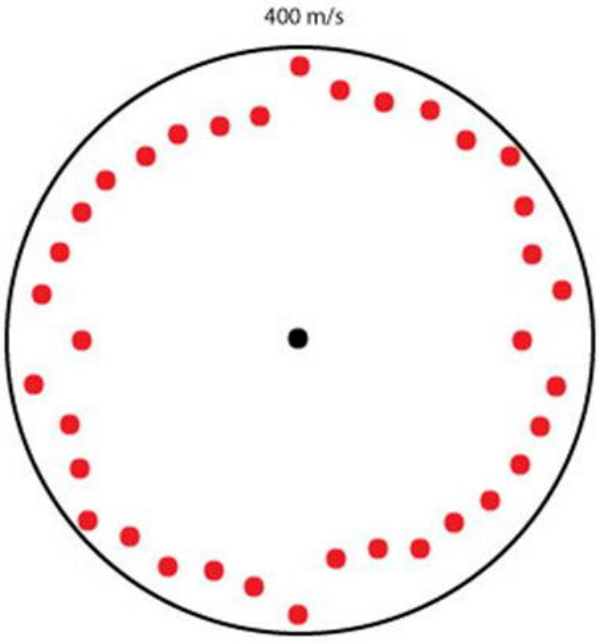

1.5 m

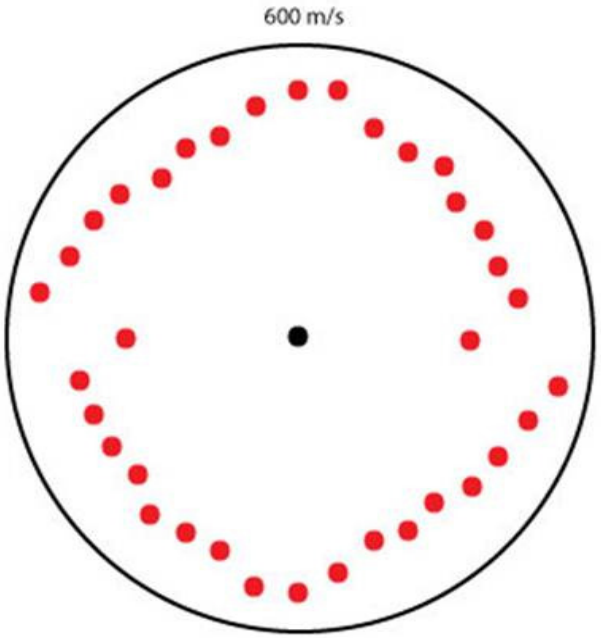

2 m

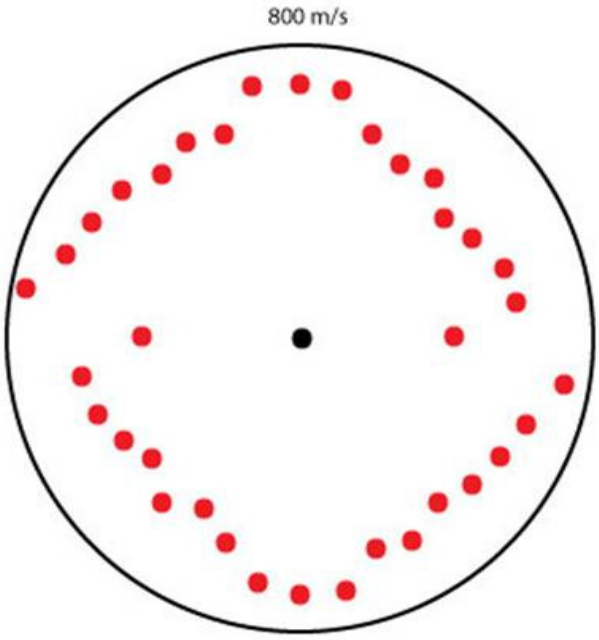

2.5 m

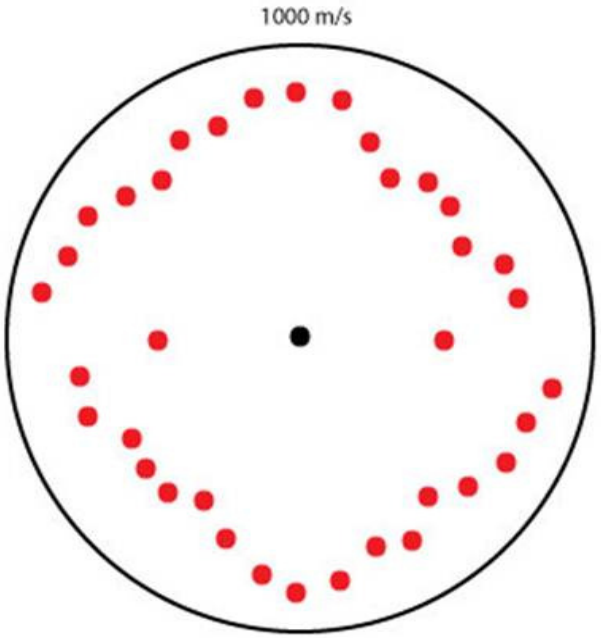

3 m

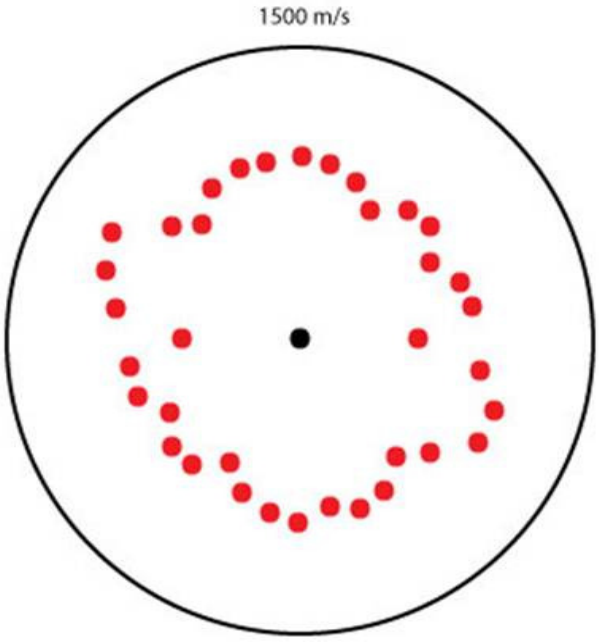

3.5 m

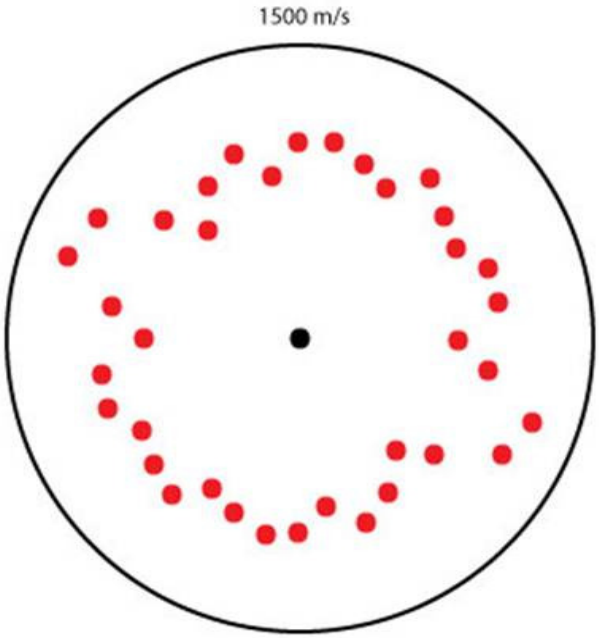

4 m

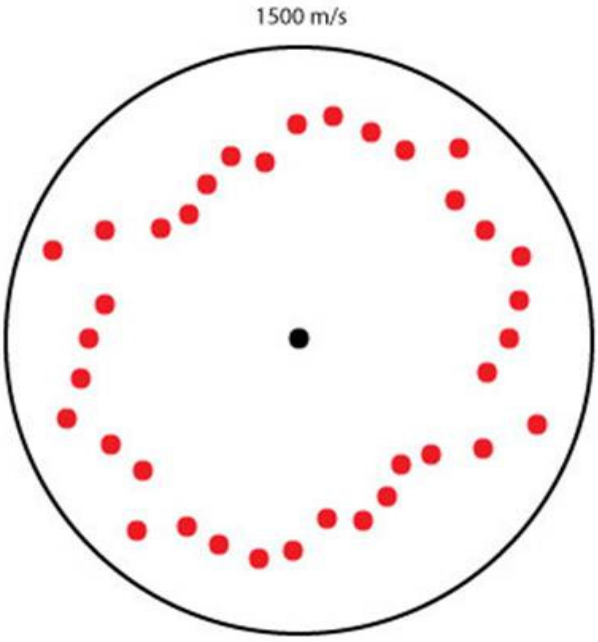

4.5 m

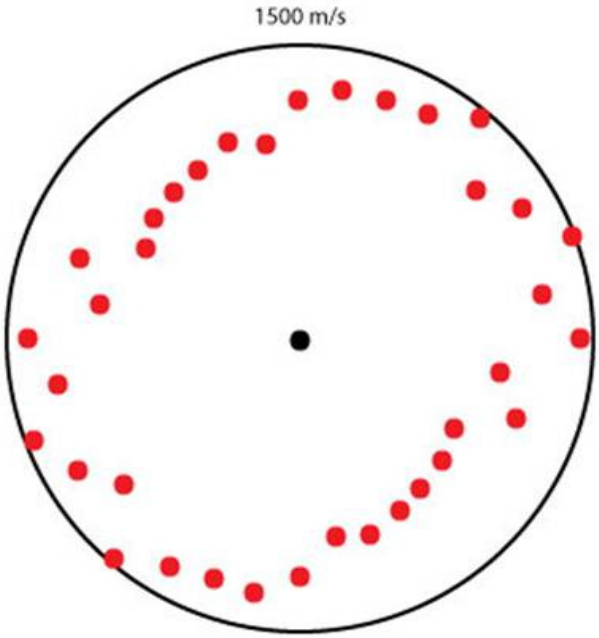

5 m

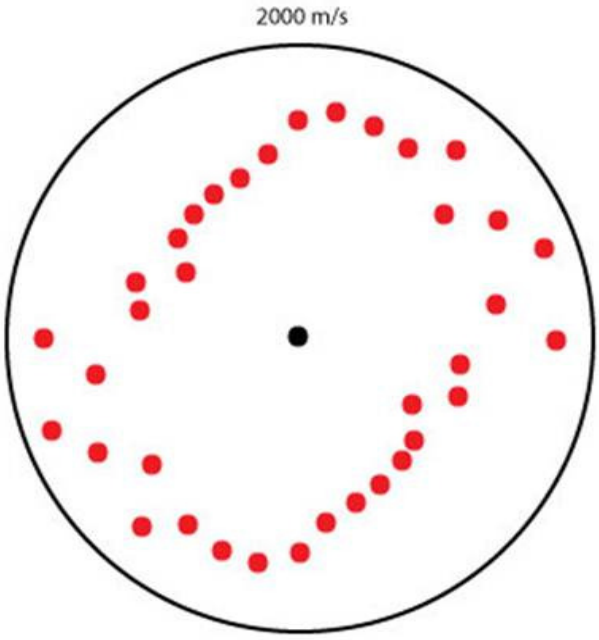

5.5 m

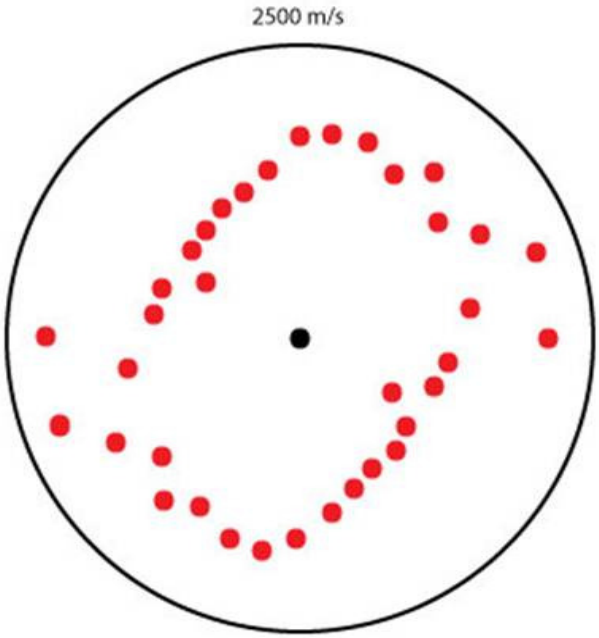

6 m

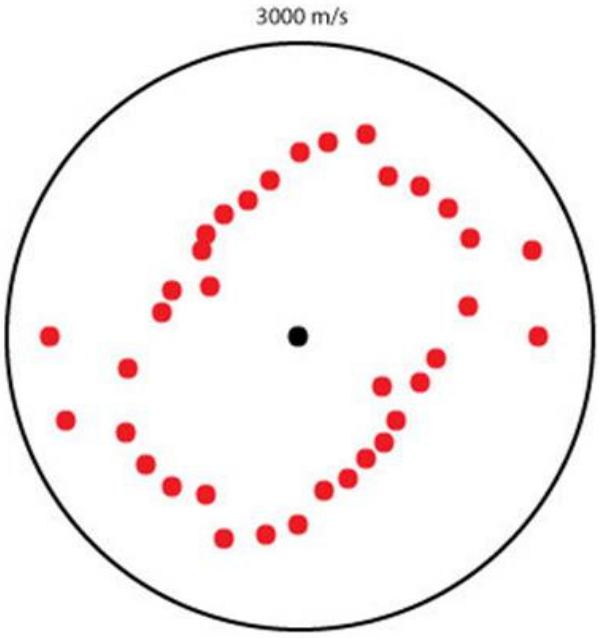

6.5 m

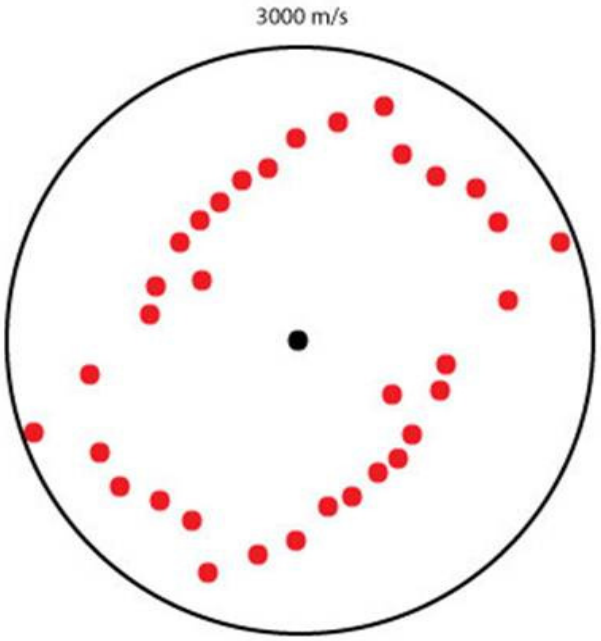

7 m

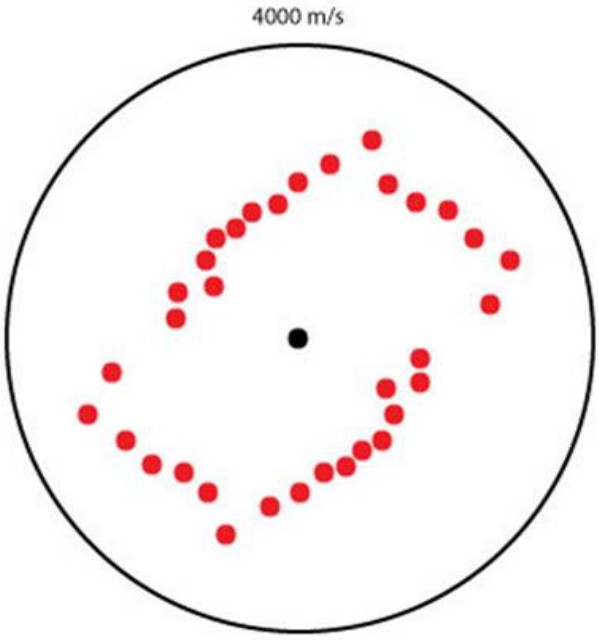

7.5 m

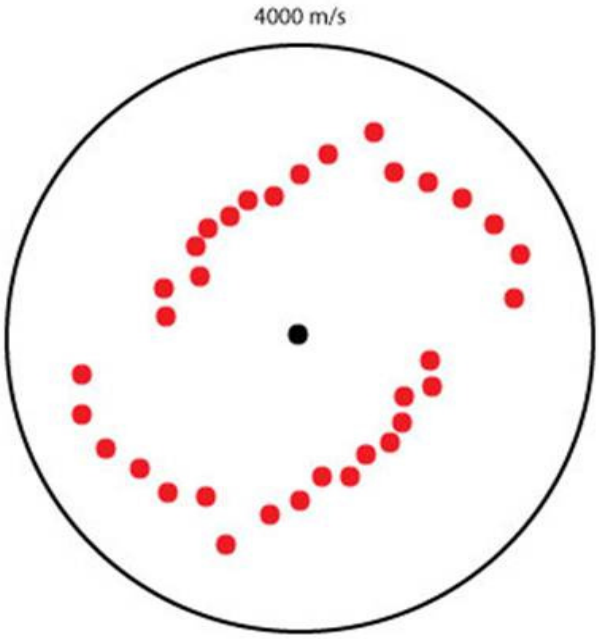

8 m

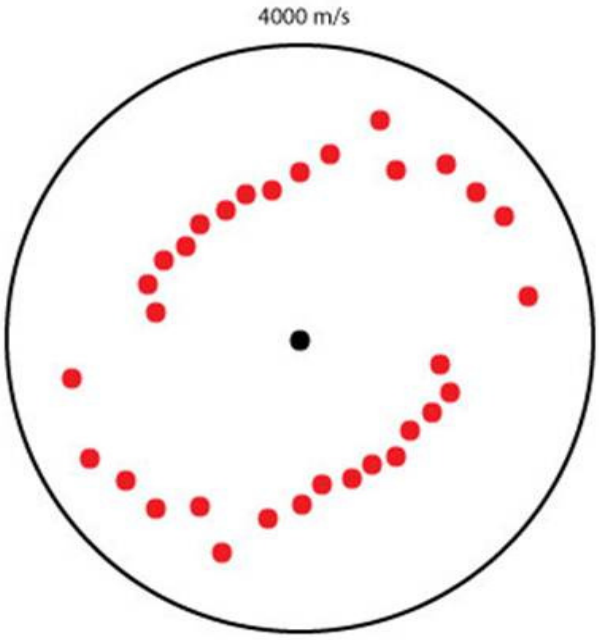

8.5 m

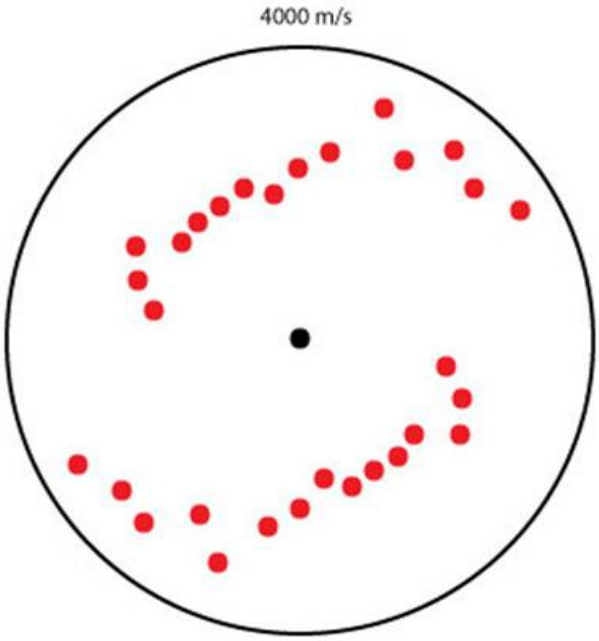

9 m

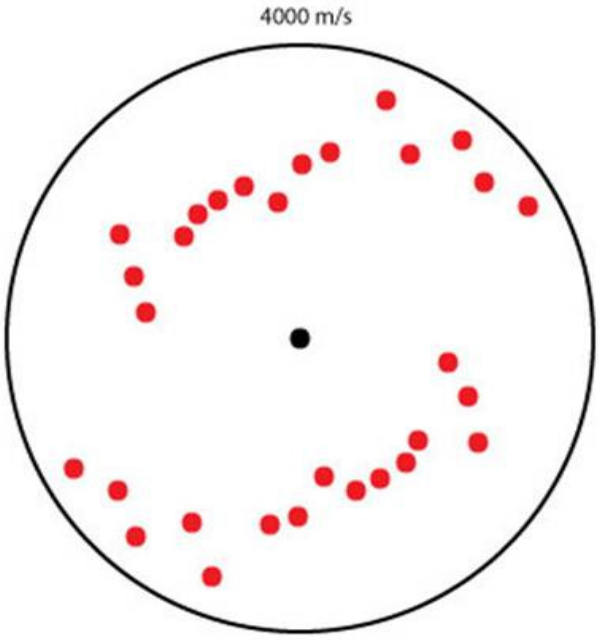

9.5 m

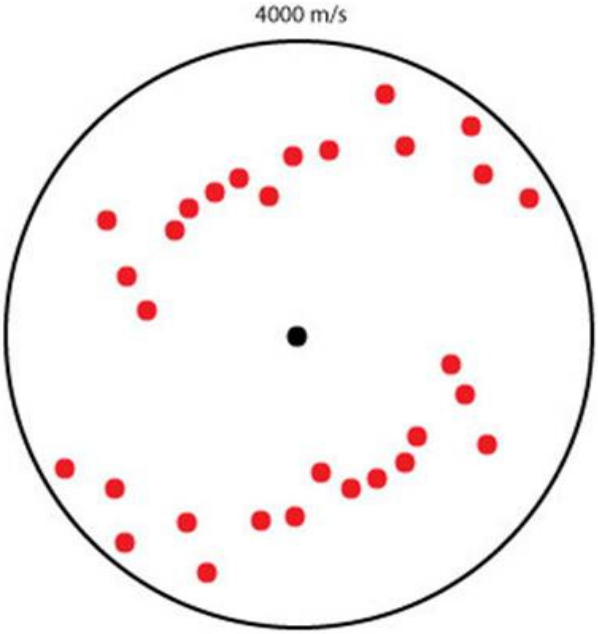

10 m

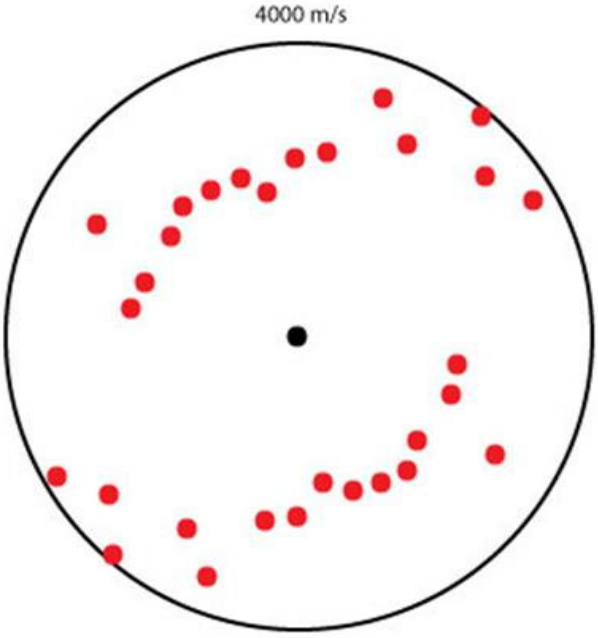

Appendix 3: Km-2 Raypath coverage diagrams, Tomograms, and Compass Diagrams

This appendix will show all raypath coverage diagrams, velocity tomograms, and velocity compass diagrams in that order. The raypath coverage diagrams and velocity tomograms will begin with those imaged from the north-south line (azimuth of 0°) and continue to the azimuth of 170°. The compass diagrams will begin at a depth of 0 m, and continue in one half meter increments to the depth of resolution limit (for the Km-2 dataset, this depth is 9.5 m)

Raypath Coverage Diagrams:

0°

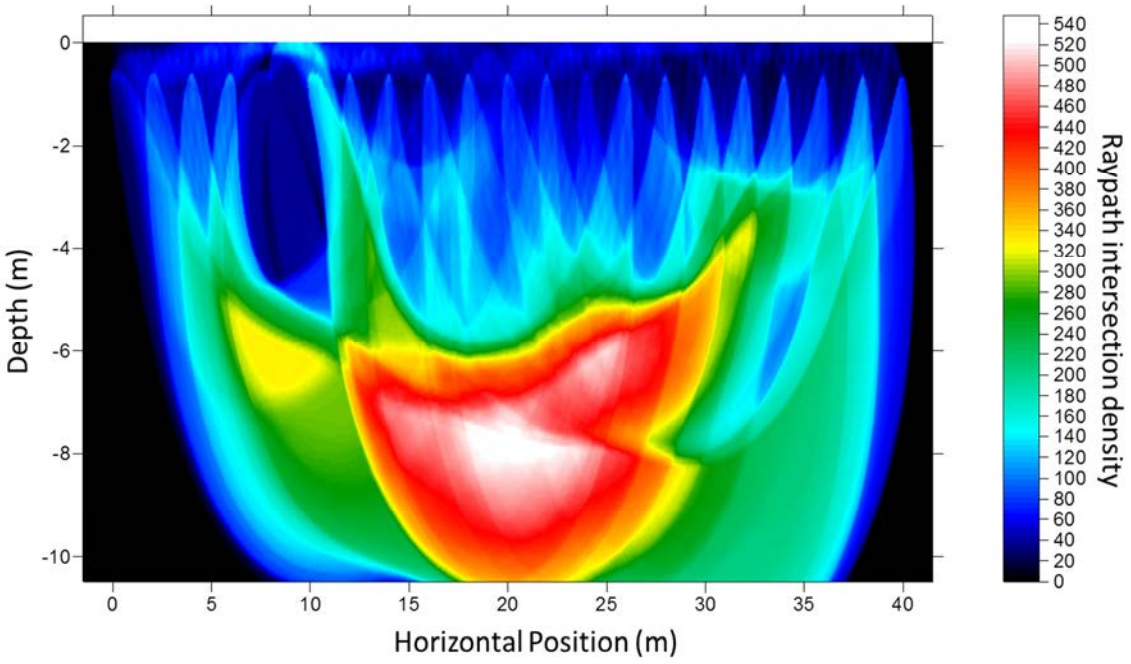

10°

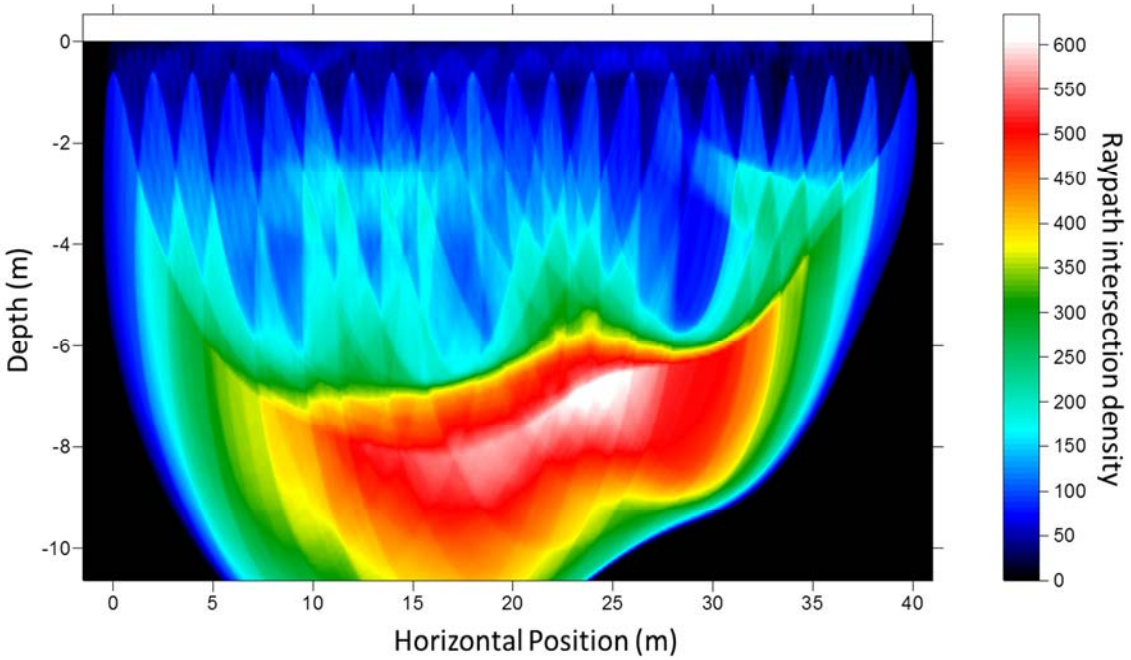
Depth (m)
0
-2
-4
-6
-8
-10
0
5
10
15
20
25
30
35
40
Horizontal Position (m)
600
550
500
450
400
350
300
250
200
150
100
50
0
Raypath intersection density

20°

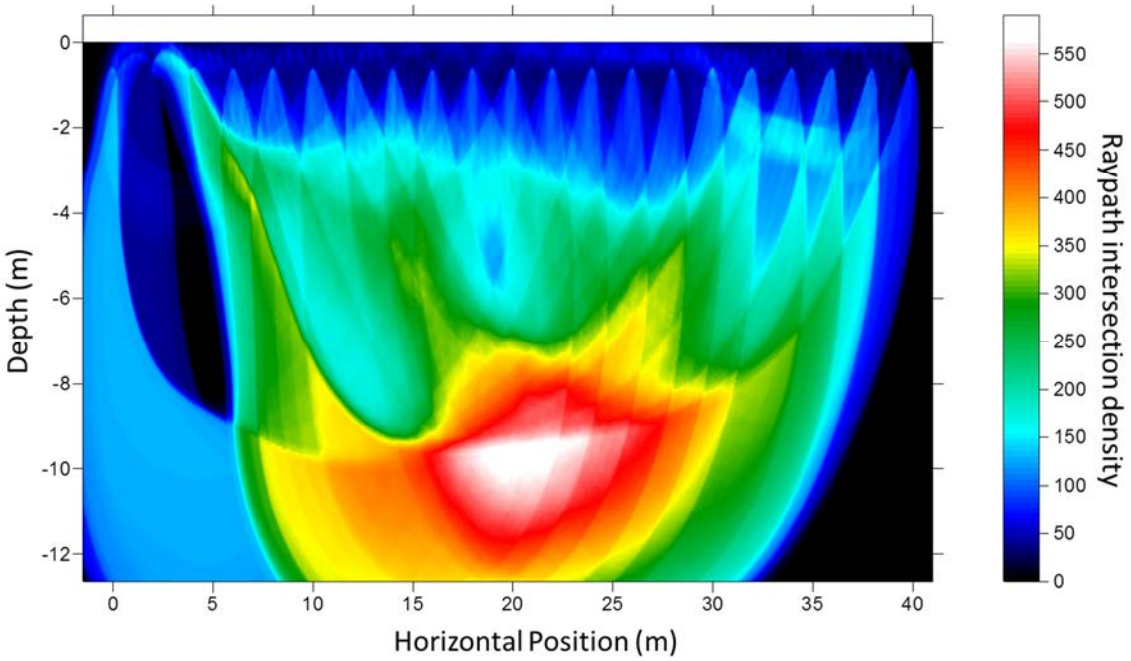
Depth (m)
0
-2
-4
-6
-8
-10
-12
0
5
10
15
20
25
30
35
40
Horizontal Position (m)
550
500
450
400
350
300
250
200
150
100
50
0
Raypath intersection density

30°

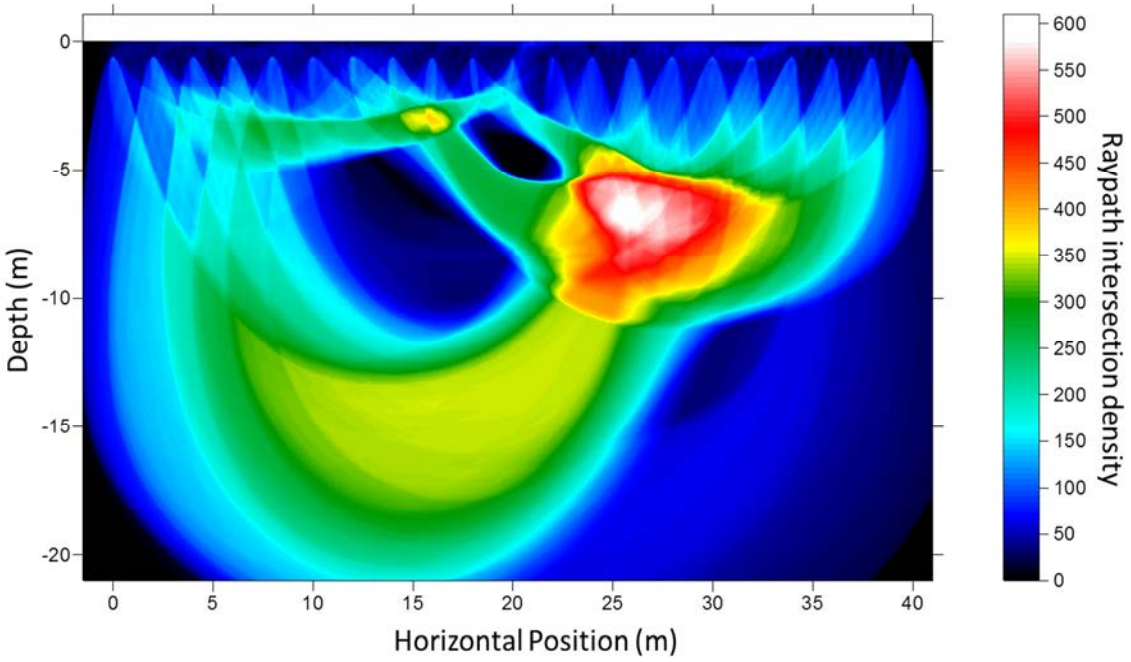
Depth (m)
0
-5
-10
-15
-20
0
5
10
15
20
25
30
35
40
Horizontal Position (m)
600
550
500
450
400
350
300
250
200
150
100
50
0
Raypath intersection density

40°

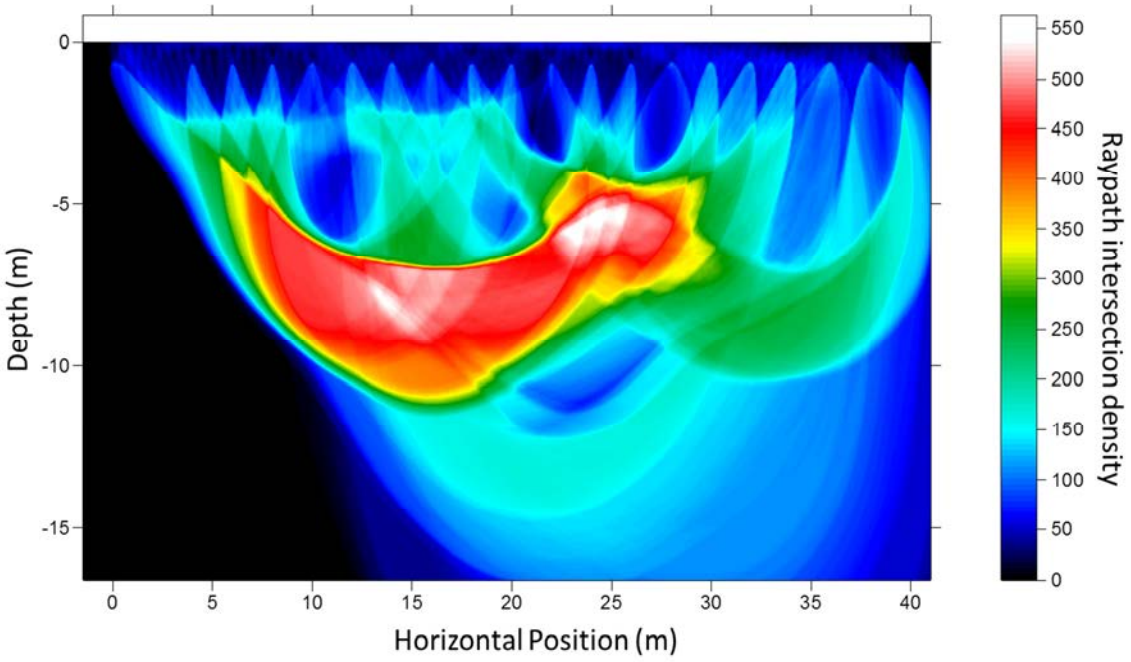
Depth (m)
0
-5
-10
-15
0
5
10
15
20
25
30
35
40
Horizontal Position (m)
550
500
450
400
350
300
250
200
150
100
50
0
Raypath intersection density

50°

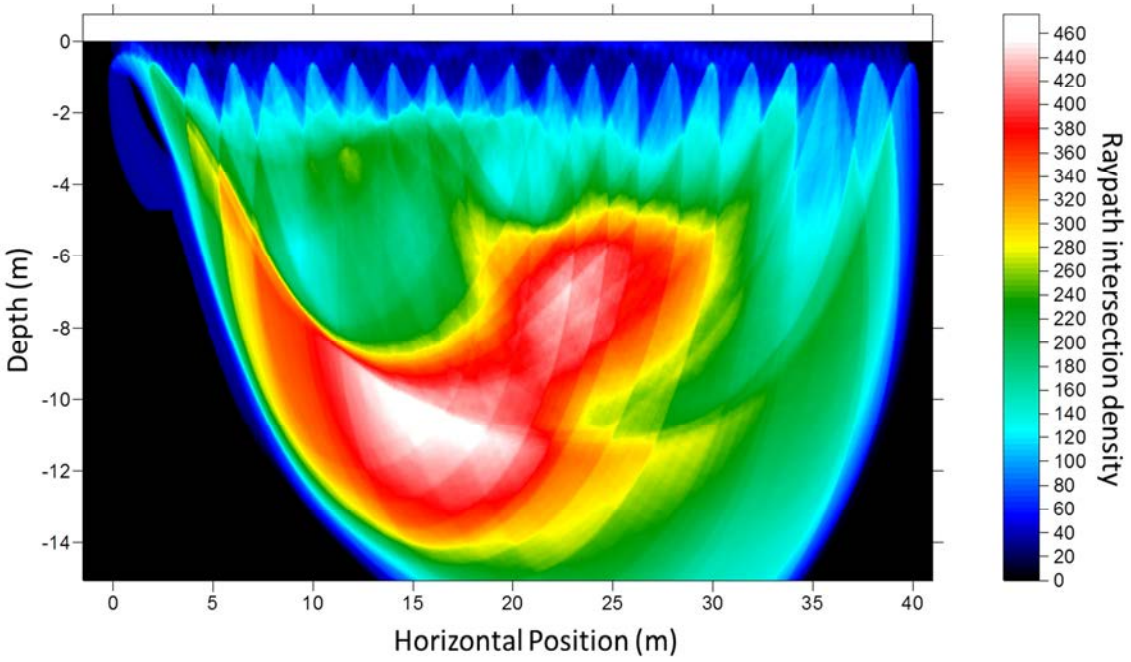
Depth (m)
0
-2
-4
-6
-8
-10
-12
-14
0
5
10
15
20
25
30
35
40
Horizontal Position (m)
Raypath intersection density
460
440
420
400
380
360
340
320
300
280
260
240
220
200
180
160
140
120
100
80
60
40
20
0

60°

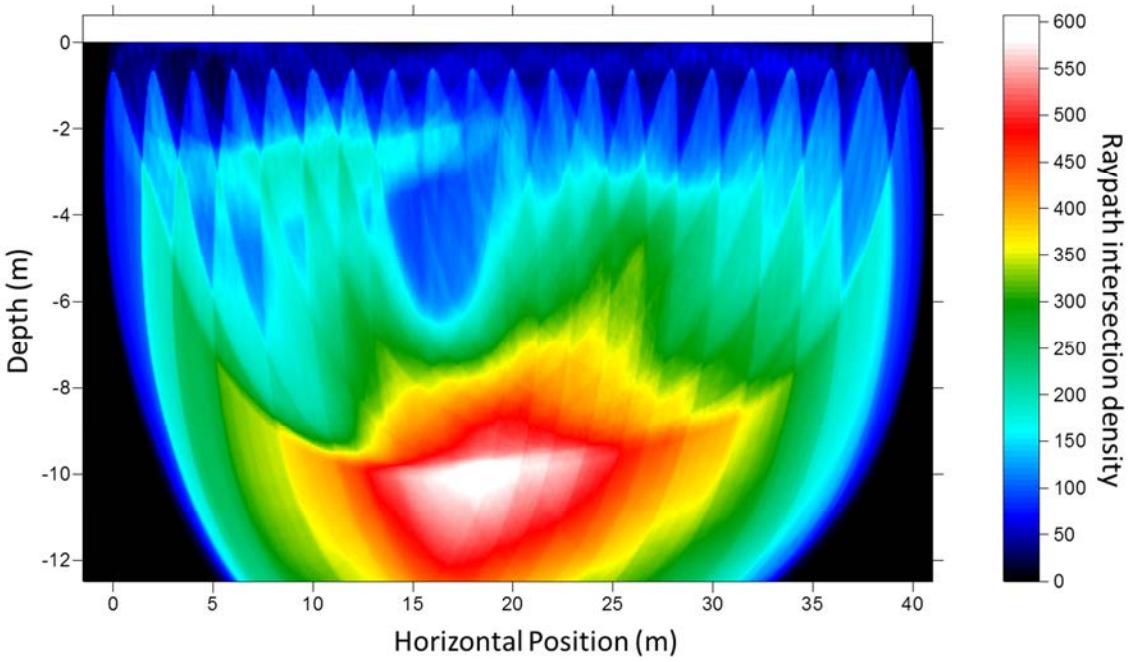
Depth (m)
0
-2
-4
-6
-8
-10
-12
0
5
10
15
20
25
30
35
40
Horizontal Position (m)
Raypath intersection density
600
550
500
450
400
350
300
250
200
150
100
50
0

70°

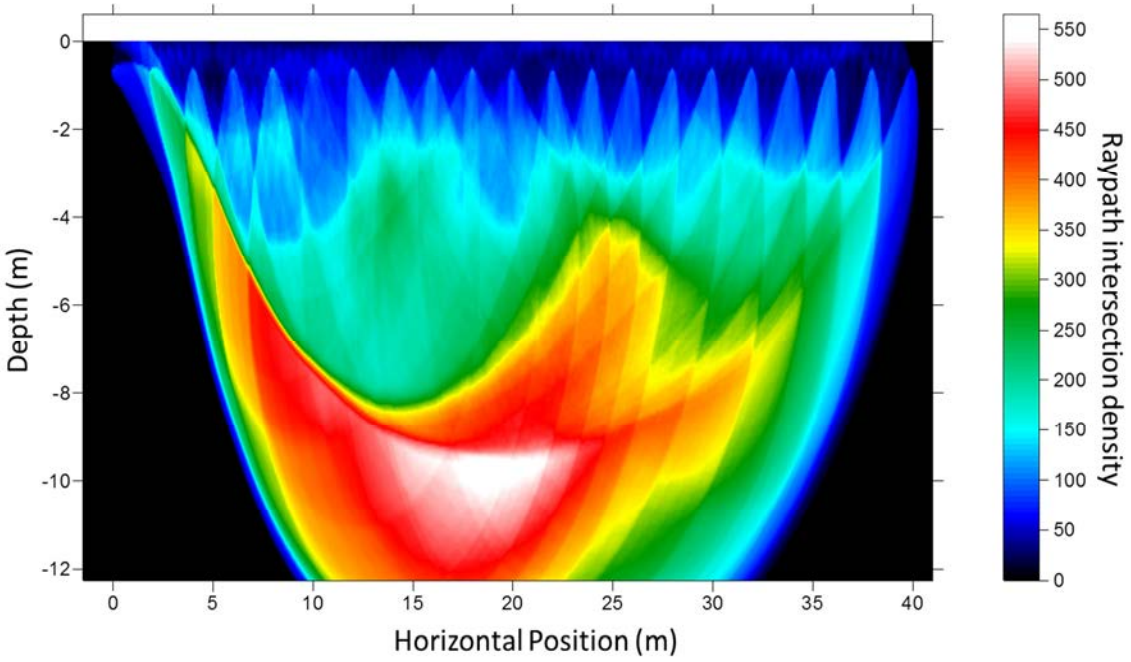
Depth (m)
0
-2
-4
-6
-8
-10
-12
0
5
10
15
20
25
30
35
40
Horizontal Position (m)
Raypath intersection density
550
500
450
400
350
300
250
200
150
100
50
0

80°

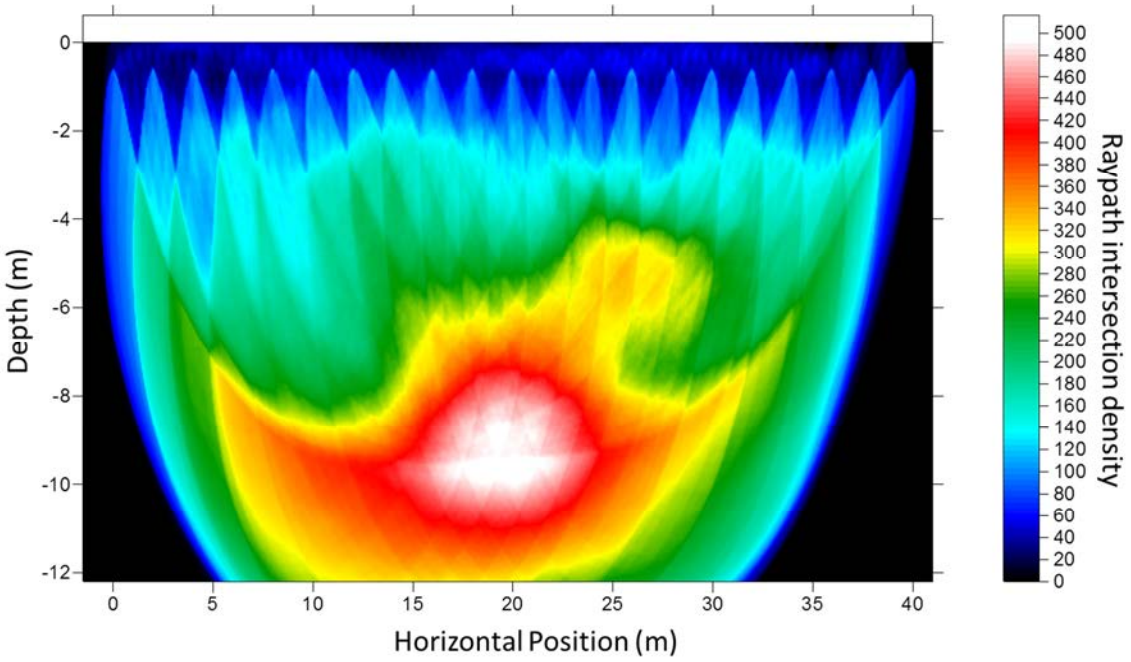
Depth (m)
0
-2
-4
-6
-8
-10
-12
0
5
10
15
20
25
30
35
40
Horizontal Position (m)
Raypath intersection density
500
480
460
440
420
400
380
360
340
320
300
280
260
240
220
200
180
160
140
120
100
80
60
40
20
0

90°

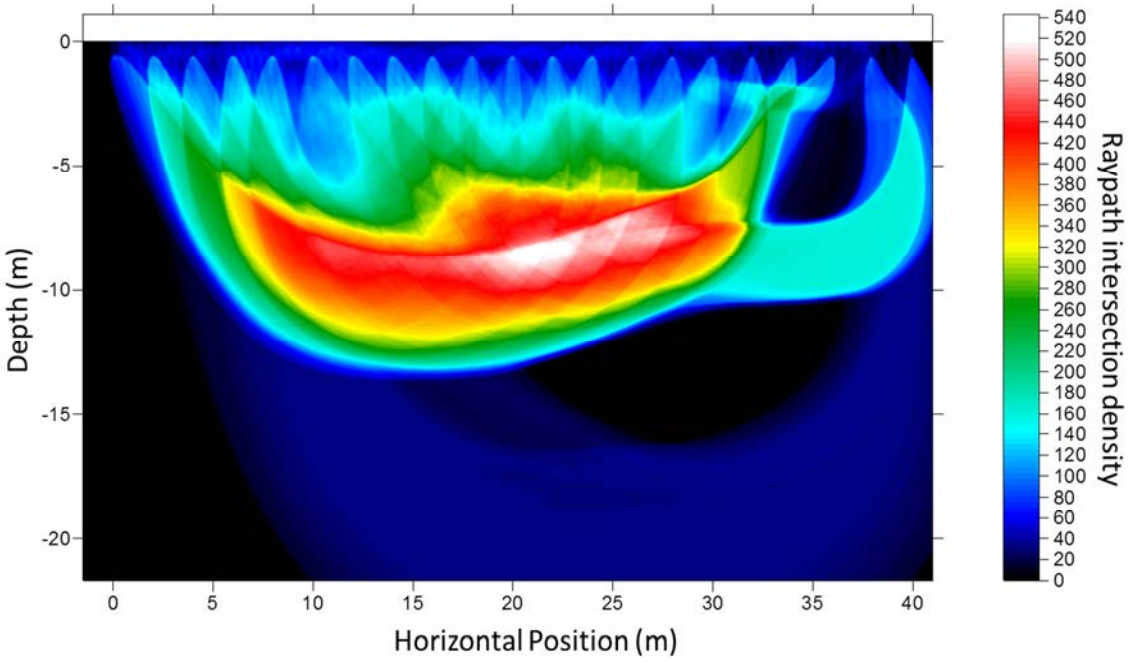
Depth (m)
0
-5
-10
-15
-20
0
5
10
15
20
25
30
35
40
Horizontal Position (m)
Raypath intersection density
540
520
500
480
460
440
420
400
380
360
340
320
300
280
260
240
220
200
180
160
140
120
100
80
60
40
20
0

100°

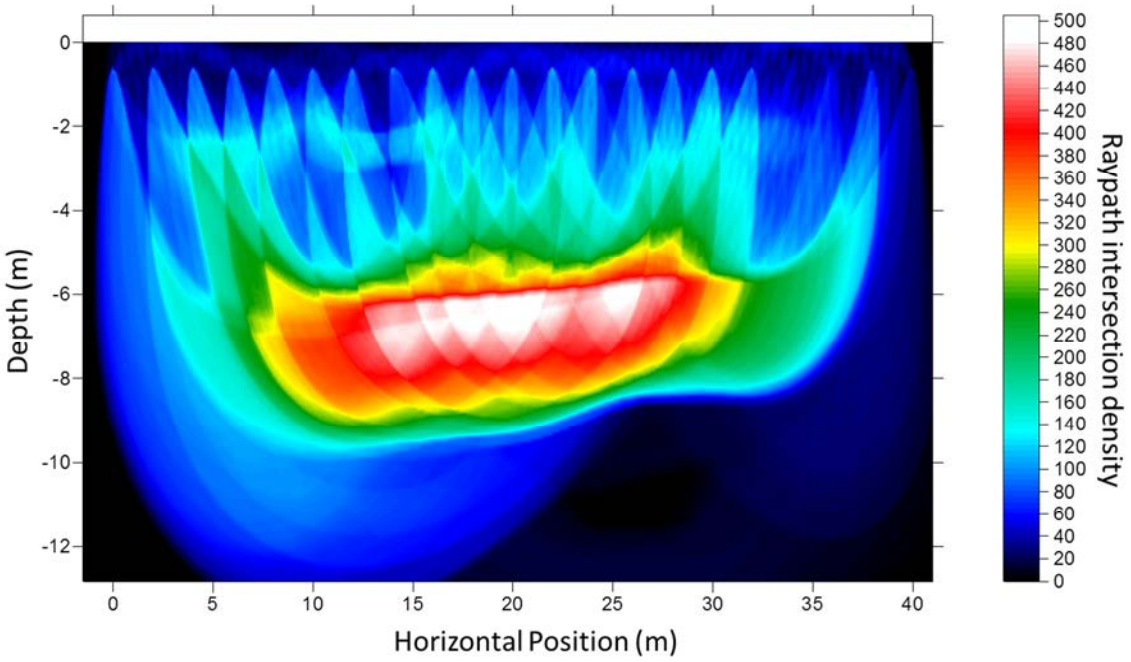
Depth (m)
0
-2
-4
-6
-8
-10
-12
0
5
10
15
20
25
30
35
40
Horizontal Position (m)
Raypath intersection density
500
480
460
440
420
400
380
360
340
320
300
280
260
240
220
200
180
160
140
120
100
80
60
40
20
0

110°

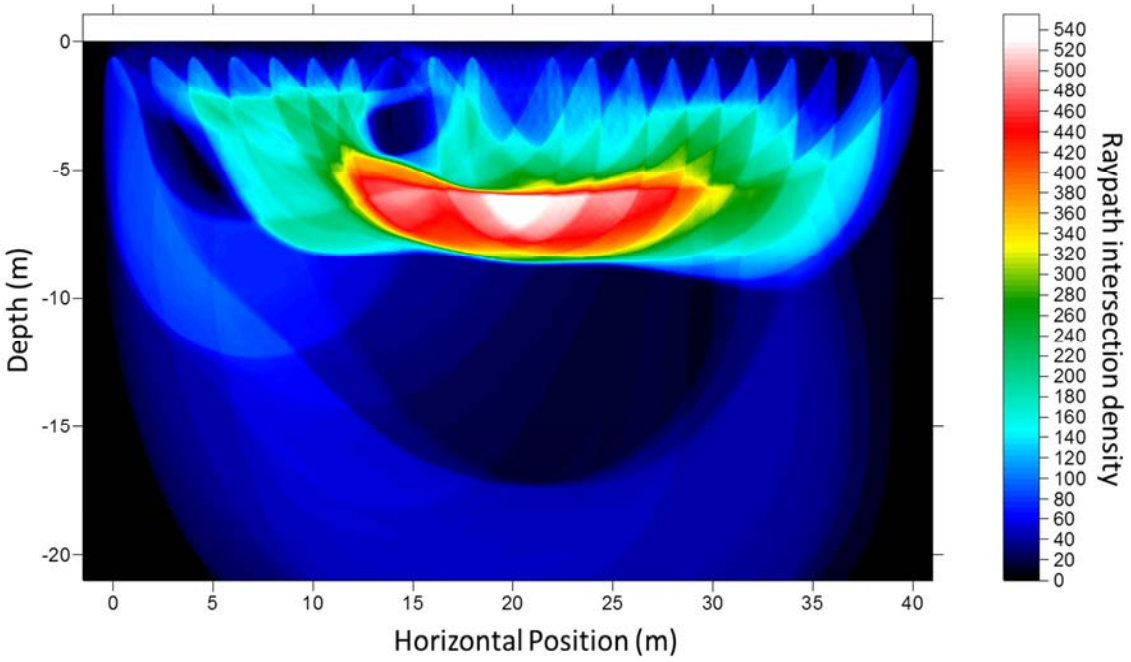
Depth (m)
0
-5
-10
-15
-20
0
5
10
15
20
25
30
35
40
Horizontal Position (m)
Raypath intersection density
540
520
500
480
460
440
420
400
380
360
340
320
300
280
260
240
220
200
180
160
140
120
100
80
60
40
20
0

120°

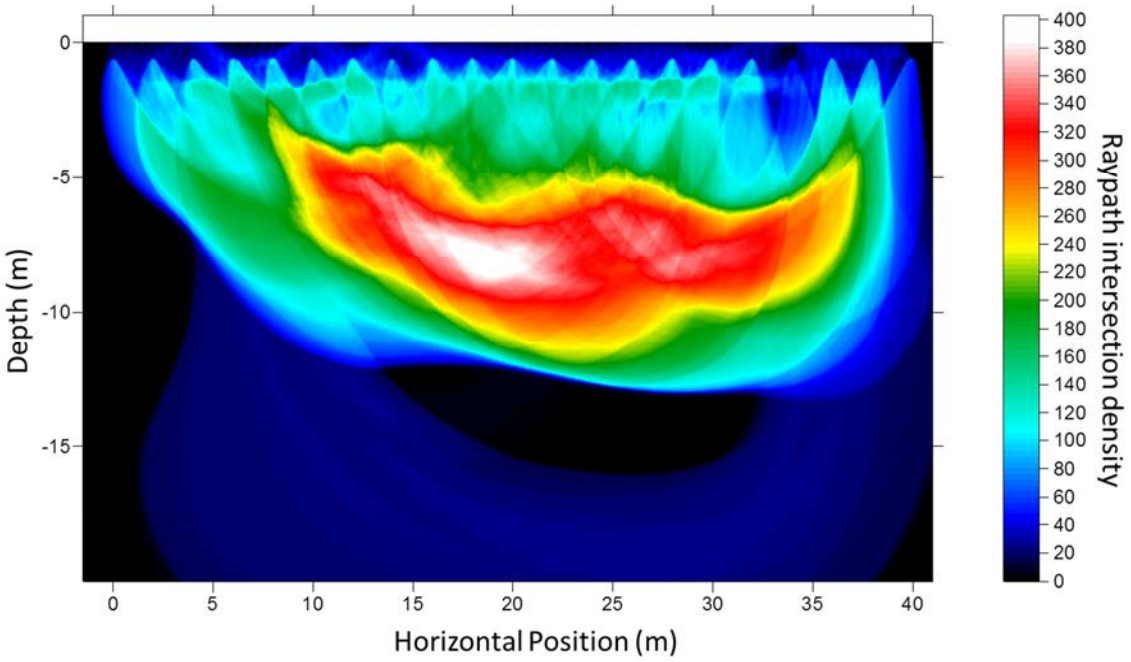
Depth (m)
0
-5
-10
-15
0
5
10
15
20
25
30
35
40
Horizontal Position (m)
Raypath intersection density
400
380
360
340
320
300
280
260
240
220
200
180
160
140
120
100
80
60
40
20
0

130°

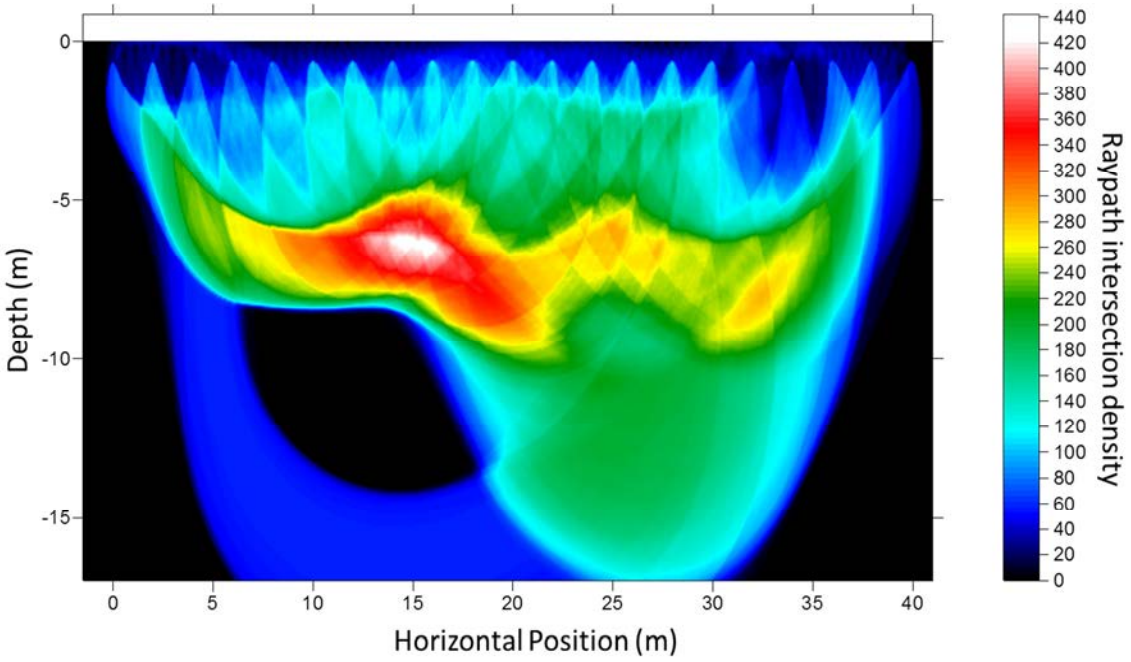
Depth (m)
0
-5
-10
-15
0
5
10
15
20
25
30
35
40
Horizontal Position (m)
Raypath intersection density
440
420
400
380
360
340
320
300
280
260
240
220
200
180
160
140
120
100
80
60
40
20
0

140°

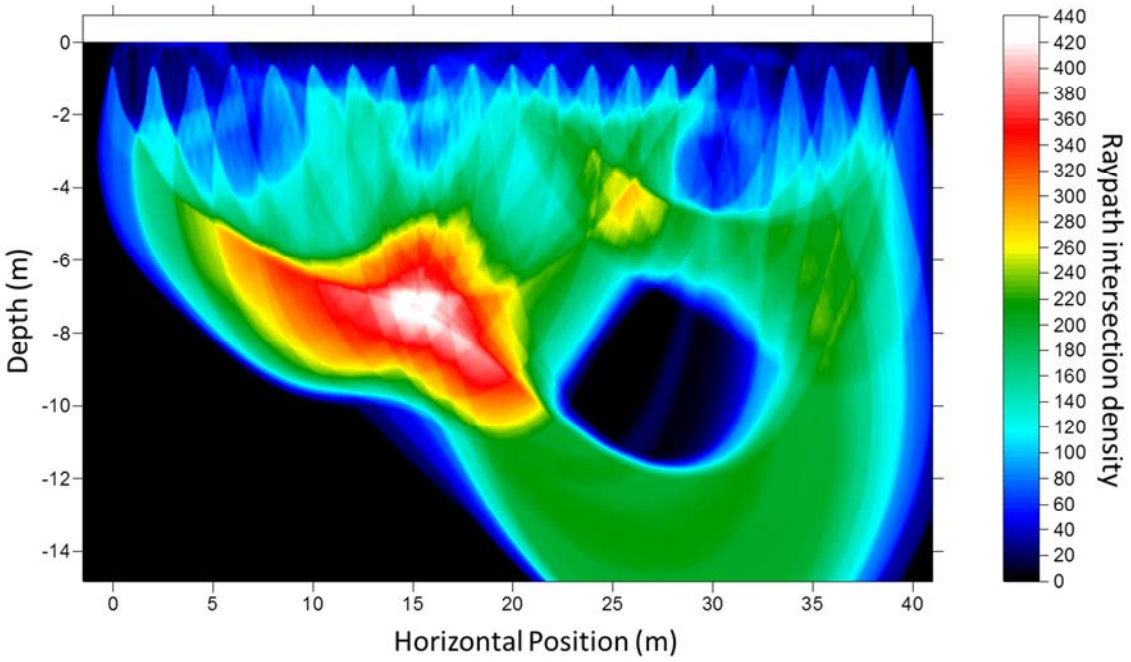
Depth (m)
0
-2
-4
-6
-8
-10
-12
-14
0
5
10
15
20
25
30
35
40
Horizontal Position (m)
Raypath intersection density
440
420
400
380
360
340
320
300
280
260
240
220
200
180
160
140
120
100
80
60
40
20
0

150°

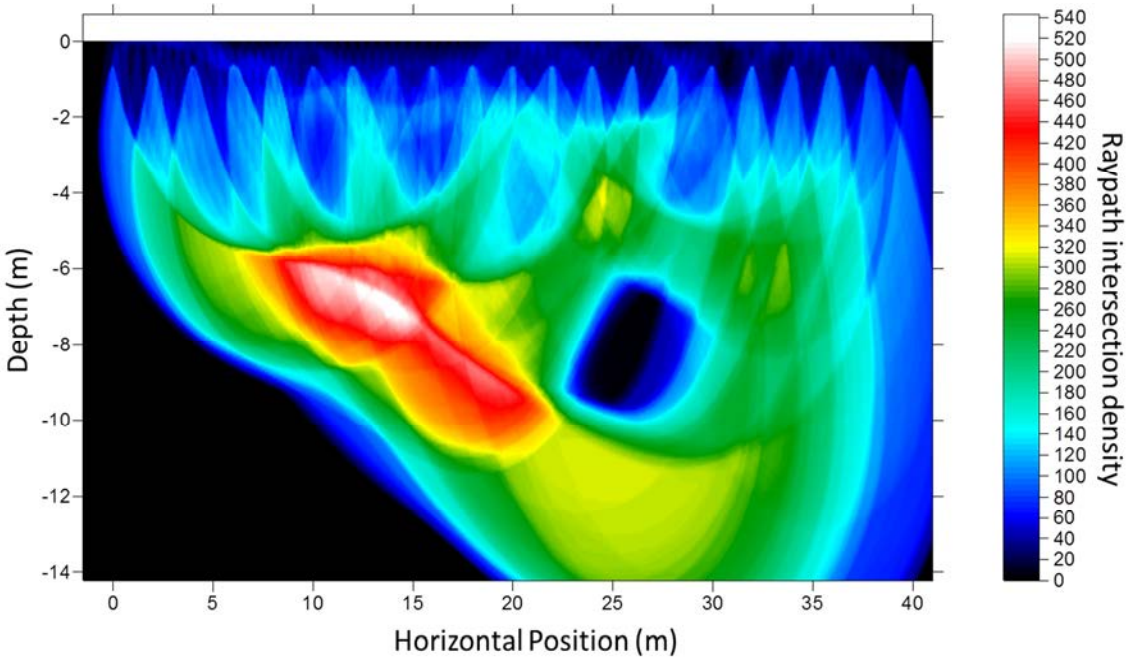
Depth (m)
0
-2
-4
-6
-8
-10
-12
-14
0
5
10
15
20
25
30
35
40
Horizontal Position (m)
Raypath intersection density
540
520
500
480
460
440
420
400
380
360
340
320
300
280
260
240
220
200
180
160
140
120
100
80
60
40
20
0

160°

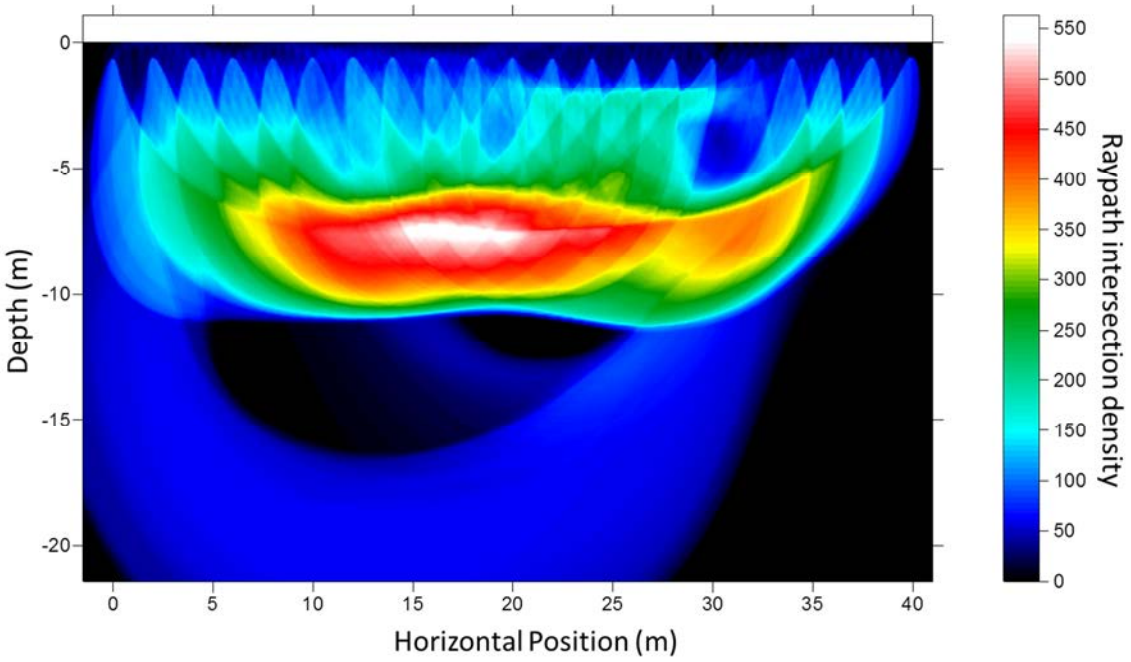
Depth (m)
0
-5
-10
-15
-20
0
5
10
15
20
25
30
35
40
Horizontal Position (m)
Raypath intersection density
550
500
450
400
350
300
250
200
150
100
50
0

170°

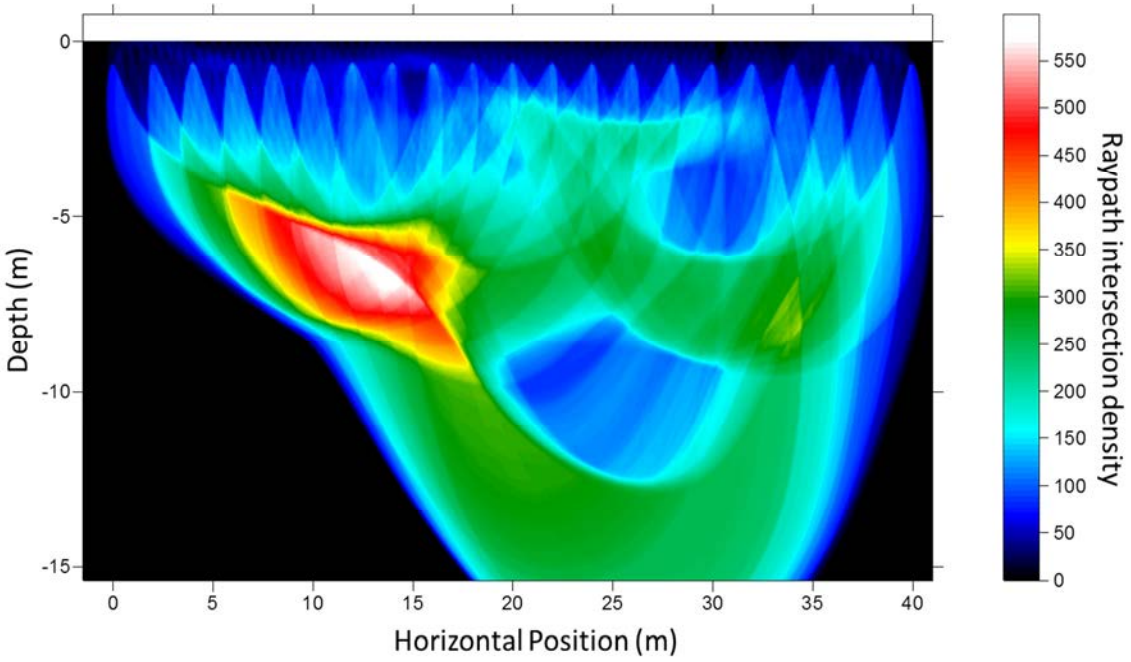

Velocity Tomograms:

0°

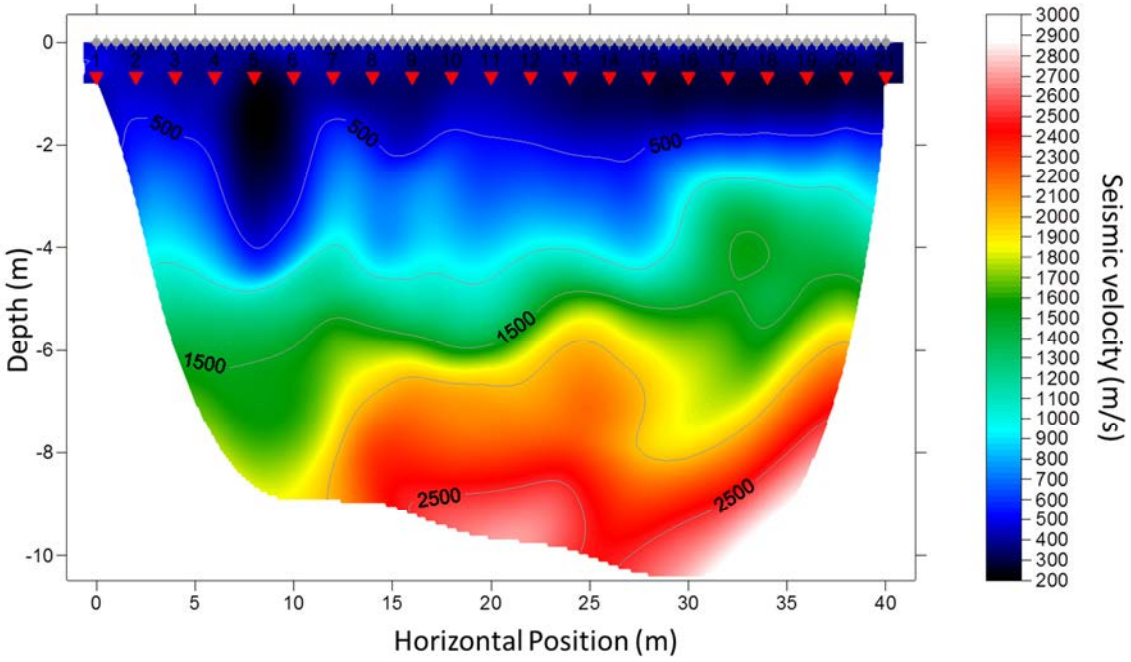

10°

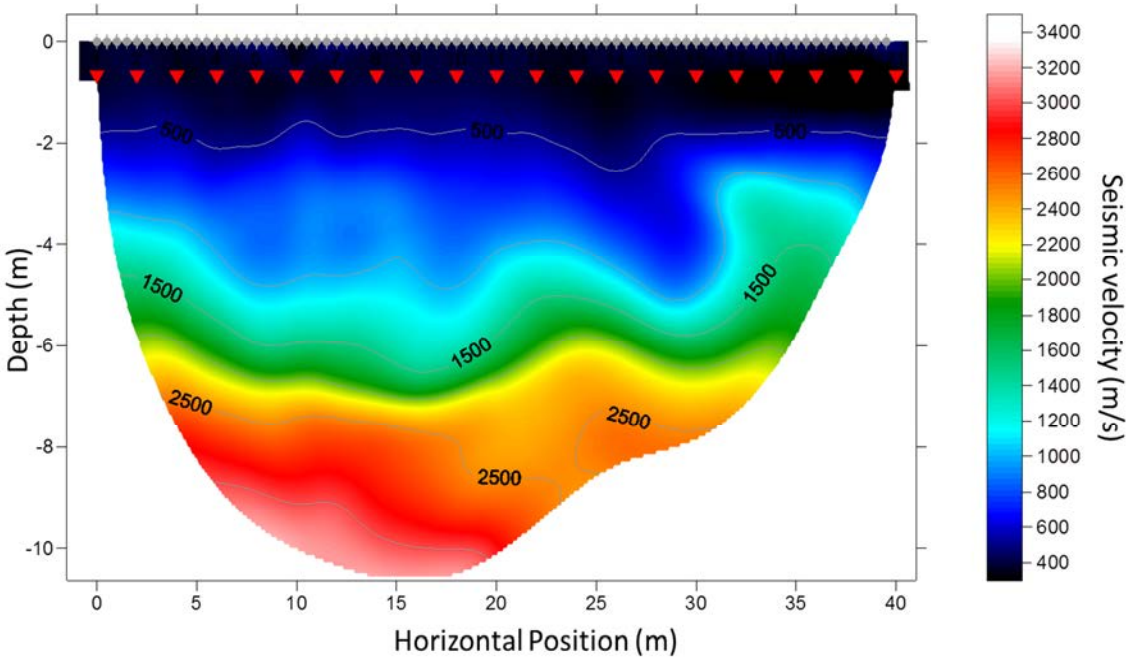
Depth (m)
Horizontal Position (m)
Seismic velocity (m/s)
500
1500
2500

20°

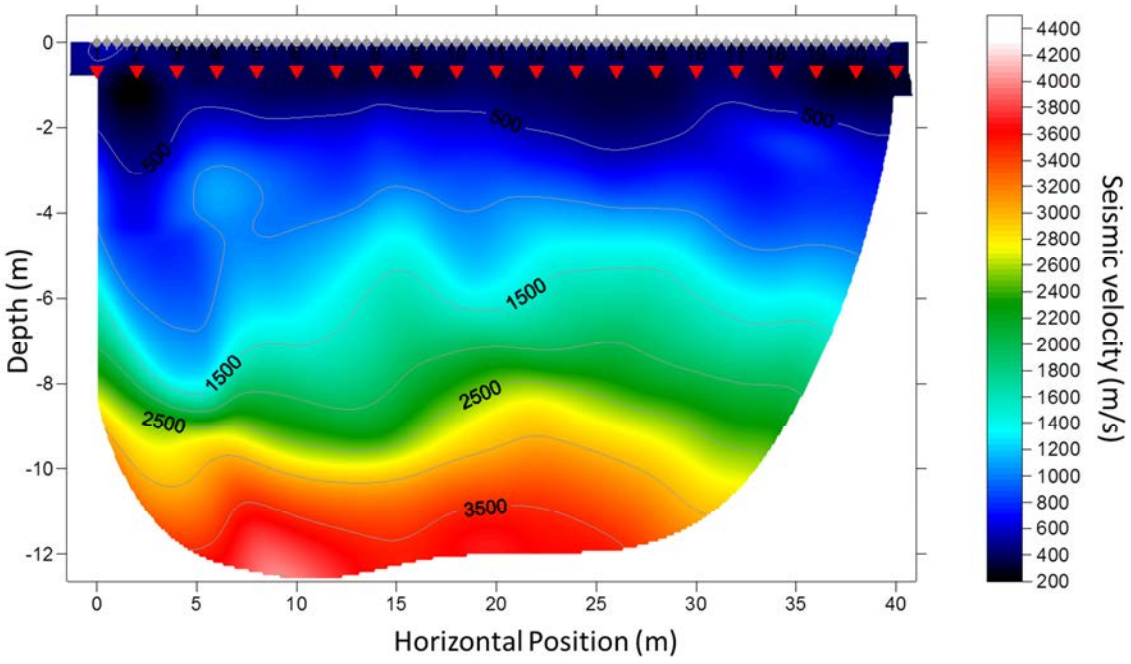
Depth (m)
Horizontal Position (m)
Seismic velocity (m/s)
500
1500
2500
3500

30°

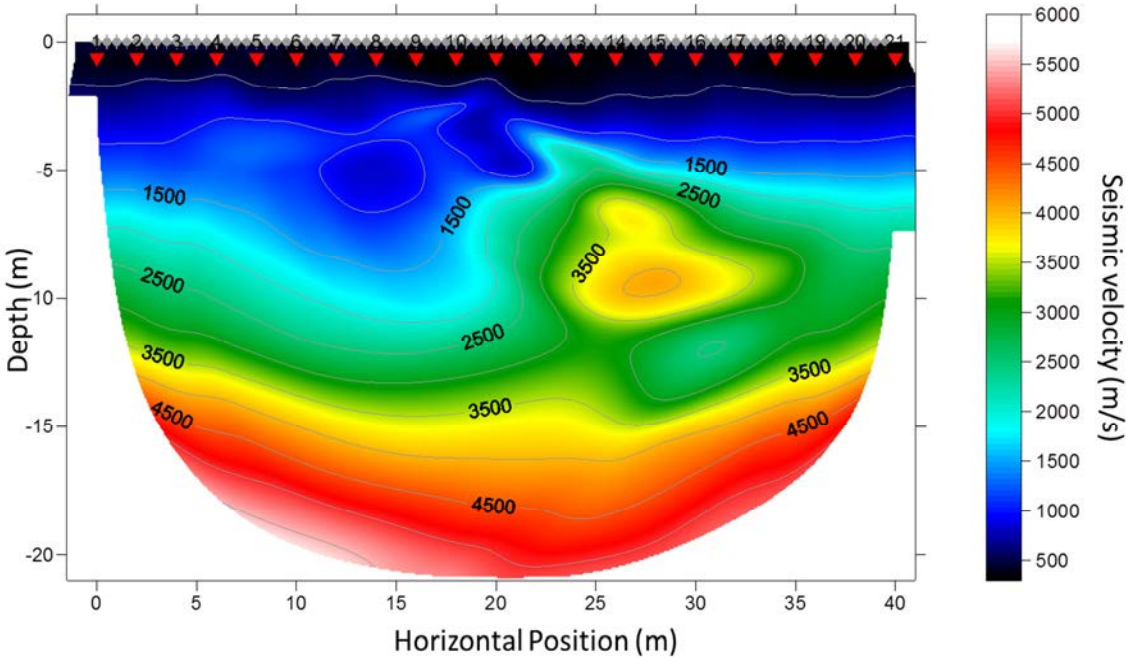
Depth (m)
Horizontal Position (m)
Seismic velocity (m/s)
1500
2500
3500
4500

40°

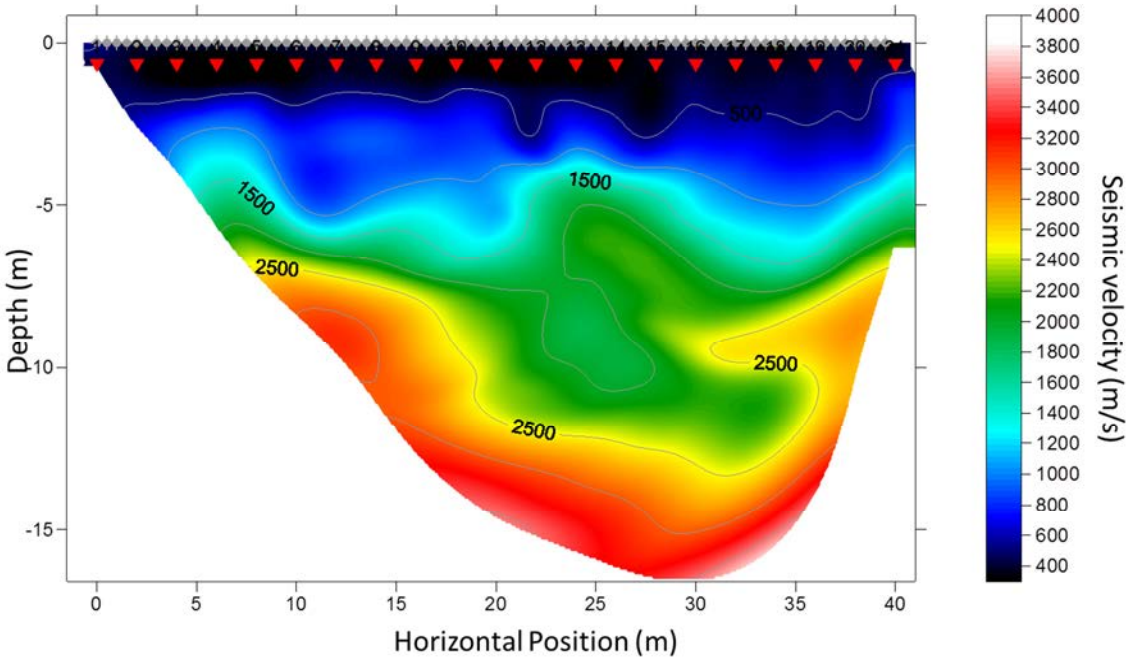
Depth (m)
Horizontal Position (m)
Seismic velocity (m/s)
500
1500
2500

50°

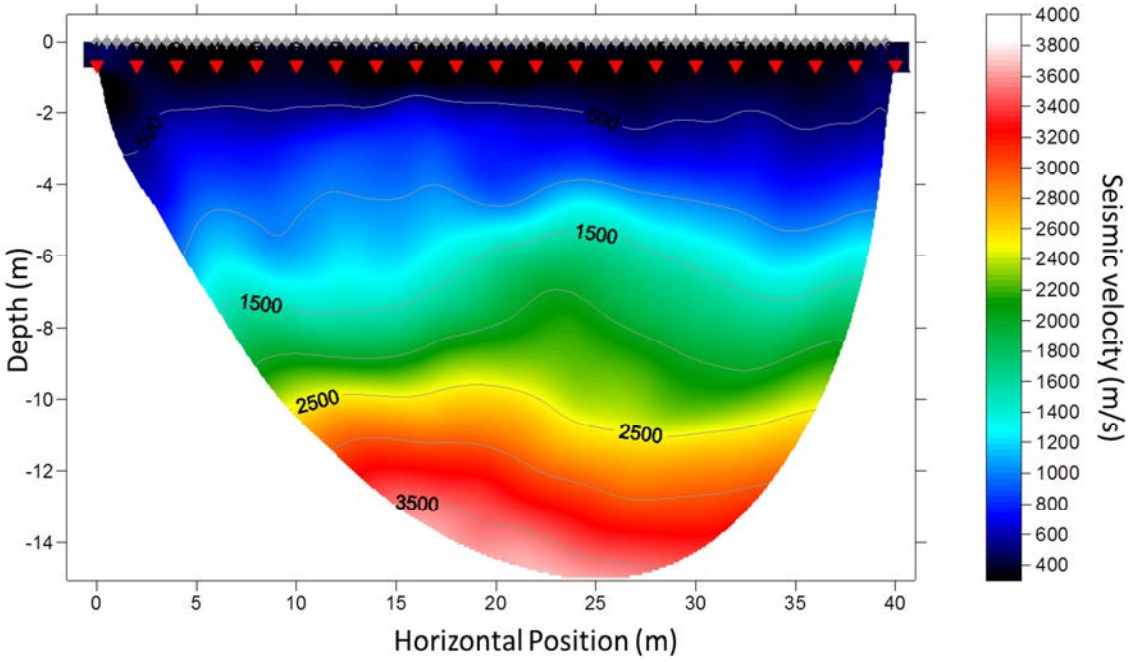
Depth (m)
0
-2
-4
-6
-8
-10
-12
-14
500
500
1500
1500
1500
2500
2500
3500
0
5
10
15
20
25
30
35
40
Horizontal Position (m)
Seismic velocity (m/s)
4000
3800
3600
3400
3200
3000
2800
2600
2400
2200
2000
1800
1600
1400
1200
1000
800
600
400

60°

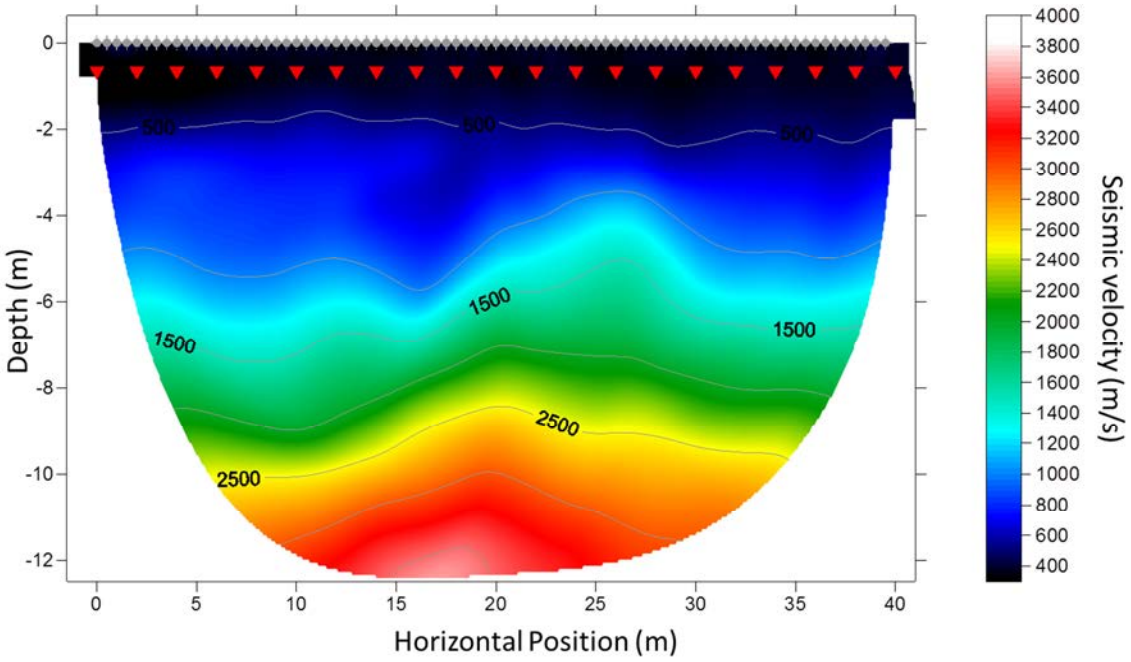
Depth (m)
0
-2
-4
-6
-8
-10
-12
500
500
500
1500
1500
1500
2500
2500
0
5
10
15
20
25
30
35
40
Horizontal Position (m)
Seismic velocity (m/s)
4000
3800
3600
3400
3200
3000
2800
2600
2400
2200
2000
1800
1600
1400
1200
1000
800
600
400

70°

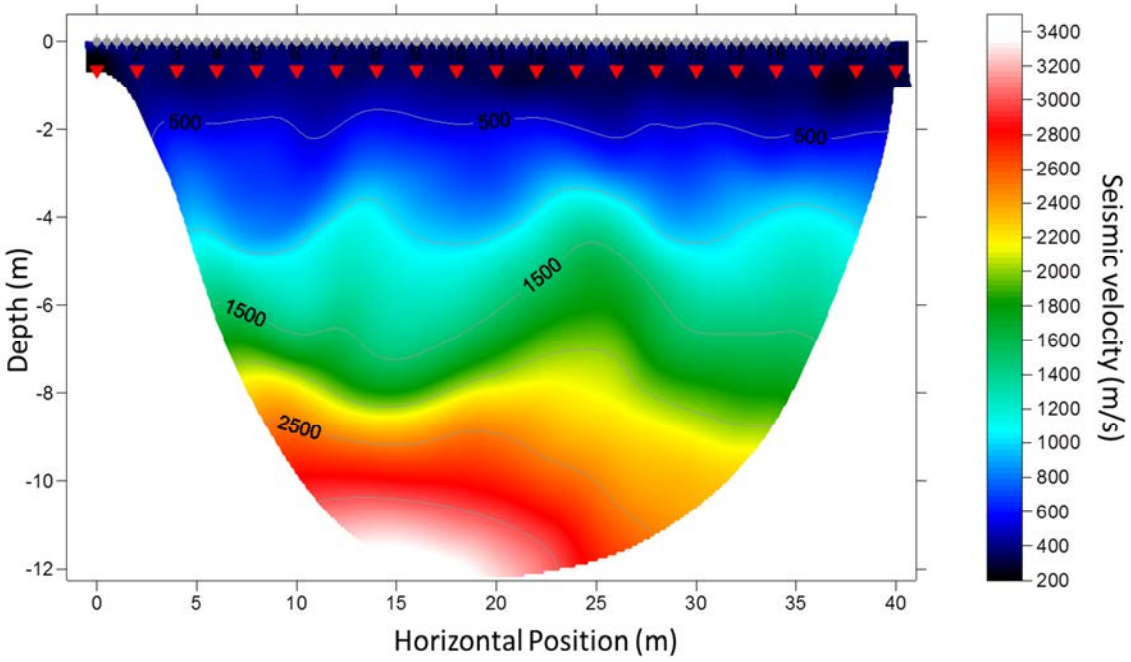
Depth (m)
0
-2
-4
-6
-8
-10
-12
500
500
500
1500
1500
2500
0
5
10
15
20
25
30
35
40
Horizontal Position (m)
Seismic velocity (m/s)
3400
3200
3000
2800
2600
2400
2200
2000
1800
1600
1400
1200
1000
800
600
400
200

80°

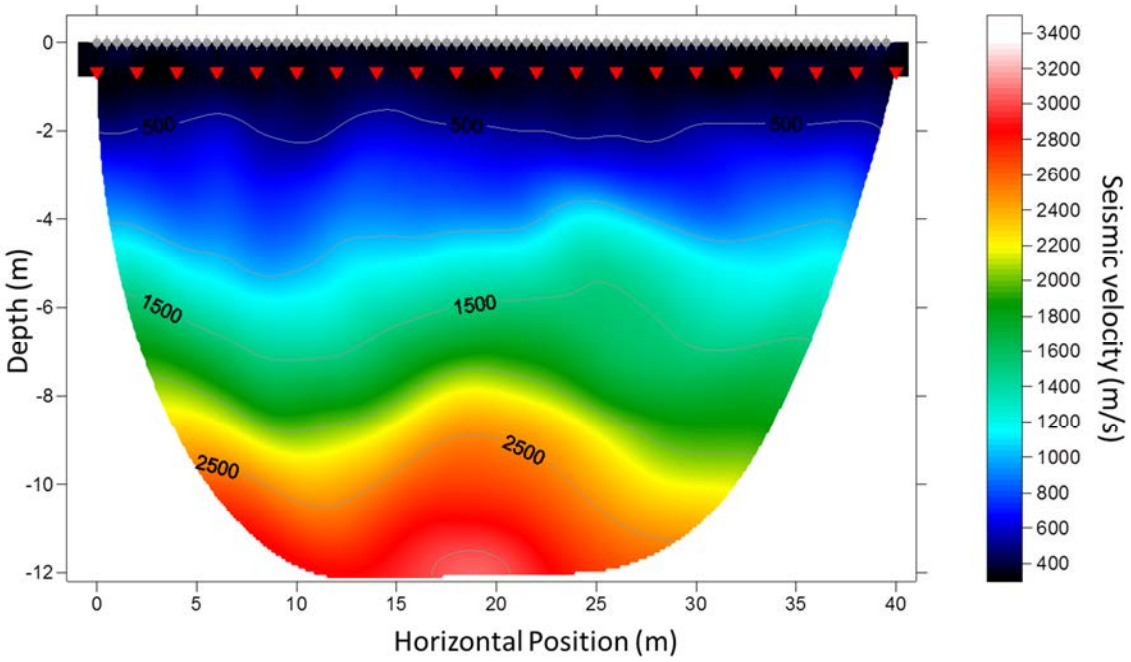
Depth (m)
0
-2
-4
-6
-8
-10
-12
500
500
500
1500
1500
2500
2500
0
5
10
15
20
25
30
35
40
Horizontal Position (m)
Seismic velocity (m/s)
3400
3200
3000
2800
2600
2400
2200
2000
1800
1600
1400
1200
1000
800
600
400

90°

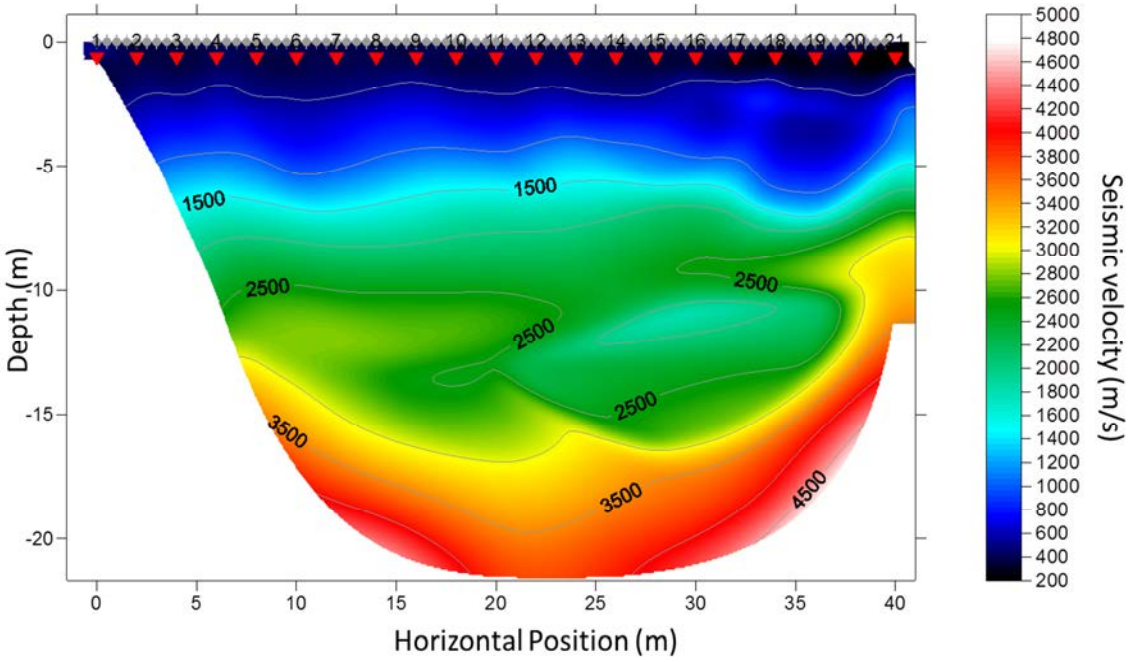
1 2 3 4 5 6 7 8 9 10 11 12 13 14 15 16 17 18 19 20 21
0
-5
-10
-15
-20
Depth (m)
1500
1500
2500
2500
2500
2500
3500
3500
4500
0 5 10 15 20 25 30 35 40
Horizontal Position (m)
5000 4800 4600 4400 4200 4000 3800 3600 3400 3200 3000 2800 2600 2400 2200 2000 1800 1600 1400 1200 1000 800 600 400 200
Seismic velocity (m/s)

100°

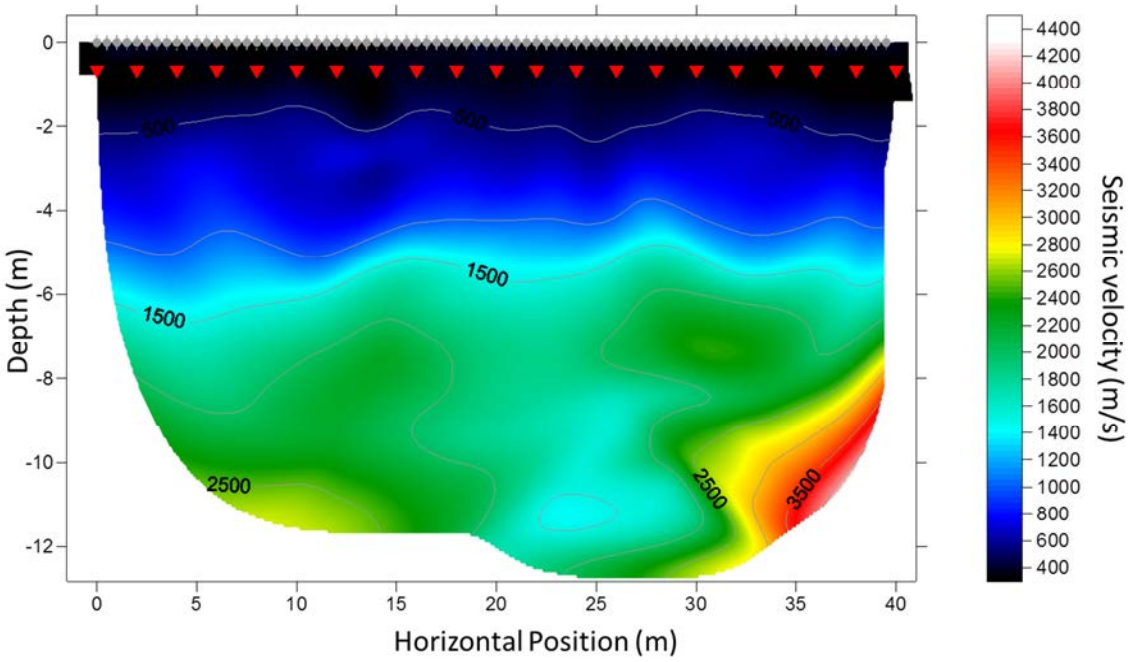
0
-2
-4
-6
-8
-10
-12
Depth (m)
500
500
500
1500
1500
2500
2500
3500
0 5 10 15 20 25 30 35 40
Horizontal Position (m)
4400 4200 4000 3800 3600 3400 3200 3000 2800 2600 2400 2200 2000 1800 1600 1400 1200 1000 800 600 400
Seismic velocity (m/s)

110°

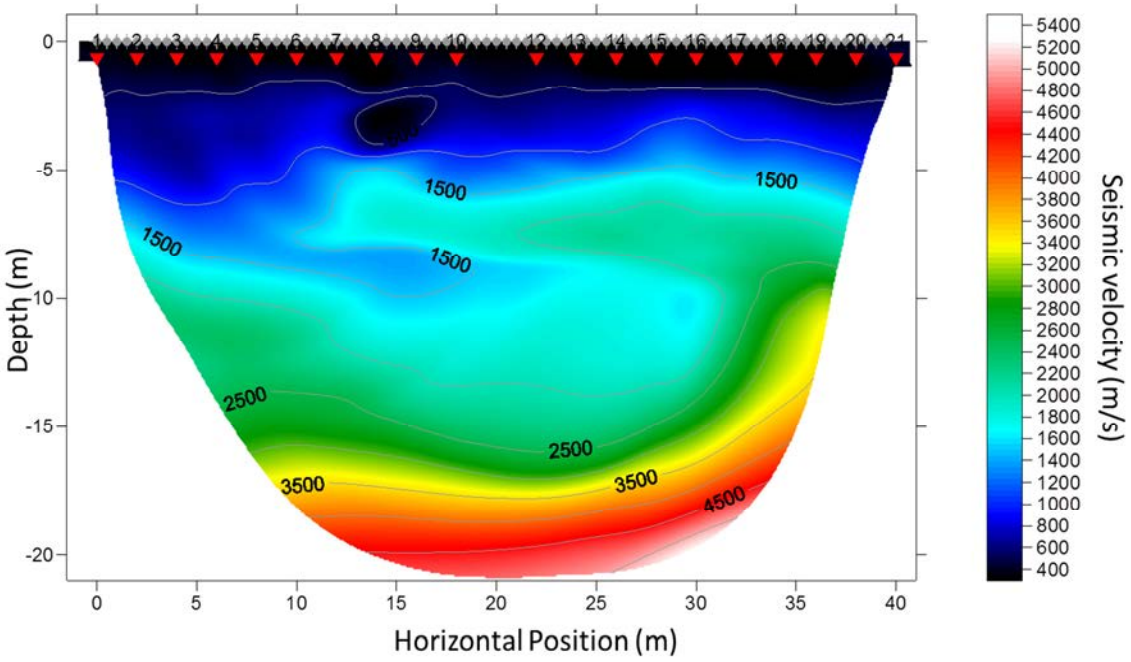
Depth (m)
Horizontal Position (m)
Seismic velocity (m/s)
1500
2500
3500
4500

120°

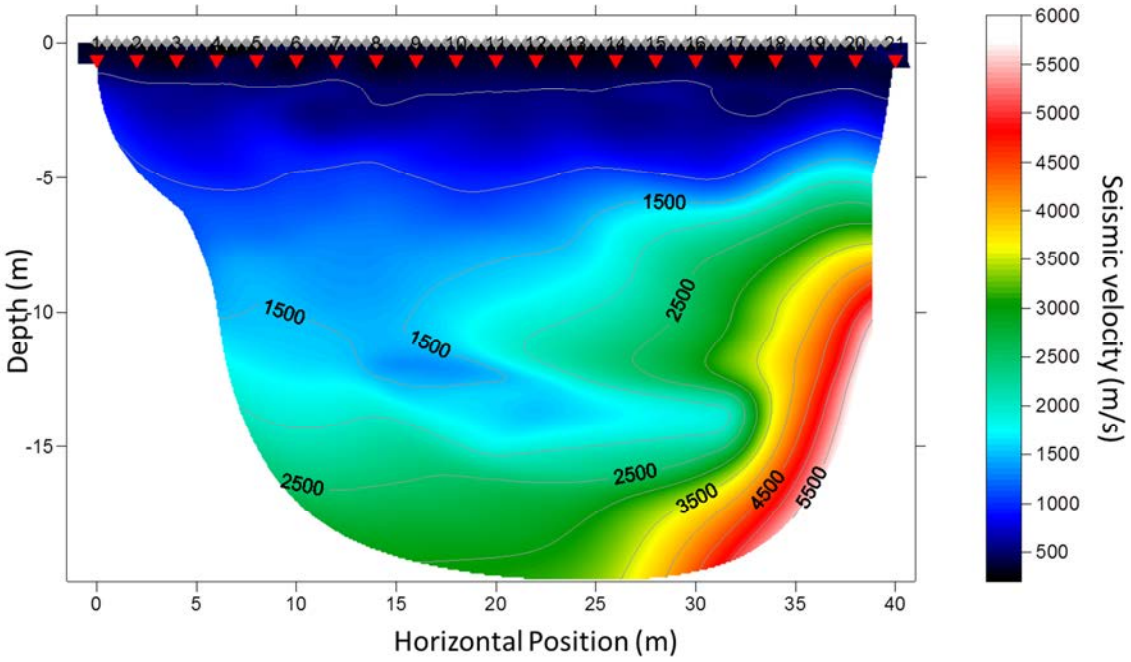
Depth (m)
Horizontal Position (m)
Seismic velocity (m/s)
1500
2500
3500
4500
5500

130°

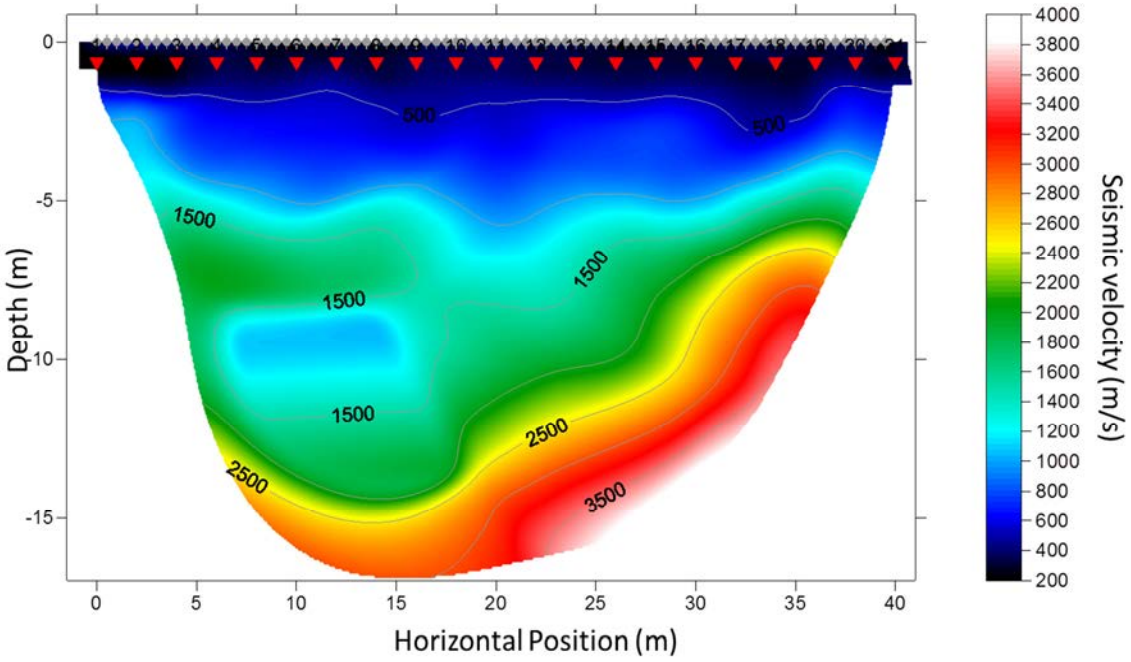
Depth (m)
0
-5
-10
-15
500
1500
2500
3500
Horizontal Position (m)
0
5
10
15
20
25
30
35
40
Seismic velocity (m/s)
4000
3800
3600
3400
3200
3000
2800
2600
2400
2200
2000
1800
1600
1400
1200
1000
800
600
400
200

140°

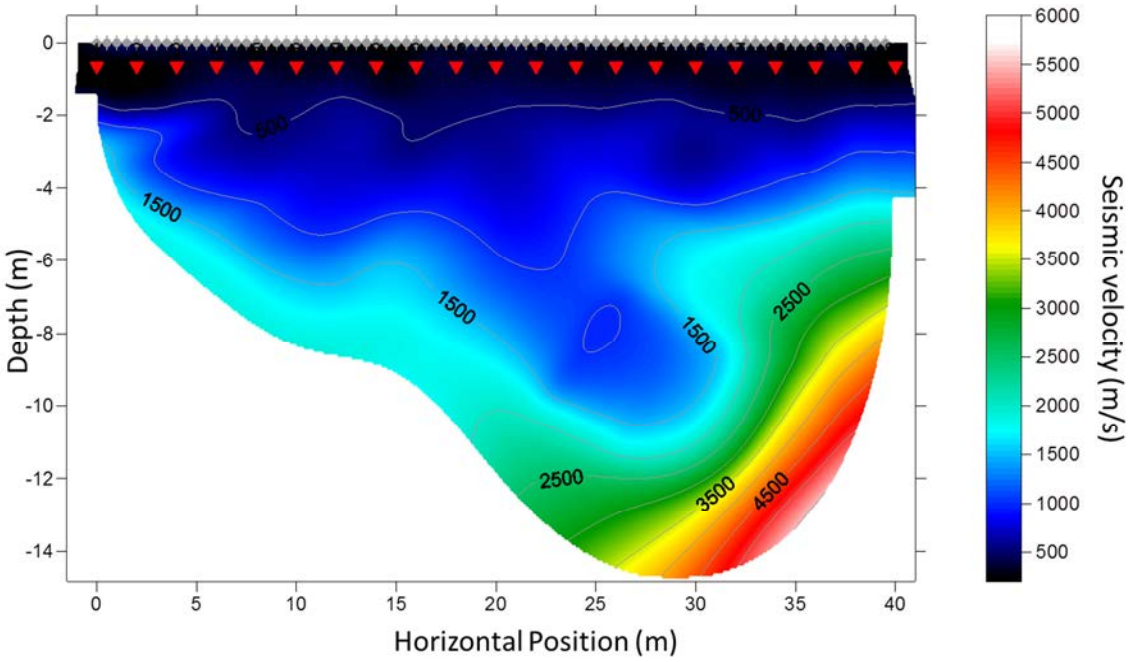
Depth (m)
0
-2
-4
-6
-8
-10
-12
-14
500
1500
2500
3500
4500
Horizontal Position (m)
0
5
10
15
20
25
30
35
40
Seismic velocity (m/s)
6000
5500
5000
4500
4000
3500
3000
2500
2000
1500
1000
500

150°

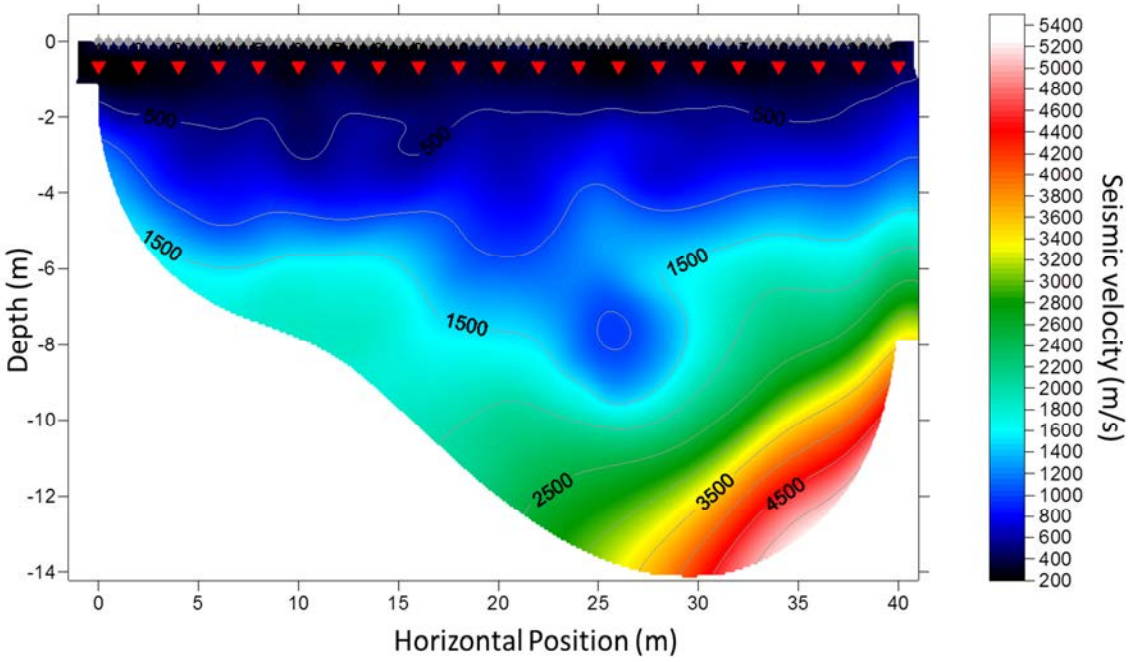
Depth (m)
Horizontal Position (m)
Seismic velocity (m/s)
500
1500
2500
3500
4500

160°

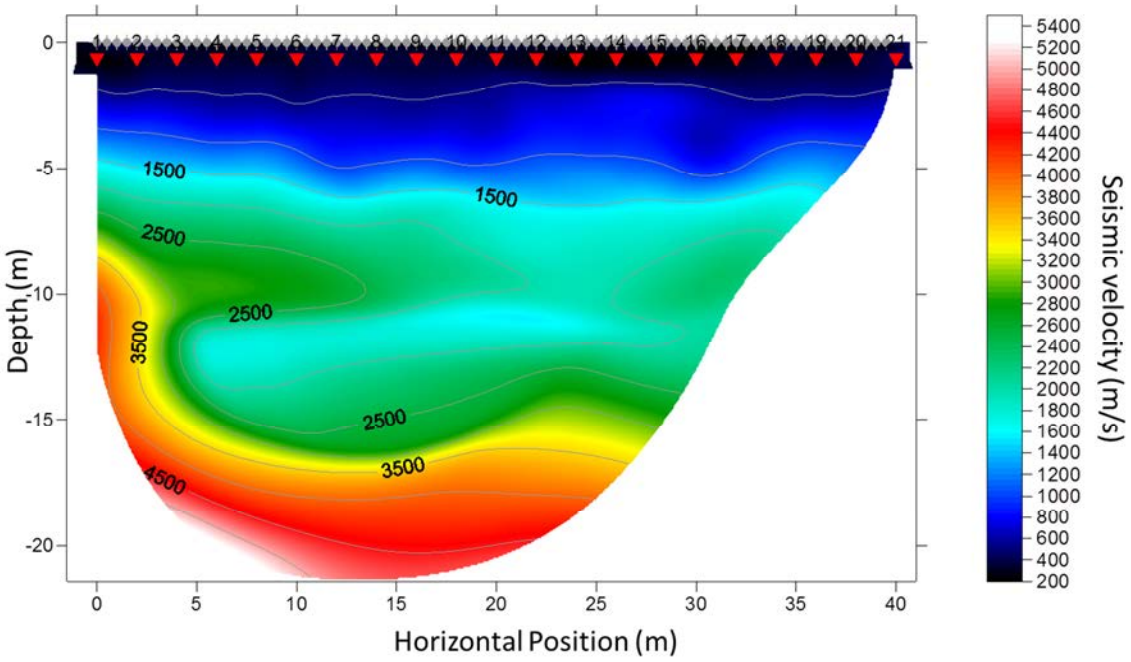
Depth (m)
Horizontal Position (m)
Seismic velocity (m/s)
1500
2500
3500
4500

170°

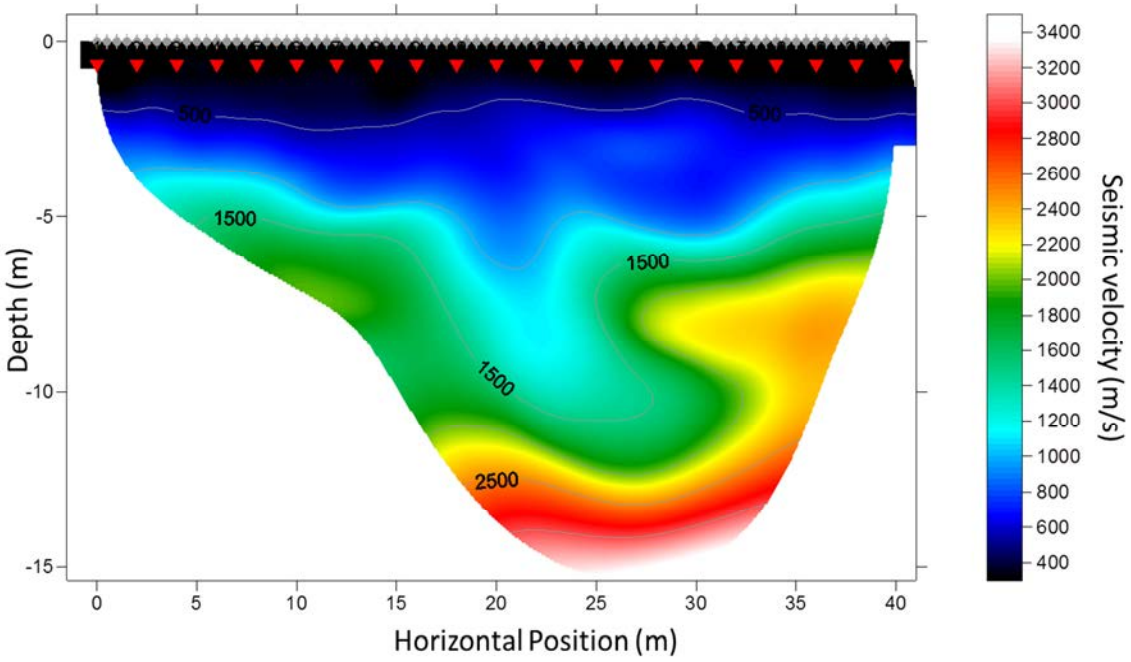

Compass Diagrams:

0 m

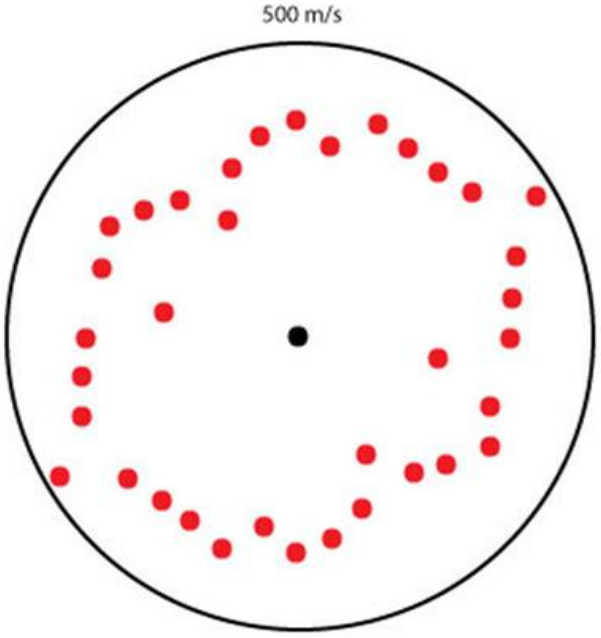

0.5 m

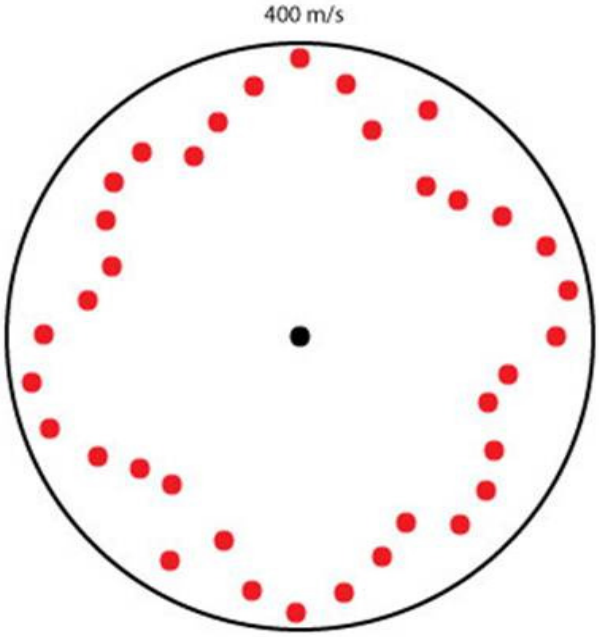

1 m

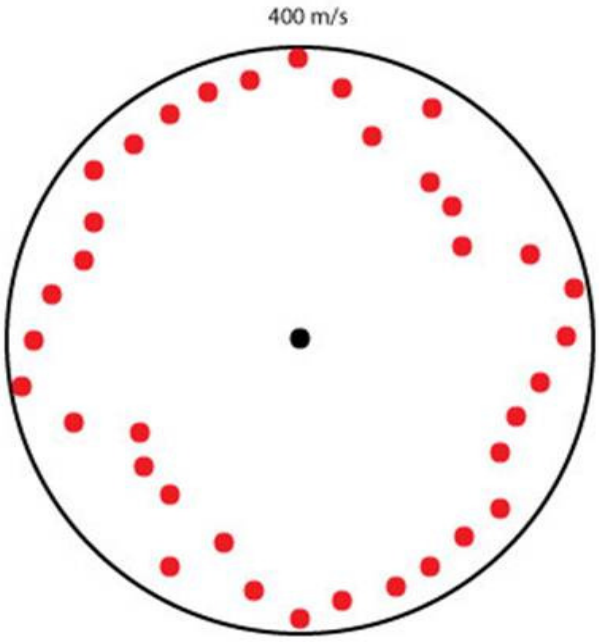

1.5 m

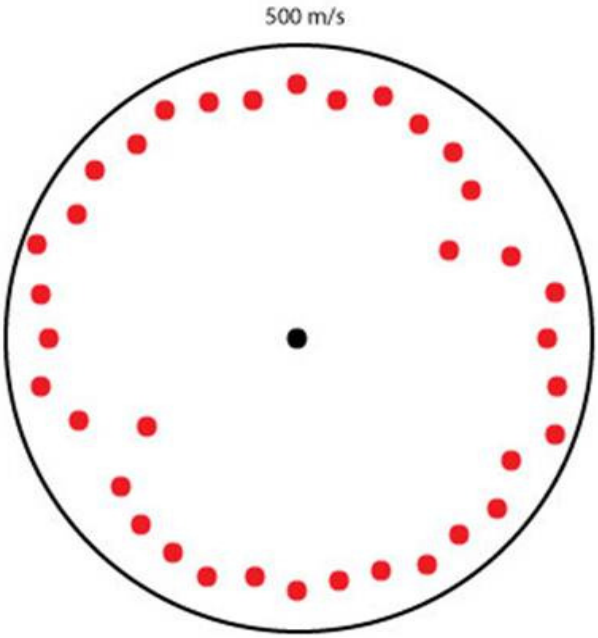

2 m

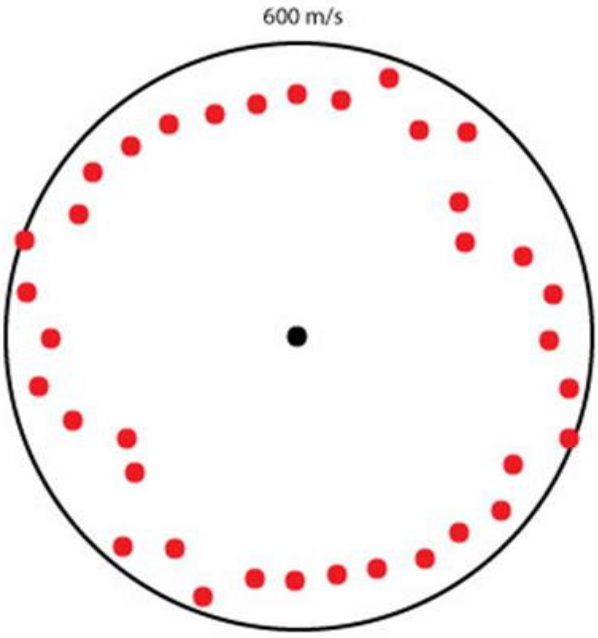

2.5 m

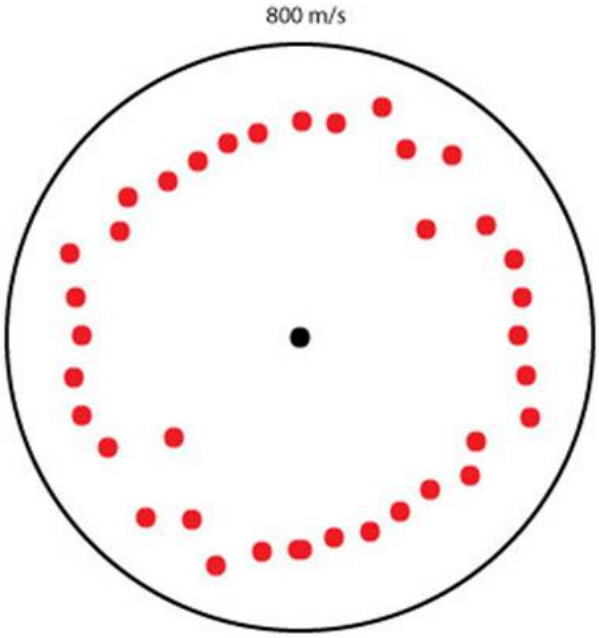

3 m

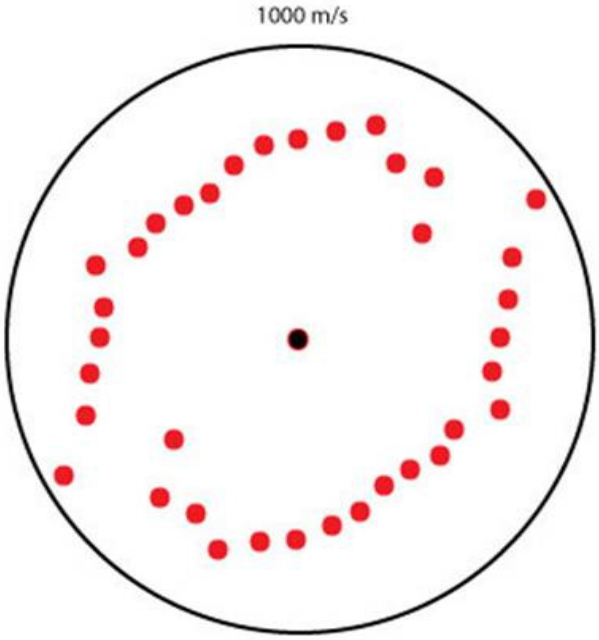

3.5 m

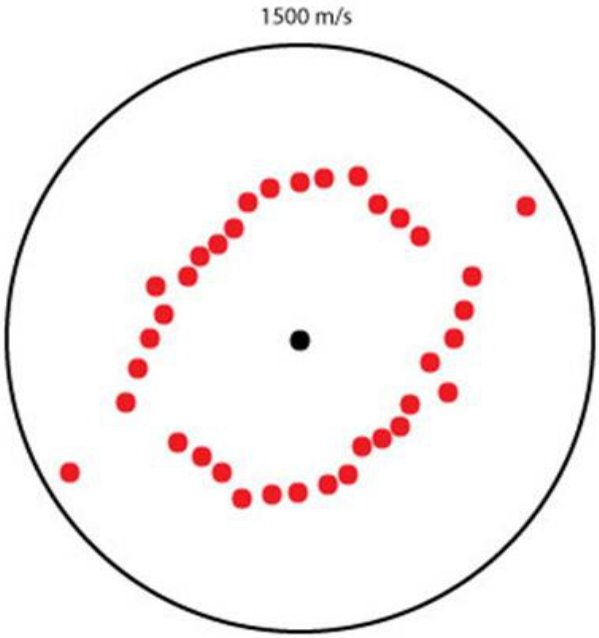

4 m

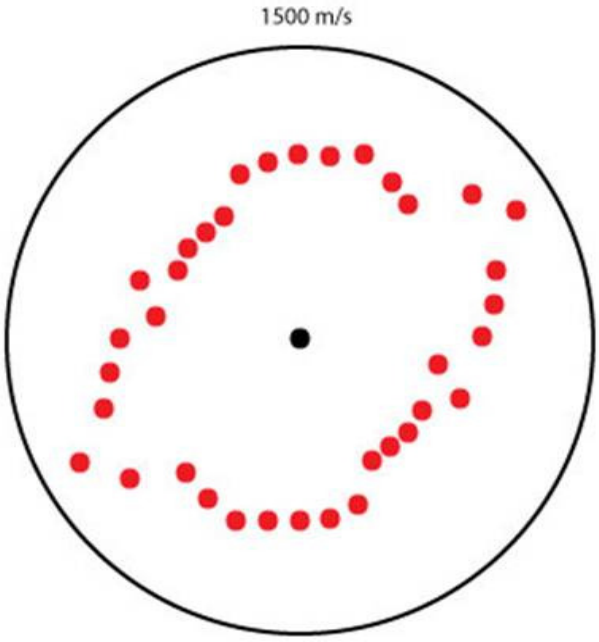

4.5 m

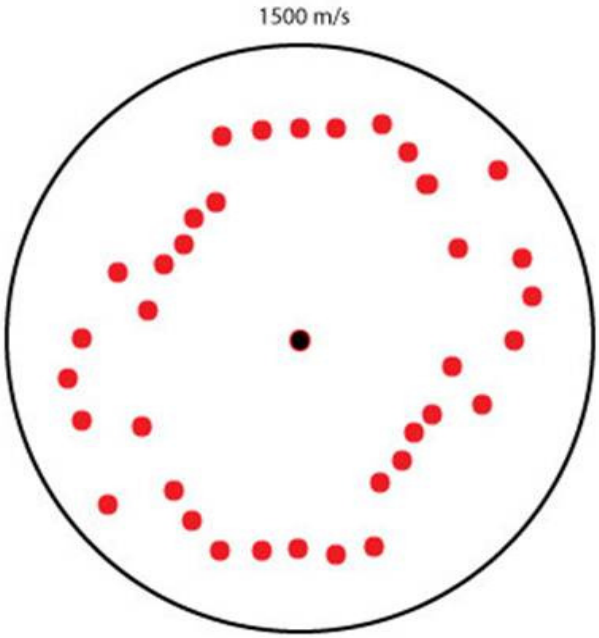

5 m

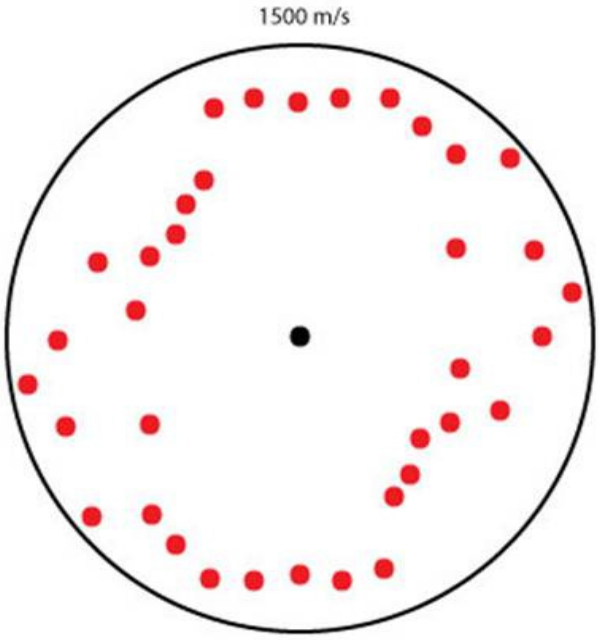

5.5 m

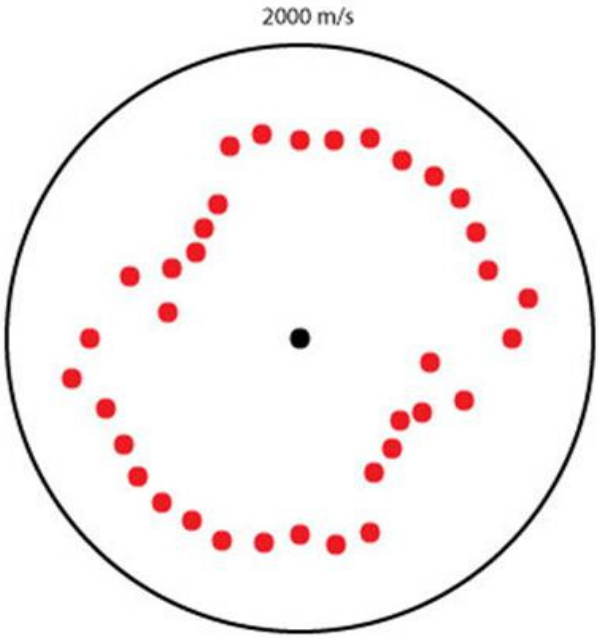

6 m

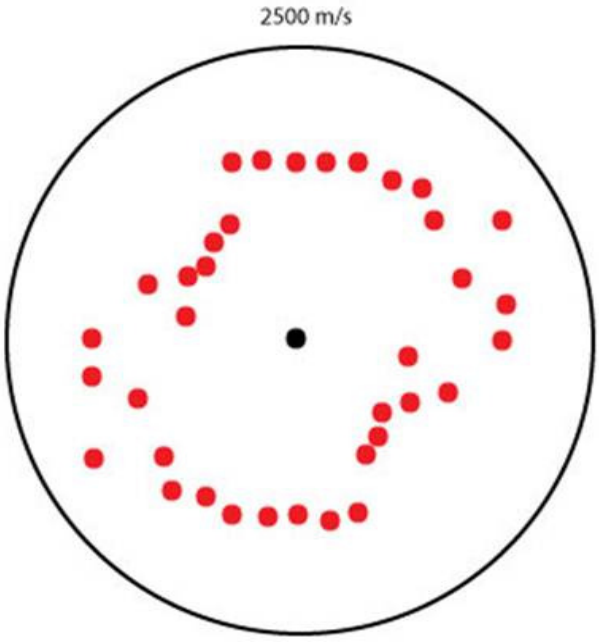

6.5 m

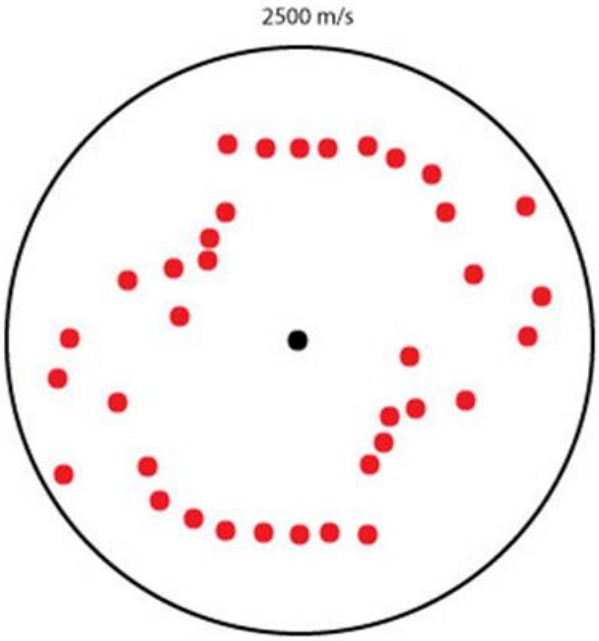

7 m

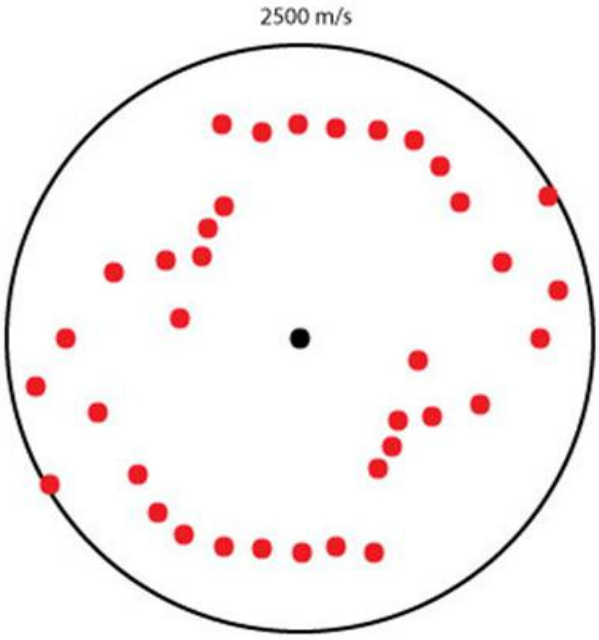

7.5 m

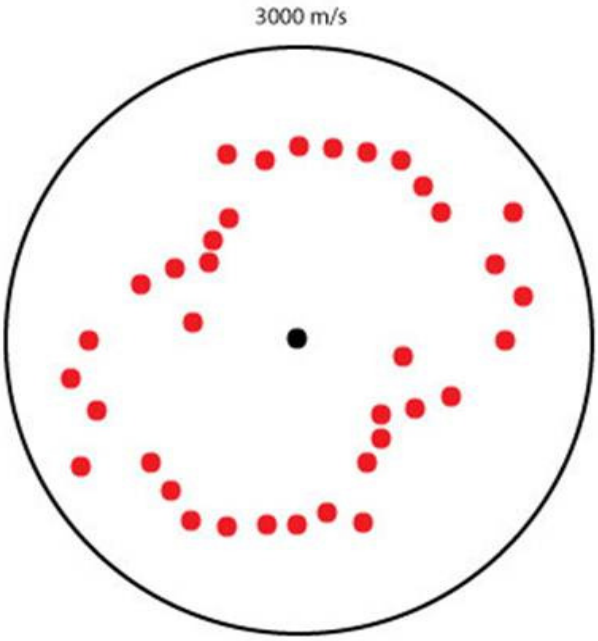

8 m

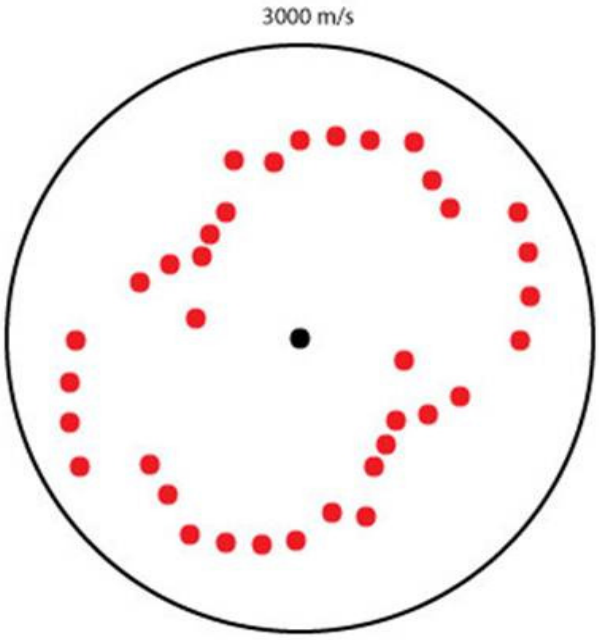

8.5 m

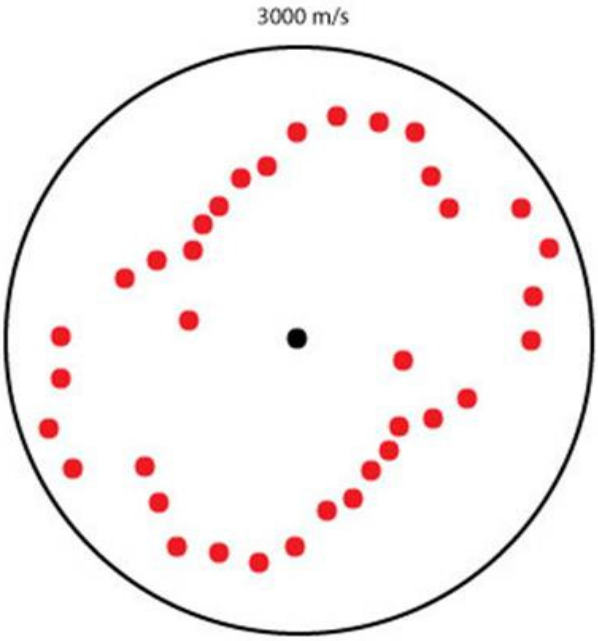

9 m

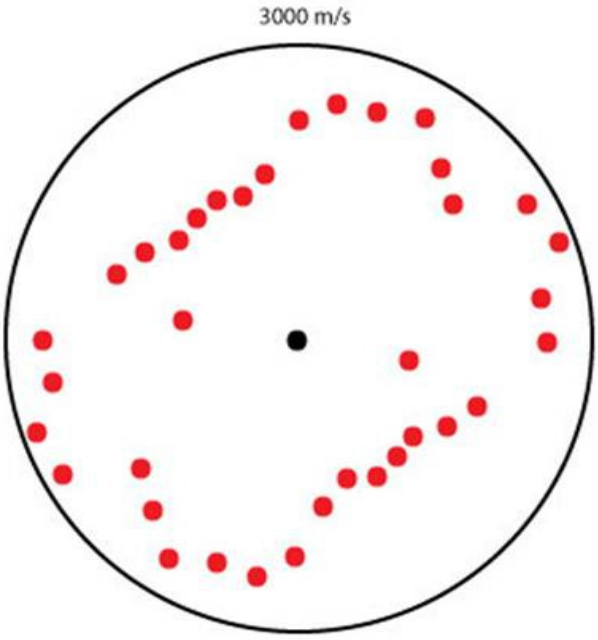

9.5 m

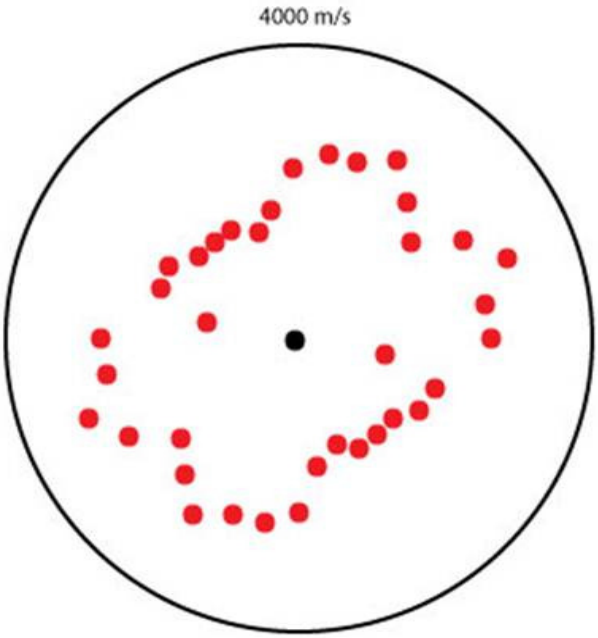

Appendix 4: Matlab code used to generate compass diagrams

```
dir = [*insert azimuth matrix*

];

vel = [*insert velocity matrix*

];

cdir = dir-90;

rdir = cdir*pi/180;

[x,y]=pol2cart(rdir,vel);

compass(x,y)
```

VITA

Matthew Edmunds was born in Montgomery, Alabama in 1982. After a short stop in Gainesville, Georgia, he made his way to Knoxville, Tennessee, where he has lived ever since. Upon admittance to the University of Tennessee, Knoxville, he underwent a long series of seemingly unrelated studies, until he discovered that he really wanted to be a geologist. Upon the conferral of his BS in Geological Science in 2010, he decided to pursue postgraduate study, and began work on (and completed) his MS in geology with an emphasis on geophysics. Now that he is done with all that business, he thinks that it might be a good idea to board his spacecraft and embark on the return journey to his homeworld… or embark on a successful career in the geosciences.